ILMATIETEEN LAITOS
METEOROLOGISKA INSTITUTET
FINNISH METEOROLOGICAL INSTITUTE

156
CONTRIBUTIONS

APPLICATION OF REMOTELY-SENSED CLOUD PROPERTIES FOR CLIMATE STUDIES

GIULIA SAPONARO

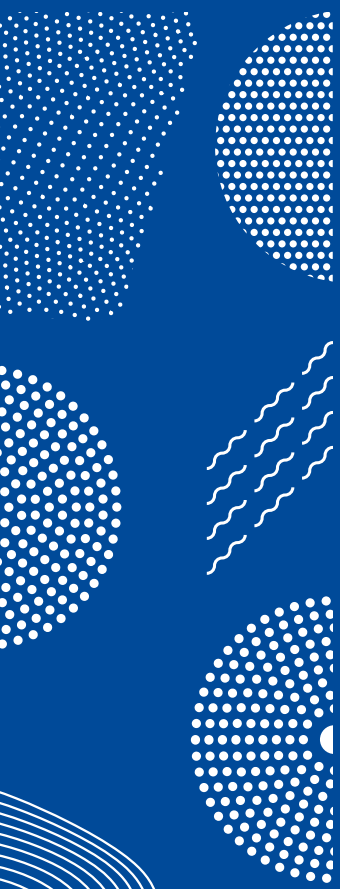

FINNISH METEOROLOGICAL INSTITUTE
CONTRIBUTIONS

No. 156

Application of remotely-sensed cloud properties for climate studies

Giulia Saponaro

Institute for Atmospheric and Earth System Research/Physics
Faculty of Science
University of Helsinki
Helsinki, Finland

ACADEMIC DISSERTATION in Physics
To be presented, with the permission of the Faculty of Science of the University of Helsinki, for public criticism in Brainstorm auditorium at Dynamicum, Erik Páklmenin Aukio 1, on January 8th, 2020, at 12 o'clock noon.

Finnish Meteorological Institute
Helsinki, 2020

Author's Address: Atmospheric Radiation
Finnish Meteorological Institute
P.O. Box 503
FI-00101 Helsinki, Finland
e-mail: giulia.saponaro@fmi.fi

Supervisors: Professor Gerrit de Leeuw, Ph.D.
Atmospheric Radiation
Finnish Meteorological Institute, Finland

Senior Scientist Pekka Kolmonen, Ph.D.
Atmospheric Radiation
Finnish Meteorological Institute, Finland

Reviewers Professor Kari Lehtinen, Ph.D.
University of Eastern Finland, Finland

Scientist Seiji Kato, Ph.D.
Climate Science Branch - Langley Research Center
National Aeronautics and Space Administration, USA

Custos Professor Veli-Matti Kerminen, Ph.D.
Institute for Atmospheric and Earth System Research
University of Helsinki, Finland

Opponent Doctor Nicolas Bellouin,
Meteorology Department
University of Reading, UK

ISBN 978-952-336-086-0 (paperback)
ISBN 978-952-336-087-7 (pdf)
ISSN 0782-6117

Printing House
Edita Prima Oy
Helsinki, 2020

Acknowledgments

The research presented in this work has been carried out at the Finnish Meteorological Institute. Ari Laaksonen, Sami Romakkaniemi and Hannele Korhonen are acknowledge for providing the work facilities.
I am deeply grateful to Prof. Gerrit de Leeuw, who originally hired me as an undergraduate student and introduced me to optical remote sensing. Thank you Gerrit for the trust you placed in me and in my work.
I ackowledge the pre-examiners Dr. Seiji Kato and Prof. Kari Lehtinen for their valuable comments on this thesis.

Thank you to all my colleagues (and friends). In particular from the Atmospheric Radiation group (former Aerosol and Cloud Remote Sensing group) I would like to mention Timo Virtanen, Larisa Sogacheva and Antti Arola for the good scientific collaboration, conversations and advices in a friendly environment. Additional and special thanks to Pekka Kolmonen, my supervisor, for his support during this PhD work.

I would like to thank my RI colleagues for cheering me trough this process to the finish line. In primis, the ACTRIS HO team: Sanna, Marjut, Eija, Anna, Niku, Silja, Edith, Päivi, Misha, Simo and Anniina.
Thank you Ulpu and Magdalena for the support, the great company during our trips and your friendship beyond work. Anca, every day I am grateful to share with you moment of joy, anger and muscles soreness.

I acknowledge the funding agencies and institutions that enabled me to attend international conferences and workshops during these years: the Maj and Tor Nessling foundation, the European Commission and, of course, the Finnish Meteorological Institute.

Finally, not by order of importance, I would like to thank my family for their support, encouragement and love. Thank you Antti for convincing me that anything is possible once you unlock what is between your ears. To my brother Andrea, thank you for the lunch-break phone calls. I owe my gratitude to my parents Enzo and Luigina: tutto ció che faccio é anche per voi.

ILMATIETEEN LAITOS
METEOROLOGISKA INSTITUTET
FINNISH METEOROLOGICAL INSTITUTE

Published by Finnish Meteorological Institute
(Erik Palménin aukio 1), P.O. Box 503
FIN-00101 Helsinki, Finland

Series title, number and report code of publication
Finnish Meteorological Institute
Contributions 156, FMI-CONT-156
Date
January 2020

Author
Giulia Saponaro

Title
Application of remotely-sensed cloud properties for climate studies

Abstract
Clouds play a vital role in Earth's energy balance by modulating atmospheric processes, thus it is crucial to have accurate information on their spatial and temporal variability. Furthermore, clouds are relevant in those processes involved in aerosol-cloud-radiation interactions. The work conducted and presented herein concentrates on the retrievals of cloud properties, as well as their application for climate studies. While remote sensing observation systems have been used to analyze the atmosphere and observe its changes for the last decades, climate models predict how climate will change in the future. Altogether, these sources of observations are needed to better understand cloud processes and their impact on climate. In this thesis aerosol and cloud properties from the three above mentioned sources are applied to evaluate their potential in representing cloud properties and applicability in climate studies on local, regional and global scales.

One aim of this thesis focuses on evaluating cloud parameters from ground-based remote-sensing sensors and from climate models using the MODerate Imaging Spectroradiometer (MODIS) data as a reference dataset. It is found that ground-based measurements of liquid clouds are in good agreement with MODIS cloud droplet size while poor correlation is found in the amount of cloud liquid water due to the management of drizzle. The comparison of the cloud diagnostic from three climate models with MODIS data, enabled through the application of a satellite simulator, helped to understand discrepancies among models, as well as discover deficiencies in their simulation processes. These findings are important to further improve the parametrization of atmospheric constituents in climate models, therefore enhancing the accuracy of climate projections.

In this thesis it is also assessed the impact of aerosol particles on clouds. Satellite data can be used to derive climatically crucial quantities that are otherwise not directly retrieved (such as aerosol index and cloud droplet number concentration) which can be used to infer the sensitivity of clouds to aerosols changes. Results on the local and regional scales show that contrasting aerosol backgrounds indicate a higher sensitivity of clouds to aerosol changes in cleaner ambient air and a lower sensitivity in polluted areas, further corroborating the notion that anthropogenic emission modify clouds. On the global scale, the estimates of the aerosol-cloud interaction present, overall, a good agreement between the satellite- and model-based values which are in line with the results from other models.

Publishing unit
Finnish Meteorological Institute

Classification (UDC)	Keywords	
591.543	Climate	
52-852	Atmosphere	
528.8	Remote sensing	
ISSN and series title		
0782-6117 Finnish Meteorological Institute Contributions		
ISBN	Language	Pages
978-952-336-086-0 (paperback), ISBN 978-952-336-087-7 (pdf)	English	62

Contents

List of publications

I G. Saponaro, P. Kolmonen, J. Karhunen, J. Tamminen, and G. de Leeuw, A neural network algorithm for cloud fraction estimation using NASA-Aura OMI VIS radiance measurements, *Atmospheric Measurement Techniques*, 6, 2301–2309, 2013.

II J. Preißler, G. Martucci, G. Saponaro, J. Ovadnevaite, A. Vaishya, P. Kolmonen, D. Cerburis, L. Sogacheva, G. de Leeuw, and C. O'Dowd, Six years of surface remote sensing of stratiform warm clouds in marine and continental air over Mace Head, Ireland, *Journal of Geophysical Research: Atmospheres*, 121, 14, 538–14, 557, 2016.

III G. Saponaro, P. Kolmonen, L. Sogacheva, E. Rodriguez, T. Virtanen and G. de Leeuw, Estimates of the aerosol indirect effect over the Baltic Sea region derived from 12 years of MODIS observations, *Atmospheric Chemistry and Physics*, 17, 4, 3133–3143, 2017.

IV G. Saponaro, M. K. Sporre, D. Neubauer, H. Kokkola, P. Kolmonen, L. Sogacheva, A. Arola, G. de Leeuw, I. H. H. Karset, A. Laaksonen, U. Lohmann, Evaluation of aerosol and cloud properties in three climate models using MODIS observations and its corresponding COSP simulator, and their application in aerosol-cloud interactions, *Atmospheric Chemistry and Physics Discussions.*

1. Introduction

Clouds play a key role in the climate system and are crucially important for climate change. As Earth's energy balance is determined by the amount of incoming shortwave solar radiation (sunlight) and the outgoing longwave radiation (mid- and thermal-infrared) emitted from the surface and the atmosphere, clouds can alter this balance and affect the Earth's climate system in a variety of ways (Stephens, 2005). Clouds can both absorb and reflect solar radiation, cooling the Earth's surface, and absorb and emit longwave radiation, warming the Earth's surface (Wallace and Hobbs, 2006; Seinfeld and Pandis, 2006; Lamb and Verlinde, 2011; Lohmann et al., 2016) as shown schematically in Fig.1.

The competition between these effects is regulated by the characteristics of clouds, such as cloud height, thickness, and radiative properties (Painemal, 2018; Goldblatt and J. Zahnle, 2011; Aebi et al., 2017). The complexity of clouds and their interactions with solar radiation represent the greatest difficulties in quantifying the effects of clouds on climate and in future projections of climate change (Flato et al., 2013). Clouds can rapidly transport air, energy, moisture, trace gases and aerosol particles from near the surface to the upper level of the atmosphere, hence quickly changing the composition and status of atmosphere. Moreover clouds are the source of precipitation and greatly regulate its distribution and amount (Lamb and Verlinde, 2011; Lohmann et al., 2016; Sun et al., 2018).

Thanks to the advances in remote sensing technologies, nowadays it is possible to accurately monitor clouds and other atmospheric constituents on local to global scales (Zhu et al., 2018). Remote sensing instruments do not directly measure the parameter of interest, for example cloud fraction, instead they detect the electromagnetic radiation transmitted, scattered, or emitted (radiance) in a given portion of the atmosphere. This electromagnetic radiation carries information about the atmosphere, and the role of a retrieval (or inversion) algorithm is to extract this information from the measurement and derive

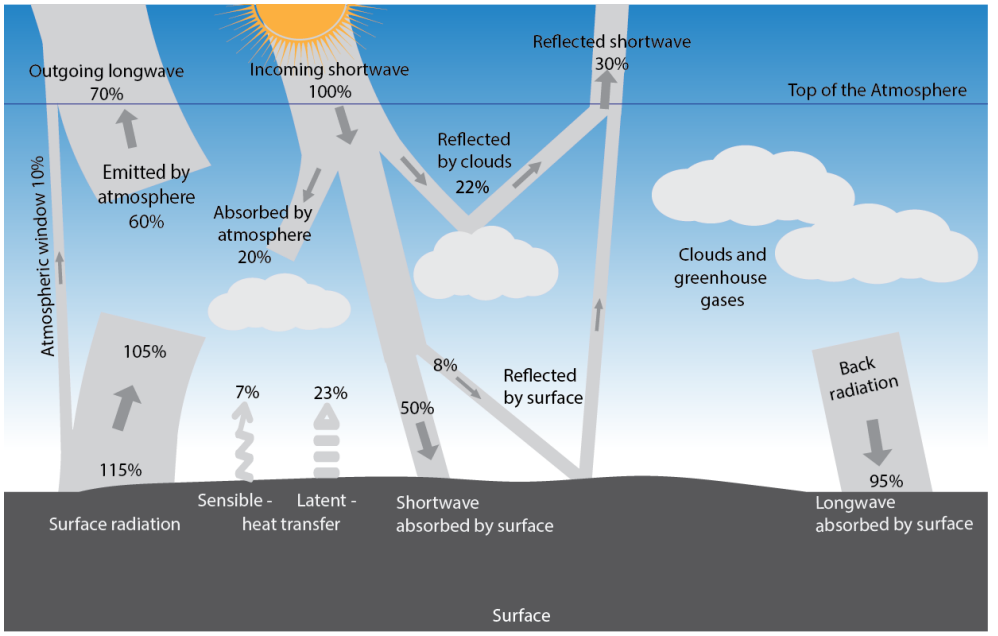

Figure 1: A schematic representation of Earth's radiation balance drawn after (Lamb and Verlinde, 2011).

the state and composition of the atmosphere. In other words, retrieval algorithms are developed to deduce properties of atmospheric constituents from the measured radiance and provide the relevant physical value (retrieval) through a suitable inversion method and an accurate forward model (inverse theory) (Huang et al., 2005).

Global data sets of cloud properties are routinely gathered using satellites, such as MODIS (Moderate Resolution Imaging Spectroradiometer), POLDER (Polarization and Anisotropy of Reflectances for Atmospheric science coupled with Observations from a Lidar), CALIPSO (Cloud-Aerosol Lidar and Infrared Pathfinder Satellite Observation), OMI (Ozone Monitoring Instrument) or AATSR (Advanced Along Track Scanning Radiometer). The traditional approaches to cloud detection (Rossow and Garder, 1993; Ackerman et al., 1998; Hulley and Hook, 2008; Hagolle et al., 2010; Heidinger et al., 2012; Zhu and Woodcock, 2014; Parmes et al., 2017) are based on the fact that the clouds tend to appear brighter and colder than the land surface. These methods imply difficulties in detecting clouds above bright (highly reflective) surfaces, such as snow, ice and deserts, because they mislead the retrieval algorithms to interpret the high measured reflectance as if it was reflected by clouds. The

detection of clouds is addressed in **Paper I** of this thesis. To this end the capability of artificial neural networks (ANN) for detecting clouds is tested using radiances measured at the top of the atmosphere with the NASA-Aura Ozone Monitoring Instrument (OMI). Besides providing cloud coverage, cloud detection is a necessary step in the retrieval of almost any atmospheric parameter from remote sensing data in the ultraviolet (UV), visible (VIS) or infrared (IR) parts of the electromagnetic spectrum (Eresmaa, 2014; Go et al., 2017; Nilo et al., 2018). Satellite observation of aerosols and clouds over the Baltic Sea countries are used in **Paper III** to study how contrasting atmospheric backgrounds (i.e. clean Fennoscandia and more polluted Central-Eastern Europe) impact upon clouds.

Satellite data are often complemented by ground-based observations which are also used as a reference in the validation for space-borne measurements (Marchand, 2016; Virtanen et al., 2018; Filonchyk et al., 2019). Unlike space-borne sensors, ground-based remote sensing provides continuous vertically resolved observations at one location. Although generally reliable, the accuracy of ground-based measurements is strictly dependent on the adopted inversion method. The retrieval algorithm SYRSOC (SYnergistic Remote Sensing Of Clouds) is applied in **Paper II** to derive microphysical and optical cloud properties of stratiform water clouds using the remote sensing suite at Mace Head, Ireland. The measurements are compared to MODIS and AATSR satellite retrievals.

Apart from the remotely-sensed observations, a branch of atmospheric science focuses on the development of representation of cloud processes in global climate models (Flato et al., 2013). Climate models represent a powerful tool for investigating the response of the climate system to various forcings as they enable climatic forecasts from seasonal to decadal timescales and for estimating projections of the future climate over the coming centuries (Collins et al., 2013; Christensen et al., 2013; Kirtman et al., 2013). Hence, the evaluation of modeling diagnostics is a crucial task that establishes the capabilities and reliability of models. **Paper IV** focused on this task and it presents the evaluation of three three climate models with MODIS cloud products.

By using remote sensing and models, the aims of this thesis are to:

- explore the capabilities and limitations of artificial neural networks for estimating cloud fraction (**Paper I**)
- compare cloud retrievals from ground-based algorithms and satellite data (**Paper II**)

- use satellite data to evaluate cloud diagnostics from climate models trough the application of satellite simulators (**Paper IV**)
- quantify the aerosol-cloud interactions and determine any contrasting results for heavily polluted areas against those for very clean areas (**Paper III** and **Paper IV**)

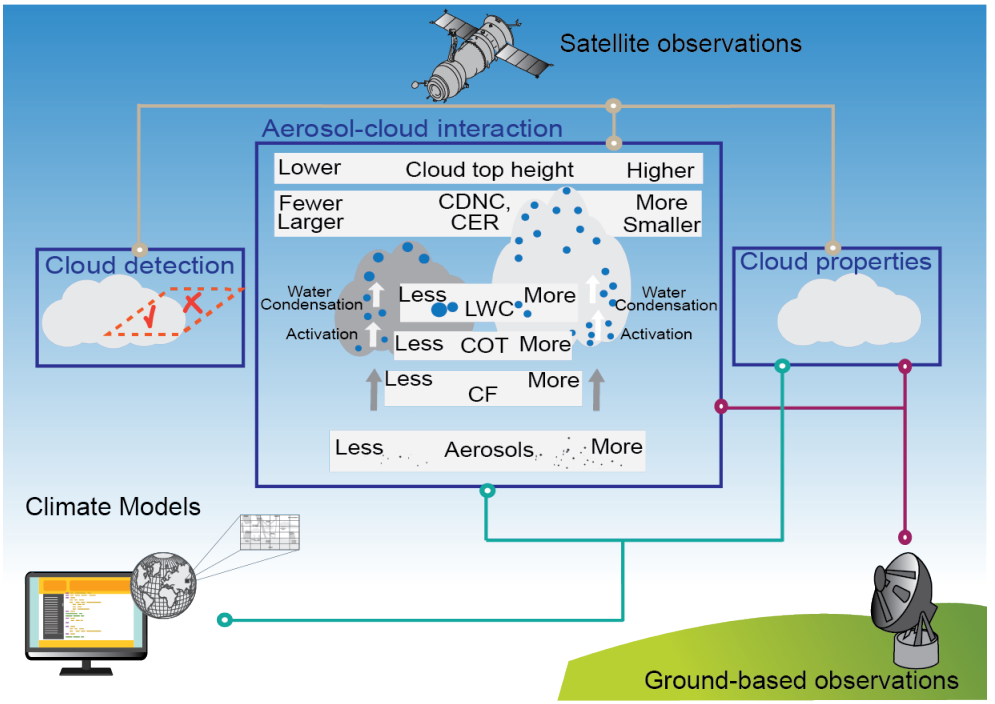

Figure 2: Schematic summary of the topics (cloud detection, cloud properties and aerosol-cloud interactions) and methods (satellite and ground-based observations, models) used in this thesis.

The introductory section of this thesis is structured as follows: Sect.2 briefly introduces the basics of clouds, aerosol and their interaction and Sect.3 presents the research methods, which are illustrated in Fig.2. Section 4 presents the main findings of this work and conclusion and future step are summarized in Sect.6.

2. Background

2.1. Light propagation through the atmosphere

Electromagnetic waves propagating through the atmosphere encounter gas molecules, aerosol particles, cloud droplets and ice crystals which modify the incident radiation by complex processes. The incoming radiation can be partly reflected or reradiated, changing the direction of propagation (scattering), and partly disappear by converting energy in heat or chemical energy (absorption). Overall, absorption and scattering processes define how solar and terrestrial radiation propagates through the atmosphere.

The nature of the interaction between electromagnetic waves and atmospheric constituents depends on the wavelength λ of the radiation and on the size distribution of the constituents (Bohren and Huffman, 2007). The absorption and scattering properties of homogeneous spherical particles with sizes comparable to λ can be derived using the Mie theory (Mie, 1908) which relates λ to the size and the chemical composition of the object.

After travelling a path of length z, the beam of light is attenuated following the Beer-Lambert law (Seinfeld and Pandis, 2006; Bohren and Huffman, 2007):

$$\frac{I(\lambda)}{I_0(\lambda)} = \exp(-\sigma_e(\lambda)z) \tag{1}$$

where I_0 is the intensity of the incoming solar light at a wavelength λ, I is the intensity of the light at a wavelength λ at a location z along the path and σ_e is the extinction coefficient of the medium at a wavelength λ. The σ_e has three main components:

- Rayleigh scattering by air molecules, which occurs when the size of the air molecules is $< 1/10$ of the λ of I_0.
- Scattering and absorption by atmospheric aerosol particles, which is discussed in more details in Sect.2.2.
- Molecular absorption, whose main contributions are molecular oxygen and ozone, which strongly absorb radiation in the ultraviolet, and water, which strongly absorbs infrared radiation.

In the atmosphere solar radiation interacts with atmospheric constituents (aerosol, clouds and gases), all of which can absorb and/or scatter the radiation in certain spectral bands. The contributions from these various atmospheric

constituents interacting with the radiation are additive (Wallace and Hobbs, 2006). Therefore, the total $\sigma_{\mathrm{E}}(\lambda)$ accounts for aerosol, clouds and gases:

$$\begin{aligned}\sigma_{\mathrm{e}}(\lambda) &= \Sigma_i \sigma_{\mathrm{e_i}} \\ &= \Sigma_i \sigma_{\mathrm{a_i}} + \Sigma_i \sigma_{\mathrm{s_i}} \\ &= \Sigma_i \sigma_{\mathrm{ag_i}}(\lambda) + \sigma_{\mathrm{sg_i}}(\lambda) + \sigma_{\mathrm{ap_i}}(\lambda) + \sigma_{\mathrm{sp_i}}(\lambda) + \Sigma_i \sigma_{\mathrm{ac_i}}(\lambda) + \sigma_{\mathrm{sc_i}}(\lambda)\end{aligned} \tag{2}$$

where the first letter of each subscript represents either absorption (a) or scattering (s) and the second the contribution of gas (g), aerosol (p) and clouds (c). Furthermore, we can define $\Sigma_{\mathrm{i}}\sigma_{\mathrm{e_i}}$, $\Sigma_{\mathrm{i}}\sigma_{\mathrm{a_i}}$ and $\Sigma_{\mathrm{i}}\sigma_{\mathrm{s_i}}$ as (Wallace and Hobbs, 2006):

$$\sigma_{\mathrm{e}}(\lambda) = \Sigma_{\mathrm{i}}\sigma_{\mathrm{e_i}} = \Sigma_{\mathrm{i}}\rho_{\mathrm{i}}\mathrm{K}_{\mathrm{e_i}} = \Sigma_{\mathrm{i}}\mathrm{N}_{\mathrm{i}}\mathrm{K}_{\mathrm{e_i}} \tag{3}$$

$$\sigma_{\mathrm{a}}(\lambda) = \Sigma_{\mathrm{i}}\sigma_{\mathrm{a_i}} = \Sigma_{\mathrm{i}}\rho_{\mathrm{i}}\mathrm{K}_{\mathrm{a_i}} = \Sigma_{\mathrm{i}}\mathrm{N}_{\mathrm{i}}\mathrm{K}_{\mathrm{a_i}} \tag{4}$$

$$\sigma_{\mathrm{s}}(\lambda) = \Sigma_{\mathrm{i}}\sigma_{\mathrm{s_i}} = \Sigma_{\mathrm{i}}\rho_{\mathrm{i}}\mathrm{K}_{\mathrm{s_i}} = \Sigma_{\mathrm{i}}\mathrm{N}_{\mathrm{i}}\mathrm{K}_{\mathrm{s_i}} \tag{5}$$

where ρ_{i} and N_{i} are the density and particle (for example aerosol) number concentration, respectively, of the ith constituent and K is the (dimensionless) extinction efficiency.

The total amount of radiation scattered by particles for a given medium in any direction is a function of particle composition and size. The composition determines the particle absorption properties. Particles that are very small compared to λ are scattering radiation in the Rayleigh regime, in which scattering efficiency is $\mathrm{K} \propto \lambda^{-4}$, therefore very effective at short wavelengths (e.g. at UV and the blue end of the visible spectrum), the scattering is divided evenly between the forward and backward direction of the radiation propagation. When particle size is comparable to λ, the Mie regime, radiation propagates preferentially along the forward-scattering direction while geometric optics apply when particles are much larger than λ (Lamb and Verlinde, 2011).

2.2. Aerosol

Minuscule liquid and solid particles suspended in the atmosphere, known as aerosol particles, can be found mainly in the closest three kilometers to Earth's surface (Tian et al., 2017; Koffi et al., 2016). Aerosol particles can enter the atmosphere directly in a particle form (i.e. dust, sea salt, pollen, organic compounds) or they can form in the atmosphere as a result of reactions between gaseous compounds in a process known as nucleation (Kazil et al., 2010; Kulmala et al., 2012). The diameter of aerosol particles ranges from 1-2 nm for freshly formed molecular clusters (Kulmala et al., 2013) to 100 μm for dust or pollen, for example. Fine aerosol, with radius between 0.1 μm and 1 μm,

can grow by condensation, where gaseous molecules condense on the particle surface, or coagulation, where smaller fine aerosols collide and stick together.

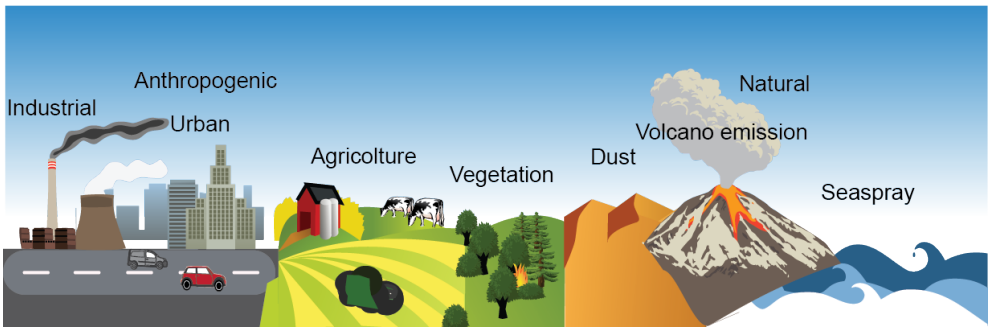

Figure 3: Examples of anthropogenic and natural sources of aerosol particles.

The Earth's atmosphere contains various types of aerosol particles (Fig.3) with different concentrations and chemical compositions originating from biological sources (i.e. spores, seeds, pollen, sea salt, smoke from wild fires), solid Earth (i.e. volcano emissions, dust), anthropogenic processes (dust from roads, biomass burning, fuel combustion, industrial activities) and in-situ formation due to condensation of gases (i.e. gas to particle conversion from precursor gases such as sulfuric acid bases and volatile organic compounds) (Wallace and Hobbs, 2006; Kalberer, 2015; Tegen and Schepanski, 2018; Hoesly et al., 2018).

Once emitted, aerosol particles are transported by the wind over long distances. Their residence time in the atmosphere varies from few days to weeks (Fig.4), depending on the particle size, until they are removed from the atmosphere by precipitation, gravitation, cloud processing, collision with larger particles or by sticking onto existing surfaces (i.e vegetation) (Kristiansen et al., 2012; Bellouin and Haywood, 2015).

Aerosol particles can be described by their physical properties, such as size, size distribution and shape, their chemical composition and optical properties, such as extinction, scattering and absorption coefficients (Hansen and Travis, 1974).

The single scattering albedo w_0 defines the scattering and absorption fractions of $\sigma_e(\lambda)$:

$$w_0 = \frac{\sigma_s}{\sigma_s + \sigma_a} \tag{6}$$

The aerosol optical depth (AOD) is one of the most common aerosol optical parameters is retrieved from aerosol remote sensing instruments, for example MODIS (Fig. 4 and 5) and AERONET sunphotometers, and it is related to

Figure 4: A true-color image from the Moderate Resolution Imaging Spectroradiometer (MODIS) over Northern Italy, on March 17, 2005. Northern Italy is a highly populated and industrialized area. The the Alps block the transport of the air between northern Italy and the rest of Europe and large amount of air pollution can accumulate in the air even for days. Therefore, it often happens that the sky in the Po valley area appears hazy: this phenomena is captured in the satellite snapshot and it can be clearly observed by human eye. From the image hazy skies extend over the Po Valley and reach the Adriatic sea. Credit: Jeff Schmaltz, MODIS Land Rapid Response Team. Reprinted with permission from NASA Goddard Space Flight Center.

the amount of aerosol in the vertical column of the atmosphere in the observed direction. It is defined as:

$$\mathrm{AOD}(\lambda) = \int_0^{\mathrm{TOA}} \sigma_{\mathrm{e_p}}(\lambda, z)\mathrm{d}z \tag{7}$$

where the extinction coefficient $\sigma_{\mathrm{e_p}}$ accounts for aerosol absorption and aerosol scattering $\sigma_{\mathrm{e_p}} = \sigma_{\mathrm{a_p}} + \sigma_{\mathrm{s_p}}$ and AOD is the integrated $\sigma_{\mathrm{e_p}}$ over the total atmospheric column, i.e. from the surface $z = 0$ to the top of the atmosphere $z =$ TOA.

The Ångström exponent (AE) describes the wavelength dependency of the AOD (Ångström, 1929):

$$\mathrm{AE} = -\frac{\log\frac{\mathrm{AOD}\lambda_1}{\mathrm{AOD}_{\lambda_2}}}{\log\frac{\lambda_1}{\lambda_2}} \tag{8}$$

and qualitatively indicates the aerosol particle size (Ångström, 1929; Moosmüller et al., 2009; Dhar et al., 2018; Lack and Langridge, 2013). Values of AE ≤ 1 are indicative of coarse particles, i.e. dust and sea salt, whereas values of AE≥ 2 indicate the presence of fine particles, typically associated with urban pollution or biomass burning (Shin et al., 2019; Zotter et al., 2017; Lack and Langridge, 2013).

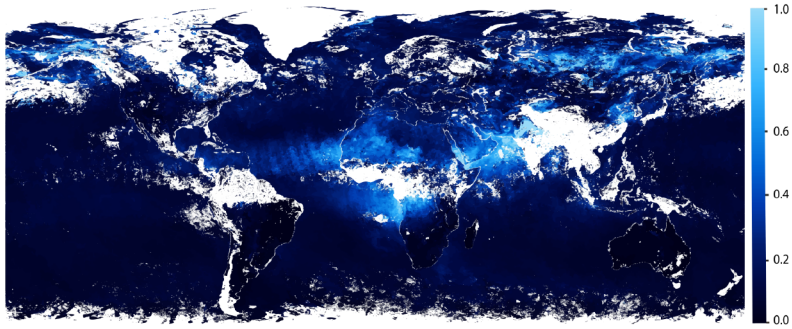

Figure 5: Monthly averaged (July 2019) AOD from MODIS/Aqua. Light blue pixels show high aerosol concentrations, while dark blue pixels show lower concentrations, and black areas show little or no aerosols. white shows where aerosol properties could not be retrieved. The image is produced using the science data set Level 2 AOD 550 Dark Target Deep Blue Combined regridded at a 0.1 degrees spatial resolution. Credit: original imagery by Reto Stockli, NASA's Earth Observatory, using data provided by the MODIS Atmosphere Science Team, NASA Goddard Space Flight Center. Modified and reprinted with permission from NASA Goddard Space Flight Center.

Depending on the the aerosol optical (determined by chemical composition) properties, aerosols can scatter or absorb the shortwave and thermal radiation. Scattering aerosols exert a cooling effect of the atmosphere, whilst absorbing aerosol particles cause a local warming of the atmosphere at the level at which they are located (Bellouin, 2015). In the recent Intergovernmental Panel on Climate Change's (IPCC) Fifth Assessment Report (AR5) (Boucher et al., 2013) these processes are called Radiative Forcing from Aerosol-Radiation Interaction (RFari). Additionally, aerosols indirectly affect climate by altering cloud properties, such as albedo, droplet size, cloud radiation properties, and precipitation (Lohmann, 2006; Rosenfeld, 2006). For example, absorbing aerosol can modify the evaporation rate of cloud droplets and warm the atmosphere, hence hindering or enhancing cloud production, and consequently affecting precipitation (Lee, 2012; Rosenfeld and Givati, 2006; Zhou et al., 2017; Stjern et al., 2017).

Aerosols may also act as cloud condensation nuclei CCN (Aitken, 1881) or ice nuclei IN (DeMott et al., 1997), which are an indispensable element in cloud formation and a relevant factor affecting cloud properties. Not all aerosols are activated into CCN or IN and their activation strongly depends on their size, chemical composition and mixing state.

2.3. Clouds

Clouds are the place in the atmosphere where water passes from its gaseous phase (water vapour) to its liquid and/or solid phase. Clouds consist of microscopic droplets of liquid water (warm clouds), ice crystals (cold clouds), or both (mixed-phase clouds). Their mean droplet radius is typically in the range 10-20 μm for liquid clouds and 25-35 μm for ice clouds, a remarkable size difference in comparison to raindrops and snowflakes which we all can see without any equipment (Fig.6).

Clouds forms as a result of saturation of the air. The air is saturated when the liquid and vapour phases are in equilibrium, the temperature is equal to the dew point and the relative humidity is 100%. Saturation is reached either by mechanisms cooling the air to its dew point or by adding moisture to the air (Lamb and Verlinde, 2011).

When saturated air cools, for example via adiabatic cooling of an air parcel by updrafts, the water vapour concentration exceeds the equilibrium value below the dew point and the air becomes supersaturated. In this condition, the supersaturated air can no longer contain the same amount of water vapor and condensation may occur. Aerosol particles are a indispensable element in cloud formation because they facilitate the conversion of water vapour into its

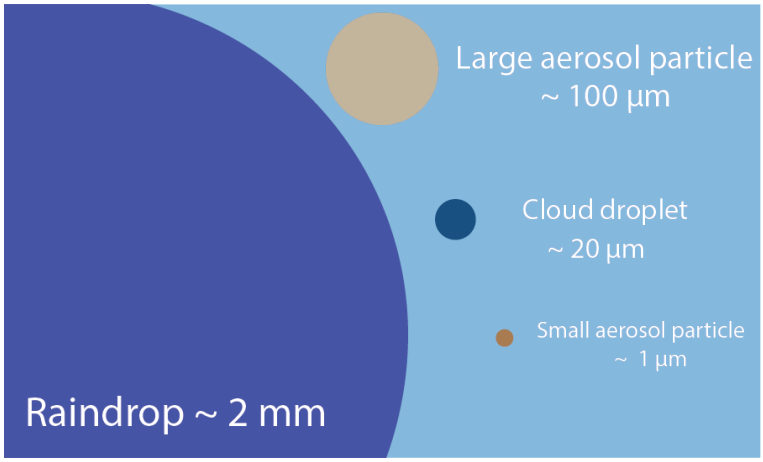

Figure 6: Comparison of typical sizes of aerosols, cloud droplet and raindrop.

liquid (rain) and/or solid phase (ice crystals) by acting as a preferred surface on which water vapour condense. For this reason, aerosol particles acting as condensation surfaces are referred to as cloud condensation nuclei (CCN). The ability of aerosol particles to activate as cloud droplets depends on aerosol properties (i.e. size and hygroscopicity) and on the meteorological conditions (i.e. water vapour, temperature and velocity updraft).

When enough vapour condenses onto the CCN and the supersaturation of the air exceed a critical value according to Kölher theory, a cloud droplet is formed (Köhler, 1936). The Kölher theory describes how the supersaturation and the critical diameter for the cloud drop activation depend upon the size and chemical composition of CCN. It indicates that as the supersaturation increases, the size at which particles can be activated decreases. In other words, the higher is the hygroscopicity and size of the particle, the lower is the required supersaturation level for cloud droplet formation (Köhler, 1936; Kulmala et al., 1996; Reutter et al., 2009; Mochida et al., 2011; Väisänen et al., 2016).

However, condensational growth alone is not enough to form rain droplets and ice-crystals. Other processes, such as collision-coalescence, riming and aggregation, are responsible for precipitation events: if droplets collide with a sufficient number of other droplets, they grow by collection into precipitation-sized droplets and reach the surface in form of rain droplets or ice-crystals.

Clouds cover roughly two thirds of the globe (Mace et al., 2009), as shown in Fig.7). The mid-latitude oceanic storm tracks and tropical precipitation belts are particularly cloudy, while continental desert regions and the central

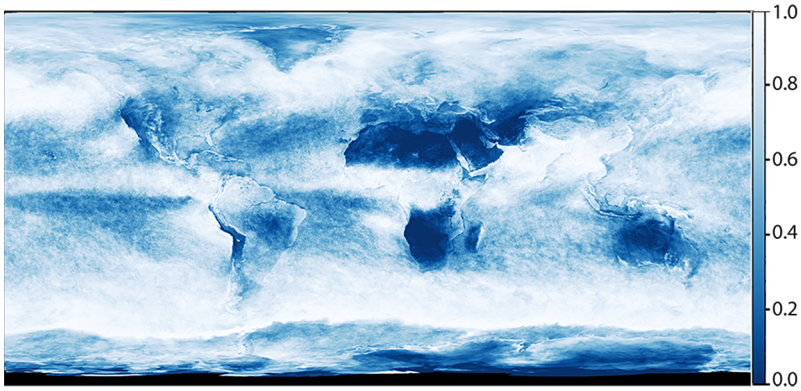

Figure 7: Monthly averaged (July 2019) cloud fraction from MODIS/Aqua. Cloud fraction is the portion of each pixel that is covered by clouds. Colors range from blue (no clouds) to white (totally cloudy). The image is produced using the scientific data set CloudFraction derived from the 1-km-pixel resolution Cloud Mask product. Credit: original imagery by Reto Stockli, NASA's Earth Observatory, using data provided by the MODIS Atmosphere Science Team. Modified and reprinted with permission from NASA Goddard Space Flight Center.

subtropical oceans are relatively cloud-free. At any given time, most clouds are not precipitating (Sun et al., 2018).

In this thesis I adopt from Boucher et al. (2013) the commonly used vertical classification of clouds that considers 'high' cloud above the 440 hPa pressure level, 'low' below the 680 hPa and in between 'mid-level'. High clouds (i.e. cirrus and deep cumulus) are mainly distributed near the equator and over tropical continents, but they also occur in the mid-latitude storm track regions and over mid-latitude continents in summer. Mid-level clouds occur prominently in the storm tracks and, less frequently, in the Intertropical Convergence Zone (ITCZ). Low-level clouds are seen over mainly over oceans (Boucher et al., 2013; Mace et al., 2009; Chepfer et al., 2010).

Clouds directly condition the transmission of sunlight and infrared radiation in the atmosphere, consequently the temperature of Earth, and ultimately climate, by scattering and absorbing incoming solar radiation and outgoing longwave radiation (see Figure 1).

In general, the role of clouds on climate depends on their altitude and thickness (Yan et al., 2016; Hang et al., 2019; L'Ecuyer et al., 2019). High-level clouds, such as cirrus clouds, consists of ice and reflect little sunlight but efficiently trap infrared light emitted from Earth's surface. Low-level clouds, and to some extent mid-level clouds, such as stratus clouds strongly reflect

incoming solar radiation and weakly impact on the outgoing infrared radiation, while cumulus clouds can block sunlight but also trap the Earth's heat depending on their heights and thicknesses. The overall effect of clouds on climate is a cooling effect because the amount of solar radiation reflected back to space by clouds is higher than the amount of infrared radiation emitted by clouds towards the surface (Hartmann, 1993; Boucher and Quaas, 2007; Lamb and Verlinde, 2011).
The cloud properties used in this thesis are introduced in Sect.3.

2.4. Aerosol-cloud interactions

As mentioned in the previous sections, aerosol particles and clouds play a key role in the processes regulating Earth's radiative budget. The recent Intergovernmental Panel on Climate Change (IPCC)'s Fifth Assessment Report (5AR) (Boucher et al., 2013) indicates the interactions between aerosols, clouds and radiation as the largest key climate uncertainty. Therefore, it is crucial to improve the level of understanding of the effects of aerosol, clouds and their interactions on atmospheric processes.

The nomenclature describing the aerosol-cloud-radiation interactions has been changing throughout the years and the IPCC 5AR (Boucher et al., 2013) introduced a new terminology, shown in Fig.8, to describe the two main mechanism perturbing Earth's radiation balance:

- the radiative forcing due to aerosol-radiation interactions (RFari) encompasses what was previously referred to as the aerosol direct effects and characterize the effect of aerosol particles interacting directly with incoming sunlight or emitted thermal radiation through scattering and absorption processes;

- the radiative forcing due to aerosol-cloud interactions (RFaci) comprises what was previously known as the aerosol first indirect effect and describes any change to the Earth's radiative budget due to the modification of cloud microphysical properties by aerosols.

The term aerosol-cloud interactions may be used in its most broad meaning to refer to any interaction between aerosol and clouds (Bellouin et al., 2019). However, in this thesis it is quantified by the metric ACI which defines the change in an observable cloud property (e.g., cloud optical depth, cloud effective radius, cloud droplet number concentration) to a change in a cloud condensation nuclei proxy (e.g. aerosol optical depth, aerosol index, or aerosol particle number concentration). If LWP is assumed to be constant

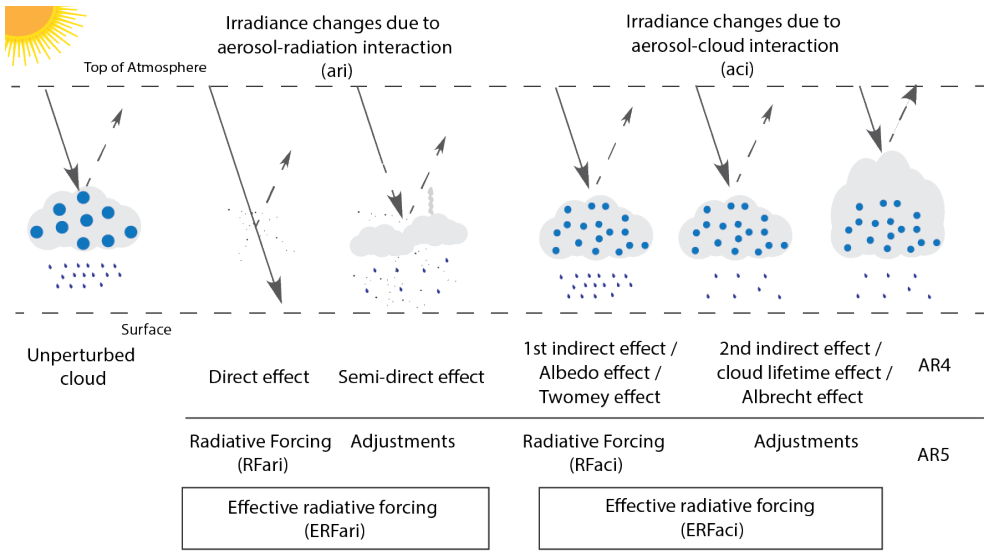

Figure 8: Schematic summary of the interactions between radiation, aerosol and clouds. The nomenclature adopted in the IPCC AR4 (Forster et al., 2007) is now being replaced by the new terminology presented in the recent IPCC AR5 (Boucher et al., 2013)

and additional CCN are inserted in a shallow warm cloud, a higher number of CCN compete for the same amount of liquid water amount, leading to a larger number cloud droplets of smaller size than the same cloud in unperturbed conditions. Consequently, the total surface area of the cloud droplets is larger, more solar radiation is reflected back to space, making the cloud brighter, and less radiation reaches the surface as the optical thickness of the cloud increases. This effect is also known as the Twomey effect or cloud albedo effect or first indirect effect (Twomey, 1977).

Furthermore, smaller droplets may also decrease the frequency of precipitation, consequently increasing the cloud lifetime (Albrecht, 1989) and cloud coverage (Kaufman and Koren, 2006). The term adjustments is used nowadays to indicate these processes (Boucher et al., 2013).

A widely-used approach to the assessment of ACI parameter is to follow the methodology introduced by Feingold et al. (2003) and attribute perturbations in a selected cloud property to changes in the chosen cloud condensation nuclei proxy:

$$\mathrm{ACI} = \frac{\mathrm{d}\ln(\delta)}{\mathrm{d}\ln(\sigma)} \tag{9}$$

where δ is the observed cloud property (COT, CER, LWP or CDNC) and σ the CCN proxy, as CCN are not a measurable quantity for most instrument techniques (i.e. for satellite instrumentation). Aerosol loading is often used as a proxy (Andreae, 2009) which is usually expressed by the aerosol optical depth (AOD) or the aerosol index (AI), derived as the product of AOD × ÅE, or the Fine Mode AOD (AODf), the part of the total AOD which is contributed by fine mode aerosol particles.

It is important to highlight that using AOD as a surrogate of CCN implies the following shortcomings:

- AOD from satellite observations are limited for aerosol particles with diameter larger then 0.1 μm (Seinfeld et al., 2016);
- high relative humidity causes aerosols to swell and create difficulties in deriving size distributions (Neubauer et al., 2017; Liu and Li, 2018);
- AOD measurements may be biased due to cloud contamination or cloud obstruction (Koren et al., 2008; Yang et al., 2014; Zhu et al., 2015);
- AOD is a total column measurement which does not provide any information regarding the proximity to clouds nor about the aerosol size distinction nor the aerosol type (Stier, 2016);

Next, some of the challenges and limitations in assessing ACI are highlighted. AOD retrievals are limited to cloud-free conditions, which creates challenges to studying the ACI where the intention is to study collocated aerosol and cloud observations. Unless height-resolving instruments (i.e. lidars) are considered, the vertical location of the AOD level is unknown. Aerosol and cloud measurements may contain retrieval errors, which are further propagated to ACI estimates, as well as they reciprocally may bias the respective retrievals (Jia et al., 2019). The interpretation of the observed aerosol-cloud relationships is complicated by the effect of meteorology (Quaas et al., 2010; Gryspeerdt et al., 2014, 2016; Brenguier et al., 2003). As cloud formation happens in high humidity conditions, aerosol humidification can severely affect the assessment of ACI by causing positive correlation between AOD and cloud properties (Myhre et al., 2007; Quaas et al., 2010; Grandey et al., 2013; Gryspeerdt et al., 2014). Additionally to aerosol particles, water vapour also affects precipitation (Boucher et al., 2013), obviously linked to the presence of clouds, and consequently causes spurious correlations between aerosols and clouds (Koren et al., 2012).

This thesis tackles the assessment of the ACI by using remote sensing observations and global modeling of warm liquid stratiform clouds deriving estimates

of ACI from local to global scales. Many studies derived ACI estimates from local to global scales using in-situ (Werner et al., 2014) and ground-based (Qiu et al., 2017) measurements, satellite observations (Ma et al., 2018) or modeling approaches (Gryspeerdt et al., 2017), or a combination of modeling diagnostics and observations (Ban-Weiss et al., 2014). The advances in the level of understanding are, however, limited by the intrinsic limitations of each approach (Seinfeld et al., 2016; Lohmann et al., 2016; Bellouin et al., 2019).

3. Data & methods

The goal of studying Earth's atmospheric constituents is to improve the understanding of atmospheric processes. A deeper knowledge on atmospheric composition enables advances in monitoring and improving air quality as well as in predicting future climate responses to changes in natural and anthropogenic emissions. Observations from satellite instruments, ground-based measurements and model diagnostics are fundamental tools for monitoring the atmosphere.

3.1. Space-borne remote sensing

3.1.1. MODIS retrievals

The Moderate Resolution Imaging Spectrometer (MODIS) is a 36-channel radiometer flying aboard the Terra and Aqua satellites since 2000 and 2002, respectively. MODIS views the entire Earth's surface every 1 to 2 days, thus providing an extensive data set of global Earth observations. MODIS delivers a wide range of atmospheric products including aerosol and cloud properties, water vapour and atmospheric stability variables.

MODIS Level-1 (L1) products are geo-located brightness temperature values, which are converted to geophysical data products at Level-2 (L2) using retrieval algorithms, which can be aggregated into a uniform space-time grid at Level-3 (L3).

The 1-km (at nadir) spatial resolution MODIS cloud mask is the basis of MODIS aerosol and cloud retrievals. The cloud mask provides the probability for a given pixel to be influenced by the occurrence of clouds, classifying the pixels as confident clear, probably clear, uncertain–probably cloudy or cloudy. Pixels falling in the former two groups are used for retrieving aerosol properties. The latter two classes are labeled as cloudy when calculating cloud fractions (Platnick et al., 2015).

The L2 aerosol products are provided over land (except over ice and snow) and ocean surfaces for cloud-free conditions during daytime at a nominal spatial resolution of 10 x 10 km^2 (Levy et al., 2015). The primary aerosol product is AOD retrieved globally at the wavelength of 550 nm, while the other parameters accounting for the aerosol size distribution, such as AE, defined in Eq.8, or fine-mode AOD, are only derived over ocean (Levy et al., 2013).

The L2 cloud parameters include cloud top properties (e.g. cloud amount, top temperature, pressure, emissivity, and height) and physical and optical properties (e.g. particle phase, effective particle size, optical thickness, water

path, fraction) under both daytime and nighttime conditions with a 1 x 1 km^2 resolution (for Collection 6 onwards) (Hubanks et al., 2018). Cloud fractions are derived at 5-km resolution by calculating the proportion of cloudy pixels from 25-pixel cloud mask groupings.

The cloud droplet effective radius (CER or r_e) is a measure of the cloud droplet size and it is defined as (Hansen and Travis, 1974):

$$\mathrm{CER} = r_e = \frac{\int_0^\infty r_e^3 n(r) \mathrm{d}r}{\int_0^\infty r_e^2 n(r) \mathrm{d}r} \tag{10}$$

where $n(r)$ is the cloud droplet size distribution.

Simultaneously to CER, the cloud optical thickness (COT) is derived. CER and COT are retrieved coupling the MODIS-measured reflectances in one of the visible (non-absorbing) channels and one near-infrared or infrared band (water-absorbing channels) by using look-up tables, which are created by a radiative transfer model calculating the amount of reflection produced by clouds characterized by a range of COT and CER as a function of the wavelength (Platnick et al., 2018). The look-up table approach has the following limitations:

- the determination of CER becomes uncertain at low COT (Cho et al., 2015; Zhang et al., 2012);
- the algorithm assumes single-layered liquid water clouds with plane-parallel geometry, which do not realistically represent all clouds, especially convective clouds. Furthermore, the plane-parallel assumption becomes weaker for low solar zenith angles (Grosvenor and Wood, 2014).
- Cloudy pixels are either defined as liquid or ice clouds, whereas most of the clouds in the atmosphere with temperature between -6 °C and -38 °C are mixed-phase clouds.

The liquid water path (LWP), the amount of liquid water per unit volume of air, is derived from the CER and COT as (Han et al., 1998)

$$\mathrm{LWP} = \frac{4\rho_\mathrm{w}}{3K_e}\mathrm{COT} \cdot \mathrm{CER} \tag{11}$$

where $\rho_\mathrm{w} = 1$ g cm-3 is the water density and $\mathrm{K_e} \approx 2$ is the extinction efficiency in the visible band used for the retrieval of COT and CER (King et al., 1997). Equation (8) presumes vertically homogeneous clouds in combination with cloud top effective radius retrievals (Borg and Bennartz, 2007).

Furthermore, three different products of the cloud properties introduced above are produced using three different water absorbing channels (1.6 μm, 2.1 μm and 3.6 μm). Zhang et al. (2012) showed that CER retrieved at 3.6 μm is less sensitive to the plane-parallel cloud assumption.

The geolocated L2 MODIS atmospheric products are aggregated in L3 onto a regular $1^\circ \times 1^\circ$ grid and averaged over a day, 8-days and a month span (Hubanks et al., 2018). In addition to the nominal atmospheric variables, L3 MODIS products come along with a suite of statistical quantities derived from the corresponding L2 data product.

The cloud droplet number concentration (CDNC), the number of water droplets in a volume of cloud, can be derived from CER and COT by combining Eqs. (6) and (9) from Bennartz (2007), resulting in the following equation:

$$\mathrm{CDNC} = \gamma \cdot \mathrm{COT}^{0.5} \cdot \mathrm{CER}^{-2.5} \tag{12}$$

where $\gamma = 1.37 \cdot 10^{-5}$ m$^{0.5}$ (Quaas et al., 2006). The assumption of not accounting for temperature effect and setting γ as a bulk costant applies rather well to the warm stratiform clouds in the marine boundary layer but less for convective clouds (Bennartz, 2007; Rausch et al., 2010; Grosvenor et al., 2018). The equation represents the "Idealized Stratiform Boundary Layer Cloud" (ISBLC) model (Bennartz and Rausch, 2017) which is based on the following assumptions:

- the cloud is horizontally homogeneous
- the LWC increases linearly from the cloud base to the cloud top
- the CDNC is constant throughout the vertical extent of the cloud

While the ISBLC model describes important aspects of stratiform boundary layer clouds, its assumption will never be fully valid for any real cloud. Issues related to the ISBLC model assumptions are extensively elaborated in Bennartz (2007); Bennartz and Rausch (2017) and references therein. However, compared to the methodology of Bennartz (2007), we use the revised and improved cloud retrievals from MODIS Collection 6 (Platnick et al., 2015, 2017).

MODIS cloud properties retrieved at 3.6 μm are used in **Paper II** and **Paper III**, while the standard 2.1 μm was used in **Paper IV** to match the wavelength used in the COSP-MODIS simulation. MODIS L2 cloud properties are used in **Paper I** and **Paper II** and MODIS L3 data are applied in **Paper III** and **Paper IV**. In **Paper II** and **Paper III**, transparent-cloudy pixels (COT < 5) were discarded to limit uncertainties (Zhang et al., 2012). MODIS L2 aerosol data are used in **Paper III** and L3 in **Paper IV**.

3.1.2. OMI retrievals

The Ozone Monitoring Instrument (OMI) is a near-UV-visible spectrometer flying on NASA's Aura satellite since 2004. OMI measures radiance at 751 wavelengths in the UV/VIS domain and it has a nominal spatial resolution of 13 $\times$ 24 km^2 at nadir, in the normal global operation mode. Complete global coverage is achieved daily (Levelt et al., 2006) between 2002 and 2008, while after 2008 the global coverage is achieved in two days due to the row anomaly (Yan et al., 2012), which affects the quality of OMI radiance data. By monitoring the global total column ozone, absorbing and non-absorbing aerosol loading, trace gases and clouds, OMI's measurements contribute to studying the recovery of the ozone layer, the sources of aerosols and trace gases affecting air quality, UV surface fluxes and climate change. OMI's radiances (Level-1b) are used in **Paper I**.

3.2. Ground-based remote sensing

Ground-based remote sensing enables continuous atmospheric observations at one location with high temporal and spatial resolution. These characteristics represent an advantageous asset for obtaining detailed insight in atmospheric processes. Ground-based techniques can be classified into active or passive ones, depending on their operational principles.

Active sensors emit electromagnetic radiation at a certain wavelength and measure the backscattered signal to study the properties of the observed target. A radar (RAdio Detection And Ranging) is a system that uses an electromagnetic wave in the radio or microwave domain. Radars operating with frequencies of 35 GHz (8 mm) or 94 GHz (3 mm) are known as cloud radars. Cloud radars are nowadays applied for determining cloud properties up to 10-15 km in altitude and high temporal resolution (1-10 s). As longer wavelengths are less sensitive to drizzle and rain while shorter wavelengths may be attenuated by smaller particles, cloud radars' application extends from the detection of hydrometeors to fog, giant aerosols and insects. A radar sample may contain several targets with different vertical velocities and shapes. Individual targets can be distinguished with the application of Doppler spectra and linear depolarization ratio techniques which enable the detection of the signatures of different targets.

Ceilometers are a sub-category of the LiDAR (LIght Detection And Ranging) system which are configured to optimize cloud observations. They are smaller and less expensive than more powerful atmospheric Lidar systems (e.g. Doppler Lidars, Rayleigh Doppler radar), but follow the same work-

ing principle: a laser beam is sent vertically into the atmosphere where part of the signal is backscattered by atmospheric constituents (e.g. aerosol, clouds, gases) and the intensity of he backscattered radiation is collected by the lidar instrument. Depending on the working combination of wavelengths, the remote mapping of different atmospheric components is enabled by identifying wavelength-dependent changes in the intensity of the returned signal. Ceilometers can be used to determine cloud types, boundaries (e.g. cloud base, top height) and precipitation.

Complimentary to cloud radars and lidars, radiometers are passive sensors measuring the energy emitted at millimetre-to-centimetre wavelengths (frequencies of 1–1000 GHz), known as microwaves, which make the sensor very sensitive to the thermal electromagnetic radiation emitted by atmospheric gases.

In **Paper II** we use 6 years of data collected in Mace Head, at the west coast of Ireland, www.macehead.org./) from a CloudNet station consisting of two active sensors, a ceilometer and a cloud radar, and a passive sensor, a microwave radiometer. The radar reflectivity and microwave radiometer profiles of temperature and humidity as well as liquid water path measurements are input to the SYROC (SYnergistic Remote Sensing Of Clouds) algorithm, a software package developed at the National University of Ireland in Galway (NUIG), that calculates the profiles of CDNC, CER and LWC from the collocated cloud radar, ceilometer or lidar, and microwave radiometer data (Martucci and O'Dowd, 2011). The ground-based measurements processed by SYRSOC are evaluated with MODIS and AATSR in **Paper II**. While SYRSOC produces profiles of the microphysical cloud properties, MODIS has a limited penetration depth into clouds and mainly retrieves microphysical cloud properties near cloud top. SYRSOC CER, COT and integrated LWC were averaged about 10 min before and 10 min after the overpass. MODIS values with COT < 5 were discarded. Additionally, measurements of aerosol composition from the ground-based in situ aerosol mass spectrometer (AMS) (Ovadnevaite et al., 2014) were also used in **Paper II**.

3.3. Climate models

Climate models represent a sophisticated tool for studying Earth's atmosphere and predicting climate change. A global atmospheric model schematically simulates Earth's atmosphere in a 3-dimensional grid. By solving the mathematical equations that describe the physical atmospheric processes, given initial conditions and parameters, models compute winds, heat transfer, radiation, relative humidity, and surface hydrology within each grid point.

One key limiting factor in the quality of climate predictions by current global atmospheric models is the realistic representation of the simulated properties (e.g. cloud cover, amount of cloud water, and number and size of droplets or ice crystals) that describe the atmospheric constituents (e.g. clouds).

The evaluation of modeling diagnostics is an important task that establishes the capabilities and reliability of models, hence it helps to improve the parametrization of modelled atmospheric variables. A robust evaluation of model diagnostics is not a straight-forward task: model-to-model and model-to-satellite intercomparison are affected by a number of limitations and incongruities intrinsic in the data. For example, the compensation of modeling errors, the uncertainties of observational data, and the possible discrepant definitions of variables between models and observational data are some of the major issues.

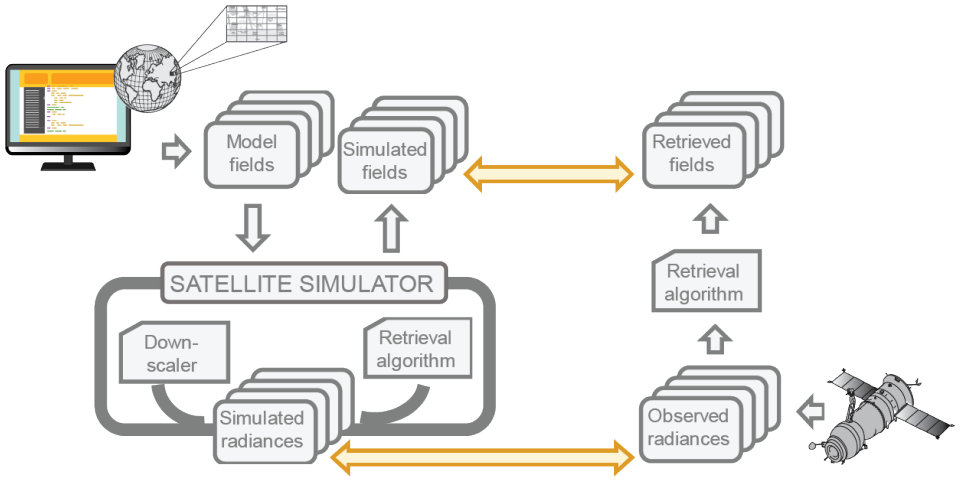

Figure 9: Schematic representation of the basic principle of COSP satellite simulator. COSP is a diagnostic tool that maps the model representation of clouds to synthetic satellite observations.

The application of a a satellite simulator, which mimics the retrieval of observational data, remedies these inconsistencies. In other words, simulators recreate what a satellite would retrieve when observing the modeled atmosphere, thus generating physical quantities fully consistent with satellite retrievals and preventing inconsistencies in the modelled outputs. Consequently, simulators represent a valuable approach not only for the application of satellite data to robustly evaluate models, but also for consistent model-to-model comparisons.

In **Paper IV** three climate models were considered, ECHAM-HAM, ECHAM-HAM-SALSA and NorESM, and in each of them the Cloud Feedback Model Intercomparison Project (CFMIP) Observation Simulator Package, COSP (Bodas-Salcedo et al., 2011) version 1.4 was implemented. COSP is a software tool developed within the CFMIP (Webb et al., 2017) which models parameters for several spaceborne active (CALIOP, CPR) and passive (MISR, MODIS) sensors (Fig.9). In our case we considered the COSP-MODIS simulator. One year of data (2008) of COSP-simulated liquid and ice cloud (CF, CER, COT, LWP) and aerosol (AOD and AI) properties was compared to MODIS L3 data. The COSP grid-averaged values were divided by the corresponding cloud fractions to match the MODIS in-cloud grid values. The model three-hour outputs were aggregated to daily averages and successively re-gridded and co-located by linear interpolation onto the finer satellite regular grid of 1°×1°. Furthermore, MODIS observations and MODIS-COSP diagnostics were screened using a minimum threshold of 30% of cloud fraction to minimize the source of errors introduced by the retrieval algorithm and to ensure the existence of large-scale clouds. Additionally to the MODIS-COSP diagnostics, I also considered the model direct outputs for CDNC which is representative of the entire vertical structure of a simulated atmospheric column. Top-column values were considered to maintain consistency with MODIS and MODIS-COSP values, which observe the top of the clouds, and they were screened for values with temperature T > 273°K to discard mixed-phase and ice clouds.

4. Overview of key results

4.1. Determination of cloud fraction

Cloud detection is a fundamental step for atmospheric observation, whether we aim to observe clouds themselves or other atmospheric constituents (Eresmaa, 2014; Go et al., 2017; Nilo et al., 2018). A faulty classification of clouds can cause an incorrect analysis of the observations.

The process of cloud detection relies upon the contrast between clouds and background (either atmosphere or surface) in the observed field (Ackerman et al., 2010). Different automated cloud detection techniques have been developed depending on the requirements of the application, for example the tolerance of the application to uncertainty in the cloud amount estimate. Cloud quantification can be deterministic providing binary products such as cloudy/cloud-free pixels (Rossow and Garder, 1993), multi-class categorical, for example cloudy, partial-cloud, cloud-free and unknown in Ackerman et al. (2010), or representative of a continuous measurement, i.e. the probability of cloud coverage or the probability of cloud-free as introduced in Aleksandrova et al. (2018).

Clouds are easily distinguishable from surface types other than snow and ice, due their high reflectivity of solar radiation at visible wavelengths. However, this distinction is limited to daytime when solar zenith angles are sufficiently large and the reflected sunlight provides enough contrast in the imagery. Many automated cloud detection approaches rely on tests using a combination of visible and infrared channels to determine the presence of clouds (Ackerman et al., 2010; Sun et al., 2017; Zhu et al., 2015). The success of these cloud test techniques depends on the determination of the thresholds used in each cloud test. The techniques which perform the best are usually the most complex and computationally heavy as they have several spectral tests and thresholds that vary with the geographic region, time of year, time of day and solar angle, for example.

In **Paper I**, a fast and automated neural networks-based solution was explored for determining cloud fraction. The method was designed specifically for the NASA Aura's satellite Ozone Monitoring Instrument (OMI) which observes back scattered solar radiation in the visible (VIS) and ultraviolet (UV), thus lacking the thermal channels. Two neural network (NN) algorithms, namely extreme learning machine (ELM) and back propagation (BP) algorithms, were developed and used to estimate cloud fractions using OMI radiance measurements from the visible channels. OMI data were divided into independent datasets for training, testing and validating the results from the neural net-

works. The results were evaluated by comparison with cloud fractions available from the MODerate Resolution Imaging Spectrometer (MODIS). OMI and MODIS both fly in the A-train constellation but on different platforms, respectively Aura and Aqua with a time difference of 15 minutes between the observations.

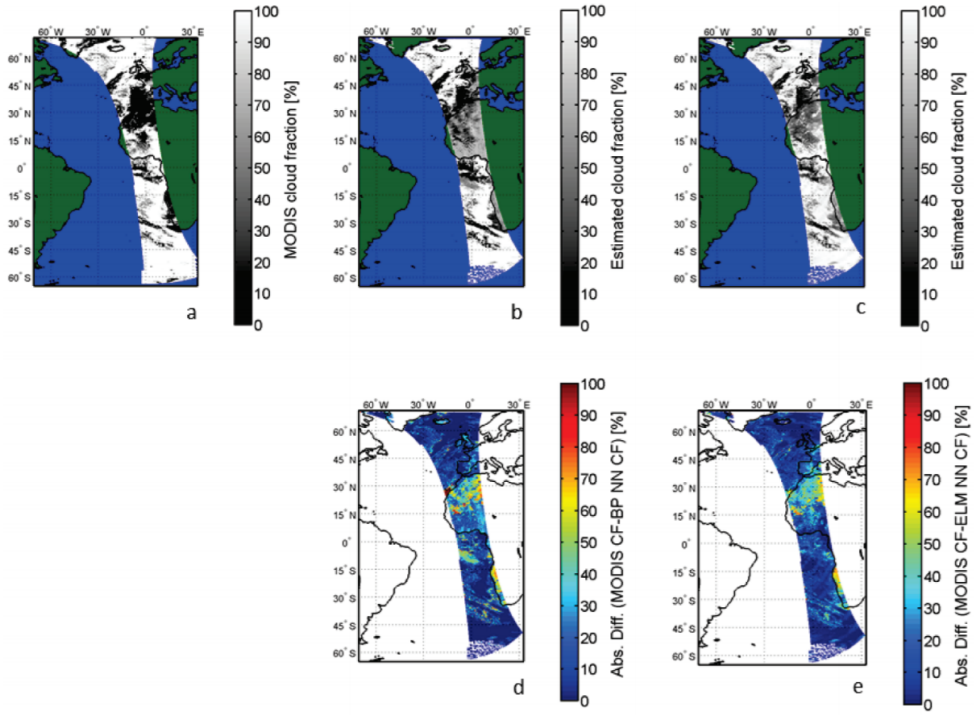

Figure 10: Cloud fractions estimated by the BP and ELM-trained NN and comparison with MODIS CF data for validation over a selected orbit. (a) Computed MODIS geometrical cloud fraction. (b) BP predicted cloud fraction. (c) ELM predicted cloud fraction. The grey-code in top-row figures (a-c) ranges from 0 (cloud free) to 100 (totally cloud covered). The bottom-row figures show the absolute difference between MODIS geometrical cloud fraction and BP-predicted cloud fraction (d) and ELM-predicted cloud fraction (e). The color-code ranges from 0 (perfect match) to 100 (complete mismatch).

Both neural networks were successfully implemented and delivered estimates of cloud fraction in a fast and automated way. However, the NNs showed limitation when estimating small cloud fractions, where the BP algorithm showed the worst results. The neural networks performed rather well in the evaluation with MODIS cloud fraction data. As the ocean provides a

homogeneous dark surface in the UV/VIS, hence providing a good contrast between cloudy and clear pixels, good correlations with R values of 0.85 and 0.88 are achieved over ocean, for ELM and BP, respectively. Over land, highly reflective surfaces, such as desert (Fig.10), or the presence of dust layers in the atmosphere, represented a challenge for the neural network and the cloud fractions were not well predicted. The ELM outperformed the BP algorithm with R values of 0.83 and 0.56, respectively, for ELM and BP.

4.2. Evaluation of cloud properties

4.2.1. Ground-based measurements and MODIS observations

Non precipitating single-layer homogenous water clouds data collected by the ground-based remote sensing instruments at the Mace Head Atmospheric Research Station from 2009 to 2015 were input into the SYRSOC algorithm to derive profiles of CER, LWC, and COT. A total of 118 stratiform clouds were identified and successively they were classified as marine or continental, based on three-day back-trajectories from the National Oceanic and Atmospheric Administration (NOAA) HYSPLIT model (HYbrid Single-Particle Lagrangian Integrated Trajectory) (Draxler and Rolph, 2014) and the synoptic conditions. 40 cases coincident with overpasses of the MODIS Aqua or Terra satellites over Mace Head were used for a comparison of the SYRSOC results with the corresponding MODIS products at 3.7 μm (Platnick et al., 2015).

MODIS data were selected and averaged over an area from 53.27 to 53.37 °N and from −9.91 to 9.89 °E, with Mace Head located at its center. MODIS pixels with COT < 5 were removed before averaging. SYRSOC produces profiles of the microphysical cloud properties. However, MODIS has a limited penetration depth into clouds and therefore only retrieves microphysical cloud properties near cloud top. Therefore, SYRSOC CER averaged from 75 m to 45 m below the radar detected cloud top, while LWP was integrated over the full cloud depth. SYRSOC CER, COT and integrated LWC were averaged over time from about 10 min before to 10 min after the MODIS overpass.

Comparison of SYRSOC results with MODIS observations shows a moderate correlation of CER (R=0.43), shown in Fig.11 a, and a rather poor agreement of COT (R=0.19). No correlation was found between the integrated SYRSOC LWC and MODIS LWP, shown in Fig.11 b. The SYRSOC algorithm discards measurements if drizzle is detected and this screening process discards cloud areas with high LWP, resulting in integrated values considerably lower than the MODIS LWP. LWP was also measured directly by the MWR and used as input for SYRSOC. Better agreement was found between the di-

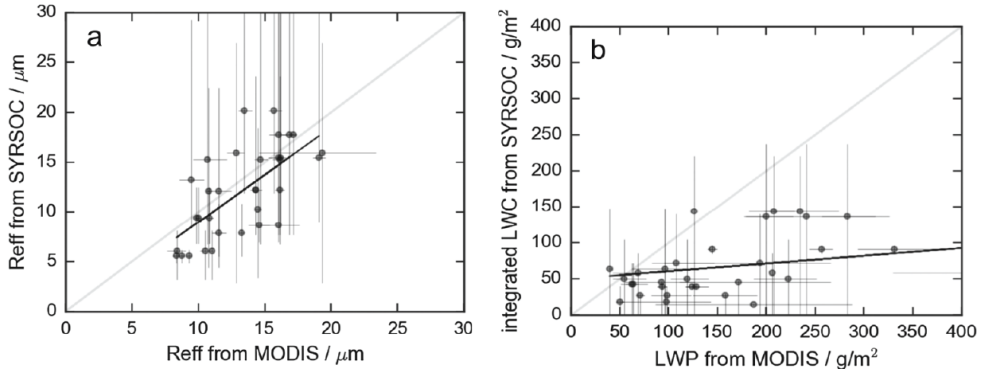

Figure 11: Comparison of (a) reff and (b) integrated LWC/LWP from MODIS and SYRSOC, including downdrafts and drizzle. Dots mark mean values, and error bars span minima to maxima. The 1:1 line and linear fit are shown in gray and black, respectively

rectly measured LWP and MODIS LWP than between SYRSOC results and MODIS products, with the exception of high-mean LWP, where the variability of both instruments was larger.

Integrated SYRSOC LWC was in many cases lower than MWR LWP. In order to investigate whether the LWP differences were caused by the drizzle screening, the SYRSOC run was repeated without drizzle screening. Agreement was improved by running SYRSOC without drizzle screening, which resulted in an increase of R2 for LWC from 0.04 to 0.14. Comparison of CER with drizzle resulted in a slope near 1 and a small offset of -1 μm. The correlation of COT was greater when drizzle was included. However, apart from CER with a slope near 1 and small offset, overall the comparison with MODIS data shows a poor agreement. Comparison with MODIS products at 1.6 μm and 2.1 μm showed similar results.

4.2.2. Model diagnostics and MODIS observations

The evaluation of modeling diagnostics with appropriate observations is an important task that establishes the capabilities and reliability of models. In this perspective, aerosol and cloud properties obtained from three different climate models, namely ECHAM-HAM, ECHAM-HAM-SALSA and NorESM, are considered.

Results for global means and geographical distributions of aerosol and cloud properties were assembled over a one-year period (2008) and compared with MODIS observations in **Paper IV** providing a quantitative evaluation of cloud

and aerosol diagnostics. Different results were obtained when considering liquid or ice clouds.

Significant biases are observed globally in NorESM ice clouds because NorESM includes radiatively active snow (Kay et al., 2012). The droplet size and water content of ice clouds are underestimated in ECHAM-HAM and ECHAM-HAM-SALSA possibly owing to the cirrus scheme which does not account for heterogenous nucleation or pre-existing ice crystals during formation of cirrus clouds (Lohmann and Neubauer, 2018; Neubauer et al., 2019).

Global differences can be also observed in liquid clouds (Figure 12). The droplet size (Figure 12 e-h) simulated by ECHAM-HAM around the mid-latitude belt are on average 5 μm smaller than in ECHAM-HAM-SALSA and NorESM, and ECHAM-HAM-SALSA simulates larger cloud droplets around the polar areas and shows a large positive bias for LWP over ocean in comparison to ECHAM-HAM. The liquid water path simulated by NorESM is larger over land areas while ECHAM-HAM shows a good agreement with MODIS (Fig.12 j-k).

Despite having identical cloud modules, the discrepancies between ECHAM-HAM and ECHAM-HAM-SALSA may originate from different amounts of activated droplets and different ice nucleation rates. The COSP diagnostics of liquid clouds CER and COT were successively used to derive the CDNC, following the approach presented in Quaas et al. (2006), and compared to the corresponding MODIS-derived values. Overall the MODIS derived CDNC is lower than that derived from COSP simulated values, but higher than the direct output values. Consequently, the CDNC from direct model output is lower than MODIS-COSP diagnostics, as also found by Ban-Weiss et al. (2014). Possible explanations could be either related to the COSP computation of cloud diagnostics or the approach itself used for deriving CDNC.

Considering the vertical distribution of the COSP-simulated clouds, both ECHAM-HAM and ECHAM-HAM-SALSA fail in simulating high level clouds while the vertical distribution of clouds simulated by NorESM is similar to MODIS.

The evaluation led to the identification of the following deficiencies in the models:

- the clouds simulated by NorESM are too thick over land and this issue is present in COSP-variables as well as in the direct model output due to a very low autoconversion parameter causing the suppression of precipitation over land, thus thicker clouds;
- ECHAM-HAM-SALSA systematically simulates lower IWC than ECHAM-HAM due to a higher cloud droplet freezing rate which con-

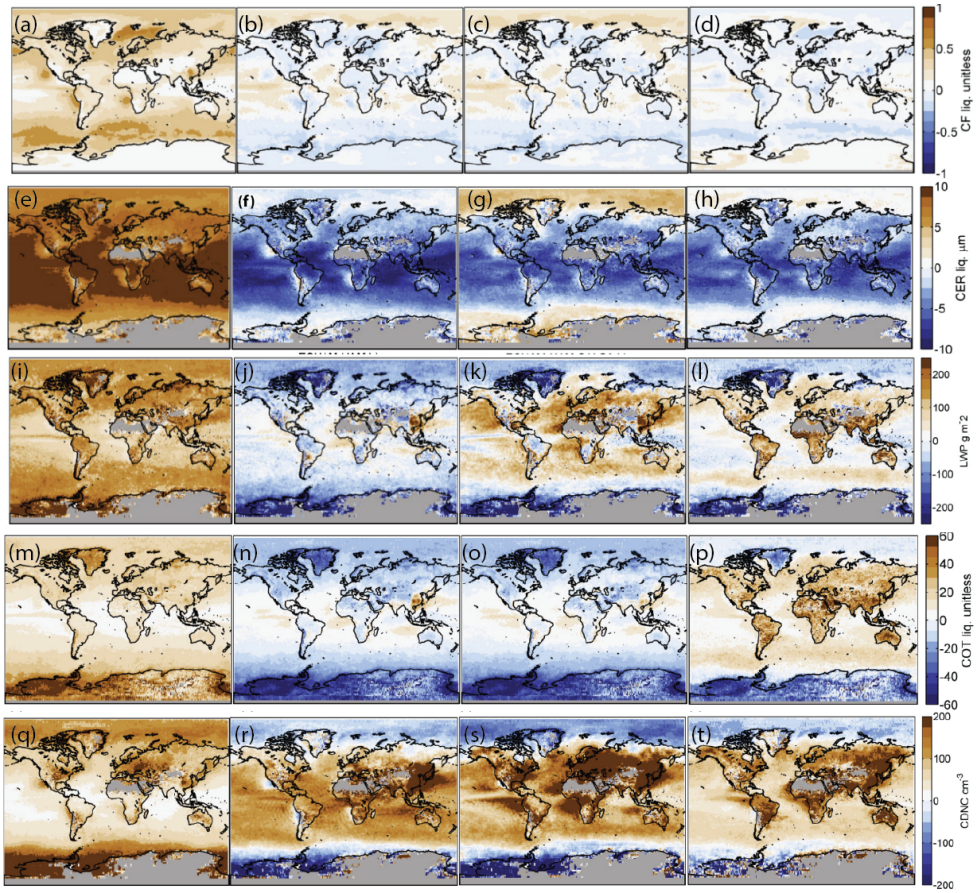

Figure 12: Annual global mean bias in the properties characterizing liquid warm clouds. The bias represents the difference calculated subtracting MODIS observation to MODIS-COSP diagnostics simulated by ECHAM-HAM, ECHAM-HAM-SALSA, and NorESM. The first image in each row presents MODIS spatial distributions as reference.

secutively triggers a reduced sedimentation of ice clouds. This outcome explains the contradictory result in ECHAM-HAM-SALSA that showed the largest global average among the models for CER despite having the highest numberof CDNC;

- the direct model output for CDNC is systematically larger than both the values derived from COSP-diagnostics and MODIS observations, supporting the results found Ban-Weiss et al. (2014).

4.3. Analysis of aerosol-cloud interactions

In this work the topic of aerosol-cloud interactions introduced in Sect.2.4 was studied using different measurement techniques (satellite observations, ground based measurements, modelling diagnostics) and approaches (spatial distribution, linear regression analysis, vertical profiling, air mass analysis) for different scales (local, regional and global).

Long-term analysis of ACI was conducted in **Paper II** and **Paper III**.
Six year measurements of remote sensing aerosol and cloud properties from Mace Head were studied in **Paper II**. The findings showed higher CDNC and lower CER during greater pollution events, confirming the Twomey effect. In marine air masses the median CDNC was 60 cm^{-3} and the median CER 10 μm. In continental air the median CDNC was 160 cm^{-3} and the median CER was 8 μm. Droplet size distributions were broader in marine cases and narrower in continental cases. Generally, clean air masses showed also lower COT and cloud albedo and higher values were found in more polluted conditions.
In **Paper III**, 12 years of aerosol and low-level liquid cloud properties were used to statistically quantify the ACI over the Baltic Sea region, including the relatively clean Fennoscandia and the more polluted central–eastern Europe. Changes in cloud structures were shown by the increase of CF, COT, LWP and CTH, and a decrease of CER as function of aerosol loading, especially at relatively low cloud-top levels, between 900 hPa and 700 hPa. Most of the studied cloud variables were unaffected by the lower-tropospheric stability (LTS), except for cloud fraction.
The ACI was studied as the change in CER as a function of aerosol concentration for fixed LWP bin values (Fig.13). Positive and statistically significant ACI values were found over the Baltic Sea and Fennoscandia, with the former having the largest values. Small negative ACI values were observed over central–eastern Europe, suggesting that large aerosol concentrations saturate the ACI and that a given change in aerosol number exerts a stronger effect in pristine regions than in polluted regions.

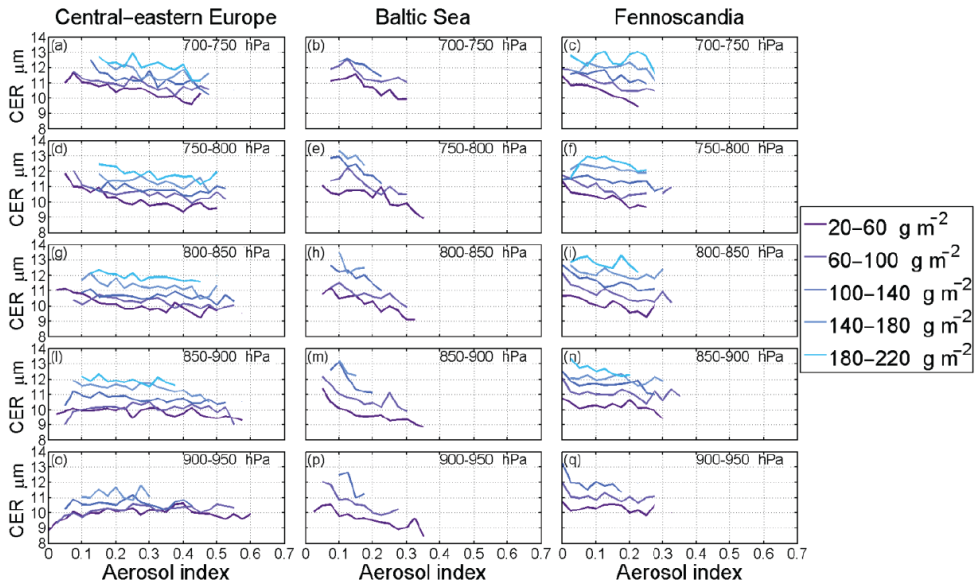

Figure 13: CER as a function of AI, stratified for subranges of CTP and LWP, for the three subregions. These three areas have generally different aerosol conditions:Central-eastern Europe has the highest values of aerosol loading with an overall AI and AOD mean value of 0.29 ± 0.03 (regional mean ± standard deviation), and 0.22 ± 0.02 respectively. The Baltic Sea presents a mean value of 0.20 ± 0.02 and 0.16 ± 0.02 for AI and AOD respectively, and the Fennoscandia the has the lowest values for both AOD (0.14 ± 0.01) and AI (0.16 ± 0.01). The legend on the right of the figure lists the LWP bins.

By using the CDNC as the cloud properties considered in Eq.9, it is possible to isolate the microphysical component of the ACI without the need for constraining the liquid water path. This approach was adopted in **Paper IV** where estimates of ACI on a global scale were computed using CDNC and AI from COSP-MODIS simulated and MODIS retrieval observations. The ACI estimates showed good agreement between the three models and, even more important, with ACI derived from MODIS observations. ACI from the model results is generally positive suggesting that changes in AI are connected with an increase of CDNC regardless of the season. However, negative ACI values were found during the winter months from MODIS observations, possibly caused by limitations intrinsic in the nature of satellite observations.

5. Review of publications and author's contribution

Paper I **Saponaro, G.**, Kolmonen, P., Karhunen, J., Tamminen, J., and de Leeuw, G., A neural network algorithm for cloud fraction estimation using NASA-Aura OMI VIS radiance measurements, *Atmos. Meas. Tech.*, 6, 2301–2309, 2013.

Overview: A study on the applicability of two artificial neural network (ANN) algorithms for estimating cloud fraction. The implemented method revealed being a time effective and automatic approach as oppose to a combination of several tests.

Author's contribution: I implemented the ANN algorithms, collected and processed the MODIS and OMI data for training, testing and validating the ANNs, all of the coding for data processing, and analysed the results. I wrote the text and collated the co-authors comments and revisions.

Paper II Preißler, J., Martucci, G., **Saponaro, G.**, Ovadnevaite, J., Vaishya, A., Kolmonen, P., Cerburis, D., Sogacheva, L., de Leeuw, G. and O'Dowd, C., Six years of surface remote sensing of stratiform warm clouds in marine and continental air over Mace Head, Ireland, *J. Geophys. Res. Atmos.*, 121, 14, 538–14, 557, 2016.

Overview: A long term analysis of cloud properties collected from the CloudNet station located in Mace Head, Ireland. The cloud data was used as input to the SYRSOC algorithm and the derived cloud parameters were compared to satellite observations. Ground-based cloud observations were also studied in function of air masses.

Author's contribution: I contributed to the study by collecting the cloud data from MODIS Collection 6 Level 2 and post-processed it to enable a robust comparison with the ground-based measurements of warm stratiform clouds. I helped in the related data interpretation and wrote the part of text concerning the MODIS observations.

Paper III **Saponaro, G.**, Kolmonen, P., Sogacheva, L., Rodriguez, E., Virtanen, T. and de Leeuw, G., Estimates of the aerosol indirect effect over the Baltic Sea region derived from 12 years of MODIS observations, *Atmos. Chem. Phys.*, 17, 4, 3133–3143, 2017.

Overview: A study on the aerosol indirect effect of aerosols on cloud properties using 12 years of MODIS observations. The study focused on the Baltic Sea region which includes the relatively clean Fennoscandia and the more polluted central-eastern Europe, thus enabling the observation of the effect of different aerosol concentrations on clouds.

Author's contribution: I carried out the design of the study and I chose the methods and metrics. I carried out the data selection, processing and analysis. I wrote the text and collated the co-authors comments and revisions.

Paper IV **Saponaro, G.**, Sporre, M. K., Neubauer, D., Kokkola, H., Kolmonen, P., Sogacheva, L., Arola, A., de Leeuw, G., Karset, I. H. H., Laaksonen, A., Lohmann, U., Evaluation of aerosol and cloud properties in three climate models using MODIS observations and its corresponding COSP simulator, and their application in aerosol-cloud interaction, *Atmos. Chem. Phys. Discussions*

Overview: An evaluation of cloud and aerosol properties simulated by a satellite simulator implemented in three climate models with MODIS observations. The modelling diagnostics and MODIS observations were also used to infer the ACI on a global scale.

Author's contribution: I carried out the design of the study, the analysis of the data and I wrote the text. The modelling data, and the corresponding descriptive sections of the models, were provided by M. Sporre, D. Neubauer and H. Kokkola. I wrote the text and collated the co-authors interpretation of the results, comments and revisions.

6. Conclusions

One main point of this thesis is the use of cloud products from different data sources to evaluate how well they compare, and how they can be used together for climate studies. I mainly focused on liquid warm homogeneous low-level clouds, except in **Paper IV** where ice clouds were also considered.
Paper I and **Paper IV** focused on the evaluation of cloud properties on a global scale. The OMI cloud fraction determined by the two artificial neural networks developed in **Paper I** showed overall good results in comparison to the MODIS cloud fraction, except over bright surfaces (i.e. snow or desert). These areas are usually critical for retrieval algorithms of atmospheric properties as higher surface reflectances can be misinterpreted as aerosol or cloud signals. In an attempt to mitigate this issue, transparent clouds were discarded from the analysis carried in **Paper II** to **Paper IV**.
In **Paper IV** a large difference was found in the two available MODIS cloud fraction products due to the different treatment of partly cloudy pixels which potentially can undermine the robustness of the evaluation of data products if not taken into consideration. The COSP-MODIS satellite simulator used in **Paper IV** avoid the issues related to scale and definition intrinsic in model-model and model-observation comparison and allow a direct evaluation of satellite and COSP diagnostics. However, the simulator diagnostics were not solely used to enable a model-satellite comparison but they were interpreted carefully also to understand the limits and deficiencies between different model set-ups.

The second aim of the thesis was to apply the above mentioned data for assessing the ACI for liquid warm homogeneous clouds on a local scale (**Paper II**), on a regional scale (**Paper III**) and globally (**Paper IV**). The aerosol and cloud observations collected over longer periods of time varying from 6 years in **Paper II** up to 12 years in **Paper III** lead to more statistically and qualitative robust ACI values than the one year data used in **Paper IV**. Implications of ACI were observable by analyzing the spatial distributions, vertical profiles and air masses of the observed atmospheric variables.
The quantification of clouds and of aerosol–cloud interactions remains a challenge. Global climate models are the tool for climate prediction and observations (satellite and surface-based) are used to evaluate the performances of models. On one hand, climate models and satellite are strategic to simulate and observe the relevant atmospheric processes. However, their estimates come with a low confidence because cloud and aerosol properties vary at scales significantly smaller than those resolved both in climate models and observed by satellites. On the other hand, fine scale models and ground-based observation provide high confidence, yet lack the connection with global scale processes.

Future work should aim at coordinating the modelling and observation (satellite and surface-based) communities toward a joint effort to design large-scale activities. Climate models should be improved in their representation of clouds (especially mixed- and ice- clouds) and tested with higher spatial resolution models. The model parametrization capabilities should be tested and evaluated in locations where models indicate sensible mutual interaction between aerosols and clouds, over a range of meteorological and aerosol conditions, and in conjunction with observations.

References

Ackerman, S., Strabala, K., P., M., Frey, R., Moeller, C., and Gumley, L.: Discriminating clear-sky from cloud with MODIS algorithm theoretical basis document (MOD35, in: MODIS Cloud Mask Team, Cooperative Institute for Meteorological Satellite Studies, University of Wisconsin, 2010.

Ackerman, S. A., Strabala, K. I., Menzel, W. P., Frey, R. A., Moeller, C. C., and Gumley, L. E.: Discriminating clear sky from clouds with MODIS, Journal of Geophysical Research: Atmospheres, 103, 32 141–32 157, https://doi.org/10.1029/1998JD200032, URL https://agupubs.onlinelibrary.wiley.com/doi/abs/10.1029/1998JD200032, 1998.

Aebi, C., Gröbner, J., Kämpfer, N., and Vuilleumier, L.: Cloud radiative effect, cloud fraction and cloud type at two stations in Switzerland using hemispherical sky cameras, Atmospheric Measurement Techniques, 10, 4587–4600, https://doi.org/10.5194/amt-10-4587-2017, URL https://www.atmos-meas-tech.net/10/4587/2017/, 2017.

Aitken, J.: XII.—On Dust, Fogs, and Clouds, Transactions of the Royal Society of Edinburgh, 30, 337–368, https://doi.org/10.1017/S0080456800029069, 1881.

Albrecht, B. A.: Aerosols, Cloud Microphysics, and Fractional Cloudiness, Science, 245, 1227–1230, https://doi.org/10.1126/science.245.4923.1227, URL http://science.sciencemag.org/content/245/4923/1227, 1989.

Aleksandrova, M., Gulev, S. K., and Belyaev, K.: Probability Distribution for the Visually Observed Fractional Cloud Cover over the Ocean, Journal of Climate, 31, 3207–3232, https://doi.org/10.1175/JCLI-D-17-0317.1, URL https://doi.org/10.1175/JCLI-D-17-0317.1, 2018.

Andreae, M. O.: Correlation between cloud condensation nuclei concentration and aerosol optical thickness in remote and polluted regions, Atmospheric Chemistry and Physics, 9, 543–556, https://doi.org/10.5194/acp-9-543-2009, URL https://www.atmos-chem-phys.net/9/543/2009/, 2009.

Ban-Weiss, G. A., Jin, L., Bauer, S. E., Bennartz, R., Liu, X., Zhang, K., Ming, Y., Guo, H., and Jiang, J. H.: Evaluating clouds, aerosols, and their interactions in three global climate models using satellite simulators and

observations, Journal of Geophysical Research: Atmospheres, 119, 10,876–10,901, https://doi.org/10.1002/2014JD021722, URL https://agupubs.onlinelibrary.wiley.com/doi/abs/10.1002/2014JD021722, 2014.

Bellouin, N.: AEROSOLS | Climatology of Tropospheric Aerosols, in: Encyclopedia of Atmospheric Sciences (Second Edition), edited by North, G. R., Pyle, J., and Zhang, F., pp. 76 – 85, Academic Press, Oxford, second edition edn., https://doi.org/https://doi.org/10.1016/B978-0-12-382225-3.00054-2, URL http://www.sciencedirect.com/science/article/pii/B9780123822253000542, 2015.

Bellouin, N. and Haywood, J.: AEROSOLS | Climatology of Tropospheric Aerosols, in: Encyclopedia of Atmospheric Sciences (Second Edition), edited by North, G. R., Pyle, J., and Zhang, F., pp. 40 – 47, Academic Press, Oxford, second edition edn., https://doi.org/https://doi.org/10.1016/B978-0-12-382225-3.00051-7, URL http://www.sciencedirect.com/science/article/pii/B9780123822253000517, 2015.

Bellouin, N., Quaas, J., Gryspeerdt, E., Kinne, S., Stier, P., Watson-Parris, D., Boucher, O., Carslaw, K., Christensen, M., Daniau, A.-L., Dufresne, J.-L., Feingold, G., Fiedler, S., Forster, P., Gettelman, A., Haywood, J., Lohmann, U., Malavelle, F., Mauritsen, T., McCoy, D., Myhre, G., Mülmenstädt, J., Neubauer, D., Possner, A., Rugenstein, M., Sato, Y., Schulz, M., Schwartz, S., Sourdeval, O., Storelvmo, T., Toll, V., Winker, D., and Stevens, B.: Bounding global aerosol radiative forcing of climate change, Reviews of Geophysics, https://doi.org/10.1029/2019RG000660, URL https://agupubs.onlinelibrary.wiley.com/doi/abs/10.1029/2019RG000660, 2019.

Bennartz, R.: Global assessment of marine boundary layer cloud droplet number concentration from satellite, Journal of Geophysical Research: Atmospheres, 112, https://doi.org/10.1029/2006JD007547, URL https://agupubs.onlinelibrary.wiley.com/doi/abs/10.1029/2006JD007547, 2007.

Bennartz, R. and Rausch, J.: Global and regional estimates of warm cloud droplet number concentration based on 13 years of AQUA-MODIS observations, Atmospheric Chemistry and Physics, 17, 9815–9836, https://doi.org/10.5194/acp-17-9815-2017, URL https://www.atmos-chem-phys.net/17/9815/2017/, 2017.

Bodas-Salcedo, A., Webb, M. J., Bony, S., Chepfer, H., Dufresne, J.-L., Klein, S. A., Zhang, Y., Marchand, R., Haynes, J. M., Pincus, R., and John,

V. O.: COSP: Satellite simulation software for model assessment, Bulletin of the American Meteorological Society, 92, 1023–1043, https://doi.org/10.1175/2011BAMS2856.1, URL https://doi.org/10.1175/2011BAMS2856.1, 2011.

Bohren, C. F. and Huffman, D. R.: Absorption and Scattering of Light by Small Particles, John Wiley Sons, Ltd, https://doi.org/10.1002/9783527618156.ch1, URL https://onlinelibrary.wiley.com/doi/abs/10.1002/9783527618156.ch1, 2007.

Borg, L. A. and Bennartz, R.: Vertical structure of stratiform marine boundary layer clouds and its impact on cloud albedo, Geophysical Research Letters, 34, https://doi.org/10.1029/2006GL028713, URL https://agupubs.onlinelibrary.wiley.com/doi/abs/10.1029/2006GL028713, 2007.

Boucher, O. and Quaas, J.: Water vapour affects both rain and aerosol optical depth, Nature Geoscience, 6, https://doi.org/10.1038/ngeo1692, URL https://doi.org/10.1038/ngeo1692, 2007.

Boucher, O., Randall, D., Artaxo, P., Bretherton, C., Feingold, G., Forster, P., Kerminen, V.-M., Kondo, Y., Liao, H., Lohmann, U., Rasch, P., Satheesh, S., Sherwood, S., Stevens, B., and Zhang, X.: Clouds and Aerosols, chap. 7, p. 571–658, Cambridge University Press, Cambridge, United Kingdom and New York, NY, USA, https://doi.org/10.1017/CBO9781107415324.016, URL www.climatechange2013.org, 2013.

Brenguier, J.-L., Pawlowska, H., and Schüller, L.: Cloud microphysical and radiative properties for parameterization and satellite monitoring of the indirect effect of aerosol on climate, Journal of Geophysical Research: Atmospheres, 108, https://doi.org/10.1029/2002JD002682, URL https://agupubs.onlinelibrary.wiley.com/doi/abs/10.1029/2002JD002682, 2003.

Chepfer, H., Bony, S., Winker, D., Cesana, G., Dufresne, J. L., Minnis, P., Stubenrauch, C. J., and Zeng, S.: The GCM-Oriented CALIPSO Cloud Product (CALIPSO-GOCCP), Journal of Geophysical Research: Atmospheres, 115, https://doi.org/10.1029/2009JD012251, URL https://agupubs.onlinelibrary.wiley.com/doi/abs/10.1029/2009JD012251, 2010.

Cho, H.-M., Zhang, Z., Meyer, K., Lebsock, M., Platnick, S., Ackerman, A. S., Di Girolamo, L., C.-Labonnote, L., Cornet, C., Riedi, J.,

and Holz, R. E.: Frequency and causes of failed MODIS cloud property retrievals for liquid phase clouds over global oceans, Journal of Geophysical Research: Atmospheres, 120, 4132–4154, https://doi.org/10.1002/2015JD023161, URL https://agupubs.onlinelibrary.wiley.com/doi/abs/10.1002/2015JD023161, 2015.

Christensen, J., Krishna, K. K., Aldrian, E., An, S.-I., Cavalcanti, I., de Castro, M., Dong, W., Goswami, P., Hall, A., Kanyanga, J., Kitoh, A., Kossin, J., Lau, N.-C., Renwick, J., Stephenson, D., Xie, S.-P., and Zhou, T.: Climate Phenomena and their Relevance for Future Regional Climate Change, chap. 14, p. 1217–1308, Cambridge University Press, Cambridge, United Kingdom and New York, NY, USA, https://doi.org/10.1017/CBO9781107415324.028, URL www.climatechange2013.org, 2013.

Collins, M., Knutti, R., Arblaster, J., Dufresne, J.-L., Fichefet, T., Friedlingstein, P., Gao, X., Gutowski, W., Johns, T., Krinner, G., Shongwe, M., Tebaldi, C., Weaver, A., and Wehner, M.: Long-term Climate Change: Projections, Commitments and Irreversibility, book section 12, p. 1029–1136, Cambridge University Press, Cambridge, United Kingdom and New York, NY, USA, https://doi.org/10.1017/CBO9781107415324.024, URL www.climatechange2013.org, 2013.

DeMott, P. J., Rogers, D. C., and Kreidenweis, S. M.: The susceptibility of ice formation in upper tropospheric clouds to insoluble aerosol components, Journal of Geophysical Research: Atmospheres, 102, 19 575–19 584, https://doi.org/10.1029/97JD01138, URL https://agupubs.onlinelibrary.wiley.com/doi/abs/10.1029/97JD01138, 1997.

Dhar, P., Banik, T., De, B. K., Gogoi, M. M., Babu, S. S., and Guha, A.: Study of aerosol types and seasonal sources using wavelength dependent Ångström exponent over North-East India: Ground-based measurement and satellite remote sensing, Advances in Space Research, 62, 1049 – 1064, https://doi.org/https://doi.org/10.1016/j.asr.2018.06.017, URL http://www.sciencedirect.com/science/article/pii/S0273117718304836, 2018.

Draxler, R. R. and Rolph, G. D.: HYSPLIT (HYbrid Single-Particle Lagrangian Integrated Trajectory) Model access via NOAA ARL READYWebsite, URL https://ready.arl.noaa.gov/HYSPLIT.php, 2014.

Eresmaa, R.: Imager-assisted cloud detection for assimilation of Infrared Atmospheric Sounding Interferometer radiances, Quarterly Journal of

the Royal Meteorological Society, 140, 2342–2352, https://doi.org/10.1002/qj.2304, URL https://rmets.onlinelibrary.wiley.com/doi/abs/10.1002/qj.2304, 2014.

Feingold, G., Eberhard, W. L., Veron, D. E., and Previdi, M.: First measurements of the Twomey indirect effect using ground-based remote sensors, Geophysical Research Letters, 30, https://doi.org/10.1029/2002GL016633, URL https://agupubs.onlinelibrary.wiley.com/doi/abs/10.1029/2002GL016633, 2003.

Filonchyk, M., Yan, H. L., Zhang, Z.and Yang, S., Li, W., and Li, Y.: Combined use of satellite and surface observations to study aerosol optical depth in different regions of China, Nature: Scientific Reports, 9, https://doi.org/10.1038/s41598-019-42466-6, URL https://doi.org/10.1038/s41598-019-42466-6, 2019.

Flato, G., Marotzke, J., Abiodun, B., Braconnot, P., Chou, S., Collins, W., Cox, P., Driouech, F., Emori, S., Eyring, V., Forest, C., Gleckler, P., Guilyardi, E., Jakob, C., Kattsov, V., Reason, C., and Rummukainen, M.: Evaluation of Climate Models, book section 9, p. 741–866, Cambridge University Press, Cambridge, United Kingdom and New York, NY, USA, https://doi.org/10.1017/CBO9781107415324.020, URL www.climatechange2013.org, 2013.

Forster, P.and Ramaswamy, V., Artaxo, P., Berntsen, T., Betts, R., Fahey, D., Haywood, J., Lean, J., Lowe, D., Myhre, G., Nganga, J., Prinn, R.and Raga, G., Schulz, M., and Van Dorland, R.: Changes in Atmospheric Constituents and in Radiative Forcing, book section 7, p. 131–217, Cambridge University Press, Cambridge, United Kingdom and New York, NY, USA, 2007.

Go, S., Kim, M., Kim, J., Park, S. S., Jeong, U., and Choi, M.: Detection of Absorbing Aerosol Using Single Near-UV Radiance Measurements from a Cloud and Aerosol Imager, Remote Sensing, 9, https://doi.org/10.3390/rs9040378, URL https://www.mdpi.com/2072-4292/9/4/378, 2017.

Goldblatt, C. and J. Zahnle, K.: Clouds and the Faint Young Sun Paradox, Climate of The Past - CLIM PAST, 6, https://doi.org/10.5194/cp-7-203-2011, 2011.

Grandey, B. S., Stier, P., and Wagner, T. M.: Investigating relationships between aerosol optical depth and cloud fraction using satellite, aerosol reanalysis and general circulation model data, Atmospheric Chemistry and

Physics, 13, 3177–3184, https://doi.org/10.5194/acp-13-3177-2013, URL https://www.atmos-chem-phys.net/13/3177/2013/, 2013.

Grosvenor, D. P. and Wood, R.: The effect of solar zenith angle on MODIS cloud optical and microphysical retrievals within marine liquid water clouds, Atmospheric Chemistry and Physics, 14, 7291–7321, https://doi.org/10.5194/acp-14-7291-2014, URL https://www.atmos-chem-phys.net/14/7291/2014/, 2014.

Grosvenor, D. P., Sourdeval, O., Zuidema, P., Ackerman, A., Alexandrov, M. D., Bennartz, R., Boers, R., Cairns, B., Chiu, J. C., Christensen, M., Deneke, H., Diamond, M., Feingold, G., Fridlind, A., Hünerbein, A., Knist, C., Kollias, P., Marshak, A., McCoy, D., Merk, D., Painemal, D., Rausch, J., Rosenfeld, D., Russchenberg, H., Seifert, P., Sinclair, K., Stier, P., van Diedenhoven, B., Wendisch, M., Werner, F., Wood, R., Zhang, Z., and Quaas, J.: Remote Sensing of Droplet Number Concentration in Warm Clouds: A Review of the Current State of Knowledge and Perspectives, Reviews of Geophysics, 56, 409–453, https://doi.org/10.1029/2017RG000593, URL https://agupubs.onlinelibrary.wiley.com/doi/abs/10.1029/2017RG000593, 2018.

Gryspeerdt, E., Stier, P., and Grandey, B. S.: Cloud fraction mediates the aerosol optical depth-cloud top height relationship, Geophysical Research Letters, 41, 3622–3627, https://doi.org/10.1002/2014GL059524, URL https://agupubs.onlinelibrary.wiley.com/doi/abs/10.1002/2014GL059524, 2014.

Gryspeerdt, E., Quaas, J., and Bellouin, N.: Constraining the aerosol influence on cloud fraction, Journal of Geophysical Research: Atmospheres, 121, 3566–3583, https://doi.org/10.1002/2015JD023744, URL https://agupubs.onlinelibrary.wiley.com/doi/abs/10.1002/2015JD023744, 2016.

Gryspeerdt, E., Quaas, J., Ferrachat, S., Gettelman, A., Ghan, S., Lohmann, U., Morrison, H., Neubauer, D., Partridge, D. G., Stier, P., Takemura, T., Wang, H., Wang, M., and Zhang, K.: Constraining the instantaneous aerosol influence on cloud albedo, Proceedings of the National Academy of Sciences, 114, 4899–4904, https://doi.org/10.1073/pnas.1617765114, URL https://www.pnas.org/content/114/19/4899, 2017.

Hagolle, O., Huc, M., Villa Pascual, D., and G., D.: A multi-temporal method for cloud detection, applied to FORMOSAT-2, VENµS,

LANDSAT and SENTINEL-2 images, Remote Sensing of Environment, 114, 1747 – 1755, https://doi.org/https://doi.org/10.1016/j.rse.2010.03.002, URL http://www.sciencedirect.com/science/article/pii/S0034425710000908, 2010.

Han, Q., Rossow, W. B., Chou, J., and Welch, R. M.: Global Survey of the Relationships of Cloud Albedo and Liquid Water Path with Droplet Size Using ISCCP, Journal of Climate, 11, 1516–1528, https://doi.org/10.1175/1520-0442(1998)011<1516:GSOTRO>2.0.CO;2, URL https://doi.org/10.1175/1520-0442(1998)011<1516:GSOTRO>2.0.CO;2, 1998.

Hang, Y., L'Ecuyer, T. S., Henderson, D. S., Matus, A. V., and Wang, Z.: Reassessing the Effect of Cloud Type on Earth's Energy Balance in the Age of Active Spaceborne Observations. Part II: Atmospheric Heating, Journal of Climate, 32, 6219–6236, https://doi.org/10.1175/JCLI-D-18-0754.1, URL https://doi.org/10.1175/JCLI-D-18-0754.1, 2019.

Hansen, J. E. and Travis, L. D.: Light scattering in planetary atmospheres, Space Science Reviews, 16, 527–610, https://doi.org/10.1007/BF00168069, URL https://doi.org/10.1007/BF00168069, 1974.

Hartmann, D. L.: The Radiative Effect of Clouds on Climate, in: Aerosol-Cloud-Climate Interactions, edited by Hobbs, P., pp. 151–170, Academic Press, 1993.

Heidinger, A. K., Evan, A. T., Foster, M. J., and Walther, A.: A Naive Bayesian Cloud-Detection Scheme Derived from CALIPSO and Applied within PATMOS-x, Journal of Applied Meteorology and Climatology, 51, 1129–1144, https://doi.org/10.1175/JAMC-D-11-02.1, URL https://doi.org/10.1175/JAMC-D-11-02.1, 2012.

Hoesly, R. M., Smith, S. J., Feng, L., Klimont, Z., Janssens-Maenhout, G., Pitkanen, T., Seibert, J. J., Vu, L., Andres, R. J., Bolt, R. M., Bond, T. C., Dawidowski, L., Kholod, N., Kurokawa, J.-I., Li, M., Liu, L., Lu, Z., Moura, M. C. P., O'Rourke, P. R., and Zhang, Q.: Historical (1750–2014) anthropogenic emissions of reactive gases and aerosols from the Community Emissions Data System (CEDS), Geoscientific Model Development, 11, 369–408, https://doi.org/10.5194/gmd-11-369-2018, URL https://www.geosci-model-dev.net/11/369/2018/, 2018.

Huang, S., Xiang, J., Du, H., and Cao, X.: Inverse problems in atmospheric science and their application, Journal of Physics: Conference Series, 12, 45–

57, https://doi.org/10.1088/1742-6596/12/1/005, URL https://doi.org/10.1088/2F1742-6596/2F12/2F1/2F005, 2005.

Hubanks, P., Platnick, S., and King, M. Ridgway, B.: MODIS ATBD for Level-3 Global Gridded Atmosphere Products (Collection 006, v4.3), 2018.

Hulley, G. C. and Hook, S. J.: A new methodology for cloud detection and classification with ASTER data, Geophysical Research Letters, 35, https://doi.org/10.1029/2008GL034644, URL https://agupubs.onlinelibrary.wiley.com/doi/abs/10.1029/2008GL034644, 2008.

Jia, H., Ma, X., Quaas, J., Yin, Y., and Qiu, T.: Is positive correlation between cloud droplet effective radius and aerosol optical depth over land due to retrieval artifacts or real physical processes?, Atmospheric Chemistry and Physics, 19, 8879–8896, https://doi.org/10.5194/acp-19-8879-2019, URL https://www.atmos-chem-phys.net/19/8879/2019/, 2019.

Kalberer, M.: AEROSOLS | Aerosol Physics and Chemistry, in: Encyclopedia of Atmospheric Sciences (Second Edition), edited by North, G. R., Pyle, J., and Zhang, F., pp. 23 – 31, Academic Press, Oxford, second edition edn., https://doi.org/https://doi.org/10.1016/B978-0-12-382225-3.00049-9, URL http://www.sciencedirect.com/science/article/pii/B9780123822253000499, 2015.

Kaufman, Y. J. and Koren, I.: Smoke and Pollution Aerosol Effect on Cloud Cover, Science, 313, 655–658, https://doi.org/10.1126/science.1126232, URL http://science.sciencemag.org/content/313/5787/655, 2006.

Kay, J. E., Hillman, B. R., Klein, S. A., Zhang, Y., Medeiros, B., Pincus, R., Gettelman, A., Eaton, B., Boyle, J., Marchand, R., and Ackerman, T. P.: Exposing Global Cloud Biases in the Community Atmosphere Model (CAM) Using Satellite Observations and Their Corresponding Instrument Simulators, Journal of Climate, 25, 5190–5207, https://doi.org/10.1175/JCLI-D-11-00469.1, URL https://doi.org/10.1175/JCLI-D-11-00469.1, 2012.

Kazil, J., Stier, P., Zhang, K., Quaas, J., Kinne, S., O'Donnell, D., Rast, S., Esch, M., Ferrachat, S., Lohmann, U., and Feichter, J.: Aerosol nucleation and its role for clouds and Earth's radiative forcing in the aerosol-climate model ECHAM5-HAM, Atmospheric Chemistry and Physics, 10, 10 733–10 752, https://doi.org/10.5194/acp-10-10733-2010, URL https://www.atmos-chem-phys.net/10/10733/2010/, 2010.

King, M. D., Tsay, S. C., Platnick, S. E., Wang, M., and Liou, K. N.: Cloud retrieval algorithm for MODIS: Optical thickness, effective particle radius, and thermodynamic phase. MODIS Algorithm Theoretical Basis Document, 1997.

Kirtman, B., Power, S., Adedoyin, J., Boer, G., Bojariu, R., Camilloni, I., Doblas-Reyes, F., Fiore, A., Kimoto, M., Meehl, G., Prather, M., Sarr, A., Schär, C., Sutton, R., van Oldenborgh, G., Vecchi, G., and Wang, H.: Near-term Climate Change: Projections and Predictability, book section 11, p. 953–1028, Cambridge University Press, Cambridge, United Kingdom and New York, NY, USA, https://doi.org/10.1017/CBO9781107415324.023, URL www.climatechange2013.org, 2013.

Koffi, B., Schulz, M., Bréon, F.-M., Dentener, F., Steensen, B. M., Griesfeller, J., Winker, D., Balkanski, Y., Bauer, S. E., Bellouin, N., Berntsen, T., Bian, H., Chin, M., Diehl, T., Easter, R., Ghan, S., Hauglustaine, D. A., Iversen, T., Kirkevåg, A., Liu, X., Lohmann, U., Myhre, G., Rasch, P., Seland, ., Skeie, R. B., Steenrod, S. D., Stier, P., Tackett, J., Takemura, T., Tsigaridis, K., Vuolo, M. R., Yoon, J., and Zhang, K.: Evaluation of the aerosol vertical distribution in global aerosol models through comparison against CALIOP measurements: AeroCom phase II results, Journal of Geophysical Research: Atmospheres, 121, 7254–7283, https://doi.org/10.1002/2015JD024639, URL https://agupubs.onlinelibrary.wiley.com/doi/abs/10.1002/2015JD024639, 2016.

Koren, I., Altaratz, O., , Remer, L. A., Feingold, G., Martins, J. V., and Heiblum, R. H.: How small is a small cloud?, Atmospheric Chemistry and Physics, 8, 3855–3864, https://doi.org/10.5194/acp-8-3855-2008, URL https://www.atmos-chem-phys.net/8/3855/2008/, 2008.

Koren, I., Oreopoulos, L., Feingold, G., Remer, L. A., and Altaratz, O.: Aerosol-induced intensification of rain from the tropics to the mid-latitudes, Nature Geoscience, 4, https://doi.org/10.1038/ngeo1364, URL https://doi.org/10.1038/ngeo1364, 2012.

Kristiansen, N. I., Stohl, A., and Wotawa, G.: Atmospheric removal times of the aerosol-bound radionuclides ^{137}Cs and ^{131}I measured after the Fukushima Dai-ichi nuclear accident ndash; a constraint for air quality and climate models, Atmospheric Chemistry and Physics, 12, 10 759–10 769, https://doi.org/10.5194/acp-12-10759-2012, URL https://www.atmos-chem-phys.net/12/10759/2012/, 2012.

Kulmala, M., Korhonen, P., Vesala, T., Hansson, H.-C., Noone, K., and Svenningsson, B.: The effect of hygroscopicity on cloud droplet formation, Tellus B: Chemical and Physical Meteorology, 48, 347–360, https://doi.org/10.3402/tellusb.v48i3.15903, URL https://doi.org/10.3402/tellusb.v48i3.15903, 1996.

Kulmala, M., , Petäjä, T., nieminen, T., Sipilä, M., Manninen, H. E., Lehtipalo, K., Dal Maso, M., Aalto, P. P., Junninen, H., Paasonen, P., Riipinen, I., Lehtinen, K. E. J., Laaksonen, A., and Kerminen, V.-M.: Measurement of the nucleation of atmospheric aerosol particles, Nature Protocols, 7, https://doi.org/10.1038/nprot.2012.091, URL https://doi.org/10.1038/nprot.2012.091, 2012.

Kulmala, M., Kontkanen, J., Junninen, H., Lehtipalo, K., Manninen, H. E., Nieminen, T., Petäjä, T., Sipilä, M., Schobesberger, S., Rantala, P., Franchin, A., Jokinen, T., Järvinen, E., Äijälä, M., Kangasluoma, J., Hakala, J., Aalto, P. P., Paasonen, P., Mikkilä, J., Vanhanen, J., Aalto, J., Hakola, H., Makkonen, U., Ruuskanen, T., Mauldin, R. L., Duplissy, J., Vehkamäki, H., Bäck, J., Kortelainen, A., Riipinen, I., Kurtén, T., Johnston, M. V., Smith, J. N., Ehn, M., Mentel, T. F., Lehtinen, K. E. J., Laaksonen, A., Kerminen, V.-M., and Worsnop, D. R.: Direct Observations of Atmospheric Aerosol Nucleation, Science, 339, 943–946, https://doi.org/10.1126/science.1227385, URL https://science.sciencemag.org/content/339/6122/943, 2013.

Köhler, H.: The nucleus in and the growth of hygroscopic droplets, Trans. Faraday Soc., 32, 1152–1161, https://doi.org/10.1039/TF9363201152, URL http://dx.doi.org/10.1039/TF9363201152, 1936.

Lack, D. A. and Langridge, J. M.: On the attribution of black and brown carbon light absorption using the Ångström exponent, Atmospheric Chemistry and Physics, 13, 10 535–10 543, https://doi.org/10.5194/acp-13-10535-2013, URL https://www.atmos-chem-phys.net/13/10535/2013/, 2013.

Lamb, D. and Verlinde, J.: Physics and chemistry of clouds, Cambridge University Press, United Kingdom, https://doi.org/10.1017/CBO9780511976377, 2011.

Lee, S. S.: Effect of Aerosol on Circulations and Precipitation in Deep Convective Clouds, Journal of the Atmospheric Sciences, 69, 1957–1974, https://doi.org/10.1175/JAS-D-11-0111.1, URL https://doi.org/10.1175/JAS-D-11-0111.1, 2012.

Levelt, P. F., van den Oord, G. H. J., Dobber, M. R., Malkki, A., Visser, H., de Vries, J., Stammes, P., Lundell, J. O. V., and Saari, H.: The ozone monitoring instrument, IEEE Transactions on Geoscience and Remote Sensing, 44, 1093–1101, https://doi.org/10.1109/TGRS.2006.872333, 2006.

Levy, R., Hsu, C., Sayer, A., Mattoo, S., and Lee, J.: The Collection 6 MODIS aerosol products over land and ocean, https://doi.org/[doi:10.5067/MODIS/MOD04_L2.006;doi:10.5067/MODIS/MYD04_L2.006], 2015.

Levy, R. C., Mattoo, S., Munchak, L. A., Remer, L. A., Sayer, A. M., Patadia, F., and Hsu, N. C.: The Collection 6 MODIS aerosol products over land and ocean, Atmospheric Measurement Techniques, 6, 2989–3034, https://doi.org/10.5194/amt-6-2989-2013, URL https://www.atmos-meas-tech.net/6/2989/2013/, 2013.

Liu, J. and Li, Z.: Significant Underestimation in the Optically Based Estimation of the Aerosol First Indirect Effect Induced by the Aerosol Swelling Effect, Geophysical Research Letters, 45, 5690–5699, https://doi.org/10.1029/2018GL077679, URL https://agupubs.onlinelibrary.wiley.com/doi/abs/10.1029/2018GL077679, 2018.

Lohmann, U.: Aerosol Effects on Clouds and Climate, Space Science Reviews, 125, 129–137, https://doi.org/10.1007/s11214-006-9051-8, URL https://doi.org/10.1007/s11214-006-9051-8, 2006.

Lohmann, U. and Neubauer, D.: The importance of mixed-phase and ice clouds for climate sensitivity in the global aerosol–climate model ECHAM6-HAM2, Atmospheric Chemistry and Physics, 18, 8807–8828, https://doi.org/10.5194/acp-18-8807-2018, URL https://www.atmos-chem-phys.net/18/8807/2018/, 2018.

Lohmann, U., Lüönd, F., and Mahrt, F.: An Introduction to Clouds: From the Microscale to Climate, Cambridge University Press, https://doi.org/10.1017/CBO9781139087513, 2016.

L'Ecuyer, T. S., Hang, Y., Matus, A. V., and Wang, Z.: Reassessing the Effect of Cloud Type on Earth's Energy Balance in the Age of Active Spaceborne Observations. Part I: Top of Atmosphere and Surface, Journal of Climate, 32, 6197–6217, https://doi.org/10.1175/JCLI-D-18-0753.1, URL https://doi.org/10.1175/JCLI-D-18-0753.1, 2019.

Ma, X., Jia, H., Yu, F., and Quaas, J.: Opposite Aerosol Index-Cloud Droplet Effective Radius Correlations Over Major Industrial Regions and Their Adjacent Oceans, Geophysical Research Letters, 45, 5771–5778, https://doi.org/10.1029/2018GL077562, URL https://agupubs.onlinelibrary.wiley.com/doi/abs/10.1029/2018GL077562, 2018.

Mace, G. G., Zhang, Q., Vaughan, M., Marchand, R., Stephens, G., Trepte, C., and Winker, D.: A description of hydrometeor layer occurrence statistics derived from the first year of merged Cloudsat and CALIPSO data, Journal of Geophysical Research: Atmospheres, 114, https://doi.org/10.1029/2007JD009755, URL https://agupubs.onlinelibrary.wiley.com/doi/abs/10.1029/2007JD009755, 2009.

Marchand, R.: ARM and Satellite Cloud Validation, Meteorological Monographs, 57, 30.1–30.11, https://doi.org/10.1175/AMSMONOGRAPHS-D-15-0038.1, URL https://doi.org/10.1175/AMSMONOGRAPHS-D-15-0038.1, 2016.

Martucci, G. and O'Dowd, C. D.: Ground-based retrieval of continental and marine warm cloud microphysics, Atmospheric Measurement Techniques, 4, 2749–2765, https://doi.org/10.5194/amt-4-2749-2011, URL https://www.atmos-meas-tech.net/4/2749/2011/, 2011.

Mie, G.: Beiträge zur Optik trüber Medien, speziell kolloidaler Metallösungen, Annalen der Physik, 330, 377–445, https://doi.org/10.1002/andp.19083300302, URL https://onlinelibrary.wiley.com/doi/abs/10.1002/andp.19083300302, 1908.

Mochida, M., Nishita-Hara, C., Furutani, H., Miyazaki, Y., Jung, J., Kawamura, K., and Uematsu, M.: Hygroscopicity and cloud condensation nucleus activity of marine aerosol particles over the western North Pacific, Journal of Geophysical Research: Atmospheres, 116, https://doi.org/10.1029/2010JD014759, URL https://agupubs.onlinelibrary.wiley.com/doi/abs/10.1029/2010JD014759, 2011.

Moosmüller, H., Chakrabarty, R., and Arnott, W.: Aerosol light absorption and its measurement: A review, Journal of Quantitative Spectroscopy and Radiative Transfer, 110, 844 – 878, https://doi.org/https://doi.org/10.1016/j.jqsrt.2009.02.035, URL http://www.sciencedirect.com/science/article/pii/S0022407309000879, 2009.

Myhre, G., Stordal, F., Johnsrud, M., Kaufman, Y. J., Rosenfeld, D., Storelvmo, T., Kristjansson, J. E., Berntsen, T. K., Myhre, A., and Isaksen, I. S. A.: Aerosol-cloud interaction inferred from MODIS satellite data and global aerosol models, Atmospheric Chemistry and Physics, 7, 3081–3101, https://doi.org/10.5194/acp-7-3081-2007, URL https://www.atmos-chem-phys.net/7/3081/2007/, 2007.

Neubauer, D., Christensen, M. W., Poulsen, C. A., and Lohmann, U.: Unveiling aerosol–cloud interactions – Part 2: Minimising the effects of aerosol swelling and wet scavenging in ECHAM6-HAM2 for comparison to satellite data, Atmospheric Chemistry and Physics, 17, 13 165–13 185, https://doi.org/10.5194/acp-17-13165-2017, URL https://www.atmos-chem-phys.net/17/13165/2017/, 2017.

Neubauer, D., Ferrachat, S., Siegenthaler-Le Drian, C., Stier, P., Partridge, D. G., Tegen, I., Bey, I., Stanelle, T., Kokkola, H., and Lohmann, U.: The global aerosol-climate model ECHAM6.3-HAM2.3 â€“ Part 2: Cloud evaluation, aerosol radiative forcing and climate sensitivity, Geoscientific Model Development Discussions, 2019, 1–52, https://doi.org/10.5194/gmd-2018-307, URL https://www.geosci-model-dev-discuss.net/gmd-2018-307/, 2019.

Nilo, S. T., Romano, F., Cermak, J., Cimini, D., Ricciardelli, E., Cersosimo, A., Di Paola, F., Gallucci, D., Gentile, S., Geraldi, E., Larosa, S., Ripepi, E., and Viggiano, M.: Fog Detection Based on Meteosat Second Generation-Spinning Enhanced Visible and InfraRed Imager High Resolution Visible Channel, Remote Sensing, 10, https://doi.org/10.3390/rs10040541, URL https://www.mdpi.com/2072-4292/10/4/541, 2018.

Ovadnevaite, J., Ceburnis, D., Leinert, S., Dall'Osto, M., Canagaratna, M., O'Doherty, S., Berresheim, H., and O'Dowd, C.: Submicron NE Atlantic marine aerosol chemical composition and abundance: Seasonal trends and air mass categorization, Journal of Geophysical Research: Atmospheres, 119, 11,850–11,863, https://doi.org/10.1002/2013JD021330, URL https://agupubs.onlinelibrary.wiley.com/doi/abs/10.1002/2013JD021330, 2014.

Painemal, D.: Global Estimates of Changes in Shortwave Low-Cloud Albedo and Fluxes Due to Variations in Cloud Droplet Number Concentration Derived From CERES-MODIS Satellite Sensors, Geophysical Research Letters, 45, 9288–9296, https://doi.org/10.1029/

2018GL078880, URL https://agupubs.onlinelibrary.wiley.com/doi/abs/10.1029/2018GL078880, 2018.

Parmes, E., Rauste, Y., Molinier, M., Andersson, K., and Seitsonen, L.: Automatic Cloud and Shadow Detection in Optical Satellite Imagery Without Using Thermal Bands—Application to Suomi NPP VIIRS Images over Fennoscandia, Remote Sensing, 9, https://doi.org/10.3390/rs9080806, URL https://www.mdpi.com/2072-4292/9/8/806, 2017.

Platnick, S., King, M. D., Meyer, K. G.and Wind, G. A. N., Marchant, B., Arnold, G. T., Zhang, Z. B., Hubanks, P. A., Ridgway, B., and Riedi, J.: MODIS Cloud Optical Properties: User Guide for the Collection 6 Level-2 MOD06/MYD06 Product and Associated Level-3 Datasets, Version 1.0, October 2015, URL availableat:http://modis-atmos.gsfc.nasa.gov/_docs/C6MOD06OPUserGuide.pdf(lastaccess:16August2017), 2015.

Platnick, S., Meyer, K. G.and King, M. D., Wind, G., Amarasinghe, N., Marchant, B., Arnold, G. T., Zhang, Z., Hubanks, P. A., Holz, R. E., Yang, P., Ridgway, W. L., and Riedi, J.: The MODIS Cloud Optical and Microphysical Products: Collection 6 Updates and Examples From Terra and Aqua, IEEE Transactions on Geoscience and Remote Sensing, 55, 502–525, https://doi.org/10.1109/TGRS.2016.2610522, 2017.

Platnick, S., Meyer, K. G., King, M. D., Wind, G., Amarasinghe, N., Marchant, B., Arnold, G. T. Zhang, Z. H. P. A., Ridgway, B., and J., R.: MODIS Cloud optical properties: User guide for the Collection 6/6.1 level-2 MOD06/MYD06 product and associated level-3 data sets. Version1.1, Tech. rep., 2018.

Qiu, Y., Zhao, C., Guo, J., and Li, J.: 8-Year ground-based observational analysis about the seasonal variation of the aerosol-cloud droplet effective radius relationship at SGP site, Atmospheric Environment, 164, 139 – 146, https://doi.org/https://doi.org/10.1016/j.atmosenv.2017.06.002, URL http://www.sciencedirect.com/science/article/pii/S1352231017303746, 2017.

Quaas, J., Boucher, O., and Lohmann, U.: Constraining the total aerosol indirect effect in the LMDZ and ECHAM4 GCMs using MODIS satellite data, Atmospheric Chemistry and Physics, 6, 947–955, https://doi.org/10.5194/acp-6-947-2006, URL https://www.atmos-chem-phys.net/6/947/2006/, 2006.

Quaas, J., Stevens, B., Stier, P., and Lohmann, U.: Interpreting the cloud cover - aerosol optical depth relationship found in satellite data using a general circulation model, Atmospheric Chemistry and Physics, 10, 6129–6135, https://doi.org/10.5194/acp-10-6129-2010, URL https://www.atmos-chem-phys.net/10/6129/2010/, 2010.

Rausch, J., Heidinger, A., and Bennartz, R.: Regional assessment of microphysical properties of marine boundary layer cloud using the PATMOS-x dataset, Journal of Geophysical Research: Atmospheres, 115, https://doi.org/10.1029/2010JD014468, URL https://agupubs.onlinelibrary.wiley.com/doi/abs/10.1029/2010JD014468, 2010.

Reutter, P., Su, H., Trentmann, J., Simmel, M., Rose, D., Gunthe, S. S., Wernli, H., Andreae, M. O., and Pöschl, U.: Aerosol- and updraft-limited regimes of cloud droplet formation: influence of particle number, size and hygroscopicity on the activation of cloud condensation nuclei (CCN), Atmospheric Chemistry and Physics, 9, 7067–7080, https://doi.org/10.5194/acp-9-7067-2009, URL https://www.atmos-chem-phys.net/9/7067/2009/, 2009.

Rosenfeld, D.: Aerosol-Cloud Interactions Control of Earth Radiation and Latent Heat Release Budgets, Space Science Reviews, 125, 149–157, https://doi.org/10.1007/s11214-006-9053-6, URL https://doi.org/10.1007/s11214-006-9053-6, 2006.

Rosenfeld, D. and Givati, A.: Evidence of Orographic Precipitation Suppression by Air Pollution–Induced Aerosols in the Western United States, Journal of Applied Meteorology and Climatology, 45, 893–911, https://doi.org/10.1175/JAM2380.1, URL https://doi.org/10.1175/JAM2380.1, 2006.

Rossow, W. B. and Garder, L. C.: Cloud Detection Using Satellite Measurements of Infrared and Visible Radiances for ISCCP, Journal of Climate, 6, 2341–2369, https://doi.org/10.1175/1520-0442(1993)006<2341:CDUSMO>2.0.CO;2, URL https://doi.org/10.1175/1520-0442(1993)006<2341:CDUSMO>2.0.CO;2, 1993.

Seinfeld, J. H. and Pandis, S. N.: Atmospheric Chemistry and Physics: From Air Pollution to Climate Change, John Wiley Sons, Inc., 2 edn., 2006.

Seinfeld, J. H., Bretherton, C., Carslaw, K. S., Coe, H., DeMott, P. J., Dunlea, E. J., Feingold, G., Ghan, S., Guenther, A. B., Kahn, R., Kraucunas, I., Kreidenweis, S. M., Molina, M. J., Nenes, A., Penner, J. E.,

Prather, K. A., Ramanathan, V., Ramaswamy, V., Rasch, P. J., Ravishankara, A. R., Rosenfeld, D., Stephens, G., and Wood, R.: Improving our fundamental understanding of the role of aerosol-cloud interactions in the climate system, Proceedings of the National Academy of Sciences, 113, 5781–5790, https://doi.org/10.1073/pnas.1514043113, URL https://www.pnas.org/content/113/21/5781, 2016.

Shin, S.-K., Tesche, M., Müller, D., and Noh, Y.: Technical note: Absorption aerosol optical depth components from AERONET observations of mixed dust plumes, Atmospheric Measurement Techniques, 12, 607–618, https://doi.org/10.5194/amt-12-607-2019, URL https://www.atmos-meas-tech.net/12/607/2019/, 2019.

Stephens, G. L.: Cloud Feedbacks in the Climate System: A Critical Review, Journal of Climate, 18, 237–273, https://doi.org/10.1175/JCLI-3243.1, URL https://doi.org/10.1175/JCLI-3243.1, 2005.

Stier, P.: Limitations of passive remote sensing to constrain global cloud condensation nuclei, Atmospheric Chemistry and Physics, 16, 6595–6607, https://doi.org/10.5194/acp-16-6595-2016, URL https://www.atmos-chem-phys.net/16/6595/2016/, 2016.

Stjern, C. W., Samset, B. H., Myhre, G., Forster, P. M., Hodnebrog, ., Andrews, T., Boucher, O., Faluvegi, G., Iversen, T., Kasoar, M., Kharin, V., Kirkevåg, A., Lamarque, J.-F., Olivié, D., Richardson, T., Shawki, D., Shindell, D., Smith, C. J., Takemura, T., and Voulgarakis, A.: Rapid Adjustments Cause Weak Surface Temperature Response to Increased Black Carbon Concentrations, Journal of Geophysical Research: Atmospheres, 122, 11,462–11,481, https://doi.org/10.1002/2017JD027326, URL https://agupubs.onlinelibrary.wiley.com/doi/abs/10.1002/2017JD027326, 2017.

Sun, L., Mi, X., Wei, J., Wang, J., Tian, X., Yu, H., and Gan, P.: A cloud detection algorithm-generating method for remote sensing data at visible to short-wave infrared wavelengths, ISPRS Journal of Photogrammetry and Remote Sensing, 124, 70 – 88, https://doi.org/https://doi.org/10.1016/j.isprsjprs.2016.12.005, URL http://www.sciencedirect.com/science/article/pii/S0924271616306189, 2017.

Sun, Q., Miao, C., Duan, Q., Ashouri, H., Sorooshian, S., and Hsu, K.-L.: A Review of Global Precipitation Data Sets: Data Sources, Estimation, and Intercomparisons, Reviews of Geophysics, 56, 79–107, https://doi.org/10.

1002/2017RG000574, URL https://agupubs.onlinelibrary.wiley.com/doi/abs/10.1002/2017RG000574, 2018.

Tegen, I. and Schepanski, K.: Climate Feedback on Aerosol Emission and Atmospheric Concentrations, Current Climate Change Reports, 4, 1–1, https://doi.org/10.1007/s40641-018-0086-1, URL https://doi.org/10.1007/s40641-018-0086-1, 2018.

Tian, P., Cao, X., Zhang, L., Sun, N., Sun, L., Logan, T., Shi, J., Wang, Y., Ji, Y., Lin, Y., Huang, Z., Zhou, T., Shi, Y., and Zhang, R.: Aerosol vertical distribution and optical properties over China from long-term satellite and ground-based remote sensing, Atmospheric Chemistry and Physics, 17, 2509–2523, https://doi.org/10.5194/acp-17-2509-2017, URL https://www.atmos-chem-phys.net/17/2509/2017/, 2017.

Twomey, S.: The Influence of Pollution on the Shortwave Albedo of Clouds, Journal of the Atmospheric Sciences, 34, 1149–1152, https://doi.org/10.1175/1520-0469(1977)034<1149:TIOPOT>2.0.CO;2, URL https://doi.org/10.1175/1520-0469(1977)034<1149:TIOPOT>2.0.CO;2, 1977.

Väisänen, O., Ruuskanen, A., Ylisirniö, A., Miettinen, P., Portin, H., Hao, L., Leskinen, A., Komppula, M., Romakkaniemi, S., Lehtinen, K. E. J., and Virtanen, A.: In-cloud measurements highlight the role of aerosol hygroscopicity in cloud droplet formation, Atmospheric Chemistry and Physics, 16, 10 385–10 398, https://doi.org/10.5194/acp-16-10385-2016, URL https://www.atmos-chem-phys.net/16/10385/2016/, 2016.

Virtanen, T. H., Kolmonen, P., Sogacheva, L., Rodríguez, E., Saponaro, G., and de Leeuw, G.: Collocation mismatch uncertainties in satellite aerosol retrieval validation, Atmospheric Measurement Techniques, 11, 925–938, https://doi.org/10.5194/amt-11-925-2018, URL https://www.atmos-meas-tech.net/11/925/2018/, 2018.

Wallace, J. M. and Hobbs, P.: Atmospheric Science: An Introductory Survey, U.K. Elsevier Inc, 3 edn., 2006.

Webb, M. J., Andrews, T., Bodas-Salcedo, A., Bony, S., Bretherton, C. S., Chadwick, R., Chepfer, H., Douville, H., Good, P., Kay, J. E., Klein, S. A., Marchand, R., Medeiros, B., Siebesma, A. P., Skinner, C. B., Stevens, B., Tselioudis, G., Tsushima, Y., and Watanabe, M.: The Cloud Feedback Model Intercomparison Project (CFMIP) contribution to CMIP6, Geoscientific Model Development, 10, 359–384, https://doi.org/10.

5194/gmd-10-359-2017, URL https://www.geosci-model-dev.net/10/359/2017/, 2017.

Werner, F., Ditas, F., Siebert, H., Simmel, M., Wehner, B., Pilewskie, P., Schmeissner, T., Shaw, R. A., Hartmann, S., Wex, H., Roberts, G. C., and Wendisch, M.: Twomey effect observed from collocated microphysical and remote sensing measurements over shallow cumulus, Journal of Geophysical Research: Atmospheres, 119, 1534–1545, https://doi.org/10.1002/2013JD020131, URL https://agupubs.onlinelibrary.wiley.com/doi/abs/10.1002/2013JD020131, 2014.

Yan, H., Chen, L., Tao, J., Su, L., Huang, J., Han, D., and Yu, C.: Corrections for OMI SO_2 BRD retrievals influenced by row anomalies, Atmospheric Measurement Techniques, 5, 2635–2646, https://doi.org/10.5194/amt-5-2635-2012, URL https://www.atmos-meas-tech.net/5/2635/2012/, 2012.

Yan, Y., Liu, Y., and Lu, J.: Cloud vertical structure, precipitation, and cloud radiative effects over Tibetan Plateau and its neighboring regions, Journal of Geophysical Research: Atmospheres, 121, 5864–5877, https://doi.org/10.1002/2015JD024591, URL https://agupubs.onlinelibrary.wiley.com/doi/abs/10.1002/2015JD024591, 2016.

Yang, W., Marshak, A., Várnai, T., and Wood, R.: CALIPSO observations of near-cloud aerosol properties as a function of cloud fraction, Geophysical Research Letters, 41, 9150–9157, https://doi.org/10.1002/2014GL061896, 2014.

Zhang, Z., Ackerman, A. S., Feingold, G., Platnick, S., Pincus, R., and Xue, H.: Effects of cloud horizontal inhomogeneity and drizzle on remote sensing of cloud droplet effective radius: Case studies based on large-eddy simulations, Journal of Geophysical Research: Atmospheres, 117, n/a–n/a, https://doi.org/10.1029/2012JD017655, URL http://dx.doi.org/10.1029/2012JD017655, d19208, 2012.

Zhou, X., Ackerman, A. S., Fridlind, A. M., Wood, R., and Kollias, P.: Impacts of solar-absorbing aerosol layers on the transition of stratocumulus to trade cumulus clouds, Atmospheric Chemistry and Physics, 17, 12 725–12 742, https://doi.org/10.5194/acp-17-12725-2017, URL https://www.atmos-chem-phys.net/17/12725/2017/, 2017.

Zhu, L., Suomalainen, J., Liu, J., Hyyppä, J., Kaartinen, H., and Haggren, H.: A Review: Remote Sensing Sensors, in: Multi-purposeful Application of

Geospatial Data, edited by Rustamov, R. B., Hasanova, S., and Zeynalova, M. H., chap. 2, IntechOpen, Rijeka, https://doi.org/10.5772/intechopen.71049, URL https://doi.org/10.5772/intechopen.71049, 2018.

Zhu, Y., Rosenfeld, D., Yu, X., and Li, Z.: Separating aerosol microphysical effects and satellite measurement artifacts of the relationships between warm rain onset height and aerosol optical depth, Journal of Geophysical Research: Atmospheres, 120, 7726–7736, https://doi.org/10.1002/2015JD023547, URL https://agupubs.onlinelibrary.wiley.com/doi/abs/10.1002/2015JD023547, 2015.

Zhu, Z. and Woodcock, C. E.: Automated cloud, cloud shadow, and snow detection in multitemporal Landsat data: An algorithm designed specifically for monitoring land cover change, Remote Sensing of Environment, 152, 217 – 234, https://doi.org/https://doi.org/10.1016/j.rse.2014.06.012, URL http://www.sciencedirect.com/science/article/pii/S0034425714002259, 2014.

Zotter, P., Herich, H., Gysel, M., El-Haddad, I., Zhang, Y., Močnik, G., Hüglin, C., Baltensperger, U., Szidat, S., and Prévôt, A. S. H.: Evaluation of the absorption Ångström exponents for traffic and wood burning in the Aethalometer-based source apportionment using radiocarbon measurements of ambient aerosol, Atmospheric Chemistry and Physics, 17, 4229–4249, https://doi.org/10.5194/acp-17-4229-2017, URL https://www.atmos-chem-phys.net/17/4229/2017/, 2017.

Ångström, A.: On the Atmospheric Transmission of Sun Radiation and on Dust in the Air, Geografiska Annaler, 11, 156–166, https://doi.org/10.1080/20014422.1929.11880498, URL https://doi.org/10.1080/20014422.1929.11880498, 1929.

I

Reprinted from
Atmospheric Measurement techniques, 6, 2301–2309,
doi:10.5194/amt-6-2301-2013

Atmos. Meas. Tech., 6, 2301–2309, 2013
www.atmos-meas-tech.net/6/2301/2013/
doi:10.5194/amt-6-2301-2013

Atmospheric Measurement Techniques Open Access

A neural network algorithm for cloud fraction estimation using NASA-Aura OMI VIS radiance measurements

G. Saponaro[1], P. Kolmonen[1], J. Karhunen[3], J. Tamminen[2], and G. de Leeuw[1,4]

[1]Finnish Meteorological Institute, Climate Change Unit, P.O. Box 503, 00101 Helsinki, Finland
[2]Finnish Meteorological Institute, Earth Observation Unit, P.O. Box 503, 00101 Helsinki, Finland
[3]Department of Information and Computer Science, Aalto University School of Science, P.O. Box 15400, 00076 Espoo, Finland
[4]Department of Physics, University of Helsinki, P.O. Box 64, 00014 Helsinki, Finland

Correspondence to: G. Saponaro (giulia.saponaro@fmi.fi)

Received: 20 October 2012 – Published in Atmos. Meas. Tech. Discuss.: 13 February 2013
Revised: 10 July 2013 – Accepted: 23 July 2013 – Published: 9 September 2013

Abstract. The discrimination of cloudy from cloud-free pixels is required in almost any estimate of a parameter retrieved from satellite data in the ultraviolet (UV), visible (VIS) or infrared (IR) parts of the electromagnetic spectrum. In this paper we report on the development of a neural network (NN) algorithm to estimate cloud fractions using radiances measured at the top of the atmosphere with the NASA-Aura Ozone Monitoring Instrument (OMI). We present and discuss the results obtained from the application of two different types of neural networks, i.e., extreme learning machine (ELM) and back propagation (BP). The NNs were trained with an OMI data sets existing of six orbits, tested with three other orbits and validated with another two orbits. The results were evaluated by comparison with cloud fractions available from the MODerate Resolution Imaging Spectrometer (MODIS) flying on Aqua in the same constellation as OMI, i.e., with minimal time difference between the OMI and MODIS observations. The results from the ELM and BP NNs are compared. They both deliver cloud fraction estimates in a fast and automated way, and they both performs generally well in the validation. However, over highly reflective surfaces, such as desert, or in the presence of dust layers in the atmosphere, the cloud fractions are not well predicted by the neural network. Over ocean the two NNs work equally well, but over land ELM performs better.

1 Introduction

The retrieval of atmospheric constituents, such as aerosols or trace gases, land or ocean surface properties from satellite data requires accurate information on the presence of clouds. Clouds strongly reflect incoming solar radiation in the ultraviolet (UV), visible (VIS) and near infrared (NIR) parts of the electromagnetic spectrum and affect the earth-emitted radiation as detected in the thermal infrared (TIR) part of the wavelength spectrum. In the UV/VIS the cloud reflectance often overwhelms the contribution of other atmospheric constituents, most land surfaces and the ocean surface, to the top-of-atmosphere (TOA) reflectance (Koelemeijer and Stammes, 1999). For instance, for the retrieval of aerosol properties all identified cloud-contaminated pixels are usually discarded (Martins et al., 2002). Cloud detection is usually performed using several tests, depending on information being available, and different algorithms have been developed to extract information on cloud microphysical properties (Ackerman et al., 1998; Kokhanovsky et al., 2011). In this paper we are concerned with cloud detection, or the determination of cloud fraction, rather than the retrieval of cloud microphysical properties. For cloud detection, the most consolidated methods are based on thresholding techniques in histograms of the measured radiance, or reflectance, at certain wavelengths using empirically estimated thresholds, or set with additional information coming from, e.g., radiative transfer models (Dybbroe et al., 2005; Loyola, 2006; Wu et al., 2006). For best results, a combination

of TIR and UV/VIS and NIR wavelength bands is required. However, such information is not always available and other methods need to be applied.

In this paper we focus on cloud detection for the Ozone Monitoring Instrument (OMI). The challenge is the coarse spatial resolution and the lack of thermal channels. The current method for the determination of the OMI cloud mask is based on two individual tests (Stammes and Noordhoek, 2002): the first one uses a radiance threshold and the UV aerosol index, while the second test considers the spatial homogeneity of the so-called small-pixel data (van den Oord, 2002). Pixels failing either of the two tests are classified as cloudy (Acarreta and de Haan, 2002). We propose an approach using neural networks (NN) for the direct determination of the cloud fraction in each OMI pixel. The approach is based on the use of the OMI radiance measurements in the VIS part of the spectrum, together with cloud information from the Aqua-MODerate Resolution Imaging Spectrometer (MODIS). OMI and MODIS both fly in the A-train constellation but on different platforms, respectively Aura and Aqua, with a time lag of about 7 min. The proposed approach is similar to that described in Preusker et al. (2008), where the cloud screening problem for the Medium Resolution Imaging Spectrometer (MERIS), suffering from a similar problem as OMI in that there are no infrared channels, was solved by applying an NN trained with a database of simulated cloudy and cloud-free spectra. In contrast, for the training we use real data obtained from MODIS, with a spatial resolution which is much higher than that of OMI, as reference data to determine the cloud fraction in an OMI pixel.

In recent years neural networks have been adopted for a wide range of applications from atmospheric sciences to electromagnetic modeling. The developed applications include, e.g., forward and inverse radiative transfer problems (Krasnopolsky, 2008), the prediction of atmospheric parameters (Grivas and Chaloulakou, 2006), the inversion and post processing of remotely sensed data (Mas and Flores, 2008; Del Frate and Schiavon, 1998), ozone retrievals (Di Noia et al., 2012; Sellitto et al., 2011, 2012), cloud classification (Christodoulou et al., 2003), land cover classification (Aitkenhead and Aalders, 2008), and feature extraction (Del Frate et al., 2005). Below, we describe the design for the cloud detection algorithm applied to OMI cloud fraction determination.

Two different learning algorithms have been used for training the neural networks, namely the back propagation (BP) and extreme learning machine (ELM). Results from the two methods are reported and their performances over land and ocean are analysed based on the comparison with an independent set of MODIS cloud fraction data. The two neural networks are trained with a training data set consisting of six randomly selected orbits. They are subsequently applied to the test data sets consisting of three other orbits, i.e., different form the training data set, and validated using the validation data set consisting of another two independent orbits.

2 Instruments

OMI is a nadir-viewing near-UV-visible spectrometer on board NASA's Earth Observing System (EOS) Aura satellite. OMI measures radiances at 751 wavelengths covering the UV/VIS wavelength range from 349–504 nmand two UV channels (UV-1: 270–314 nm, UV-2: 306–380 nm). The nominal ground footprint is 13×24 km^2 at nadir, in the normal global operation mode. Complete global coverage was achieved daily (Levelt et al., 2006) between 2002 and 2008, while after 2008 the global coverage is achieved in two days due to the row anomaly (Yan et al., 2012) which affects the quality of OMI level 1b radiance data. Aura flies in the A-train satellite constellation, in a polar sun-synchronous orbit. MODIS, on-board Aqua, produces many cloud related products (e.g., cloud fraction, cloud top pressure, cloud optical thickness) (Hubanks, 2012; King and Bhartia, 1992; King et al., 1998). In view of the short time separation between Aura and Aqua of about 7 minutes, the MODIS products can be used together with OMI products with quite high confidence (Stammes et al., 2008; Vasilkov, 2008; Sneep et al., 2008).

3 Neural Networks

Neural network algorithms aim at identifying the relationship between input and output variables by learning either from real or simulated reference data, rather than directly from the application of a representative physical model (Haykin, 1999; Karayiannis and Venetsanopoulos, 1993).

Owing to the fact that cloud properties are highly variable and sometimes difficult to measure directly, neural networks with their adaptive learning nature offer an attractive and computationally efficient alternative for cloud screening. It has been proven that neural networks algorithms are able to approximate any continuous multivariate non-linear function, provided that the learning data set is statistically representative of the process to be modeled and an appropriate structure for the network has been selected (Hornik et al., 1989). Some applications to atmospheric sciences were referenced in the Introduction.

One important class of neural networks is the multilayer perceptron (MLP) (Werbos, 1974). Figure 1 shows the architectural graph of a multilayer perceptron with one input layer, one hidden layer and an output layer. The input signal is fed into the input layer, flows through the network on a layer-by-layer basis, and emerges at the output layer of the network as an output signal, the response of the network to the inputs.

A node receives inputs from neighbors or external sources and uses them to compute an output signal that is propagated to other units. Within the neural network there are three types of nodes: input nodes, which receive data from outside of the network, output nodes, which send data out of the network, and hidden nodes, whose input and output signals remain within the network. The behavior of the output node

depends on the activity of the hidden nodes and the weights between the hidden and output nodes. The weights between the input and the hidden nodes determine when each hidden node is active. In the MLP, the activation function of the nodes is based on a differentiable non-linear activation function, yielding a value called the unit's activation. These functions enable the network to learn complex tasks by extracting features from the input signal. Biases are simply weights from a single node whose location is outside of the main network and whose activation is always one (Bishop, 2008). A multilayer perceptron requires to be trained and several training algorithms have been developed for an MLP structure for example Levenberg–Marquardt, or Batch which are discussed in Karayiannis and Venetsanopoulos (1993). More details on artificial neural networks can be found in Bishop (2008), Ham and Kostanic (2001) and Haykin (1999).

In this work, two learning algorithms were applied to train the MLP neural network, i.e., back propagation (BP) and extreme learning machine (ELM).

3.1 Back propagation

The error back-propagation algorithm (Rumelhart et al., 1986) is a popular learning algorithm used to train neural networks by modifying the weights during the training phase in order to model a particular learning task correctly for the training examples (Haykin, 1999). The training phase updates the weights iteratively using the negative gradient of a cost function defined as the square of the norm of the error of the current training input. Basically, error back-propagation algorithms perform two passes through each layer of the network: the first pass starts with the application of the input vector to the input nodes of the network, and its effect is forwarded trough the layers. This is the forward pass during which all weights of the network are fixed. Then, a set of output data is produced as the response of the network to the input signal, and is subtracted from a desired (target) response to produce an error signal. The error signal is propagated backward through the network. This process represents the backward pass. During the backward pass the weights are adjusted to move the actual response of the network closer to the desired one in a statistical sense. The model of each node is based on a non-linear activation function.

A sigmoid activation function is used for the hidden nodes and it is presented in the following equation:

$$g(x) = \tanh(ax), \tag{1}$$

where $a > 0$ is a scaling parameter, x is the activation function input, and $g(x)$ is the activation value. This function is especially advantageous for use in neural networks trained by back propagation, because it is easy to differentiate, and thus can dramatically reduce the computation burden for training. It applies to applications whose desired output values are between 0 and 1.

The back-propagation learning does not guarantee that the final solution is the best one as the convergence of the MSE is not checked. This should be taken into account when the solution is analyzed.

3.2 Extreme Learning Machine

The extreme learning machine (Huang et al., 2006) uses a special MLP network structure with one hidden layer where the weights between the input layer and the nodes of the hidden layer are chosen randomly beforehand, and similarly for the bias terms of the hidden layer nodes. The output layer is to be taken linear. The extreme learning machine method for neural networks consists of the following steps:

- Assume that we have a training set $x_i, t_i, i = 1, 2, \ldots, N$, where x_i is the i th input vector of dimension n, t_i is the corresponding target vector of dimension m, and N is the number of training data pairs.
- Choose the activation function $g(t)$ and number of nodes M in the hidden layer. In our case, the selected activation function is $g(x) = \tanh(wx + \beta)$.
- Assign randomly the hidden layer scaling parameter vectors w_j and biases β_j, $j = 1, 2, ..., M$.
- Calculate the $N \times M$ hidden layer output matrix $\mathbf{H}$. Its elements are

$$h_{ij} = g(w_j^{\mathrm{T}} x_i + \beta_j). \tag{2}$$

- Calculate the $M \times m$ weight matrix $\mathbf{B}$ of the output layer from

$$\mathbf{B} = \mathbf{H}^{+}\mathbf{T}, \tag{3}$$

where $\mathbf{T} = [t_1, t_2, \ldots, t_N]^T$ is the $m \times N$ target matrix and $\mathbf{H}^{+}$ is the pseudo-inverse of the matrix $\mathbf{H}$. The matrix $\mathbf{B}$ is

$$\mathbf{B} = \begin{bmatrix} w_{1,m} \\ w_{2,m} \\ \cdot \\ \cdot \\ \cdot \\ w_{M,m} \end{bmatrix}. \tag{4}$$

This learning method requires an easy implementation and it runs extremely fast as compared, for example, to the standard back-propagation algorithms (see Huang et al., 2006, for more detailed information). Since this type of algorithm does not require tuning and the hidden layer parameters can be fixed, the optimal solution can be found with a system of linear equations using the least-squares method (pseudo-inverse) and avoiding problems related to gradient learning methods (Bishop, 2008), such as local minima encountered in the back propagation (Haykin, 1999).

4 Application of neural networks to cloud detection using OMI VIS radiance measurements

To investigate the potential and limits of the application of neural networks for cloud screening, a representative data set for the observed phenomena is required. The training data set needs to be as complete as possible and of sufficient quality. In the NN training phase of the cloud detection method, the input consists of OMI measurements of TOA radiances in the VIS part of the electromagnetic spectrum and collocated (in space) MODIS cloud fraction products as described below.

4.1 The OMI training input

This section describes the OMI products included in the training data set.

OMI measures radiances at a large number of wavelengths in the VIS band, but only part of these are used as described in the next section. Radiances are converted to reflectances and scaled so that the input information for the neural networks has values between 0 and 1. The conversion was done using equation:

$$\rho(\lambda) = \frac{I(\lambda)\pi}{\cos(\theta_z)L(\lambda)}, \quad (5)$$

where ρ is the calculated reflectance, I is the OMI measured radiance at wavelengths between 349 nm and 504 nm, θ_z is the solar zenith angle, and L is the solar irradiance at wavelength λ.

OMI provides, at one wavelength (388 nm in the VIS), a five times higher spatial sampling in the flight direction than normal which is called small-pixel data. This capability can be used to provide information about spatial inhomogeneity in a pixel caused by, e.g., clouds and is therefore used as one of the cloud detection criteria as mentioned in the Introduction. The small pixel radiances are included in the level-1B data set (van den Oord, 2002) and, after conversion to small-pixel reflectances using Eq. (5), were used to calculate the variance of the reflectance in each OMI pixel. This value was added to the training data set.

The solar zenith angle (SZA), providing information about the measurement geometry, and the OMI Surface Reflectance Climatology Data Product (OMLER) were also included to the training data set. OMLER is an OMI product describing the monthly climatology of the earth's surface Lambertian equivalent reflectance (LER). LER is defined as the reflectance of an isotropic surface which matches the observed top of the atmosphere (TOA) reflectance in a purely Rayleigh scattering atmosphere, i.e., in cloud- and aerosol-free conditions. The product has a spatial resolution of 0.5×0.5 degrees and has been built by using five years of OMI data, obtained between January 2005 and December 2009 (Kleipool, 2010).

4.2 Singular value decomposition for the OMI reflectance

During the training phase, the outputs of a NN come to approximate the target values given the inputs in the training set. This ability may be useful in itself, but the purpose of using a NN is to have the outputs approximating target values given inputs that are not in the training set (generalization). Selection of an appropriate number of input variables is an important issue in building a neural network with satisfactory generalization capabilities. The purpose of input variable selection is to find the smallest set of features that can avoid overfitting the NN and produce a smaller number of local minima. The OMI reflectance data consists of 751 measurements for each pixel and a dimensionality reduction is desirable to save on computation time. Dimensionality reduction is the transformation of high-dimensional data into a representation of lower dimensionality without losing valuable information. To achieve this, we have used singular value decomposition (SVD), which is a method that converts a matrix to its diagonal form (Golub and Van Loan, 1996). In the present study the SVD procedure was implemented as follows.

Consider an $N \times M$ matrix $\mathbf{X}$ where $N \geq M$. It is possible to represent this matrix in the r-dimensional subspace where $r \leq M$. Let $\mathbf{U} = \mathbf{X}\mathbf{X}^{\mathbf{T}}$ and $\mathbf{V} = \mathbf{X}^{\mathbf{T}}\mathbf{X}$ be non-negative symmetric matrices with the same eigenvalues $\lambda_1, \lambda_2, ..., \lambda_r$, which are ordered such that $\lambda_1 \geq \lambda_2 \geq \lambda_3 \geq \ldots \lambda_r$. The square roots of these eigenvalues are called the singular values of $\mathbf{X}$. If we form matrices Ψ and Φ from the corresponding eigenvectors of $\mathbf{U}$ and $\mathbf{V}$, then $\mathbf{X}$ can be diagonalized as

$$\mathbf{X} = \Psi \Lambda \Phi^{\mathbf{T}}, \quad (6)$$

where Λ is the diagonal matrix of the eigenvalues, i.e., $\mathrm{diag}(\Lambda) = [\sqrt{\lambda_1}, \sqrt{\lambda_2}, \ldots, \sqrt{\lambda_r}]$. Basically, each singular value represents the information content of the matrix $\mathbf{X}$, projected into each subspace.

The reduction of the reflectance data set is achieved by using only that part of the diagonalized system where the eigenvalues are significant.

4.3 MODIS cloud fraction training data

MODIS cloud fraction is used as reference data for training the neural networks. The spatial matching between OMI and MODIS pixels was performed using the method described by Stammes et al. (2008). In this procedure OMI ground pixel latitude-longitude corner (OMPIXCOR) data are used to construct boxes representing the pixel area. OMPIXCOR is a separate product which was used because the OMI Level 1B data product provides geodetic latitude and longitude only for the center of each ground pixel. The MODIS geolocated data is then searched for measurements falling within each box and a MODIS pixel is considered to fall within a

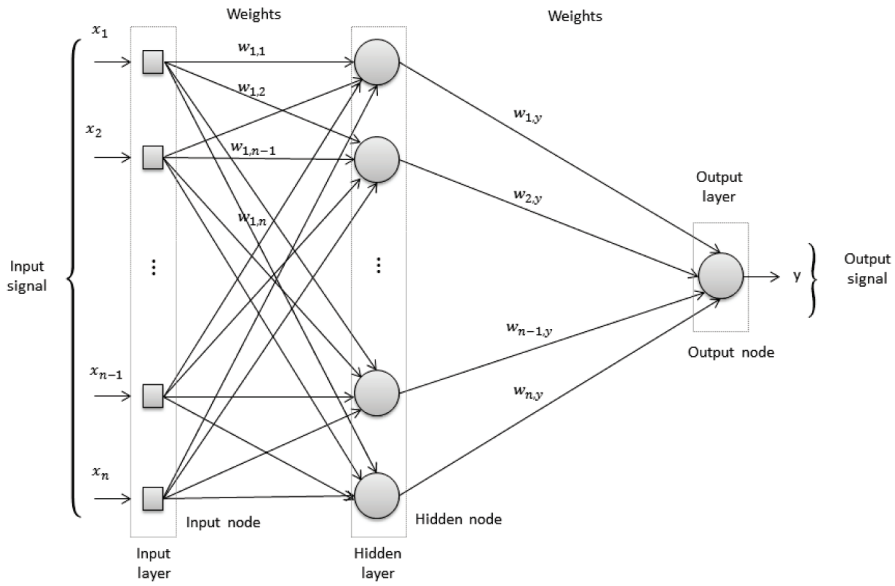

Fig. 1. Neural-network feedforward structure. x_i represents the nth input unit, and y represents the output unit.

particular OMI box if the center lies inside the OMI pixel boundary. The co-locations allow the use of MODIS data to determine the cloud fraction within an OMI pixel as the number of cloudy pixels divided by the total number of MODIS pixels falling within the considered OMI pixel. The re-gridded data is then included in the training input as the reference data.

4.4 Data set composition for training and NN structure

The data set used in this study consists of the reflectance obtained from 11 randomly chosen OMI orbits. These orbits are divided in three subsets as follows: six orbits are used for the training data set, three orbits for the test data sets and the last two are used for independent validation.

The input data set for the NN consists of the OMI SVD-reduced reflectance values, the OMLER climatological data, the solar zenith angles and the small pixel variances. The reference data set consists of the corresponding MODIS geometrical cloud fraction. The different components of the training data set which represents the input to the neural network are shown in the block diagram in Fig. 2. The neural network processes this information and provides the predicted cloud fraction.

Because of the large differences between ocean and land measurements, different models for each situation are used for each of the two neural networks used in this study (BP and ELM). To avoid overfitting of the NNs, optimization of the number of eigenvalues needed for the SVD and the number of hidden neurons was necessary. We trained several NNs with BP and ELM and monitored the MSE and RMSE, for BP and ELM, respectively, as a function of the number of eigenvalues and hidden nodes. The combination of these parameters leading to the best performance on the test data set was used in the optimized NN. Each neural network was trained with a separate model for land and ocean. Then BP and ELM were compared as regards their performance when applied to the third, independent, validation subset.

5 Results

The back-propagation and extreme learning machine algorithms were trained with the training data set and the final weights were applied to each single orbit of the test and validation data sets. The accuracy of the cloud fraction estimates was determined. The performance of the learning algorithms in predicting cloud fraction was assessed in terms of the percentages of the pixels resulting from the test and validation data sets which were estimated to be cloudy or clear by the NN, in comparison with the same percentages as given by the MODIS re-gridded cloud fraction.

In these evaluations, two cloud thresholds were considered, i.e., 60 % and 30 %. A threshold $thr = 60\,\%$ implies that 60 % of an OMI pixel contains clouds. Larger values of thr imply that the pixel is cloudy while pixels with values below the thresholds indicate they are cloud-free (clear). The OMI and MODIS results are compared in Fig. 3.

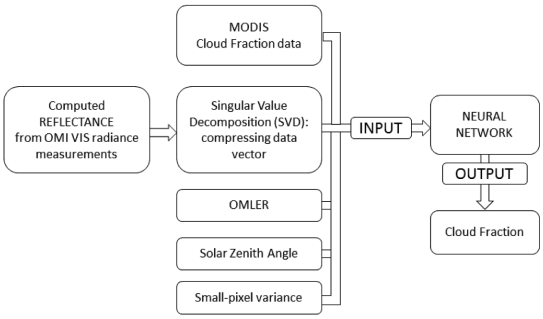

Fig. 2. Block diagram of the proposed approach for training the neural network. The training data set is composed of the target data represented by the MODIS cloud fraction re-gridded onto the OMI orbit, the compressed OMI reflectance vector data, and additional data such as climatological data (OMLER), the solar zenith angle and the computed small-pixel variance. These data form the input vector which is fed to the neural network. The neural network response is a predicted cloud fraction for the given orbit.

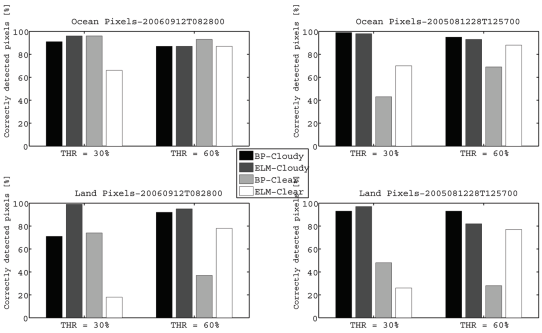

Fig. 3. Performance of backpropagation and extreme learning machine in predicting cloud fraction for divided land and ocean pixels.

The histograms in Fig. 3 represent the percentages of correctly detected cloudy and cloud-free pixels for land and ocean pixels in the validation subset for the two different thresholds and for cloudy and clear situations. The data in Fig. 3 show that both learning algorithms, BP and ELM, lead to correct estimates of cloudy pixels for both threshold values over both ocean and land in most situations. The NNs present inaccuracy when it comes to estimate small cloud fractions and on this problem the BP performs the worst.

The cloud fractions estimated from OMI data using the neural network trained by ELM or BP are compared with the MODIS re-gridded cloud fractions for each orbit of the validation data set over ocean Fig. 4 and over land Fig. 5. The color scales provide a measure for the density number of points. The images are organized in a matrix where the two rows represent the two NNs and the two columns divide the

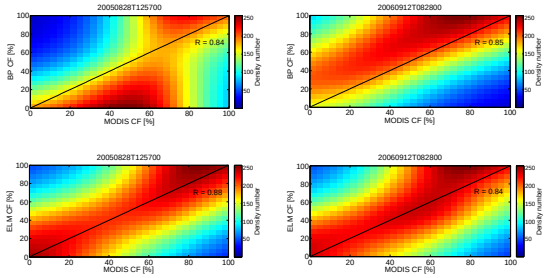

Fig. 4. Density plots showing the correlation between the cloud fraction estimated by the neural networks used in this study and MODIS data over ocean. Correlation coefficients (R) are shown in each plot.

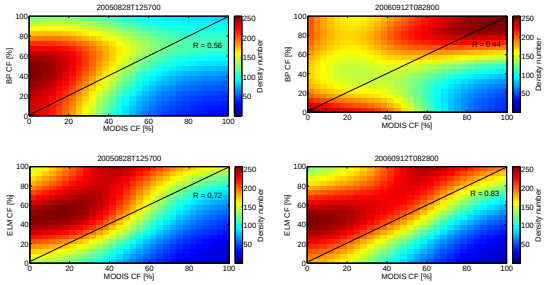

Fig. 5. Density plots showing the correlation between the cloud fraction estimated by the neural networks used in this study and MODIS data over land. Correlation coefficients (R) are shown in each plot.

orbits of the validation subset. Good correlations with R values of 0.85 and 0.88 are observed over ocean, for ELM and BP, respectively. The ocean provides a homogeneous dark surface in the UV / VIS and a good contrast between cloudy and clear pixels is expected. Over land the high reflectance measurements from bright surface represent a challenge for the NNs, although the ELM seems to be less effected than BP resulting in a R of 0.83 and 0.56, respectively, for ELM and BP.

The cloud fraction obtained with the NN using BP or ELM is compared with the MODIS geometrical CF for two validation orbits in Fig. 6 and Fig. 7. In these figures, (a) shows the MODIS geometrical cloud fraction and the grey scale indicates the cloud fraction between 0 (cloud-free) and 100 (100 % cloud-covered). (b, c) show the estimated cloud fraction from BP and ELM neural networks. (d, e) show the difference between MODIS geometrical cloud fraction and the NNs estimates: the value 0 of the color scale represents a perfect agreement between the cloud fraction of the two data sets, while a value of 100 indicates a total mismatch. The results in Fig. 6 and Fig. 7 show that the cloud features are well detected, except over bright land surfaces (deserts).

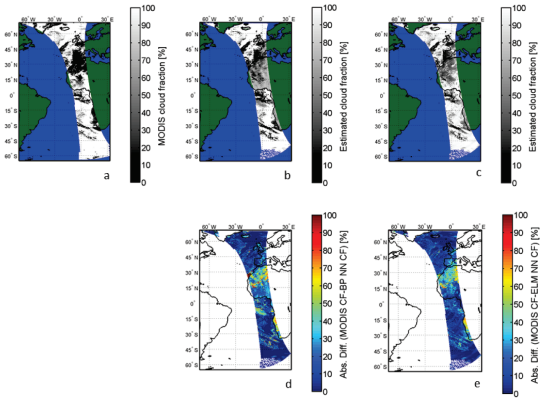

Fig. 6. Cloud fractions estimated by the BP and ELM-trained NN and comparison with MODIS CF data for the validation orbit 2005m0828t1257. **(a)** Computed MODIS geometrical cloud fraction re-located onto the OMI grid. **(b)** BP predicted cloud fraction. **(c)** ELM predicted cloud fraction The grey-code in figures a-c ranges from 0 (cloud free) to 100 (totally cloud covered). **(d)** Absolute difference between MODIS geometrical cloud fraction and BP-predicted cloud fraction. The color-code ranges from 0 (perfect match) to 100 (complete mismatch). **(e)** Absolute difference between MODIS geometrical cloud fraction and ELM-predicted cloud fraction. The color-code in panels **(d)** and **(e)** range from 0 (perfect match) to 100 (complete mismatch)

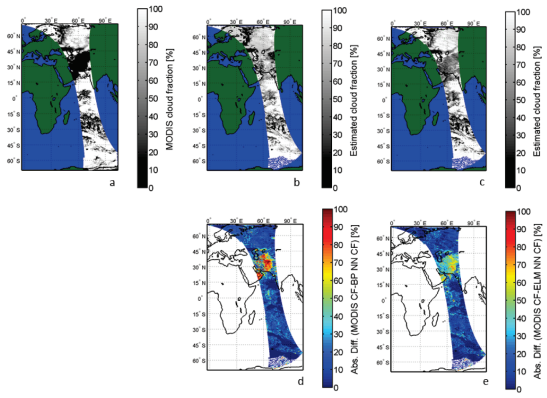

Fig. 7. Cloud fractions estimated by the BP and ELM-trained NN and comparison with MODIS CF data for the validation orbit 2006m0912t0828. **(a)** Computed MODIS geometrical cloud fraction re-located onto the OMI grid. **(b)** BP predicted cloud fraction. **(c)** ELM predicted cloud fraction The grey-code in **(a–c)** ranges from 0 (cloud free) to 100 (totally cloud covered). **(d)** Absolute difference between MODIS geometrical cloud fraction and BP-predicted cloud fraction. The color-code ranges from 0 (perfect match) to 100 (complete mismatch). **(e)** Absolute difference between MODIS geometrical cloud fraction and ELM-predicted cloud fraction. The color-code in panels **(d)** and **(e)** range from 0 (perfect match) to 100 (complete mismatch)

The contribution of high ground reflectance to TOA misleads the NNs to interpret the satellite radiance measurements as if they were back reflected by clouds.

6 Conclusions

A neural networks-based solution has been explored as a contribution to detect the cloud fraction in OMI pixels using TOA radiation detected in the OMI VIS channels. This study serves as a proof of concept rather than a full study with extensive training and validation. Therefore only a limited number of OMI orbits have been used in this study, i.e., a data set of 11 OMI orbits was split in three independent data sets for training, testing and validation. In view of the vast amount of data in the VIS channels from OMI, an SVD procedure was applied to reduce the 751 channels without loss of information. This information, together with relevant auxiliary information, was used as input to two neural network learning algorithms, back propagation and ELM, and the results were compared with MODIS geometrical cloud fraction data. To this end, the selected models of the NN provide good performances during validation. The correlation coefficients between the reference MODIS cloud fraction and the estimated cloud fraction from NNs are found to be approximately 0.85 over ocean. Worst performances are observed over land where the ground reflectance from bright surfaces, such as deserts, misleads the NNs to interpret the high measured reflectance as if it was reflected by clouds. The spectral features alone can discriminate cloudy from clear pixels with a reasonable accuracy when proper optimization of the NNs has been performed.

Neural networks are attractive for cloud screening because of their capability of high computational speed for large data sets. Moreover, they rely on auxiliary data only during the training and they are independent from the instrument platform which makes the approach portable to other combinations of instruments such as the combination of the TROPOspheric Monitoring Instrument (TROPOMI) (Veefkind et al., 2012) and the Visible Infrared Imaging Radiometer Suite (VIIRS).

Acknowledgements. All RGB MODIS granules are publicly available and are provided by the NASA Level1 and Atmoshere Archive and Distribution System (LAADS) website: http://ladsweb.nascom.nasa.gov/data/search.html. The authors would like to acknowledge support from and discussions with the KNMI-OMI team. Funding for this work was provided by the PP-TROPOMI project and Tekes (the Finnish funding Agency for Technology and Innovation and Ministry of Transport and Communications).

Edited by: A. Kokhanovsky

References

Acarreta, J. R. and de Haan, J. F.: Cloud pressure algorithm based on the O_2-O_2 absorption, OMI Algorithm Theoretical Basis Document (ATBD), vol. III, Clouds, Aerosols, and Surface UV Irradiance, edited by: P. Stammes, R. Neth. Meteorol. Inst., De Bilt, 17–29, 2002.

Ackerman, S. A., Strabala, K. I., Menzel, W. P., Frey, R. A., Moeller, C. C., and Gumley, L. E.: Discriminating clear sky from clouds with MODIS, J. Geophys. Res., 103, 32141–32157, 1998.

Aitkenhead, M. J. and Aalders, I. H.: Classification of Landsat Thematic Mapper imagery for land covering using neural networks, Int. J. Remote Sens., 29, 2075–2084, 2008.

Bishop, C. M.: Neural networks for patter recognition, Clarendom press, Oxford, 1995.

Christodoulou, C. I., Michaelides, S. C., and Pattichis, C. S.: Multifeature texture analysis for the classification of clouds in satellite imagery, IEEE Trans. Geosci. Remote Sens., 41, 11, 2662–2668, doi:10.1109/TGRS.2003.815404, 2003.

Del Frate, F. and Schiavon, G.: A combined natural orthogonal function/neural network technique for the radiometric estimation of atmopheric profiles, Radio Sci., 33, 405–410, 1998.

Del Frate, F., Iapaolo, M., Casadio, S., Godin-Beekman, S., and Petitdidier, M.: Neural network for the dimensionality reduction of GOME measurement vector in the estimation of ozone profiles, J. Quant. Spectrosc. Radiat. Trans., 92, 275–291, 2005.

Di Noia, A., Sellitto, P., Del Frate, F., and de Laat, J.: Global tropospheric ozone column retrievals from OMI data by means of neural networks, Atmos. Meas. Tech. Discuss., 5, 7675–7727, doi:10.5194/amtd-5-7675-2012, 2012

Dybbroe, A., Karlsson, K.-G., and Thoss, A.: NWSAF AVHRR cloud detection and analysis using dynamic thresholds and radiative transfer modeling. Part I: Algorithm description., J. Appl. Meteor., 44, 39–54, 2005.

Grivas, G. and Chaloulakou, A.: Artificial neural networks for prediction of PM10 hourly concentrations in the Greater Area of Athens, Greece, Atmos. Environ., 40, 1216–1229, 2006.

Golub, G. H. and Van Loan, C. F.: Matrix computations, JHU Press, 1996.

Ham, F. and Kostanic, I:, Principles of neurocomputing for science and engineering, McGraw-Hill, 2001.

Haykin, S.: Neural Networks A Comprehensive Foundation, Prantice Hall, 1999.

Hornik, K. Stinchcombe, M., and White, H.: Multilayer feedforward networks are universal approximators, Neural Netw., 2, 359–366, 1989.

Huang, G. B., Zhu, Q. Y., and Siew, C. K.: Extreme learning machine: theory and applications, Neurocomp., 70, 489–501, 2006.

Hubanks, P. A.: MODIS Atmosphere QA Plan for Collection 005 and 051, Version 3.1, 2012.

Karayiannis, N. and Venetsanopoulos, A. N.: Artificial neural networks: learning algorithms, performance evaluation, and applications, The Springer International Series in Engineering and Computer Science, 209, 460 pp., 1993.

King, M. D., Kaufman, Y. J., Menzel, W. P., and Tanre, D.: Remote sensing of cloud, aerosol, and water vapor properties from the Moderate Resolution Imaging Spectrometer (MODIS), IEEE Trans. Geosci. Remote Sens., 30, 1–27, 1992.

King, M. D., Tsay, S. C., Platnick, S. E., Wang, M., and Liou, K. N.: Cloud retrieval algorithms for MODIS: optical thicknes, effective particle radius, and thermodynamic phase, Tech. Rep. ATBD-MOD-05, NASA, Washington, DC, 1998.

Kleipool, Q.: OMI surface reflectance climatology README, Version 2.0, data product version: 003, 2010.

Koelemeijer, R. B. A. and Stammes, P.: Effetcs of clouds on the ozone column retrieval from GOME UV measurements, J. Geophys. Res., 104, 8281–8294, 1999.

Kokhanovsky, A. A., Platnick , S., and King, M. D.: Remote sensing of terrestrial clouds from space using backscattering and thermal emission techniques, The remote sensing of tropospheric composition from space, physics of earth and space environments, Springler-Verlag, Berlin, doi:10.1007/978-3-642-14791-3, 2011.

Krasnopolsky, V. M.: Neural network applications to solve forward and inverse problems in atmospheric and oceanic satellite remote sensing Artificial Intelligence Methods in the Environmental Sciences, Springer-Verlag, Germany, 2008.

Levelt, P. F., van den Oord, G. H. J., Dobber, M. R., Malkki, A., Visser, H., de Vries, J., Stammes, P., Lundell, J. O. V., and Saari, H.: The Ozone Monitoring Instrument, IEEE Trans. Geosci. and Remote Sens., 44, 1093–1101, 2006.

Loyola R., D. G.: Applications of neural network methods to the processing of earth observation satellite data, Neur. Netw., 19, 168–177, doi:10.1016/j.neunet.2006.01.010, 2006.

Martins, J. V., Tanra, D., Remer, L., Kaufman, Y., Mattoo, S., and Levy, R.: MODIS Cloud screening for remote sensing of aerosols over oceans using spatial variability, Geophys. Res. Lett., 29, MOD4-1–MOD4-4, doi:10.1029/2001GL013252, 2002.

Mas, J. F. and Flores, J. J.: The application of artificial neural networks to the analysis of remotely sensed data, Int, J. Remote Sens., 29, 617–663, 2008.

Preusker, R., Hunerbein, A., Fischer, J., Brockmann, C., and Kramer, U.: MERIS Global land surface albedo maps: ATBD Cloud detection, available at: http://www.brockmann-consult.de/albedomap/pdf/atbd cloud detection amap 5.pdf, 2008.

Rumelhart, D. E., McClelland, J. L., and the PDP Research Group: Parallel Distributed Processing: Explorations in the Microstructure of Cognition, Vol.1 and 2, MIT Press, Cambridge, Mass., 1986.

Sellitto, P., Bojkov, B. R., Liu, X., Chance, K., and Del Frate,F: Tropospheric ozone column retrieval at northern mid-latitudes from the Ozone Monitoring Instrument by means of a neural network algorithm, Atmos. Meas. Tech., 4, 2375–2388, doi:10.5194/amt-4-2375-2011, 2011.

Sellitto, P., Del Frate, F., Solimini, D., and Casadio, S.: Tropospheric ozone column retrieval from ESA-Envisat SCIAMACHY Nadir UV/VIS radiance measurements by means of a neural network algorithm, IEEE Trans. Geosci. and Remote Sens., 50, 998–1011, doi:10.1109/TGRS.2011.2163198, 2012.

Sneep, M., de Haan, J. F., Stammes, P., Wang, P., Vanbauce, C., Joiner, J., Vasilkov, A., and Levelt, P.: Three-way comparison between OMI and PARASOL cloud pressure products, J. Geophys.Res., 113, D15S23, doi:10.1029/2007JD008694, 2008.

Stammes, P. and Noordhoek, R.: OMI algorithm theoretical basis document Volume 3, Cloud, aerosols, and surface UV irradiance, ATBD-OMI-03, Version 2.0, 2002.

Stammes, P., Sneep, M., de Haan, J. F., Veefkind, J. P., Wang, P., and Levelt, P. F.: Effective cloud fraction from Ozone Monitoring Instrument. Theoretical framework and validation, J. Geophys.

Res., 113, D16S38, doi:10.1029/2007JD008820, 2008.
van den Oord, B.: OMI small pixel data, TN-OMIE-KNMI-397, 1, 2002.
Vasilkov, A., Joiner, J., Spurr, R., Bhartia, P. K., Levelt, P., and Stephens, G.: Evaluation of the OMI cloud pressure derived from rotational Raman scattering by comparison with other satellite data and radiative transfer simulations, J. Geophys. Res., 13, D15S19, doi:10.1029/2007JD008689, 2008.
Veefkind, J. P., Aben, I., McMullan, K., Förster, H., de Vries, J., Otter, G., Claas, J., Eskes, H. J., de Haan, J. F., Kleipool, Q., van Weele, M., Hasekamp, O., Hoogeveen, R., Landgraf, J., Snel, R., Tol, P., Ingmann, P., Voors, R., Kruizinga, B., Vink, R., Visser, H., and Levelt, P. F.: TROPOMI on the ESA Sentinel-5 Precursor; a GMES mission for Global Observation of the Atmospheric Composition Climate, Air Qual. Appl. Rem. Sens. Envir., 120, 70–83, 2012.
Werbos, P. J.: Beyond Regression: New Tools for Prediction and Analysis in the Behavioral Sciences, PhD thesis, Harvard University, 1974.
Wu, D. L., Jiang, J. H., and Davis, C. P.: EOS MLS cloud ice measurements and cloudy-sky radiative transfer model, IEEE Trans. Geosci. and Remote Sens., 44, 1156–1165, doi:10.1109/TGRS.2006.869994, 2006.
Yan, H., Chen, L., Tao, J., Su, L., Huang, J., Han, D., and Yu, C.: Corrections for OMI SO_2 BRD retrievals influenced by row anomalies, Atmos. Meas. Tech., 5, 2635–2646, doi:10.5194/amt-5-2635-2012, 2012.

Reprinted with permission from
Journal of Geophysical Research: Atmospheres, 121, 24, 14538–14557,
doi:10.1002/2016JD025360

II

AGU PUBLICATIONS

JGR

Journal of Geophysical Research: Atmospheres

RESEARCH ARTICLE
10.1002/2016JD025360

Key Points:
- microphysical and optical properties of stratiform liquid water clouds
- impact of air mass transport on cloud properties
- cloud characterization using a large data set

Correspondence to:
J. Preißler,
jana.preissler@nuigalway.ie

Citation:
Preißler, J., G. Martucci, G. Saponaro, J. Ovadnevaite, A. Vaishya, P. Kolmonen, D. Ceburnis, L. Sogacheva, G. de Leeuw, and C. O'Dowd (2016), Six years of surface remote sensing of stratiform warm clouds in marine and continental air over Mace Head, Ireland, *J. Geophys. Res. Atmos.*, *121*, 14,538–14,557, doi:10.1002/2016JD025360.

Received 13 MAY 2016
Accepted 15 NOV 2016
Accepted article online 22 NOV 2016
Published online 20 DEC 2016

Six years of surface remote sensing of stratiform warm clouds in marine and continental air over Mace Head, Ireland

Jana Preißler[1], Giovanni Martucci[2], Giulia Saponaro[3], Jurgita Ovadnevaite[1], Aditya Vaishya[4], Pekka Kolmonen[3], Darius Ceburnis[1], Larisa Sogacheva[3], Gerrit de Leeuw[3], and Colin O'Dowd[1]

[1]Centre for Climate and Air Pollution Studies, National University of Ireland Galway, Galway, Ireland, [2]Federal Office of Meteorology and Climatology MeteoSwiss, Ch. De l'Aérologie, Payerne, Switzerland, [3]Climate Research Unit, Finnish Meteorological Institute, Helsinki, Finland, [4]Space Physics Laboratory, Vikram Sarabhai Space Centre, Thumba, India

Abstract A total of 118 stratiform water clouds were observed by ground-based remote sensing instruments at the Mace Head Atmospheric Research Station on the west coast of Ireland from 2009 to 2015. Microphysical and optical characteristics of these clouds were studied as well as the impact of aerosols on these properties. Microphysical and optical cloud properties were derived using the algorithm SYRSOC (SYnergistic Remote Sensing Of Clouds). Ground-based in situ measurements of aerosol concentrations and the transport path of air masses at cloud level were investigated as well. The cloud properties were studied in dependence of the prevailing air mass at cloud level and season. We found higher cloud droplet number concentrations (CDNC) and smaller effective radii (r_{eff}) with greater pollution. Median CDNC ranged from 60 cm^{-3} in marine air masses to 160 cm^{-3} in continental air. Median r_{eff} ranged from 8 μm in polluted conditions to 10 μm in marine air. Effective droplet size distributions were broader in marine than in continental cases. Cloud optical thickness (COT) and albedo were lower in cleaner air masses and higher in more polluted conditions, with medians ranging from 2.1 to 4.9 and 0.22 to 0.39, respectively. However, calculation of COT and albedo was strongly affected by liquid water path (LWP) and departure from adiabatic conditions. A comparison of SYRSOC results with MODIS (Moderate-Resolution Imaging Spectroradiometer) observations showed large differences for LWP and COT but good agreement for r_{eff} with a linear fit with slope near 1 and offset of −1 μm.

1. Introduction

Besides directly absorbing and scattering sunlight, aerosols also have an indirect effect on the global radiation budget by altering cloud properties. Twomey first proposed an influence of aerosols on cloud albedo by increasing cloud droplet number concentration (CDNC) and consequently reducing droplet sizes [*Twomey*, 1974, 1977]. Besides this, there are other interactions between aerosols and clouds. For example, aerosols can alter cloud lifetime [*Albrecht*, 1989], cloud water content [*Coakley and Angevine*, 2002], and droplet size distribution [*Vong and Covert*, 1998].

According to the Fifth Assessment Report of the Intergovernmental Panel on Climate Change, the physical basis of the albedo effect introduced by Twomey is fairly well understood [*Boucher et al.*, 2013]. However, uncertainties still remain considering the lifetime effect and the shape of the droplet size distribution [*Brenguier et al.*, 2011; *Boucher et al.*, 2013]. *Brenguier et al.* [2003] confirmed the expectations of *Twomey* [1977] of a negative correlation between cloud optical thickness (COT) and cloud droplet effective radius (r_{eff}). Strongly polluted clouds, however, had a positive correlation. In general, r_{eff} of cloud droplets is smaller in clouds affected by polluted air masses than in clean clouds [*Lohmann and Feichter*, 2005, and references therein]. This effect was also observed by *Ferek et al.* [2000] investigating marine clouds influenced by ship emissions. They also found drizzle suppression in ship tracks. *Rosenfeld et al.* [2008] discussed the role of aerosols as cloud condensation nuclei (CCN) and their ambivalent impact on precipitation: on one hand, evaporation or prevention of clouds in heavily polluted conditions, and on the other hand, prevention of long-lived clouds in the tropics due to clean conditions and fast rain out. A review of publications discussing marine and

continental stratiform clouds was done by *Miles et al.* [2000]. They found clear differences between these two types in terms of total CDNC, effective diameter, liquid water content (LWC), among others.

For continuous vertically resolved observations of the atmosphere, ground-based remote sensing is advantageous. Better spatial coverage can be achieved by satellite-borne sensors such as the cloud profiling radar on CloudSat [*Stephens et al.*, 2002] or the aerosol lidar CALIOP (Cloud Aerosol Lidar with Orthogonal Polarization) [*Winker et al.*, 2007] on CALIPSO (Cloud-Aerosol Lidar and Infrared Pathfinder Satellite Observations) but at the expense of temporal resolution. Ground-based remote sensing offers continuous monitoring of the atmosphere at one location, with high vertical and temporal resolution. This gives valuable detailed insights into highly complex cloud processes.

Mace Head, located at the west coast of Ireland, receives clean air masses at ground level from a wide sector to the west and polluted air from other sectors [*Jennings et al.*, 2003; *O'Connor et al.*, 2008]. Numerous studies of in situ observations at Mace Head have been published, many addressing marine aerosol [*Ovadnevaite et al.*, 2012; *Ceburnis et al.*, 2014], including CCN [*Reade et al.*, 2006]. *Jennings et al.* [1997] focussed on the characterization of marine and continental aerosols and found lowest aerosol number concentration for polar marine air masses and highest for continental air masses.

The remote sensing suite at Mace Head has previously been used to study clouds. For example, *Martucci et al.* [2010] compared cloud base heights from different colocated ceilometers. Furthermore, the algorithm SYRSOC (SYnergistic Remote Sensing Of Clouds) was developed to provide microphysical cloud properties from data obtained by ceilometer, cloud radar, and microwave radiometer [*Martucci and O'Dowd*, 2011]. This retrieval algorithm was also used for the investigation of the impact of volcanic aerosol and sea spray on clouds (*Martucci et al.* [2012] and *Ovadnevaite et al.* [2011], respectively). Besides, remote sensing data from Mace Head was used in combination with ground-based and airborne in situ measurements [*Dall'Osto et al.*, 2010 and *Martucci et al.*, 2013, respectively). These studies focused on limited time periods. What is missing are long-term cloud observations, their microphysical, and optical properties and the impact of aerosols upon them. The present study provides more than 6 years of ground-based cloud remote sensing at Mace Head. It aims to underpin findings from single case studies or intensive campaigns by using a large data set of carefully selected cloud cases from continuous measurements.

2. Instruments and Methodology

The remote sensing division at Mace Head (53.33°N, 9.90°W) is located 21 m above sea level, about 300 m from the water line. It has been a Cloudnet station [*Illingworth et al.*, 2007] since 2009 and comprises a cloud radar, a ceilometer, and a microwave radiometer (MWR). The radar is a MIRA36, a 35.5 GHz Ka-band Doppler cloud radar from Metek [*Bauer-Pfundstein and Goersdorf*, 2007; *Melchionna et al.*, 2008], which measures in-cloud reflectivity, linear depolarization ratio, and vertical velocity at vertical and temporal resolutions of 30 m and 10 s. The radar was also used to detect cloud top altitude. A calibration offset of the radar reflectivity due to finite receiver loss [*Probert-Jones*, 1962] was taken into account by adding 2 dBZ to the radar reflectivity output (M. Bauer-Pfundstein, METEK, personal communication, 2016). The ceilometer is a CHM15k from Lufft (formerly Jenoptik) [*Heese et al.*, 2010; *Martucci et al.*, 2010] measuring at 1064 nm. It detects photons backscattered from atmospheric targets such as cloud droplets or aerosol particles at vertical and temporal resolutions of 15 m and 30 s. It is capable of detecting aerosol layers, as well as clouds up to a certain penetration depth depending on the cloud optical depth. The ceilometer was used to detect cloud base altitude. The MWR is an RPG-HATPRO [*Crewell and Löhnert*, 2003; *Löhnert and Crewell*, 2003; *Löhnert et al.*, 2009] water vapor and oxygen multichannel microwave profiler [*Martucci and O'Dowd*, 2011]. SYRSOC uses temperature profiles and liquid water path (LWP) from MWR. MWR profiles have a decreasing vertical resolution with range and a temporal resolution of about 15 s. LWP was obtained by quadratic regression retrieval based on brightness temperatures.

This set of instruments enables vertically resolved determination of microphysical cloud properties such as CDNC, r_{eff}, and LWC from the ground. The SYRSOC algorithm was used to retrieve these microphysical cloud properties as well as cloud optical properties, i.e., cloud optical thickness (COT) and cloud albedo. SYRSOC works under the assumptions of a monomodal droplet size distribution with constant shape parameters of 8 (marine and marine-modified clouds) and 9 (continental and continental-modified clouds) [*Miles et al.*, 2000], and uses an explicit subadiabaticity scheme. SYRSOC was described in detail by *Martucci and O'Dowd* [2011],

but unlike the outline in this first publication, CDNC in the present work was obtained using radar reflectivity following the approach of *Brandau et al.* [2010] solving equation (5) therein for CDNC, $N(h)$

$$N(h) = k_6 \left(\frac{6\rho_{\mathrm{air}} A_{\mathrm{ad}}}{\pi \rho_w}^2 \frac{1}{Z(h)} f^2(h) h^2 \right), \tag{1}$$

with the constant coefficient k_6 depending on the shape parameter of the droplet-size distribution [*Brandau et al.*, 2010, equation (19)], the density of air, ρ_{air}, the adiabatic lapse rate of LWC mixing ratio, A_{ad}, the density of water, ρ_w, the height, h, the profile of radar reflectivity, $Z(h)$, and the profile of the subadiabatic function, $f(h)$. This approach for obtaining CDNC is also implemented in the SYRSOC algorithm. Determination of CDNC from the extinction coefficient with SYRSOC, as introduced by *Martucci and O'Dowd* [2011], works well for certain cloud cases. However, this retrieval is sensitive to uncertainties in the extinction profile. Due to necessary assumptions in the inversion of the ceilometer data, the algorithm cannot provide sufficiently accurate profiles of the extinction coefficient in all cases. Use of a Raman lidar and directly measured extinction coefficient profiles, at least at cloud base, could improve the extinction-based CDNC retrieval of SYRSOC. From CDNC, r_{eff}, LWC, COT, and cloud albedo were calculated. Vertical and temporal resolutions of the output are 15 m and 10 s.

Retrieval of r_{eff} and LWC was described by *Martucci and O'Dowd* [2011]. COT was calculated from a so-called reconstructed extinction coefficient, σ_{re}, obtained from the CDNC:

$$\sigma_{re}(h) = C * \left(N(h)^{1/3}\right) * \left(f(h) * A_{\mathrm{ad}} * \left(h - h_{\mathrm{cb}}\right)\right)^{2/3}, \tag{2}$$

with h_{cb} the cloud base altitude and

$$C = \pi^{1/3} * Q * k_2 * (4/3)^{-2/3} * \left(\rho_w / \rho_{\mathrm{air}}\right)^{-2/3} * 10^5, \tag{3}$$

with the extinction efficiency Q, which is approximately 2 for the considered wavelength [*Boers et al.*, 2000], and k_2 depending on the shape parameter of the droplet size distribution [*Brandau et al.*, 2010, equation (20)]. COT is then obtained by integrating over the reconstructed extinction coefficient:

$$\mathrm{COT} = \int \sigma_{re}(h) \mathrm{d}h. \tag{4}$$

Cloud albedo is calculated from COT using a fixed ratio found by *Lacis and Hansen* [1974]:

$$\mathrm{Albedo} = \mathrm{COT}/(\mathrm{COT} + 7.7). \tag{5}$$

The data set analyzed here includes clouds observed from February 2009 to April 2015. From these 6 years of cloud observations, homogeneous parts of less than 1 h duration of all single-layer nonprecipitating water clouds were selected. Maximum duration of 1 h was chosen to ensure homogeneity. Clouds were classified as homogeneous if cloud base and cloud top height changed by less than 50 m during that period and the variability in radar reflectivity was less than 1 dBZ. Selection of single-layer clouds was necessary because column LWP was used to calculate LWC profiles. Additionally, cases were restricted to nonprecipitating water clouds to match the monomodal droplet size distribution assumption of SYRSOC.

Large drizzle drops can have a strong impact on radar reflectivity without strongly affecting LWC [*Sauvageot and Omar*, 1987; *Fox and Illingworth*, 1997]. This distorts the calculation of microphysical cloud properties. As SYRSOC assumes monomodal size distributions, the drizzle mode cannot be represented. Drizzle was avoided by excluding regions of high radar reflectivity. In accordance with *Comstock et al.* [2004] and *Zuidema et al.* [2005], the threshold reflectivity for light drizzle was set to −17 dBZ.

The true uncertainties of the SYRSOC results are difficult to evaluate, because some contributions to the overall uncertainty can cancel each other. An uncertainty propagation approach would therefore lead to unrealistic results. Instead, a Monte Carlo approach was used to estimate uncertainties. Input parameters were randomly varied within the limits given in Table 1. Owing to the complexity of the calculations, this leads to 8000 samples per profile (i.e., per time step). The uncertainty was then calculated as the ratio of the standard deviation of the mean and the mean value of those 8000 samples. This can give an indication of the uncertainties introduced

Table 1. Input Parameters, Their Variability, and Number of Random Samples for Monte Carlo Error Estimation

Parameter	Instrument	Variability	Samples
Temperature	MWR	±2 K	20
Liquid water path	MWR	±20 g/m^2	20
Reflectivity	cloud radar	±1 dBZ	20

by random errors in the measurements. Drizzle screening causes an additional bias for some cloud cases. This bias was estimated by running SYRSOC for clouds that included drizzle and for the same clouds with drizzle threshold applied. In drizzle-screened clouds, CDNC was on average about 60% higher and r_{eff} and LWC about 50% and 25% lower, respectively. There are further uncertainties related to drizzle, as both calculations for this estimate are based on the monomodality assumption. However, all SYRSOC results are obtained under a set of assumptions, mentioned earlier, which might not reflect reality and therefore could introduce further uncertainties, which are not discussed here. Uncertainties given with SYRSOC results below are those estimated by the Monte Carlo approach.

Three-day back trajectories from the National Oceanic and Atmospheric Administration (NOAA) HYSPLIT model (HYbrid Single-Particle Lagrangian Integrated Trajectory, *Draxler and Rolph* [2014]), were calculated for each case. Based on the prevailing synoptic situation and back trajectories, the cloud cases were classified as marine, coming from the Atlantic Ocean, or continental, coming from Europe. The classes "marine modified" and "continental modified" were introduced to categorize ambiguous cases: from the Atlantic, but with brief transport over Ireland or Great Britain, and for cases from Europe with transport over the ocean, respectively. Furthermore, black carbon (BC) concentrations measured in situ near the surface by a multiangle absorption photometer were used as further indication for clean cases. Marine cases with BC concentrations < 15 ng/m^3 were classified as clean marine, whereas all other marine cases were allocated to the marine modified class since they were likely influenced by anthropogenic sources [*O'Dowd et al.*, 2014; *Ovadnevaite et al.*, 2014]. Aerosol composition from the ground-based in situ aerosol mass spectrometer (AMS) [*Ovadnevaite et al.*, 2014] measurements were studied as well. AMS at Mace Head continuously samples SO_4, NH_4, NO_3, sea-salt, and organic aerosol concentrations. Fine-mode particulate matter (PM1) was obtained as sum of individual concentrations measured by the AMS. CCN concentrations near the surface were monitored with a Droplet Measurements Technology CCN counter [*Lance et al.*, 2006] at 0.75% supersaturation.

MODIS (Moderate-Resolution Imaging Spectroradiometer) level 2 data from both Terra and Aqua satellites [*Platnick et al.*, 2015a, 2015b] were used to verify the performance of SYRSOC. MODIS data at 3.7 μm, available at 1 km horizontal resolution, was only processed in cases of single-layered clouds. Data pixels with a cloud optical thickness smaller than 5 were removed, as the instrument might detect surface reflectance through these clouds. This would lead to unreliable retrieved cloud parameters for optically thin clouds.

3. Results

A total of 118 water clouds were analyzed for a better understanding of cloud microphysics as well as to provide insight into the impact of aerosols. Considering a data set of 6 years, this may seem like a small number, roughly covering 52 h of observations, especially since cloud-free conditions are rare at Mace Head. Instrument downtime was 20 to 25% per instrument (radar, ceilometer, and MWR), and they were seldom coincidental. Additionally, rigorous cloud screening limited the data set to the cases presented here. Using 3 day back trajectories, 78 of these cases were classified as marine (23 clean marine and 55 marine modified) and 40 cases were classified as continental (26 continental and 14 continental modified). Predominance of marine air masses reflects the overall Mace Head characteristics [*Jennings et al.*, 2003; *Reade et al.*, 2006], although *Jennings et al.* [2003] found only 52% of maritime air. This difference can be explained by the exclusive study of stratiform clouds within this work. The formation of stratiform clouds at Mace Head has a prevailing marine origin, while air masses from Europe are generally drier, thus suppressing cloud formation.

The 118 selected cloud periods were each about 10 to 30 min long. With a temporal resolution of 10 s they provided over 18,000 time steps. In total, 2339 of them were classified as clean marine, 9836 as marine modified, 4169 as continental, and 2516 as continental modified.

Table 2 contains information on the distribution of different air masses during the four seasons. Spring (March to May), autumn (September to November) and winter (December to February) were similar, with the

Table 2. Number of Time Steps Per Season and Their Fraction According to Air Mass Transport[a]

	MAM	JJA	SON	DJF
Total number	3927	6235	4411	4287
Fraction marine	9%	22%	6%	8%
Fraction marine modified	37%	75%	44%	41%
Fraction continental modified	23%	3%	16%	17%
Fraction continental	31%	0%	34%	34%

[a]MAM (March–May) = spring; JJA (July–August) = summer; SON (September–November) = autumn; and DJF (December–February) = winter.

most cloud cases in marine modified conditions, followed by continental, continental modified, and marine. Conditions were very different for clouds observed in summer (June to August). Stratiform clouds were almost exclusively observed during marine and marine modified periods. Only a few cloud cases were recorded for continental modified air masses.

3.1. Air Mass Characterization

Figure 1 shows the distributions of BC, CCN, and PM1 concentrations at ground level during the cloud observations. In situ data were not available for all cloud cases. The number of data points in each distribution is shown on the top axis. Figure 1d also shows SYRSOC CDNC concentrations for comparison. SYRSOC results are discussed in section 3.2.2 below. Generally, BC concentrations agreed well with the trajectory analysis, showing higher concentrations for air masses advected from the continent and lower concentrations for air masses transported over the Atlantic (Figure 1a). This is reflected in all mean values and percentiles shown. The medians (and mean values) were 5 ng/m^3 (5 ng/m^3) for marine cases, 24 ng/m^3 (33 ng/m^3) for marine modified cases, 60 ng/m^3 (89 ng/m^3) for continental modified cases, and 127 ng/m^3 (230 ng/m^3) for continental cases. The overall spread is largest for the continental class, ranging from 41 ng/m^3 to 774 ng/m^3 (5th and 95th percentiles).

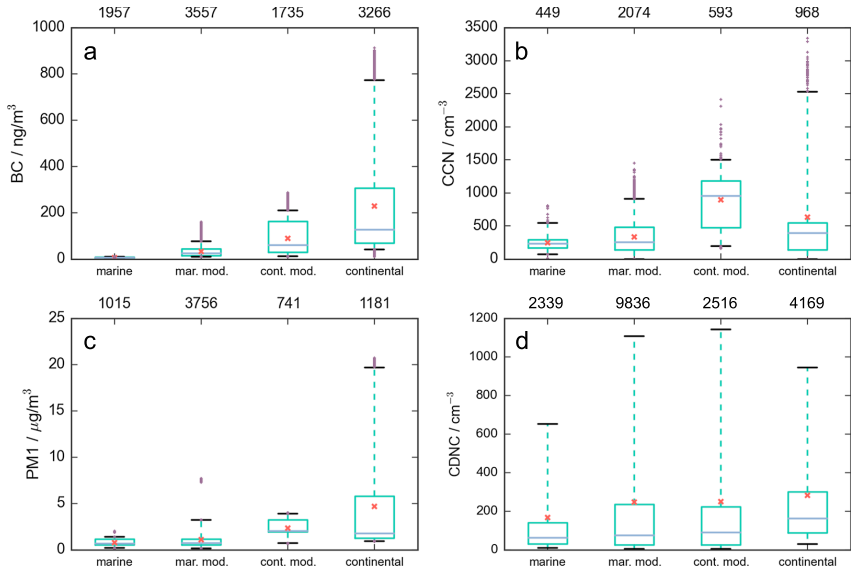

Figure 1. Box plots of (a) BC, (b) CCN, (c) PM1, and (d) CDNC concentrations, sorted by the air mass transport according to HYSPLIT back trajectories (mar. mod. = marine modified; cont. mod. = continental modified). Shown are the median (blue horizontal line), 25th and 75th percentiles (box), 5th and 95th percentiles (whiskers), mean value (red cross), and data points out of the 5th to 95th percentiles (purple dots). The number of data points per class is shown on the top axis.

The lowest CCN mean value was found for marine cases with 230 cm^{-3}, while the median was 250 cm^{-3}. Both, median and mean CCN concentrations, marine modified cases were slightly larger than those of marine cases with 260 cm^{-3} and 340 cm^{-3}, respectively. CCN concentrations of continental modified cases were on average highest (Figure 1b) with median and mean of 960 cm^{-3} and 890 cm^{-3}, respectively. The highest absolute values were observed in continental air masses. However, this 400 cm^{-3} median was closer to marine and marine-modified medians. This indicates no clear relationship between CCN concentrations and air mass transport paths. This is due to the fact that not only BC but also other components like SO_4 and sea salt can act as CCN [*Pierce and Adams*, 2006; *O'Dowd et al.*, 1999].

Mean PM1 concentrations and overall distributions well represented the air masses (Figure 1c). During 95% of marine cases, PM1 was below 1.4 $\mu g/m^3$, median and mean value were 0.68 $\mu g/m^3$ and 0.76 $\mu g/m^3$, respectively. All shown percentiles were similar or higher for marine modified cases, and all were even higher for continental modified cases. The medians (and mean values) for those two classes were 0.74 $\mu g/m^3$ (1.12 $\mu g/m^3$) and 2.04 $\mu g/m^3$ (2.37 $\mu g/m^3$), respectively. Highest PM1 concentrations were observed within continental air masses, where 95th percentile, 75th percentile, 5th percentile, and mean (4.70 $\mu g/m^3$) were highest. The 1.79 $\mu g/m^3$ median and 25th percentile (1.25 $\mu g/m^3$) were lower than median and 25th percentile of the continental modified class.

BC, CCN, and PM1 concentrations in Figure 1 show a smaller spread between the 25th and 75th percentiles of the marine and marine modified cases than those of the continental modified and continental cases. Relative broadness with respect to mean was also smaller in marine cases than in continental cases. This is especially remarkable, because the marine modified class includes the largest number of data points. This hints at more uniform conditions at ground level during air mass advection from the Atlantic. Air masses from Europe can contain different grades of pollution and mixtures of different aerosol types. Additionally, the ground-based in situ observations in these cases were more likely influenced by local and regional emissions.

Box plots for BC and PM1 per season are shown in Figure 2. Median, 25th percentile, and 75th percentile of seasonal BC, CCN, and PM1 concentration distributions are also listed in Table 6. Distributions of BC and PM1 concentrations were very narrow in summer with 25th percentile and 75th percentile of 7 ng/m^3 and 34 ng/m^3 (BC) and 0.64 $\mu g/m^3$ and 1.21 $\mu g/m^3$ (PM1). Median and mean were 15 ng/m^3 and 24 ng/m^3 (BC) and 0.86 $\mu g/m^3$ and 1.28 $\mu g/m^3$ (PM1). All spring percentiles were higher with median, 25th percentile, and 75th percentile of 39, 14, and 67 ng/m^3 (BC) and 0.88, 0.71, and 1.86 $\mu g/m^3$ (PM1). Narrow distributions during spring and summer were observed for SO_4, NH_4, NO_3, and organic aerosol concentrations (not shown). The BC autumn distribution was widest with median, 25th percentile, and 75th percentile of 61, 18, and 206 ng/m^3. In winter, median was largest with 106 ng/m^3. Few cases of very high BC concentrations (shown as outliers) were detected in spring, autumn, and winter. The highest BC concentrations were observed in autumn. PM1 distributions were broader in spring and winter, compared to summer and autumn (Figure 2b), with much higher 95th percentile. Highest PM1 concentrations were detected in spring. Relative broadness with respect to mean was largest in autumn. Median CCN concentrations (Table 6) were similar in spring and summer. Highest mean values, percentiles, and extreme values of CCN were observed in winter, which might indicate an influence of local pollution due to household heating. Enhanced sea-salt concentrations due to high wind speeds, which occur more frequently in winter [*Mulcahy et al.*, 2008; *Yoon et al.*, 2007], likely contributed to the CCN concentrations. On average, CCN concentrations were lowest in autumn.

3.2. Ground-Based Remote Sensing

One advantage of active remote sensing methods such as radar and lidar is the possibility to observe vertical distributions of scatterers at high range resolution. In the following, the observed cloud base and top heights as well as the cloud depth are discussed. Cloud base altitude was obtained from ceilometer data and cloud top altitude from radar reflectivity, by analyzing signal gradients [*Martucci et al.*, 2010].

3.2.1. Cloud Boundaries

As mentioned above, only homogeneous single-layer nonprecipitating water clouds were included in this study. They barely reached cloud top altitudes greater than 2.5 km above ground level (agl). Most of the clouds were 260 to 420 m deep. The medians and percentiles (25% and 75%) of the cloud boundaries and cloud depths are shown in Table 3. The seasonal behavior of the cloud base altitudes was similar to the cloud top altitudes. Cloud base medians were highest in summer and lowest in spring. Cloud top median were highest in summer and autumn and lowest in spring. Cloud depths were slightly larger in autumn and winter with

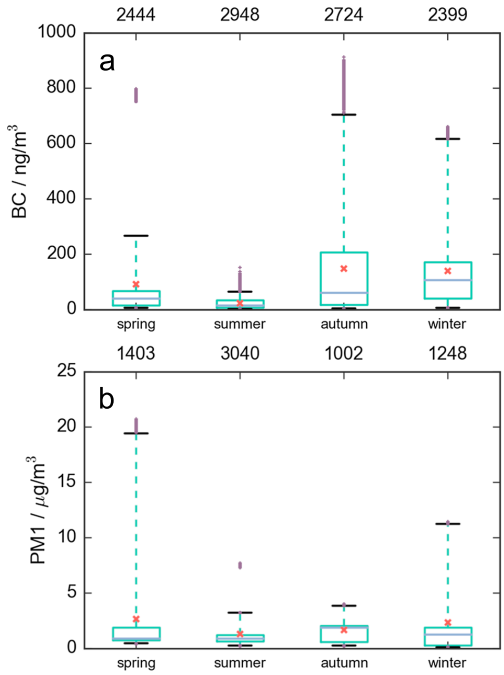

Figure 2. Box plots of (a) BC and (b) PM1 concentrations, sorted by season (spring = March to May, summer = June to August, autumn = September to November, and winter = December to January). Shown are the median (blue horizontal line), 25th and 75 percentiles (box), 5th and 95th percentiles (whiskers), mean value (red cross), and data points out of the 5th to 95th percentiles (purple dots). The number of data points per class is shown above the top axes.

medians of 0.34 and 0.35 km, respectively, suggesting a larger water vapor vertical flux during these seasons. Medians during spring and summer were 0.33 and 0.32 km, respectively.

Figure 3 shows hour average cloud base heights (Figure 3a) and cloud depths (Figure 3b) for all clouds. Local time is the same as UTC in winter and UTC+1 h in summer. Each hourly interval includes 140 to 1510 data points. No clear diurnal cycle is indicated. The spread of cloud base values (5th and 95th percentiles) was larger during nighttime and morning, whereas the 25th and 75th percentiles included a larger range during the day. The hourly distributions of cloud depths were stable throughout the day, with slightly increased ranges in late afternoon and evening. Such small diurnal variation in cloud depth can be expected for the studied stratiform cloud type.

Cloud boundary dependence on air masses are given in Table 4. Again, cloud base and cloud top heights showed a similar pattern. On average, clouds observed during marine air mass advection were slightly higher and thinner than those in continental cases. The small variation may be explained by the focus of this study on one particular cloud type. Selection of drizzle-free clouds limits the data set to shallow clouds, because thicker clouds will inevitably form drizzle. Moreover, limitation to liquid clouds restricts cloud base and top altitudes.

Table 3. Median and Range (25%–75%) of Cloud Top Altitude, Cloud Base Altitude, and Cloud Depth by Season

	Spring (MAM)	Summer (JJA)	Autumn (SON)	Winter (DJF)
cloud top (km agl)	1.0 (0.9–1.4)	1.4 (1.1–1.6)	1.4 (1.2–1.5)	1.1 (1.0–1.3)
cloud base (km agl)	0.7 (0.5–1.1)	1.1 (0.6–1.3)	1.0 (0.8–1.3)	0.8 (0.6–1.0)
cloud depth (km)	0.33 (0.26–0.42)	0.32 (0.27–0.39)	0.34 (0.27–0.41)	0.35 (0.30–0.42)

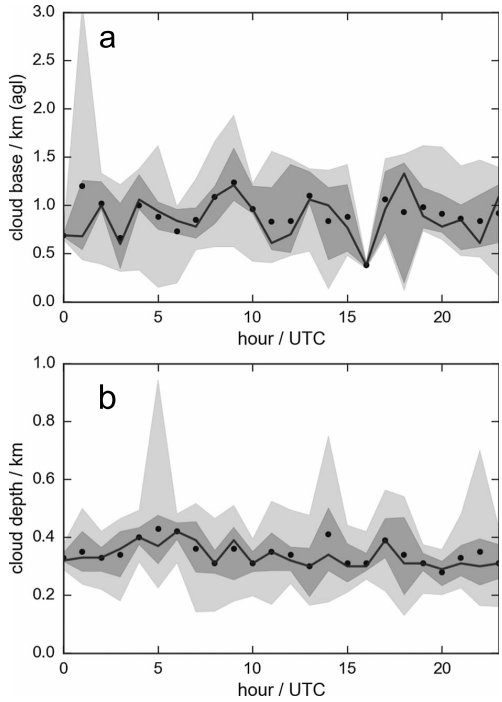

Figure 3. Daily cycle of (a) cloud base altitude and (b) cloud depth. Shown are the median (black line), 25th and 75th percentiles (dark gray shaded area), 5th and 95th percentiles (light gray shaded area), and mean values (dots).

3.2.2. Microphysical Cloud Properties

CDNC, r_{eff}, and LWC were averaged over the duration of the individual cloud periods between about 10 and 30 min. The mean in-cloud profiles were then normalized to cloud depth, so that each profile starts at 0 and ends at 1. Figure 4 shows profiles of a marine example case of 28 July 2010 and a continental case of 2 September 2014. The marine CDNC profile from 28 July 2010 was fairly constant with height. This agrees with the marine clouds of *Miles et al.* [2000] and *Noble and Hudson* [2015]. CDNC on 2 September 2014 (continental case) increased at cloud base and top. CDNC increase at the cloud top may indicate entrainment from above. Mixing of CCN into the cloud would increase CDNC and reduce r_{eff}. Another explanation might be nonuniform radar beam filling at the cloud boundaries, which leads to a virtual decrease in reflectivity in the first or last range bin, also resulting in smaller r_{eff} and larger CDNC. *Miles et al.* [2000] found large variations in profile shapes of CDNC in continental clouds.

Median r_{eff} generally increased from cloud base to cloud top, with a slight decrease near the top on 2 September 2014, corresponding to the CDNC increase. LWC followed a subadiabatic profile with a subadiabaticity of about 0.18 on 28 July 2010 and 0.07 on 2 September 2014. Increasing LWC from cloud base

Table 4. Number of Time Steps As Well As Median and Range (25%–75%) of Cloud Top and Base Altitude and Cloud Depth by Air Mass Transport

	Marine	Marine Modified	Continental Modified	Continental
Total number	2339	9836	2516	4169
Cloud top (km agl)	1.2 (0.9–1.4)	1.4 (1.1–1.5)	1.1 (0.9–1.3)	1.3 (1.0–1.5)
Cloud base (km agl)	0.8 (0.5–1.1)	1.0 (0.7–1.2)	0.7 (0.4–0.8)	0.9 (0.6–1.2)
Cloud depth (km)	0.31 (0.23–0.44)	0.33 (0.27–0.39)	0.37 (0.31–0.44)	0.35 (0.28–0.42)

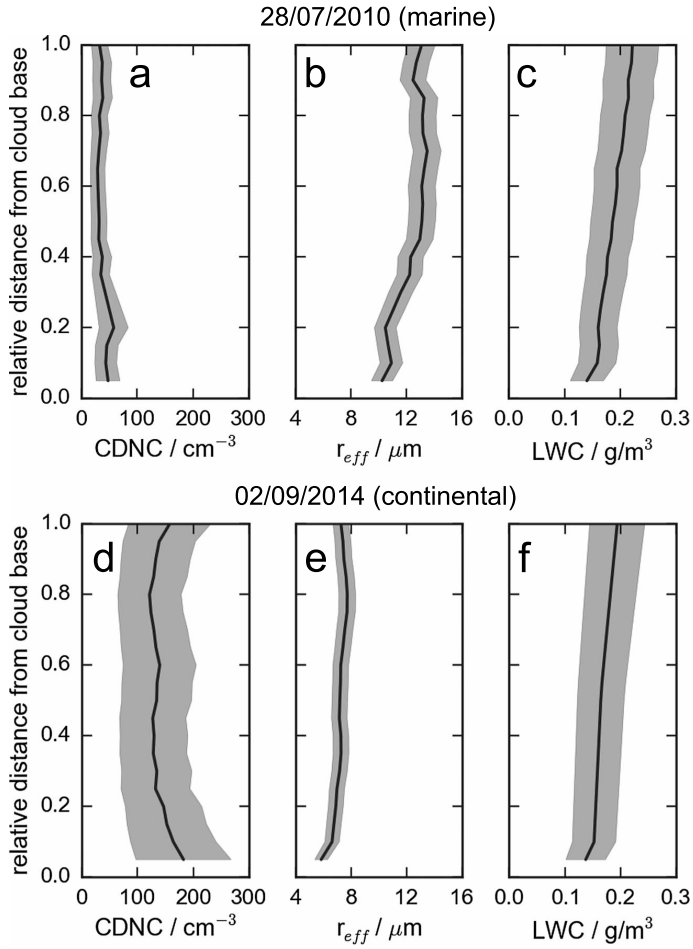

Figure 4. Profiles of (a, d) CDNC, (b, e) r_{eff}, and (c, f) LWC on 28 July 2010 (Figures 4a–4c) and 2 September 2014 (Figures 4d–4f). Shown are median (black line) and uncertainties obtained by Monte Carlo approach (shaded area).

throughout the cloud was also found by *Miles et al.* [2000], *Hudson and Yum* [1997], and *Noble and Hudson* [2015]. Uncertainties in the marine (and continental) case were about 43% (45%), 7% (8%), and 21% (24%) for CDNC, r_{eff}, and LWC, respectively.

Relative uncertainties (err), obtained by the Monte Carlo approach, were averaged over all profiles. They were nearly constant with altitude, only slightly higher at cloud base, for all three microphysical cloud properties (not shown). Median err_{CDNC} was below 50%. The 25th and 75th percentiles of err_{CDNC} were 30% and 80%. The 25th and 75th percentiles of err_{LWC} spread from about 10% to 40%, with a median of 20%. Median and range of $err_{r_{eff}}$ were lowest, ranging between 5 and 15%.

Results discussed in the following, contain data of the entire cloud, except those parts excluded by the radar reflectivity threshold. The normalized distributions of CDNC, r_{eff}, and LWC are plotted in Figure 5 according to the air mass transports. The corresponding medians and 25th and 75th percentiles are given in Table 5.

Medians and percentiles of CDNC were smallest for clean marine air masses (see also Figure 1d). The distribution of marine cases was monomodal, whereas the marine modified cases showed a slightly bimodal behavior, with broad modes centered near 60 and 150 cm^{-3} (Figure 5a). This indicates a mixture of air masses but might

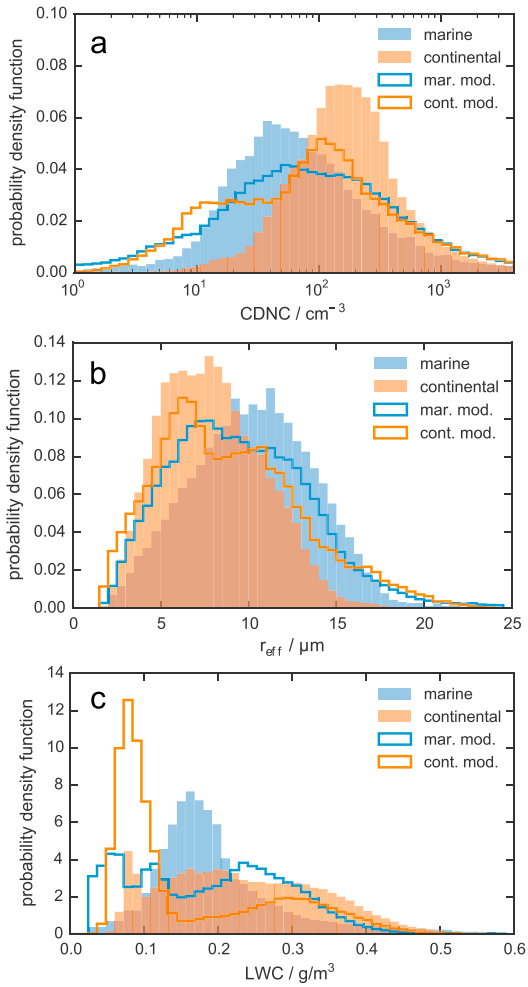

Figure 5. Distributions of (a) CDNC (logarithmic scale), (b) r_{eff}, and (c) LWC by air mass transport. Modified air masses (mar. mod. = marine modified; cont. mod. = continental modified) are plotted as lines.

also be due to air mass misclassification based on back trajectories. The bimodal continental modified CDNC distributions had one broad mode centered near 20 cm^{-3} and one peak near 100 cm^{-3}. Relative to the other air mass classes, few cloud cases were classified as clean marine or continental modified. This means that one outlier can strongly influence these distributions, which would produce broader or multiple modes. The distribution of continental cases had one peak near 200 cm^{-3}. On average, the CDNC was highest for continental cases, although small fractions of high CDNC were also found in the modified air mass types.

The marine r_{eff} distribution was wider than in continental conditions (Figure 5b). The median r_{eff} was 10 µm and 9 µm for marine and marine modified air masses. The r_{eff} distribution of marine modified cases was bimodal with the main peak near 8 µm and one at 12 µm. As with the CDNC distribution, this indicates the influence of both clean and polluted air masses within this class. Continental modified cases also showed a bimodal distribution for the same reasons, as mentioned before. The main peak was near 7 µm, and the smaller one was near 11 µm. The distribution of r_{eff} in continental cases had a broad mode centered at 7 µm.

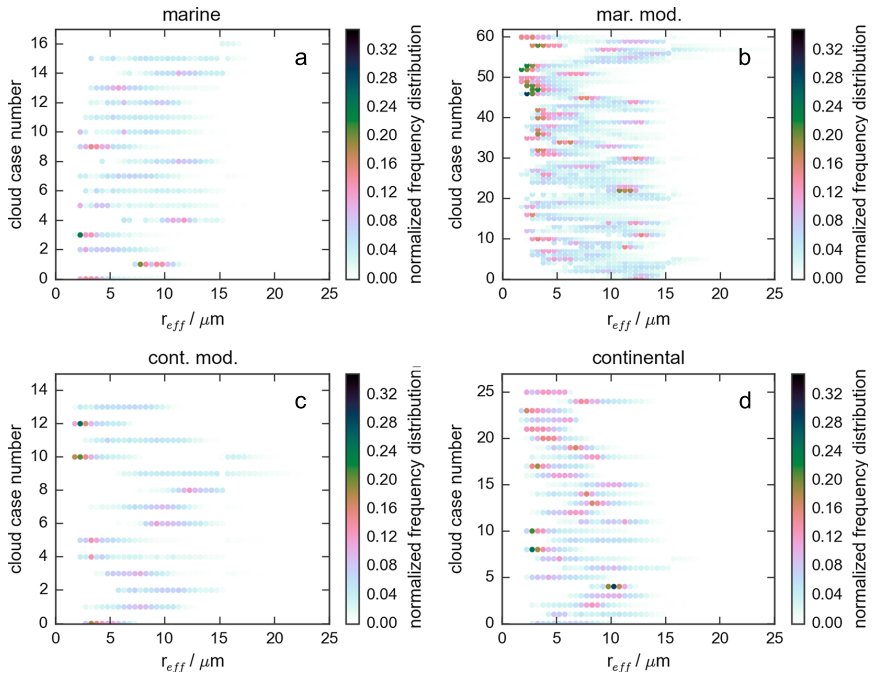

Figure 6. Size distributions, color coded according to the normalized frequency distribution, separately for each cloud case. Each panel shows a different air mass (mar. mod. = marine modified; cont. mod. = continental modified).

These results confirm the inverse relationship between CDNC and r_{eff} in agreement with the literature [*Ferek et al.*, 2000; *Lohmann and Feichter*, 2005]. This relationship is forced by the algorithm at each time step. However, the data set studied here confirms the general validity of this assumption from more than 18,000 time steps. All distributions of CDNC and r_{eff} were broad, covering a wide range of values. This is due to the large number of data points and the coarse estimation of the air mass transport path 3 days prior to observation. Investigation of the actual origin of air masses and aerosol content at cloud level was not part of this study. Classification uncertainties would produce broader distributions. Averaging over whole cloud profiles contributes to further broadening. However, the peaks and medians can be considered statistically robust, owing to the number of time steps.

LWC distributions (Figure 5c) show two or more peaks for all classes except clean marine, which has one peak near 0.17 g/m^3. Whereas the medians were similar for marine, marine-modified, and continental cases, the median of continental modified cases was much lower due to a strong peak just below 0.1 g/m^3. The distribution of marine modified conditions had not only small peaks near 0.05 g/m^3 and 0.12 g/m^3 but also a broader mode centered near 0.23 g/m^3. The peak of the marine modified LWC distribution at 0.05 g/m^3 was linked to small LWP (10–20 g/m^2). LWC distributions for continental cases also had several modes, with a narrow one at 0.08 g/m^3 and two broad ones centered at 0.2 g/m^3 and 0.3 g/m^3. Median, 25th and 75th percentiles of continental LWC distributions were the highest. This seems counterintuitive; however, drizzle was excluded from this data. The more polluted air masses advected from the continent probably held more liquid water before forming drizzle than the cleaner air masses from the ocean. This would be due to rain suppression in more polluted air masses [*Albrecht*, 1989; *Hudson and Yum*, 2001; *Yum and Hudson*, 2002; *Hudson et al.*, 2009], i.e., second indirect aerosol effect [*Hudson*, 1993]. Moreover, some nondrizzling cloud parts with small CDNC, high r_{eff}, and high LWC possibly were removed from this analysis by applying the reflectivity threshold.

Individual droplet size distributions were calculated separately for each cloud case from r_{eff} and CDNC. The averaged distributions normalized by CDNC are shown in Figure 6. Each horizontal line represents the cloud droplet size distribution of one cloud case, with darker colors at high normalized frequencies and lighter colors

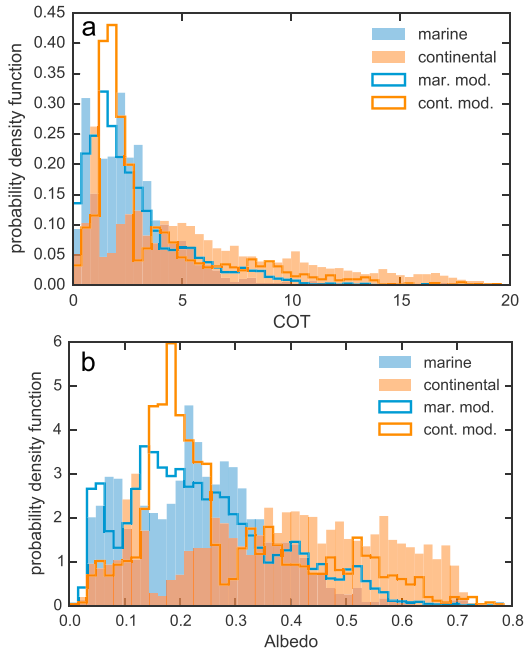

Figure 7. Distributions of (a) COT and (b) cloud albedo by air mass transport. Modified air masses (mar. mod. = marine modified; cont. mod. = continental modified) are plotted as lines.

at low normalized frequencies. Overall, the marine and marine-modified size distributions (Figures 6a and 6b) were broader, with lower maxima, than the continental size distributions (Figure 6d), which showed more pronounced peaks at smaller r_{eff}. Already in the 1950s, *Squires* [1958] found broad distributions associated with low CDNC and *Hudson and Yum* [1997] confirmed that the size distribution broadening in marine stratus is associated with larger r_{eff}. Very high maxima at low r_{eff} in some marine and marine-modified cases might indicate problems with drizzle detection or long-range transport of aerosol at cloud altitude.

Cloud optical properties were also investigated. Figure 7 shows distributions of COT and cloud albedo. COT median, 25th percentile and 75th percentiles were similar for marine, marine-modified, and continental-modified cases (Table 5). The main peaks of these distributions were at 2.5, 2.1, and 2.3, respectively. The two modified classes show a second broad mode centered near 5 (marine modified) and 4 (continental modified). The distribution of the continental cases looks very different. There is one sharp peak at COT of 1, a smaller peak near 3 and a broad mode centered near 5. The percentiles reflect this difference. Median, 25th percentile, and 75th percentiles were highest for continental cases.

Table 5. Median and Range (25%–75%) of Cloud Properties by Air Mass Transport

	Marine	Marine Modified	Continental Modified	Continental
CDNC (cm^{-3})	60 (30–140)	80 (30–230)	90 (20–220)	160 (90–300)
r_{eff} (μm)	10 (8–13)	9 (7–12)	9 (6–12)	8 (6–10)
LWC (g/m^3)	0.18 (0.14–0.23)	0.19 (0.10–0.27)	0.10 (0.08–0.26)	0.22 (0.15–0.31)
LWP (g/m^2)	70 (37–94)	70 (36–103)	36 (26–111)	75 (44–131)
f	0.10 (0.09–0.14)	0.12 (0.06–0.16)	0.09 (0.06–0.17)	0.15 (0.09–0.23)
COT	2.4 (1.3–3.6)	2.1 (1.2–3.6)	2.2 (1.6–4.7)	4.9 (2.5–8.7)
Albedo	0.23 (0.15–0.32)	0.22 (0.14–0.32)	0.23 (0.17–0.38)	0.39 (0.24–0.53)

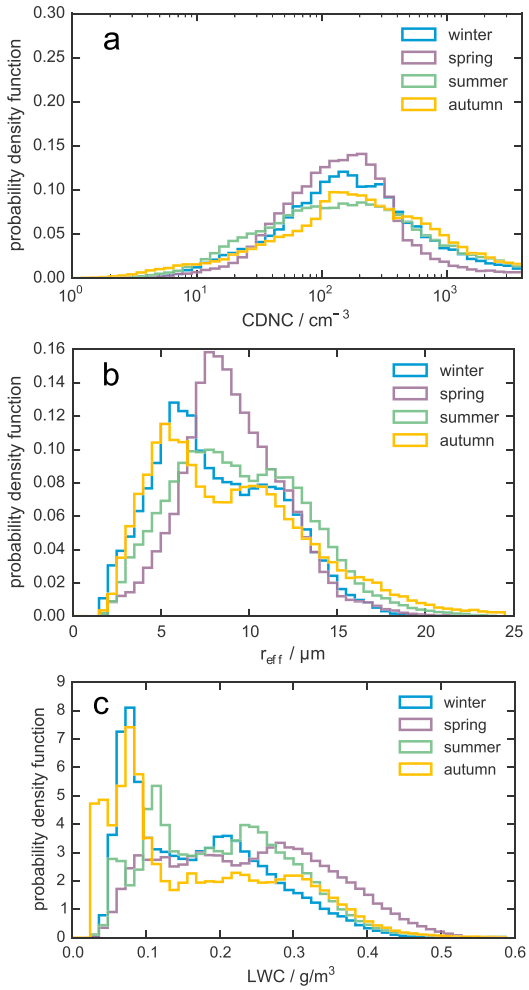

Figure 8. Distributions of (a) CDNC, (b) r_{eff}, and (c) LWC by season.

Similar to COT, there were clear cloud albedo differences between marine and modified classes and the continental class. Median, 25th percentile, and 75th percentiles of the two marine distributions and the continental-modified distribution were similar, with the smallest median and 25th percentile for marine-modified cases but smallest 75th percentiles for marine cases. The cloud albedo distributions in Figure 7b show two main peaks of the marine distribution at 0.08 and 0.22. Those first peaks of marine and marine modified cases are likely related to small LWP. There is another broad peak of the marine modified distribution at 0.14 followed by small broad modes centered near 0.41 and 0.52. The continental modified distribution has one sharp peak at 0.2, followed by some smaller broad modes at higher values. Moreover, there is a very broad main distribution for continental cases with albedos higher than 0.2 and an additional narrow peak centered at 0.12. Mean values of albedo and COT were lower in marine and marine-modified air than in continental and continental-modified air.

Overall, COT and albedo were lower in cleaner air masses and higher in more polluted conditions, which is in agreement with *Twomey* [1977], *Brenguier et al.* [2003], and others. Lower COT and albedo medians were linked to high r_{eff} medians and low CDNC medians for marine and marine-modified cases (Table 5), and vice versa

Table 6. Median and Range (25%–75%) of Cloud Properties, As Well As BC, CCN, and PM1 Concentrations by Season

	Spring (MAM)	Summer (JJA)	Autumn (SON)	Winter (DJF)
CDNC (cm^{-3})	110 (50–220)	80 (30–250)	100 (20–280)	110 (40–260)
r_{eff} (μm)	9 (7–11)	9 (7–12)	8 (5–11)	9 (6–12)
LWC (g/m^3)	0.24 (0.15–0.32)	0.20 (0.12–0.27)	0.14 (0.08–0.26)	0.16 (0.09–0.24)
LWP (g/m^2)	75 (35–134)	69 (37–102)	51 (22–100)	76 (38–104)
f	0.17 (0.10–0.24)	0.11 (0.07–0.14)	0.09 (0.03–0.14)	0.14 (0.09–0.19)
COT	3.7 (1.7–8.0)	2.3 (1.4–3.6)	1.8 (1.1–3.8)	2.8 (2.0–5.0)
Albedo	0.32 (0.18–0.51)	0.23 (0.15–0.31)	0.19 (0.13–0.33)	0.27 (0.21–0.39)
BC (ng/m^3)	39 (14–67)	15 (7–34)	61 (18–206)	106 (40–172)
CCN (cm^{-3})	440 (200–760)	370 (230–500)	180 (70–400)	520 (240–1250)
PM1 ($\mu g/m^3$)	0.9 (0.7–1.9)	0.9 (0.6–1.2)	1.9 (0.6–2.0)	1.3 (0.2–1.9)

for continental cases. The seemingly contradictory behavior in continental modified cases can be attributed to a strong peak at low LWC (Figure 5c). A similar LWC peak, although lower, is present in marine modified cases and might be linked to transport paths influenced by both, marine and continental conditions. Table 5 also shows minimum LWP and, consequently, lowest median subadiabaticity in continental modified cases. This did not impact CDNC or r_{eff} but strongly influenced the calculation of COT and albedo.

Besides air mass classification, a separate analysis of the distributions of microphysical cloud properties by season was done. CDNC, r_{eff} and LWC are shown in Figure 8. The medians, 25th percentile, and 75th percentile of these distributions are also listed in Table 6. The shapes of all CDNC distributions were similar, as were the medians, 25th percentile and 75th percentiles in spring, autumn, and winter with lower values in summer. This indicates stronger influence of continental air masses during these seasons compared to summer. Indeed, Table 2 gives the highest proportion of continental plus continental modified cases in spring, with 54%, followed by winter (51%) and autumn (50%). Median CDNC was lowest in summer (Table 6). This can be explained by the observed air mass characteristics. No continental and very few continental modified cases were observed in summer (Table 2), most likely because the continental air masses transported from Europe were characterized by thermodynamic conditions less favorable to the formation of the stratiform clouds investigated in this study, e.g., higher mean temperature, lower relative humidity, and larger convective available potential energy. Of the 6235 summer data points, 22% were marine and 75% were marine modified (Table 2). BC and PM1 concentrations were also smallest during summer (Table 6), which thus agreed with the observed air mass types.

Differences in r_{eff} were less pronounced in medians, 25th percentile and 75th percentile (Table 5) than in distribution shapes. The only monomodal distribution, though broad, was obtained from spring cases. This may be due to the smaller number of data points, relative to the other seasons (see Table 2). The median and 25th percentile of r_{eff} in autumn were slightly lower than those during the other seasons. Median LWC was lowest in autumn and highest in spring. As mentioned earlier, this is linked to the high LWP and consequently less adiabatic conditions in autumn. Seasonal values of LWP and subadiabaticity, f, are listed in Table 6. Unlike all other seasonal distributions, the spring distribution does not show a peak at low LWC. The optical properties by season are also given in Table 6. The link between LWC, subadiabaticity, and optical properties forced by the algorithm is clearly represented, with low COT and albedo at low LWC, and vice versa. COT and albedo medians were higher in winter and spring than in summer and autumn.

3.3. Comparison With MODIS

Out of the data set described above, 40 cases were coincident with overpasses of the Aqua or Terra satellite over Mace Head. These cases were used for a comparison of SYRSOC results with MODIS cloud products at 3.7 μm [*Platnick et al.*, 2015a, 2015b], namely, r_{eff} at cloud top, the cloud water path (CWP or LWP), and COT. MODIS data were averaged over an area from 53.27 to 53.37°N and from −9.91 to −9.89°E, with Mace Head at its center. MODIS pixels with COT smaller than 5 were removed before averaging. MODIS provided uncertainties of COT, LWP, and r_{eff} ranging from 3% to 15%, 10% to 28%, and 5% to 9%, respectively.

SYRSOC produces profiles of the microphysical cloud properties. However, MODIS has a very small penetration depth into clouds and therefore only retrieves microphysical cloud properties near cloud top. Therefore,

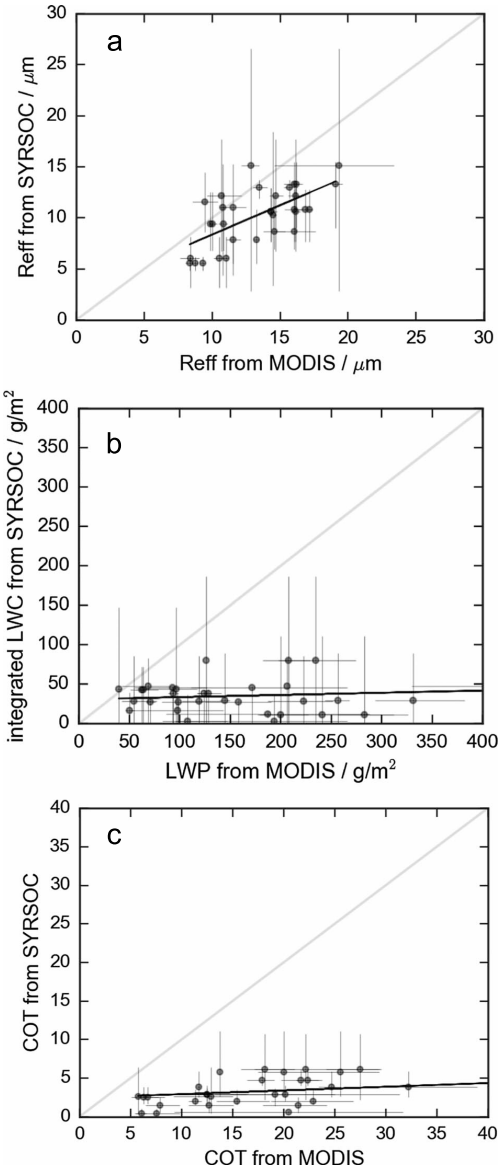

Figure 9. Comparison of (a) r_{eff}, (b) integrated LWC/LWP, and (c) COT from MODIS and SYRSOC. Dots mark mean values, and error bars span minima to maxima. The 1:1 line and linear fit are shown in gray and black, respectively.

SYRSOC r_{eff} was averaged from 75 to 45 m below the radar detected cloud top (three data points), while LWC was integrated over the full cloud depth. Subsequently, r_{eff}, COT and integrated LWC were averaged about 10 min before and 10 min after the overpass. The comparisons of mean values for all available cases are shown in Figure 9. Error bars represent minimum and maximum values. The best linear fits of MODIS products and SYRSOC results were calculated. Regression lines are plotted, and fitting parameters are given in Table 7.

Table 7. Fitting Parameters of the Linear Fit of MODIS Products and SYRSOC Results

	Slope		*y* Intercept		R [R^2]			
	With Drizzle	Without Drizzle	With Drizzle	Without Drizzle	With Drizzle		Without Drizzle	
Effective radius	0.95	0.57	−1 µm	3 µm	0.67	[0.45]	0.65	[0.43]
Integrated LWC	0.11	0.03	50 g/m^2	31 g/m^2	0.38	[0.14]	0.20	[0.04]
LWP	0.11	0.11	57 g/m^2	57 g/m^2	0.36	[0.13]	0.36	[0.13]
COT	0.05	0.05	2	2	0.44	[0.19]	0.43	[0.18]

The r_{eff} seems to be systematically underestimated by SYRSOC or overestimated by MODIS. In most cases, SYRSOC r_{eff} showed a larger variability than MODIS r_{eff}. COT was also underestimated by SYRSOC or overestimated by MODIS to a greater extent at higher COT. MODIS COT ranges were larger than SYRSOC COT ranges. As mentioned earlier, drizzle detection is done by SYRSOC to assure stability of the algorithm and representable results. However, this screening process can exclude parts of the clouds that MODIS detects. This is obvious in the comparison of the integrated LWC with MODIS LWP. Cloud areas with high LWC are excluded, and therefore, the integrated values are lower than the MODIS LWP.

LWP was measured directly from ground by the MWR. These data were used as input for SYRSOC. For the 40 cloud cases, LWP from the ground-based radiometer at Mace Head was compared with MODIS LWP (Figure 10). The agreement of directly measured LWP was clearly better than the agreement of SYRSOC results with MODIS products. However, there were large differences, especially at high-mean LWP, where the variability of both instruments was larger. Measurement and retrieval uncertainties should be considered as well. They were estimated to be 20 g/m^2 for MWR LWP and were provided as 10% to 28% of MODIS LWP. Integrated SYRSOC LWC was in many cases lower than MWR LWP because of SYRSOC drizzle screening.

In order to test the assumption that LWP differences were due to drizzle screening, the SYRSOC run was repeated without drizzle screening. The resulting comparisons of SYRSOC and MODIS are shown in Figure 11. The mean and maximum SYRSOC r_{eff} was higher for cases affected by drizzle. The mean values of integrated LWC from SYRSOC agreed much better with the input LWP from the ground-based MWR in the drizzle run (compare Figure 10). In addition, agreement with satellite LWP was improved.

The fitting parameters for runs with and without drizzle screening are listed in Table 7. The correlations of r_{eff} and LWC were better for the run with drizzle. The agreement of LWP from the MWR changed because time steps were added that were not included earlier due to drizzle screening. The integrated LWC agreed better with the MODIS LWP with drizzle included. The correlation of COT was greater when drizzle was included. Apart from r_{eff} with a slope near 1 and small offset, overall agreement was poor. Comparison with MODIS products at 1.6 and 2.1 µm showed similar results. SYRSOC is based on the assumption of

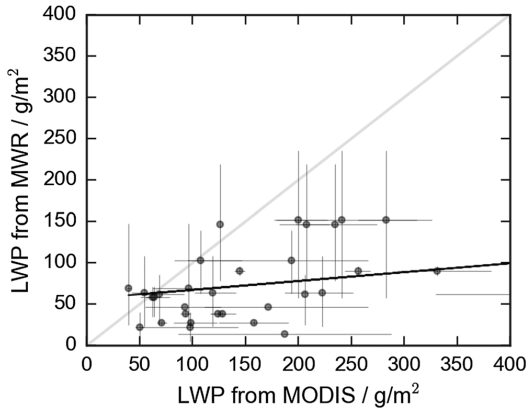

Figure 10. Comparison of MODIS LWP with LWP from the ground-based MWR. Dots mark mean values, and error bars span minima to maxima. The 1:1 line and linear fit are shown in gray and black, respectively.

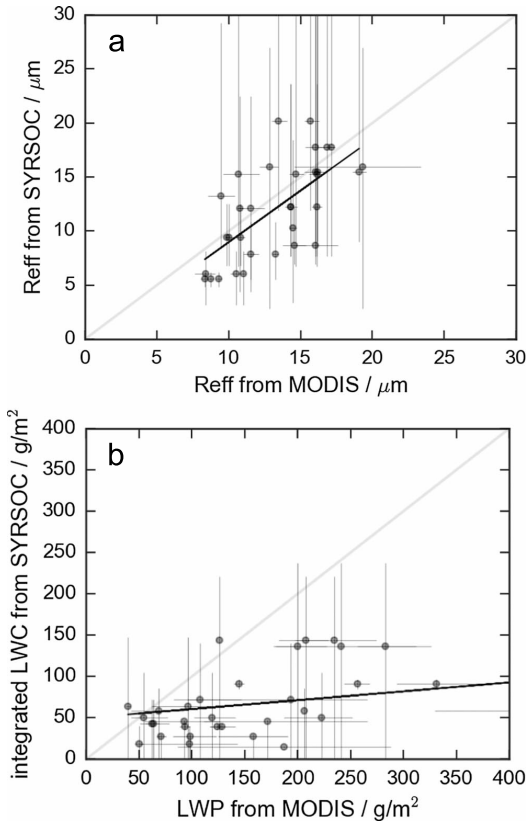

Figure 11. Comparison of (a) r_{eff} and (b) integrated LWC/LWP from MODIS and SYRSOC, including downdrafts and drizzle. Dots mark mean values, and error bars span minima to maxima. The 1:1 line and linear fit are shown in gray and black, respectively.

a monomodal gamma size distribution, which thus does not include drizzle. Therefore, even including time steps affected by drizzle, a realistic representation of drizzle properties cannot be provided. This limits a comparison of our carefully selected data with an all-cloud average from MODIS. This work focusses on temporal homogeneity over 10 min to a maximum of 1 h. This can include horizontally inhomogeneous clouds, especially since they are observed at a land-sea boundary. Surface inhomogeneity can affect cloud properties.

4. Conclusions

Ground-based remote sensing observations of cloud microphysical properties have been made at the coastal site of Mace Head, Ireland, starting in 2009. Homogeneous single-layer nonprecipitating water clouds were selected from a 6 year database. This comprehensive study of 118 cloud cases with a total of more than 18,000 data points (time steps) is statistically representative, compared to single case studies. It is, to the authors' knowledge, the first work analyzing a large number of stratiform liquid water clouds observed at a coastal site over a period of more than 6 years using a synergy of three ground-based remote sensing instruments. The size of the studied data set and the comprehensive air mass characterizations allow a robust interpretation of the results.

Ground-based in situ measurements of aerosol concentrations also revealed the cleanest conditions in summer and highest aerosol concentrations in autumn and winter. Transport paths of air masses at cloud level

were determined using back trajectories. Air mass characteristics showed lowest ground-level concentrations in marine conditions and highest ground-level concentrations in continental conditions, as expected.

Cloud properties were classified according to prevailing cloud level air mass and season. Cloud base and top altitudes were highest in summer and lowest in spring. Clouds in marine-modified air masses were the highest, and cloud base altitudes were lowest in continental modified air. Cloud depth was slightly larger in autumn and winter than in spring and summer. Mainly, marine and marine-modified air masses were observed in summer, although the largest number of data points were obtained in this season. In summer, continental air masses transported from Europe were probably characterized by thermodynamic conditions less favorable for the formation of the stratiform clouds that were investigated here. Aerosol concentrations were lowest during summer, which agreed well with the observed air mass types.

The results presented here confirm the theory and previous findings of higher CDNC and lower r_{eff} with greater pollution. It is important to validate such theories on a statistically significant scale, as was done by using the large data set presented here. Generally, the median CDNC ranged from 60 cm^{-3} in marine air masses to 160 cm^{-3} in continental air. The median r_{eff} ranged from 8 μm in continental modified air to 10 μm in marine air. Droplet size distributions were broader in marine cases and narrower in continental cases. Overall, COT and albedo were lower in cleaner air masses and higher in more polluted conditions, with medians of 2.1 and 4.9, and 0.22 and 0.39, respectively. However, the calculations of COT and albedo were strongly affected by the observed LWP and resulting subadiabaticity.

Comparison of SYRSOC results with MODIS observations showed a moderate correlation of r_{eff} ($R^2 = 0.43$) and a rather poor agreement of COT ($R^2 = 0.19$). No correlation was found between the integrated SYRSOC LWC and MODIS CWP due to SYRSOC drizzle screening. Agreement was improved by rerunning SYRSOC without drizzle screening, thus changing R^2 of LWC from 0.04 to 0.14. Comparison of r_{eff} with drizzle resulted in a slope near 1 and a small offset of −1 μm.

This study ties together large data sets of multiple ground-based and satellite-borne sensors, using sophisticated analysis tools, in order to obtain thorough insights into cloud characteristics. It investigated cloud microphysical properties under the influence of different air masses and, hence, different aerosol types and concentrations. The number of cases spread over a period of more than 6 years, allowed a statistically sound interpretation of the results. Generally, this work confirms findings from case studies [*Miles et al.*, 2000; *Martucci and O'Dowd*, 2011] and model studies [*Rémillard et al.*, 2013]. Additionally, application of the method on such a large scale contributes to the understanding of processes and effects of aerosol-cloud interactions.

Acknowledgments
The authors would like to thank the Irish Environmental Protection Agency (EPA) for fellowship 2012-CCRP-FS.13 and acknowledge support through HEA (Higher Education Authority)PRTLI4. Besides, we gratefully acknowledge the NOAA Air Resources Laboratory (ARL) for provision of the HYSPLIT transport and dispersion model. This work benefits from involvement in Cloudnet; European Research Infrastructure for the observation of Aerosol, Clouds, and Trace gases ACTRIS and ACTRIS-2 (grant agreement numbers 262254 and 654109); European FP7 collaborative project BACCHUS (Impact of Biogenic versus Anthropogenic emissions on Clouds and Climate: towards a Holistic UnderStanding, grant agreement number 603445); and COST actionES1303: TOPROF (Towards operational ground based profiling with ceilometers, doppler lidars and microwave radiometers for improving weather forecasts) supported by COST (European Cooperation in Science and Technology). We acknowledge the Terra and Aqua mission scientists and associated NASA personnel for production and provision of MODIS data. SYRSOC results for the 118 cloud cases are published in netcdf format under http://doi.org/10.5281/zenodo.154137.

References

Albrecht, B. A. (1989), Aerosols, cloud microphysics, and fractional cloudiness, *Science*, *245*, 1227–1230, doi:10.1126/science.245.4923.1227.

Bauer-Pfundstein, M. R., and U. Goersdorf (2007), Target separation and classification using cloud radar Doppler-spectra, paper presented at 33rd Conference on Radar Meteorology, p. 11B.2, Cairns Queensland, 6–10 Aug.

Boers, R., H. Russchenberg, J. Erkelens, and V. Venema (2000), Ground-based remote sensing of stratocumulus properties during CLARA, 1996, *J. Appl. Meteorol.*, *39*, 169–181, doi:10.1175/1520-0450(2000)039<0169:GBRSOS>2.0.CO;2.

Boucher, O., et al. (2013), Clouds and aerosols, in *Climate Change 2013: The Physical Science Basis. Contribution of Working Group I to the Fifth Assessment Report of the Intergovernmental Panel on Climate Change*, edited by T. F. Stocker et al., pp. 571–657, Cambridge Univ. Press, Cambridge, U. K., and New York.

Brandau, C. L., H. W. J. Russchenberg, and W. H. Knap (2010), Evaluation of ground-based remotely sensed liquid water cloud properties using shortwave radiation measurements, *Atmos. Res.*, *96*, 366–377, doi:10.1016/j.atmosres.2010.01.009.

Brenguier, J.-L., H. Pawlowska, and L. Schüller (2003), Cloud microphysical and radiative properties for parameterization and satellite monitoring of the indirect effect of aerosol on climate, *J. Geophys. Res.*, *108*(D15), 8632, doi:10.1029/2002JD002682.

Brenguier, J.-L., F. Burnet, and O. Geoffroy (2011), Cloud optical thickness and liquid water path does the k coefficient vary with droplet concentration?, *Atmos. Chem. Phys.*, *11*, 9771–9786, doi:10.5194/acp-11-9771-2011.

Ceburnis, D., M. Rinaldi, J. Keane-Brennan, J. Ovadnevaite, G. Martucci, L. Giulianelli, and C. D. O'Dowd (2014), Marine submicron aerosol sources, sinks and chemical fluxes, *Atmos. Chem. Phys. Discuss.*, *14*, 23,847–23,889, doi:10.5194/acpd-14-23847-2014.

Coakley, S. A., and W. M. Angevine (2002), Boundary layer height and entrainment zone thickness measured by lidars and wind-profiling radars, *J. Appl. Meteorol.*, *39*, 1233–1247.

Comstock, K. K., R. Wood, S. E. Yuter, and C. S. Bretherton (2004), Reflectivity and rain rate in and below drizzling stratocumulus, *Q. J. R. Meteorol. Soc.*, *130*, 2891–2918, doi:10.1256/qj.03.187.

Crewell, S., and U. Löhnert (2003), Accuracy of cloud liquid water path from ground-based microwave radiometry 2. Sensor accuracy and synergy, *Radio Sci.*, *38*(3), 8042, doi:10.1029/2002RS002634.

Dall'Osto, M., et al. (2010), Aerosol properties associated with air masses arriving into the North East Atlantic during the 2008 Mace Head EUCAARI intensive observing period: An overview, *Atmos. Chem. Phys.*, *10*, 8413–8435, doi:10.5194/acp-10-8413-2010.

Draxler, R. R., and G. D. Rolph (2014), *HYSPLIT (HYbrid Single-Particle Lagrangian Integrated Trajectory) Model access via NOAA ARL READY Website*, NOAA Air Resour. Lab., Silver Spring, Md. [Available at http://ready.arl.noaa.gov/HYSPLIT.php.]

Ferek, R. J., et al. (2000), Drizzle suppression in ship tracks, *J. Atmos. Sci.*, *57*, 2707–2728, doi:10.1175/1520-0469(2000)057<2707:DSIST>2.0.CO;2.

Fox, N. I., and A. J. Illingworth (1997), The retrieval of stratocumulus cloud properties by ground-based cloud radar, *J. Appl. Meteorol.*, *36*, 485–492, doi:10.1175/1520-0450(1997)036<0485:TROSCP>2.0.CO;2.
Heese, B., H. Flentje, D. Althausen, A. Ansmann, and S. Frey (2010), Ceilometer lidar comparison: Backscatter coefficient retrieval and signal-to-noise ratio determination, *Atmos. Meas. Tech.*, *3*, 1763–1770, doi:10.5194/amt-3-1763-2010.
Hudson, J. G. (1993), Cloud condensation nuclei, *J. Appl. Meteorol.*, *32*, 596–607, doi:10.1175/1520-0450(1993)032<0596:CCN>2.0.CO;2.
Hudson, J. G., and S. S. Yum (1997), Droplet spectral broadening in marine stratus, *J. Atmos. Sci.*, *54*, 2642–2654, doi:10.1175/1520-0469(1997)054<2642:DSBIMS>2.0.CO;2.
Hudson, J. G., and S. S. Yum (2001), Maritime-continental drizzle contrasts in small cumuli, *J. Atmos. Sci.*, *58*, 915–926, doi:10.1175/1520-0469(2001)058<0915:MCDCIS>2.0.CO;2.
Hudson, J. G., S. Noble, V. Jha, and S. Mishra (2009), Correlations of small cumuli droplet and drizzle drop concentrations with cloud condensation nuclei concentrations, *J. Geophys. Res.*, *114*, D05201, doi:10.1029/2008JD010581.
Illingworth, A. J., et al. (2007), Cloudnet—Continuous evaluation of cloud profiles in seven operational models using ground-based observations, *Bull. Am. Meteorol. Soc.*, *88*, 883–898, doi:10.1175/BAMS-88-6-883.
Jennings, S. G., M. Geever, F. M. McGovern, J. Francis, T. G. Spain, and T. Donaghy (1997), Microphysical and physio-chemical characterization of atmospheric marine and continental aerosol at Mace Head, *Atmos. Environ.*, *31*, 2795–2808, doi:10.1016/S1352-2310(97)00039-3.
Jennings, S. G., C. Kleefeld, C. D. O'Dowd, C. Junker, T. G. Spain, P. O'Brien, A. F. Roddy, and T. C. O'Connor (2003), Mace Head Atmospheric Research Station—Characterization of aerosol radiative parameters, *Boreal Environ. Res.*, *8*, 303–314.
Lacis, A. A., and J. E. Hansen (1974), A parameterization for the absorption of solar radiation in the Earth's atmosphere, *J. Atmos. Sci.*, *31*, 118–133, doi:10.1175/1520-0469(1974)031<0118:APFTAO>2.0.CO;2.
Lance, S., J. Medina, J. N. Smith, and A. Nenes (2006), Mapping the operation of the DMT continuous flow CCN counter, *Aerosol Sci. Technol.*, *40*, 1–13, doi:10.1080/02786820500543290.
Lohmann, U., and J. Feichter (2005), Global indirect aerosol effects: A review, *Atmos. Chem. Phys.*, *5*, 715–737, doi:10.5194/acp-5-715-2005.
Löhnert, U., and S. Crewell (2003), Accuracy of cloud liquid water path from ground-based microwave radiometry 1. Dependency on cloud model statistics, *Radio Sci.*, *38*(3), 8041, doi:10.1029/2002RS002654.
Löhnert, U., D. D. Turner, and S. Crewell (2009), Ground-based temperature and humidity profiling using spectral infrared and microwave observations. Part I: Simulated retrieval performance in clear-sky conditions, *J. Appl. Meteorol. Climatol.*, *48*, 1017–1032, doi:10.1175/2008JAMC2060.1.
Martucci, G., and C. D. O'Dowd (2011), Ground-based retrieval of continental and marine warm cloud microphysics, *Atmos. Meas. Tech.*, *4*, 2749–2765, doi:10.5194/amt-4-2749-2011.
Martucci, G., C. Milroy, and C. D. O'Dowd (2010), Detection of cloud base height using Jenoptik CHM15K and Vaisala CL31 ceilometers, *J. Atmos. Oceanic Technol.*, *27*, 305–318, doi:10.1175/2009JTECHA1326.1.
Martucci, G., J. Ovadnevaite, D. Ceburnis, H. Berresheim, S. Varghese, D. Martin, R. Flanagan, and C. D. O'Dowd (2012), Impact of volcanic ash plume aerosol on cloud microphysics, *Atmos. Environ.*, *48*, 205–218, doi:10.1016/j.atmosenv.2011.12.033.
Martucci, G., C. Milroy, K. Bower, M. Gallagher, G. Lloyd, and C. D. O'Dowd (2013), Comparison of in-situ, satellite and ground-based remote sensing retrievals of liquid cloud microphysics during MACLOUD,paper presented at 19th International Conference on Nucleation and Atmospheric Aerosols and Nucleation Symposium, AIP Conference, vol. 1527, pp. 828–831, Fort Collins, Colo., 23–28 Jun., doi:10.1063/1.4803399.
Melchionna, S., M. Bauer, and G. Peters (2008), A new algorithm for the extraction of cloud parameters using multipeak analysis of cloud radar data: First application and results, *Meteorol. Z.*, *17*, 613–620, doi:10.1127/0941-2948/2008/0322.
Miles, N. L., J. Verlinde, and E. E. Clothiaux (2000), Cloud droplet size distributions in low-level stratiform clouds, *J. Atmos. Sci.*, *57*, 295–311, doi:10.1175/1520-0469(2000)057<0295:CDSDIL>2.0.CO;2.
Mulcahy, J. P., C. D. O'Dowd, S. G. Jennings, and D. Ceburnis (2008), Significant enhancement of aerosol optical depth in marine air under high wind conditions, *Geophys. Res. Lett.*, *35*, L16810, doi:10.1029/2008GL034303.
Noble, S. R., and J. G. Hudson (2015), MODIS comparisons with northeastern Pacific in situ stratocumulus microphysics, *J. Geophys. Res. Atmos.*, *120*, 8332–8344, doi:10.1002/2014JD022785.
O'Connor, T. C., S. G. Jennings, and C. D. O'Dowd (2008), Highlights from 50 years of aerosol measurements at Mace Head, *Atmos. Res.*, *90*, 338–355, doi:10.1016/j.atmosres.2008.08.014.
O'Dowd, C., D. Ceburnis, J. Ovadnevaite, A. Vaishya, M. Rinaldi, and M. C. Facchini (2014), Do anthropogenic, continental or coastal aerosol sources impact on a marine aerosol signature at Mace Head?, *Atmos. Chem. Phys.*, *14*, 10,687–10,704, doi:10.5194/acp-14-10687-2014.
O'Dowd, C. D., J. A. Lowe, and M. H. Smith (1999), Coupling sea-salt and sulphate interactions and its impact on cloud droplet concentration predictions, *Geophys. Res. Lett.*, *26*, 1311–1314, doi:10.1029/1999GL900231.
Ovadnevaite, J., D. Ceburnis, G. Martucci, J. Bialek, C. Monahan, M. Rinaldi, M. C. Faccini, H. Berresheim, D. R. Worsnop, and C. O'Dowd (2011), Primary marine organic aerosol: A dichotomy of low hygroscopicity and high CCN activity, *Geophys. Res. Lett.*, *38*, L21806, doi:10.1029/2011GL048869.
Ovadnevaite, J., D. Ceburnis, M. Canagaratna, H. Berresheim, J. Bialek, G. Martucci, D. R. Worsnop, and C. O'Dowd (2012), On the effect of wind speed on submicron sea salt mass concentrations and source fluxes, *J. Geophys. Res.*, *117*, D16201, doi:10.1029/2011JD017379.
Ovadnevaite, J., D. Ceburnis, S. Leinert, M. Dall'Osto, M. Canagaratna, S. O'Doherty, H. Berresheim, and C. O'Dowd (2014), Submicron NE Atlantic marine aerosol chemical composition and abundance: Seasonal trends and air mass categorization, *J. Geophys. Res. Atmos.*, *119*, 11,850–11,863, doi:10.1002/2013JD021330.
Pierce, J. R., and P. J. Adams (2006), Global evaluation of CCN formation by direct emission of sea salt and growth of ultrafine sea salt, *J. Geophys. Res.*, *111*, D06203, doi:10.1029/2005JD006186.
Platnick, S., et al. (2015a), *MODIS/Terra Level-2 (L2) Cloud Product (06_L2)*, NASA MODIS Adaptive Processing System, Goddard Space Flight Center, U.S.A., doi:10.5067/MODIS/MOD06_L2.006.
Platnick, S., et al. (2015b), *MODIS/Aqua Level-2 (L2) Cloud Product (06_L2)*, NASA MODIS Adaptive Processing System, Goddard Space Flight Center, U.S.A., doi:10.5067/MODIS/MYD06_L2.006.
Probert-Jones, J. R. (1962), The radar equation in meteorology, *Q. J. R. Meteorol. Soc.*, *88*, 485–495, doi:10.1002/qj.49708837810.
Reade, L., S. G. Jennings, and G. McSweeney (2006), Cloud condensation nuclei measurements at Mace Head, Ireland, over the period 1994-2002, *Atmos. Res.*, *82*, 610–621, doi:10.1016/j.atmosres.2006.02.017.
Rémillard, J., P. Kollias, and W. Szyrmer (2013), Radar-radiometer retrievals of cloud number concentration and dispersion parameter in nondrizzling marine stratocumulus, *Atmos. Meas. Tech.*, *6*, 1817–1828, doi:10.5194/amt-6-1817-2013.
Rosenfeld, D., U. Lohmann, G. B. Raga, C. D. O'Dowd, M. Kulmala, S. Fuzzi, A. Reissell, and M. O. Andreae (2008), Flood or drought: How do aerosols affect precipitation?, *Science*, *321*, 1309–1313, doi:10.1126/science.1160606.

Sauvageot, H., and J. Omar (1987), Radar reflectivity of cumulus clouds, *J. Atmos. Oceanic Technol.*, *4*, 264–272, doi:10.1175/1520-0426(1987)004<0264:RROCC>2.0.CO;2.

Squires, P. (1958), The microstructure and colloidal stability of warm clouds: Part I—The relation between structure and stability, *Tellus A*, *10*, 256–261.

Stephens, G. L., et al. (2002), The CloudSat mission and the A-train—A new dimension of space-based observations of clouds and precipitation, *Bull. Am. Meteorol. Soc.*, *83*, 1771–1790, doi:10.1175/BAMS-83-12-1771.

Twomey, S. (1974), Pollution and the planetary albedo, *Atmos. Environ.*, *8*, 1251–1256, doi:10.1016/0004-6981(74)90004-3.

Twomey, S. (1977), The influence of pollution on shortwave albedo of clouds, *J. Atmos. Sci.*, *34*, 1149–1152, doi:10.1175/1520-0469(1977)034<1149:TIOPOT>2.0.CO;2.

Vong, R. J., and D. S. Covert (1998), Simultaneous observations of aerosol and cloud droplet size spectra in marine stratocumulus, *J. Atmos. Sci.*, *55*, 2180–2192, doi:10.1175/1520-0469(1998)055<2180:SOOAAC>2.0.CO;2.

Winker, D. M., W. H. Hunt, and M. J. McGill (2007), Initial performance assessment of CALIOP, *Geophys. Res. Lett.*, *34*, L19803, doi:10.1029/2007GL030135.

Yoon, Y. J., et al. (2007), Seasonal characteristics of the physicochemical properties of North Atlantic marine atmospheric aerosols, *J. Geophys. Res.*, *112*, D04206, doi:10.1029/2005JD007044.

Yum, S. S., and J. G. Hudson (2002), Maritime/continental microphysical contrasts in stratus, *Tellus B*, *54*, 61–73, doi:10.1034/j.1600-0889.2002.00268.x.

Zuidema, P., E. R. Westwater, C. Fairall, and D. Hazen (2005), Ship-based liquid water path estimates in marine stratocumulus, *J. Geophys. Res.*, *110*, D20206, doi:10.1029/2005JD005833.

Reprinted from
Atmospheric Chemistry and Physics, 17, 3133–3143,
doi:10.5194/acp-17-3133-2017

III

Atmos. Chem. Phys., 17, 3133–3143, 2017
www.atmos-chem-phys.net/17/3133/2017/
doi:10.5194/acp-17-3133-2017

Atmospheric Chemistry and Physics Open Access EGU

Estimates of the aerosol indirect effect over the Baltic Sea region derived from 12 years of MODIS observations

Giulia Saponaro[1], Pekka Kolmonen[1], Larisa Sogacheva[1], Edith Rodriguez[1], Timo Virtanen[1], and Gerrit de Leeuw[1,2]

[1]Finnish Meteorological Institute, Helsinki, 00560, Finland
[2]Department of Physics, University of Helsinki, Helsinki, 00560, Finland

Correspondence to: Giulia Saponaro (giulia.saponaro@fmi.fi) and Pekka Kolmonen (pekka.kolmonen@fmi.fi)

Received: 26 July 2016 – Discussion started: 27 October 2016
Revised: 2 February 2017 – Accepted: 13 February 2017 – Published: 28 February 2017

Abstract. Retrieved from the Moderate Resolution Imaging Spectroradiometer (MODIS) on-board the Aqua satellite, 12 years (2003–2014) of aerosol and cloud properties were used to statistically quantify aerosol–cloud interaction (ACI) over the Baltic Sea region, including the relatively clean Fennoscandia and the more polluted central–eastern Europe. These areas allowed us to study the effects of different aerosol types and concentrations on macro- and microphysical properties of clouds: cloud effective radius (CER), cloud fraction (CF), cloud optical thickness (COT), cloud liquid water path (LWP) and cloud-top height (CTH). Aerosol properties used are aerosol optical depth (AOD), Ångström exponent (AE) and aerosol index (AI). The study was limited to low-level water clouds in the summer.

The vertical distributions of the relationships between cloud properties and aerosols show an effect of aerosols on low-level water clouds. CF, COT, LWP and CTH tend to increase with aerosol loading, indicating changes in the cloud structure, while the effective radius of cloud droplets decreases. The ACI is larger at relatively low cloud-top levels, between 900 and 700 hPa. Most of the studied cloud variables were unaffected by the lower-tropospheric stability (LTS), except for the cloud fraction.

The spatial distribution of aerosol and cloud parameters and ACI, here defined as the change in CER as a function of aerosol concentration for a fixed LWP, shows positive and statistically significant ACI over the Baltic Sea and Fennoscandia, with the former having the largest values. Small negative ACI values are observed in central–eastern Europe, suggesting that large aerosol concentrations saturate the ACI.

1 Introduction

Aerosols and especially their effect on the microphysical properties of clouds are among the key components that influence the Earth's climate. As the magnitude and sign of such effects are not well known, understanding and quantifying the influence of aerosols on cloud properties constitutes a fundamental step towards understanding the mechanisms of anthropogenic climate change (Boucher, 2013).

As aerosols may act as cloud condensation nuclei (CCN), an increase in their number concentration can lead to an increase in the number of cloud droplets in super saturation conditions and a decrease in the cloud droplet radius. The decrease in the droplet effective radius resulting in an increase of the cloud albedo, under the assumption of a constant liquid water path, is known as the Twomey effect (Twomey, 1977). The decrease in droplet size can also impact the precipitation cycle, as the smaller droplets require longer time to grow into precipitating droplet sizes. Additionally, a possible decrease in the precipitation frequency of liquid clouds increases the lifetime of clouds (Albrecht, 1989). These impacts of aerosols are called the first and second indirect effects.

A quantitative evaluation of the effects of aerosols on clouds may be possible mainly in a statistical sense because of the local interactions between meteorological conditions and aerosols (Tao et al., 2012). Satellite-based remote sensing instruments can provide a large data set for statistical analysis from long-term observations of the aerosol indirect effect on a large spatial scale with daily global coverage, complementing localized ground measurements and providing necessary parameters for climate models.

A common approach in the satellite-based investigation of the first aerosol indirect effect (AIE) is the concept of the aerosol–cloud interaction (ACI), which relates the cloud optical thickness (COT), cloud effective radius (CER) or cloud droplet number concentration (CDNC) to the aerosol loading. The aerosol loading is usually expressed by the aerosol optical depth (AOD) or aerosol index (AI, defined in Sect. 3), which are used as proxies for the CCN concentration.

Many studies describe the interaction between aerosols and clouds through the correlation of the satellite-retrieved aerosol concentration and cloud droplet size on a global or regional scale. Inverse correlations on a global (Bréon et al., 2002; Myhre et al., 2007; Nakajima et al., 2001) and a regional scale (Costantino and Bréon, 2010; Ou et al., 2013) have been found, while Sekiguchi et al. (2003) and Grandey and Stier (2010), applying satellite data on a global scale, found either positive, negative or negligible correlations between the CER and AOD depending on the location of the observations. Jones et al. (2009) emphasized that the ACI should be inferred in aerosols or cloud regimes determined on a regional scale, as the relevance of aerosol type, aerosol concentration and meteorological conditions differs around the world.

Areas located at high latitudes are excluded from most of the studies due to a seasonal limitation of the satellite coverage and a smaller number of observations when compared to the global averages over the year. Lihavainen et al. (2010) compared in situ and satellite measurements to quantify the ACI on low-level clouds over Pallas (Finland), a northern high-latitude site, and concluded that the ACI values derived from ground-based measurements were higher than those obtained from satellite observations. Unlike the in situ instruments, the wavelengths used in the satellite retrievals constrain the detection of fine particles to those larger than about 100 nm, thus making it impossible to account for all CCN. Sporre et al. (2014a, b) combined aerosol measurements from two clean northern high-latitude sites with satellite cloud retrievals and observed that the aerosol number concentration affects the CER, while no impact on the COT was observed. As both studies focused on specific locations, no information was thus provided on a larger scale in the Baltic region. This work investigates whether the first indirect effect can also be observed by means of satellite-derived observations over the Baltic Sea region, a region that offers a northern clean atmospheric background (Fennoscandia) contrasted by a more polluted one (central–eastern Europe).

To determine whether it is possible to observe the response of the properties of low-level liquid clouds to different aerosol loadings in different atmospheric conditions, 12 years of aerosol and cloud properties available from the Moderate Resolution Imaging Spectroradiometer (MODIS) retrievals were investigated on a regional scale.

The satellite retrieval products are introduced in Sect. 2, the approach adopted for the ACI analysis is described in Sect. 3 and the results of the analyses are presented in Sect. 4.

2 Data

The area covered in this study is situated at high latitudes (50° N, 10° E, 70° N, 35° E). At these latitudes the solar zenith angle (SZA) constrains the available satellite data set: a large value of the SZA implies higher uncertainties on the retrieved parameters. Due to the SZA and data coverage constraints, we limit the data set to the summer (June, July, August) observations that were collected by the MODIS instrument between 2003 and 2014. Data are analysed only from the MODIS/Aqua platform that crosses the equator at 13:30 LT (local time), when the clouds are fully developed.

The MODIS Collection 06 Level 3 (C6 L3) product provides cloud and aerosol parameters at daily time resolution and at a regular $1° \times 1°$ spatial grid. The application of MODIS satellite data to ACI studies is often criticized for the lack of coincidental aerosol and cloud retrievals. Studies such as Avey et al. (2007), Bréon et al. (2002) and Anderson et al. (2003) showed that in the case of daily products at $1° \times 1°$ resolution it is unnecessary to individually couple the aerosol and cloud measurements. Therefore, in this study aerosol and cloud data are assumed to be co-located.

The MODIS C6 L3 product includes cloud microphysical parameters (CER, COT, cloud liquid water path (LWP)) with statistics (mean, minimum, maximum, standard deviation) determined at three different wavelengths (1.6, 2.1 and 3.7 µm) for each cloud phase (liquid, ice, undetermined) separately.

We filtered the MODIS cloud data according to the following criteria:

- Cloud parameters were only considered in the liquid phase.
- To eliminate possible outliers, retrievals with a standard deviation higher than the mean values were discarded.
- Observations with a mean cloud-top temperature less than 273 K were eliminated to ensure only warm liquid cloud regimes.
- The multilayer flag was applied to select only single-layer clouds.
- Transparent-cloudy pixels ($COT < 5$) were discarded to limit uncertainties (Zhang et al., 2012).
- The CER derived from the 3.7 µm wavelength was chosen since it has been shown to be less affected by the subpixel heterogeneity (Zhang et al., 2012).
- To exclude precipitating cases, observations were discarded when the difference between CER at 3.7 µm and CER at 2.1 µm was greater than 10 µm (Zhang et al., 2012).

The science data sets (SDSs) for the atmospheric aerosol information in the MODIS C6 L3 provide the AOD retrieved at several wavelengths and as a product from

the application of either the "Deep Blue" or "Dark Target" algorithm, or a combination of both retrievals (Levy et al., 2013; Sayer et al., 2014). The SDS "Aerosol_Optical_Depth_Land_Ocean_Mean" is the sole product providing the AOD at 0.55 µm globally, while the other aerosol SDSs provide the AOD over land and water separately. As C6 provides the Ångström exponent (AE) over land only, the AOD at the wavelengths of 0.46 and 0.66 µm present in both "Aerosol_Optical_Depth_Land_Mean" and "Aerosol_Optical_Depth_Ocean_Mean" were used to derive the AE globally as shown in Sect. 3.

To assess the effect of meteorological conditions on cloud properties, the ECMWF ERA-Interim reanalysis data were applied to derive the lower-tropospheric stability (LTS). Although not a ready-to-use product, the LTS is computed as the difference between the potential temperature at 700 hPa and at the surface (Klein and Hartmann, 1993), describing the magnitude of the inversion strength for the lower troposphere.

3 Methods

After selecting the cloud parameters as listed in the previous section, the number of observations were binned for both aerosol and cloud products. From the obtained histograms, 95 % of the most frequent ranges were selected from the total data set by filtering out 2.5 % of data from the extremes. These statistically more robust data sets were used in further analysis.

The product of the AOD, representing the column-integrated optical extinction of aerosol at a given wavelength, and the derived AE, describing the spectral dependency of the AOD, results in a third aerosol property of interest, the aerosol index (AI). The AI is used as a proxy for the fine-mode aerosol particles, which have a larger contribution to the CCN than the coarse-mode particles (Nakajima et al., 2001). MODIS Collection 6 provides the AE only over land. To homogeneously estimate the AI over the Baltic Sea and the surrounding land areas, the AE is evaluated by applying equation

$$\mathrm{AE} = -\log(\mathrm{AOD}_{\lambda_1}/\mathrm{AOD}_{\lambda_2})/\log(\lambda_1/\lambda_2) \quad (1)$$

to the wavelength pair of $\lambda_1 = 0.66\,\mu\mathrm{m}$ and $\lambda_2 = 0.46\,\mu\mathrm{m}$, which are available both over land and over sea. The C6 MODIS aerosol algorithm does not, however, allow the determination of the AE for coastal and inland water regions (Levy et al., 2013). This would leave large parts of the Baltic region under investigation in this work out of the analysis (see Fig. 3b and c). For this reason, the ACI was analysed, in addition to the AI, with the AOD. Seasonal mean values of aerosol (AOD, AE, AI) and cloud parameters (CER, cloud fraction (CF), COT) were computed for the period of 2003–2014.

Aiming to observe how the variation in aerosol conditions influences cloud properties, we adopted the approach of Koren et al. (2005) to analyse the average vertical distribution of the relationships between aerosols and cloud properties. The AOD and AI data sets were firstly sorted in ascending order and successively divided into five equally sampled classes that represent the averages of aerosol conditions for each of the classes. The cloud properties were then divided according to these AI and AOD classes and plotted as functions of cloud-top pressure.

The response of the cloud properties to clean-versus-polluted aerosol conditions was studied spatially. The 25th and 75th percentiles of the AI and AOD (AI–AOD) were computed for each spatial grid point, the former constituting the upper limit for the AI–AOD values representing low aerosol loadings and the latter representing the lower limit for the AI–AOD values for heavy aerosol loadings. These percentile values were then used to divide cloud parameters for clean and polluted aerosol conditions. The difference between a cloud parameter value in low- and high-aerosol conditions is

$$\Delta\mathrm{Cloud\_}X = \mathrm{Cloud\_}X_{25\mathrm{th\,percentile}} - \mathrm{Cloud\_}X_{75\mathrm{th\,percentile}}, \quad (2)$$

where the considered cloud parameters, Cloud_X, are the CER, cloud-top pressure (CTP), COT, CF and LWP. The subscripts indicate that the cloud parameter is representative for clean atmospheric conditions, Cloud_$X_{25\mathrm{th\,percentile}}$, or for polluted atmospheric conditions, Cloud_$X_{75\mathrm{th\,percentile}}$. The difference ($\Delta$Cloud_$X$) between the cloud parameter Cloud_X in clean (Cloud_$X_{25\mathrm{th\,percentile}}$) and polluted (Cloud_$X_{75\mathrm{th\,percentile}}$) aerosol evidences the impact of these two aerosol cases on the parameter Cloud_X.

Matsui et al. (2006) found that aerosols impact the CER stronger in an unstable environment (low LTS) than in a stable environment (high LTS) where the intensity of the ACI is reduced due to the dynamical suppression of the growth of cloud droplets. Following this result, we also compared cloud microphysical properties with both the AI–AOD and the LTS.

The area of this study was divided into three subregions as presented in Fig. 1: Area 1 covers the Baltic Sea, while Area 2 and Area 3 include only land pixels over Fennoscandia and central–eastern Europe respectively.

The ACI related to the CER was computed using the formulation from McCominsky and Feingold (2008):

$$\mathrm{ACI} = -\left.\frac{\partial \ln \mathrm{CER}}{\partial \ln \alpha}\right|_{\mathrm{LWP}}, \quad (3)$$

which indicates how a change in the CER depends on a change in the aerosol loading α, given by either the AI or the AOD, for a constant LWP. The ACI was computed by dividing the CER and the AI–AOD over LWP bins ranging from 20 to 300 g m^{-2} with an interval of 40 g m^{-2} and then by performing a linear regression analysis with the logarithms of

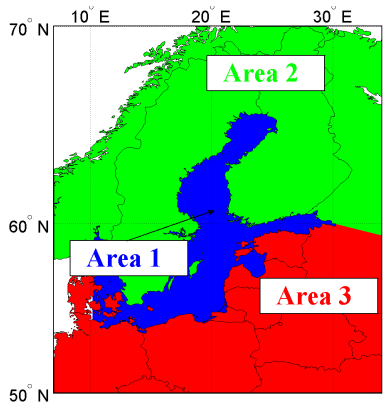

Figure 1. The area covered in this study and its division into three subregions: Area 1, the Baltic Sea, is represented by the colour blue; Area 2, covering the land areas of Fennoscandia, is represented by the colour green and Area 3, in red, includes the land areas of central–eastern Europe.

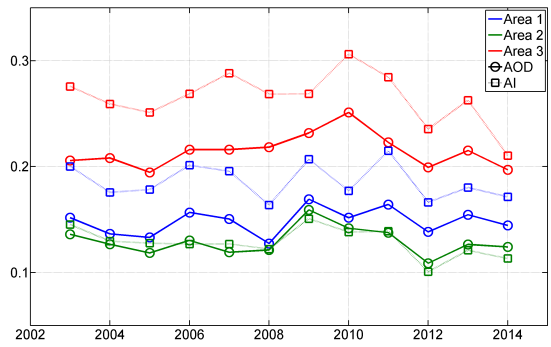

Figure 2. Time series of summer (JJA) averages for AOD (circles) and AI (squares) for the three subregions. The three subregions are colour-coded as in Fig. 1.

the CER and α in each LWP bin. Two approaches were applied to present the ACI: in the first, the ACI were obtained for each subregion and plotted as a function of the LWP, while in the second approach the ACI was computed in a 2° spatial grid. In the grid approach we chose the LWP interval that provided statistically significant ACI estimates for each of the three subregions. The statistical significance is determined by the null hypothesis test scoring a p value < 0.05 (Fisher, 1958).

4 Results

Figure 2 presents the time series of AI and AOD averages during the summer months from 2003 to 2014 for each subregion. It is easy to see in Fig. 2 that these three areas have generally different aerosol conditions: within the land subregions, the lower AI and AOD averages occur over Area 2, while over Area 3 these values are higher during the entire period. Area 1, the Baltic Sea, is considered as a third subregion per se due to the dominance of maritime aerosol conditions. The AI is highest over Area 3 (central–eastern Europe), with an overall AI mean value of 0.29 ± 0.03 (regional mean $\pm$ standard deviation), followed by Area 1 (Baltic Sea) with a mean value of 0.20 ± 0.02, while over Area 2 (Fennoscandia) the lowest AI mean value of 0.16 ± 0.01 is found. Area 3 also presents the highest averages for the AOD, 0.22 ± 0.02, but Area 2 and Area 1 have comparable AOD values: 0.16 ± 0.02 and 0.14 ± 0.01 respectively.

The spatial variations of the aerosol and cloud properties are shown in Fig. 3. A decreasing south–north gradient of AOD is observed in Fig. 3a where the highest values are found over Area 3 (northern Germany and Poland), and the lowest are found over Area 2 (the Atlantic coast of Norway and northern Sweden). While no discontinuities can be seen for the AOD distribution over Area 1 and Area 2, a clear distinction is evident in the AE (Fig. 3b). Indicating the dominance of fine particles, high values of the AE are found over the entire Area 1, over the eastern part of Area 3 and over the north-western part of Area 2. Low values (AE < 1) are only partially found over the land of Areas 2 and 3. The validity of the MODIS AE over land is generally considered unrealistic. Nonetheless, in the case of the dominance of fine-mode aerosols, the MODIS AE agrees with AERONET (Levy et al., 2010), while disagreements occur in coarse aerosol cases (Jethva et al., 2007; Mielonen et al., 2011). Over ocean, a good agreement between MODIS AE and AERONET is found globally with the limitation of AOD > 0.2 (Levy et al., 2015), a restriction that cannot be applied in our study area where the regional AOD is about 0.2. As the sensitivity of AE to AOD errors is especially critical for low AOD values, pixels with AOD < 0.2 are expected to have a less-qualitatively accurate AE. Nevertheless, the AE over Area 1 (Fig. 3b) matches the median range of 1.46–1.49 obtained from a validation study that compares the AE retrieved by SeaWiFS and MODIS Aqua or Terra with the three AERONET stations over the Baltic Sea (Melin et al., 2013). Comparable high AE values were collected by Rodriguez et al. (2012) from 2002 to 2011 at the subarctic ALOMAR Observatory (Andøya, Norway): the AE peaks during the summer season with a multi-annual mean and standard deviation of 1.3 ± 0.4. The AI (Fig. 3c) over Area 1 is comparable to the values over Area 3, while the lowest values occur over Area 2. The spatial distributions of the cloud properties (COT, CER, CF) are shown in Fig. 3d–f. As in the aerosol case, Area 2 presents a distinctive discontinuity between land and water pixels (Fig. 3d–f). These results are confirmed in Karlsson (2003), where Area 1 (the Baltic

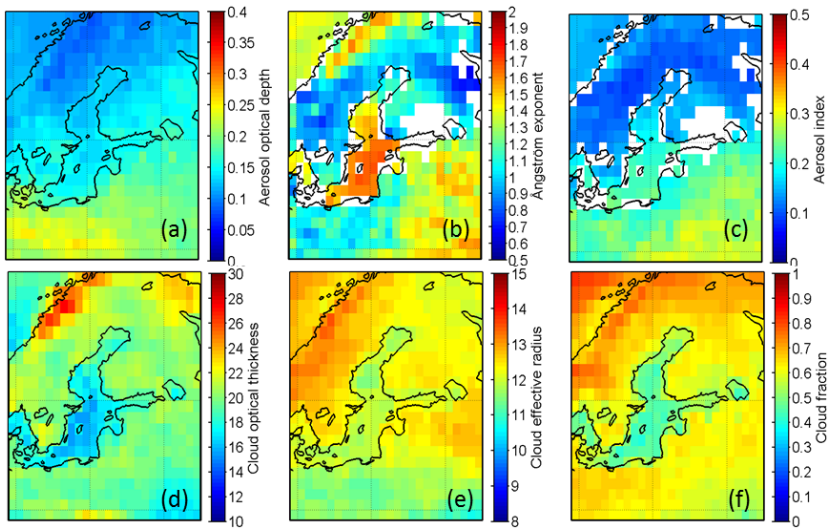

Figure 3. Spatial distributions of AOD **(a)**, AE **(b)**, AI **(c)**, COT **(d)**, CER **(e)** and CF **(f)** averages for summer seasons between 2003 and 2014.

Sea) exhibits low cloudiness while high cloud amounts are found over the Scandinavian mountain range (Area 2) and the Norwegian Sea. Considering the theory of the first AIE, that is, an increase in aerosol loading leads to larger CDNC and smaller CER for a fixed LWP, the CER (Fig. 3e) shows correlation with the AOD spatial distribution (Fig. 3a), while the worst comparison is found between CER (Fig. 3e) and AI (Fig. 3c). Over the Norwegian coast the high values of COT, CER and the CF can be explained by high hygroscopicity of sea spray aerosols, which makes these particles very efficient CCN. Another feature of Fig. 3e is the low effective droplet radius over Area 1 (the Baltic Sea). Unlike Area 3 (central–eastern Europe), Area 1 does not match with any high aerosol loading (Fig. 3a, c) when compared to the surrounding area. In fact, the AOD over Area 1 is as low as in Area 2 (Fig. 2), even though the CER is about 1–2 µm larger for these land areas.

Figure 4 presents the 10-year average of the cloud properties, divided into five classes of the AI (Fig. 4a–d) and AOD (Fig. 4e–h) plotted as a function of cloud-top pressure. It can be observed that the lowest values of CTP correspond to the higher classes of AI–AOD. Assuming the CTP to be an indicator of the cloud-top height, this may suggest an enhancement of the cloud vertical structure. This result was also found by Koren et al. (2005), where convective clouds over the North Atlantic showed a strong correlation between the aerosol loading and the vertical development of the clouds. Furthermore, the cloud droplet effective radius (Fig. 4a, e) has smaller values in higher AI–AOD classes. The opposite behaviour, lower average values corresponding to the lower classes of the AI–AOD can be seen for the COT (Fig. 4c, g) and LWP (Fig. 4d, h), while the CF (Fig. 4b, f) shows a weaker signal for both AI and AOD cases. Overall, Fig. 4 reveals that the cloud parameters are clearly affected by the AI–AOD segregation at lower levels of CTP. For this reason, we limit our data set to cloudy pixels where the CTP is between 700 and 900 hPa.

In Fig. 5 the CER is plotted as a function of AI for fixed values of the LWP (five intervals as above) and the CTP (between 700 and 950 hPa, in 50 hPa bins). The highest AI in Area 1 (the Baltic Sea) is around 0.35 for the lowest clouds (CTP 900–950 hPa), decreasing to 0.3 for the highest clouds (CTP 700–750 hPa). Over Area 2 (Fennoscandia) the aerosol loading is not clearly connected to the cloud height, showing a constant AI average of approximately 0.25. As expected, Area 3 has the highest average of AI out of the three subregions, with values as high as 0.6 for the lowest clouds and a small decrement for the highest clouds. The cloud droplet size in Area 1 (the Baltic Sea) and Area 2 (Fennoscandia) shows a strong negative correlation with the AI, while a weak correlation is observed over Area 3 (central–eastern Europe). Area 1 has no results for the high LWP bins: during summer months few or no convective clouds form over the Baltic Sea and mainly thin stratiform clouds are identified in the cloud cover. Similar results are also found when the AOD is substituted by the AI (not shown).

Applying Eq. (2) to the cloud parameters, the impact of low and high aerosol loading (ΔCloud_X) on cloud properties (Cloud_X) is presented in Fig. 6. Resulting from a grid-based analysis, ΔCloud_$X < 0$ means that the observed cloud

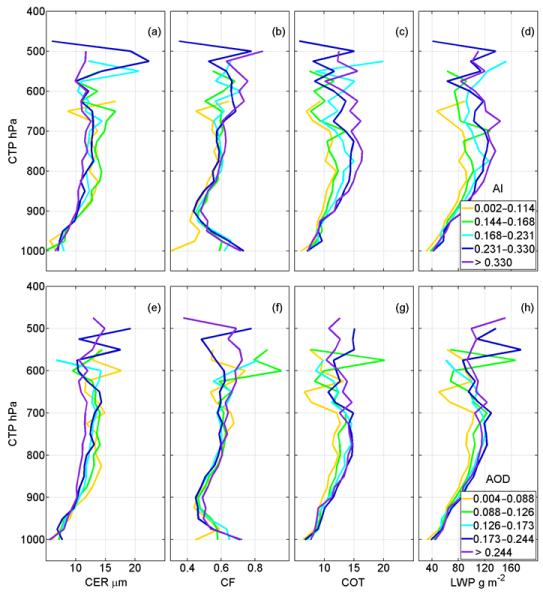

Figure 4. Cloud properties, 10-year averaged, as a function of cloud-top pressure: CER **(a, e)**, CF **(b, f)**, COT **(c, g)** and LWP **(d, h)** as functions of cloud-top pressure (CTP) for five classes of AI **(a–d)** and AOD **(e–h)**. Each class of AI–AOD contains an equal number of samples in that interval.

parameter Cloud_X has a larger value in polluted cases (AI–AOD > 75th percentile) than in clean atmospheric conditions (AI–AOD < 25th percentile) for that grid cell and vice versa when ΔCloud_X has a positive value. As similar results were obtained by applying the AOD and AI, only the results for the AOD are shown. ΔCF (Fig. 6a) presents only negative values, suggesting that the CF is always significantly larger in the polluted atmospheric conditions. The positive values of ΔCTP (Fig. 6d) over Area 2 (Fennoscandia) and Area 3 (central–eastern Europe) agree with the idea of the vertical development of clouds for higher aerosol loadings (Fig. 4). However, other factors, such as surface heating, might also be contributing to the results: the presence of stronger turbulence over land cause the clouds to rise higher than in the presence of lower turbulence, for example, over a cooler water surface. The CER (Fig. 6c) shows a different behaviour over land (Area 3) than over water (Area 1). Over Area 3 ΔCER is predominantly negative: although small ($< 2\,\mu$m) negative values of the ΔCER indicate that the CER is larger over areas with higher aerosol loadings than over cleaner areas. This result is in contradiction with the theory of the AIEs. The presence of aerosol appears to have little or no effect on ΔCOT (Fig. 6b) and ΔLWP (Fig. 6e).

In an attempt to connect the link between aerosol and clouds with meteorology, we evaluated the variability of low-level liquid cloud properties as a function of aerosol conditions (AOD–AI) and lower troposphere stability (LTS). Figure 7 shows the cloud properties (LWP, CER, CF and COT) plotted as a function of the LTS and AI–AOD. While the CF shows a gradient for both directions of the LTS and the AI–AOD, the other cloud variables (LWP, CER, COT) are mainly affected by aerosols with little to no correlation with changes in the LTS. Higher aerosol values correspond to a smaller CER (Fig. 7b, f) and higher CF (Fig. 7c, g) and LWP (Fig. 7a), in agreement with the AIEs, except for the LWP (Fig. 7e), which decreases as a function of the AOD. The LWP (Fig. 7e) shows a non-monotonic response by increasing when the AOD ranges between 0.3 and 0.4 because at high aerosol concentrations the cloud droplets are smaller and less likely to precipitate, and furthermore the LWP slightly decreases. A possible explanation of a better correlation of the LWP with the AI than with AOD might be found by looking at the LWP vertical distributions in Fig. 4, which indicate a more distinctive separation of the LWP for the AI-based classes than for AOD.

Figure 8 illustrates the ACI estimate for the CER (Fig. 8a) and its corresponding correlation coefficient r (Fig. 8b) calculated for the three subregions as a function of the LWP bins for both AOD and AI. The lines are colour-coded according to the three areas as defined in Fig. 1. The ACI estimates for Area 1 (Baltic Sea) are positive and statistically significant for most of the LWP range, increasing, as a function of LWP, from a minimum of 0.06 to a maximum of 0.16 and with a corresponding r ranging from -0.1 to -0.53. The values of the ACI for Area 2 range between 0.02 and 0.06, with fewer statistically significant points and a smaller r than in Area 1. The results collected over both Area 1 and Area 2 appear to be little affected by whether the AOD or AI is applied in the computation of the ACI. For Area 3, two points of the ACI results are statistically significant but with very low values for correlations ($r < 0.1$) for the first two bins of the LWP and, unlike the other two subregions, they show a negative sign. The ACI values are statistically significant for the three subregions for the first two bins of LWP and when the AOD is chosen over the AI as α. With a combination of these requirements, we derived the spatial distribution of the ACI and r, which are shown in Fig. 9. Positive correlations are found predominantly over Area 3 and scattered over Area 2, while negative values cover the majority of Area 1 and, more sparsely, Area 2. The relationship between CER and AOD is, paradoxically, positively correlated over Area 3, suggesting that high aerosol loading corresponds to larger cloud effective radius (Figs. 6c, 8, 9). One possible explanation might be the indication of the relationship between CTP and AOD: the CTP decreases for increasing AOD (Fig. 4), and at the same time the CER increases with decreasing CTP (higher altitude) in convective clouds (Rosenfeld and Lensky, 1998). Nonetheless, this result must be treated with care because other factors, such as hygroscopic effect, influence the rela-

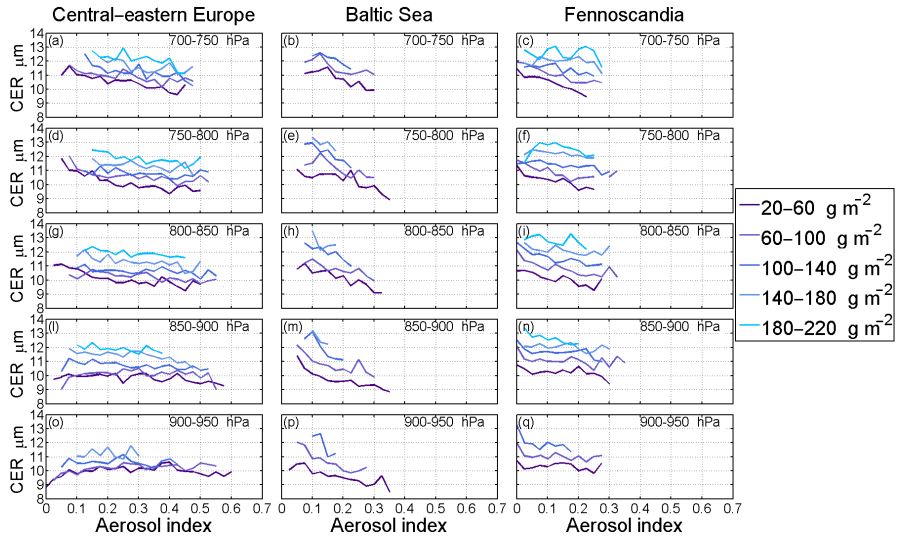

Figure 5. CER as a function of AI, stratified for subranges of CTP and LWP, for the three subregions. The legend on the right of the figure lists the LWP bins.

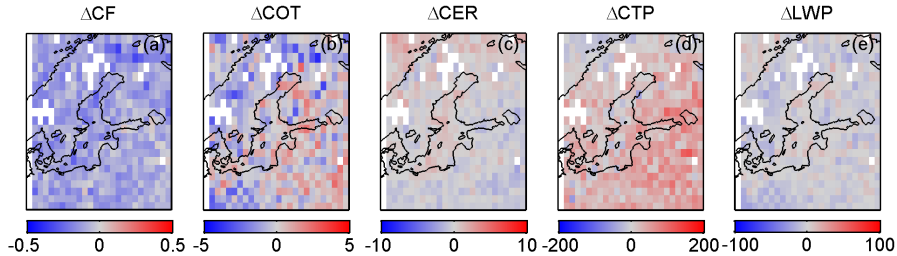

Figure 6. Spatial distributions of the difference of the cloud properties CF **(a)**, COT **(b)**, CER **(c)**, CTP **(d)**, and LWP **(e)** for low aerosol loading (AOD < 25th percentile) and heavy aerosol loading (AOD > 75th percentile) calculated from Eq. (2).

tionship between AOD and cloud parameters and cannot be fully ignored.

5 Discussion and Conclusions

In this work we have studied the applicability of satellite-based information for quantifying the ACI over the Baltic Sea region. Distinct subregional differences were found in the estimates of the ACI related to the effective radius of cloud droplets. No clear ACI results were observed for the other cloud parameters, which suggests that these may be influenced by other factors, such as the local meteorological conditions. The meteorological conditions are represented here by the LTS, which was compared to the cloud parameters. The LTS is correlated with the CF, while no effect was observed upon the other cloud parameters. In particular, there is no clear evidence of the effect of LTS on the interaction between aerosols and cloud effective radius.

One of the key aspects of this study was to find out whether a rigorously filtered Level 3 MODIS data set can be applied for ACI studies at a regional level. As the northerly location of the region of interest here restrains the availability of the MODIS observations to the summer months (JJA), one of the challenges is the limited data coverage. Moreover, the selection of specific cloud regimes and the co-location of aerosol and cloud observations are additional essential key factors in building up a robust data set, which, however, further decreases the amount of data points available. As far as the authors know, no previous results on ACI from a satellite perspective are provided over this area.

This study shows that the different aerosol conditions characterizing the Baltic Sea countries have an impact on the ACI and this can be also observed on a regional scale. According

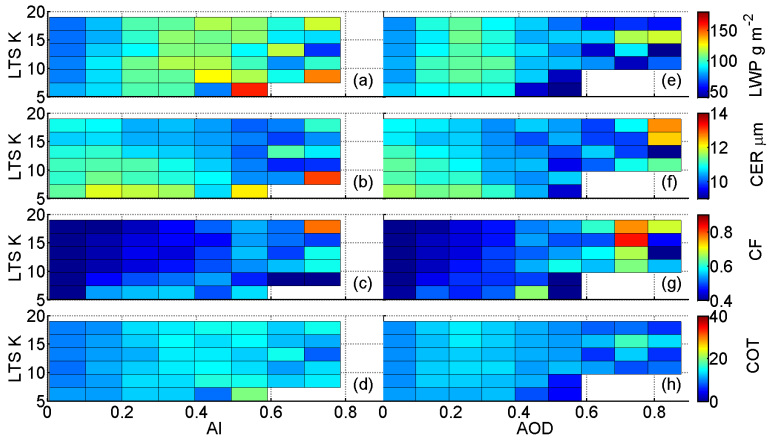

Figure 7. Mean low-level liquid cloud properties plotted as a function of LTS and AI **(a–d)** or AOD **(e–h)**.

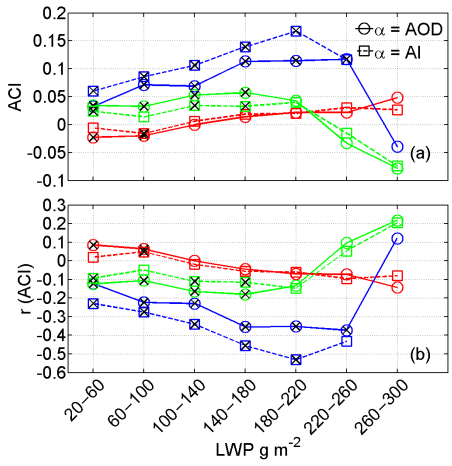

Figure 8. ACI estimates computed for the CER as a function of the LWP and by applying both the AI and AOD as proxies for the CCN are shown in **(a)**. The correlation coefficients are presented in **(b)**. The colour-coded lines refer to the three subregions determined in Fig. 1: Area 1 (blue), Area 2 (green) and Area 3 (red). The line styles define whether the AOD or AI were used as the CCN proxy, α. Markers signed with a cross represent points fulfilling the null hypothesis (p value < 0.05), which are hence statistically significant.

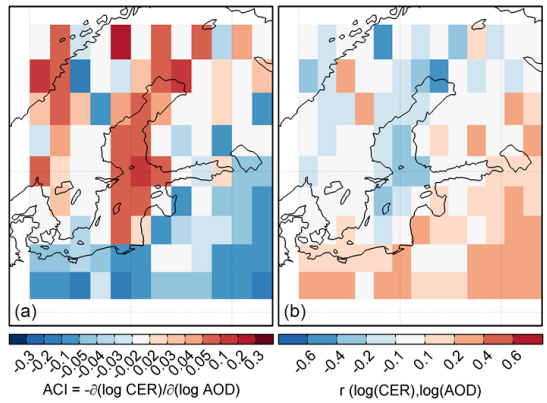

Figure 9. Applying the AOD as a proxy for the CCN, estimates of the ACI and correlation coefficient for the CER and for the interval of the LWP between 20 and 60 g m^{-2} were calculated on a grid basis. The obtained spatial distribution of the ACI is shown on the left and the correlation coefficient is shown on the right.

to ACI theory, polluted atmospheric conditions are connected with clouds characterized by lower cloud-top pressure, larger coverage and optical thickness. However, the cloud effective radius strictly follows the AIE's theory only over Area 1 (the Baltic Sea), which also agrees with the results presented by Feingold (1997). As reported in this study, the CER retrieved in clean clouds is mainly affected by the LWP and aerosol presence, while when detected under polluted conditions, it additionally shows a high dependence on other factors.

The cleaner atmosphere characterizing Area 1 (the Baltic Sea) and Area 2 (Fennoscandia) reveals statistically significant and positive ACI estimates between the CER and AOD that are in agreement with the values obtained from ground-based measurements collected at the sites of Pallas and Hyytiälä in Finland and Vavihill in Sweden (Lihavainen et al., 2010; Sporre et al., 2014b), while over the more polluted Area 3 (central–eastern Europe), the sensitivity to locally determine the ACI is smaller. It can be assumed that

more aerosols lead to a high concentration of the CCN and this lowers the average droplet radius, as can be seen in Fig. 3e when the radius is compared between areas located south (high aerosol load) and north (low aerosol load) of the Baltic Sea.

Our analysis of the ACI for the CER shown in Fig. 8 leads to the following conclusions:

- The lowest values of the ACI can be seen over Area 3. This is also the subregion with the highest average AOD values, leading to the smallest cloud droplet size. A further addition of aerosol particles and thus possibly also CCN does not decrease the cloud droplet size any further. Most of the ACI values are actually negative but very close to zero.
- The positive ACI values for Area 2 show that the addition of aerosols to a relatively clean atmosphere does decrease the droplet size.
- The AI over the land areas in the study should be considered unrealistic because the average inland AE can have values below 1.
- The average AE over Area 1 has values as high as 1.4 to 1.5. These values, however, can be trusted and have been evaluated by Melin et al. (2013).
- The low CER over Area 1 requires further explanation. The most probable cause for the low values, based on the MODIS cloud retrieval, is the relatively low cloud-top height over the sea. As cloud droplets generally grow in size from the cloud base towards the cloud top (McFiggans et al., 2006), Fig. 4 confirms that the average CER increases with the decreasing CTP. Furthermore, in Fig. 5 there is a distinctive lack of results for high LWP values, indicating that there are fewer clouds at higher top heights. These reasons altogether lead to low values of the CER over Area 1 since the MODIS instrument retrieves the droplet radius at cloud top, and the top height CER results are low when compared to the surrounding over-land values.
- The ACI over Area 1 has considerably higher values than over the land subregions, and there is a difference in the magnitude between the ACI values determined using the AOD or AI. The clean maritime atmospheric conditions lead to the high sensitivity of droplet size to changes in fine-particle concentrations. The AOD and AI difference in ACI, the latter being the higher, indicates that the ACI is caused by fine particles as expected.

Another way to assess the aerosol-induced changes in cloud parameters would be to analyse time series to find out whether dynamically decreasing or increasing aerosol loading has an effect on clouds. This sort of approach was not attempted in this work.

Another important result of this work is the comparison of the ACIs obtained using the AI and AOD, chosen as proxies for the CCN, in order to determine which option leads to more realistic results. Even though theoretically the AI would be a better parameter than AOD to indicate the presence of fine-mode aerosol particles, the impact of uncertainties of the derived AI might be substantial.

6 Data availability

All data used in this study are publicly available. The satellite data from the MODIS instrument used in this study were obtained from https://ladsweb.nascom.nasa.gov/search/ (Saponaro, 2015a). The ECMWF ERA-Interim data were collected from the ECMWF data server http://www.ecmwf.int/en/research/climate-reanalysis/browse-reanalysis-datasets (Saponaro, 2015b).

Competing interests. The authors declare that they have no conflict of interest.

Acknowledgements. This research was funded by the Maj and Tor Nessling Foundation (grant no. 201600287). The authors also acknowledge the Academy of Finland Centre of Excellence (grant no. 272041).

Edited by: F. Yu
Reviewed by: two anonymous referees

References

Albrecht, B. A: Aerosols, cloud microphysics, and fractional cloudiness, Science, 245, 1227–1230, 1989.

Anderson, T. L., Charlson, R. J., Winker, D. M., Ogren, J. A., and Holmen, K.: Mesoscale variations of tropospheric aerosols, J. Atmos. Sci., 60, 119–136, doi:10.1175/1520-0469(2003)060<0119:MVOTA>2.0.CO;2, 2003.

Avey, L., Garrett, T. J., and Stohl, A.: Evaluation of the aerosol indirect effect using satellite, tracer transport model, and aircraft data from the International Consortium for Atmospheric Research on Transport and Transformation, J. Geophys. Res., 112, 2156–2202, doi:10.1029/2006JD007581, 2007.

Boucher, O., Randall D., Artaxo, P., Bretherton, C., Feingold, G., Forster, P., Kerminen, V.-M., Kondo, Y., Liao, H., Lohmann, U., Rasch, P., Satheesh, S. K., Sherwood, S., Stevens, B., and Zhang, X. Y.: Clouds and Aerosols, in: Climate Change 2013: The Physical Science Basis. Contribution of Working Group I to the Fifth Assessment Report of the Intergovernmental Panel on Climate Change, edited by: Stocker, T. F., Qin, D., Plattner, G.-K., Tignor, M., Allen, S. K., Boschung, J., Nauels, A., Xia, Y., Bex V., and Midgley P. M., Cambridge University Press, Cambridge, United Kingdom and New York, NY, USA, 571–657, 2013.

Bréon, F.-M., Tanré, D., and Generoso, S.: Aerosol effect on cloud droplet size monitored by satellite, Science, 295, 834–838, L11801, doi:10.1126/science.1066434, 2002.

Costantino, L. and Bréon, F.-M.: Analysis of aerosol-cloud interaction from multi-sensor satellite observations, Geophys. Res. Lett., 37, L11801, doi:10.1029/2009GL041828, 2010.

Feingold, G.: Modeling of the first indirect effect: Analysis of measurements requirements, Geophys. Res. Lett., 30, 1–4, doi:10.1029/2003GL017967, 1997.

Fisher, R.: Statistical methods for research workers, Hafner, New York, 1958.

Grandey, B. S. and Stier, P.: A critical look at spatial scale choices in satellite-based aerosol indirect effect studies, Atmos. Chem. Phys., 10, 11459–11470, doi:10.5194/acp-10-11459-2010, 2010.

Jethva, H., Satheesh, S. K., and Srinivasan, J.: Assessment of second-generation MODIS aerosol retrieval (Collection 005) at Kanpur, India, Geophys. Res. Lett., 34, 1944–8007, doi:10.1029/2007GL029647, 2007.

Jones, T. A., Christopher, S. A., and Quaas, J.: A six year satellite-based assessment of the regional variations in aerosol indirect effects, Atmos. Chem. Phys., 9, 4091–4114, doi:10.5194/acp-9-4091-2009, 2009.

Karlsson, K.-G.: A 10 year cloud climatology over scandinavia derived from NOAA advanced very high resolution radiometer imagery, Int. J. Climatol., 23, 1023–1044, doi:10.1002/joc.916, 2003.

Klein, S. A. and Hartmann, D. L.: The seasonal cycle of low stratiform clouds, J. Climate, 6, 1587–1606, doi:10.1175/1520-0442(1993)006<1587:TSCOLS>2.0.CO;2, 1993.

Koren, I., Kaufman, Y. J., Rosenfeld, D., Remer, L. A., and Rudich, Y.: Aerosol invigoration and restructuring of Atlantic convective clouds, Geophys. Res. Lett., 32, L14828, doi:10.1029/2005GL023187, 2005.

Levy, R. C., Remer, L. A., Kleidman, R. G., Mattoo, S., Ichoku, C., Kahn, R., and Eck, T. F.: Global evaluation of the Collection 5 MODIS dark-target aerosol products over land, Atmos. Chem. Phys., 10, 10399–10420, doi:10.5194/acp-10-10399-2010, 2010.

Levy, R. C., Mattoo, S., Munchak, L. A., Remer, L. A., Sayer, A. M., Patadia, F., and Hsu, N. C.: The Collection 6 MODIS aerosol products over land and ocean, Atmos. Meas. Tech., 6, 2989–3034, doi:10.5194/amt-6-2989-2013, 2013.

Levy, R. C., Munchak, L. A., Mattoo, S., Patadia, F., Remer, L. A., and Holz, R. E.: Towards a long-term global aerosol optical depth record: applying a consistent aerosol retrieval algorithm to MODIS and VIIRS-observed reflectance, Atmos. Meas. Tech., 8, 4083–4110, doi:10.5194/amt-8-4083-2015, 2015.

Lihavainen, H., Kerminen, V.-M., and Remer, L. A.: Aerosol-cloud interaction determined by both in situ and satellite data over a northern high-latitude site, Atmos. Chem. Phys., 10, 10987–10995, doi:10.5194/acp-10-10987-2010, 2010.

Matsui, T., Masunaga, H., Kreidenweis, S. M., Pielke, R. A., Tao, W.-K., Chin, M., and Kaufman, Y. J.: Satellite-based assessment of marine low cloud variability associated with aerosol, atmospheric stability, and dyurnal cycle, J. Geophys. Res., 111, D17204, doi:10.1029/2005JD006097, 2006.

McCominsky, A. and Feingold, G.: Quantifying error in the radiative forcing of the first aerosol effect, Geophys. Res. Lett., 35, L02810, doi:10.1029/2007GL032667, 2008.

McFiggans, G., Artaxo, P., Baltensperger, U., Coe, H., Facchini, M. C., Feingold, G., Fuzzi, S., Gysel, M., Laaksonen, A., Lohmann, U., Mentel, T. F., Murphy, D. M., O'Dowd, C. D., Snider, J. R., and Weingartner, E.: The effect of physical and chemical aerosol properties on warm cloud droplet activation, Atmos. Chem. Phys., 6, 2593–2649, doi:10.5194/acp-6-2593-2006, 2006.

Melin, F., Zibordi, G., Carlund, T., Holben, B., and Stefan, S.: Validation of SeaWiFS and MODIS Aqua/Terra aerosol products in coastal regions of European marginal seas, Oceanologia, 55, 27–51, doi:10.5697/oc.55-1.027, 2013.

Mielonen, T., Levy, R. C., Aaltonen, V., Komppula, M., de Leeuw, G., Huttunen, J., Lihavainen, H., Kolmonen, P., Lehtinen, K. E. J., and Arola, A.: Evaluating the assumptions of surface reflectance and aerosol type selection within the MODIS aerosol retrieval over land: the problem of dust type selection, Atmos. Meas. Tech., 4, 201–214, doi:10.5194/amt-4-201-2011, 2011.

Myhre, G., Stordal, F., Johnsrud, M., Kaufman, Y. J., Rosenfeld, D., Storelvmo, T., Kristjansson, J. E., Berntsen, T. K., Myhre, A., and Isaksen, I. S. A.: Aerosol-cloud interaction inferred from MODIS satellite data and global aerosol models, Atmos. Chem. Phys., 7, 3081–3101, doi:10.5194/acp-7-3081-2007, 2007.

Nakajima, T., Higurashi, A., Kawamoto, K., and Penner, J. E.: A possible correlation between satellite-derived cloud and aerosol microphysical parameters, Geophys. Res. Lett., 28, 1171–1174, 2001.

Ou, S., Liou, K., Hsu, N., and Tsay, S.: Satellite remote sensing of dust aerosol indirect effects on cloud formation over Eastern Asia, Int. J. Remote Sens., 33, 7257–7272, doi:10.1080/01431161.2012.700135, 2013.

Rodriguez, E., Toledano, C., Cachorro, V. E., Oritz, P., Stebel, K., Berjón, A., Blindheim, S., Gausa, M., and de Frutos, A. M.: Aerosol characterization at the sub-arctic site Andenes (69° N, 16° E), by the analysis of columnar optical properties, Q. J. Roy. Meteor. Soc., 138, 471–482, doi:10.1002/qj.921, 2012.

Rosenfeld, D. and Lensky, I. M.: Satellite-based insights into precipitation formation processes in continental and maritime convective clouds, B. Am. Meteorol. Soc., 79, 2457–2476, 1998.

Saponaro, G.: Finnish Meteorological Institute, MODIS Atmosphere L3 Daily Gridded Product, available at: https://ladsweb.nascom.nasa.gov/search/, last access: 15 July 2015a.

Saponaro, G.: Finnish Meteorological Institute, ERA-Interim reanalysis data set, available at: http://www.ecmwf.int/en/research/climate-reanalysis/browse-reanalysis-datasets, last access: 28 September 2015b.

Sayer, A. M., Munchak, L. A., Hsu, N. C., Levy, R. C., Bettenhausen, C., and Jeong, M.-J.: MODIS Collection 6 aerosol products: Comparison between Aqua's e-Deep Blue, Dark Target, and "merged" data sets, and usage recommendations, J. Geophys. Res.-Atmos., 119, 13965–13989, doi:10.1002/2014JD022453, 2014.

Sekiguchi, M., Nakajima, T., Suzuki, K., Kawamoto, K., Higurashi, A., Rosenfeld, D., Sano, I., and Mukai, S.: A study of the direct and indirect effects of aerosols using global satellite data sets of aerosols and cloud parameters, J. Geophys. Res.-Atmos., 108, 4699, doi:10.1029/2002JD003359, 2003.

Sporre, M. K., Swietlicki, E., Glantz, P., and Kulmala, M.: A long-term satellite study of aerosol effects on convective clouds in Nordic background air, Atmos. Chem. Phys., 14, 2203–2217, doi:10.5194/acp-14-2203-2014, 2014a.

Submitted to
Atmospheric Chemistry and Physics Discussions
doi:10.5194/acp-2019-631

https://doi.org/10.5194/acp-2019-631
Preprint. Discussion started: 13 September 2019

Atmospheric Chemistry and Physics Discussions

Evaluation of aerosol and cloud properties in three climate models using MODIS observations and its corresponding COSP simulator, and their application in aerosol-cloud interaction

Giulia Saponaro[1], Moa K. Sporre[2], David Neubauer[3], Harri Kokkola[1], Pekka Kolmonen[1], Larisa Sogacheva[1], Antti Arola[1], Gerrit de Leeuw[1], Inger H.H. Karset[2], Ari Laaksonen[1], and Ulrike Lohmann[3]

[1]Finnish Meteorological Institute, P.O. Box 503 FI-00101 Helsinki
[2]Department of Geosciences, University of Oslo, Norway
[3]Institute for Atmospheric and Climate Science, ETH Zurich, Zurich, 8092, Switzerland

Correspondence to: Giulia Saponaro (giulia.saponaro@fmi.fi)

Abstract.

The evaluation of modeling diagnostics with appropriate observations is an important task that establishes the capabilities and reliability of models. In this study we compare aerosol and cloud properties obtained from three different climate models ECHAM-HAM, ECHAM-HAM-SALSA, and NorESM with satellite observations using MOderate Resolution Imaging Spectrometer (MODIS) data. The simulator MODIS-COSP version 1.4 was implemented into the climate models to obtain MODIS-like cloud diagnostics, thus enabling model to model and model to satellite comparisons. Cloud droplet number concentrations (CDNC) are derived identically from MODIS-COSP simulated and MODIS-retrieved values of cloud optical depth and effective radius. For CDNC, the models capture the observed spatial distribution of higher values typically found near the coasts, downwind of the major continents, and lower values over the remote ocean and land areas. However, the COSP-simulated CDNC values are higher than those observed, whilst the direct model CDNC output is significantly lower than the MODIS-COSP diagnostics. NorESM produces large spatial biases for ice cloud properties and thick clouds over land. Despite having identical cloud modules, ECHAM-HAM and ECHAM-HAM-SALSA diverge in their representation of spatial and vertical distribution of clouds. From the spatial distributions of aerosol optical depth (AOD) and aerosol index (AI), we find that NorESM shows large biases

https://doi.org/10.5194/acp-2019-631
Preprint. Discussion started: 13 September 2019

Atmospheric Chemistry and Physics Discussions

for AOD over bright land surfaces, while discrepancies between ECHAM-HAM and ECHAM-HAM-SALSA can be observed mainly over oceans. Overall, the AIs from the different models are in good agreement globally, with higher negative biases on the Northern Hemisphere. We computed the aerosol-cloud interactions as the sensitivity of dln(CDNC)/dln(AI) on a global scale. However, one year of data may be considered not enough to assess the similarity or dissimilarities of the models due to large temporal variability in cloud properties. This study shows how simulators facilitate the evaluation of cloud properties and expose model deficiencies which are necessary steps to further improve the parametrization in climate models.

1 Introduction

A climate model is a powerful tool for investigating the response of the climate system to various forcings, enabling climate forecasts on seasonal to decadal time scales, and therefore can be used for estimating projections of the future climate over the coming centuries based on future greenhouse gas and aerosol forcing scenarios (Flato, 2011). Based on physical principles, climate models reproduce many key aspects of the observed climate and primarily aid to understand the dynamics of the physical components of the climate systems.

The evaluation of modeling diagnostics is an important task that establishes the capabilities and reliability of models. When key properties of the atmosphere (e.g., clouds, aerosols) are considered, the model assessment is relevant to assure that the climate model correctly captures key features of the climate system. The interest in the reliability of climate models reaches outside the scientific community, as these simulations will form the basis for future climate assessments and negotiations. Therefore, understanding the level of reliability is a necessary step to strengthen the robustness of climate projections and, if necessary, improve the model parametrizations for the relevant processes.

For the evaluation of parametrizations of aerosol indirect effects in global models, satellite data have been proven to be useful (Quaas et al., 2009; Boucher et al., 2013) as they provide large spatial coverage at suitable temporal resolution. Satellite instruments measure the intensity of radiation coming from a particular direction in a selected wavelength range. From the observed radiances, the geophysical quantities are then inferred by inverse modeling using a retrieval algorithm.

https://doi.org/10.5194/acp-2019-631
Preprint. Discussion started: 13 September 2019

Atmospheric Chemistry and Physics Discussions

The compensation of modeling errors, the intrinsic uncertainties of observational data, and the possible discrepant definitions of variables between models and observational data are major issues affecting the crucial task of model evaluation. For that, satellite simulators have been developed to mimic the retrieval of observational data and to avoid ambiguities in the definition of variables mentioned above. Simulators recreate what the satellite would retrieve when observing the modeled atmosphere. By reprocessing model fields using radiative transfer calculations, they generate physical quantities fully consistent with the satellite retrievals. By including microphysical assumptions, which usually differ between models, inconsistencies in the simulators are avoided. Hence, simulators represent a robust and consistent approach not only for the application of satellite data to evaluate models, but also for model-to-model comparisons. Simulators have been widely used, and their implementation in several models enables intercomparison studies on atmospheric variables, such as clouds, aerosols (Quaas et al., 2009; Williams and Bodas-Salcedo, 2017; Zhang et al., 2010; Luo et al., 2017), and upper atmospheric humidity (Bodas-Salcedo et al., 2011).

Two prominent examples of simulators are the International Satellite Cloud Climatology Project, ISCCP, (Klein and Webb, 2009; Yu et al., 1996) and the CFMIP (Cloud Feedback Model Intercomparison Project) Observation Simulator Package, COSP (Bodas-Salcedo et al., 2011). CFMIP is part of The Coupled Model Intercomparison Project (CMIP) (Eyring et al., 2016b; Webb et al., 2017), which is a framework providing the modeling community with guidelines for the development, tuning and evaluation of models (Eyring et al., 2016a, c). COSP is a software tool developed within the CFMIP (Webb et al., 2017) which extracts parameters for several spaceborne active (CALIOP, CPR) and passive (MISR, MODIS) sensors.

In this study the COSP version 1.4 was implemented in three climate models, namely ECHAM-HAM, ECHAM-HAM-SALSA and NorESM, and the diagnostic outputs of the MODIS simulator were compared to MODIS observational data collected during the year 2008. The main goal of this study is to evaluate the models' capability to realistically represent clouds by employing MODIS satellite observations and its corresponding COSP simulator. A secondary goal of the study is to estimate the aerosol-cloud interaction (ACI) through the use of cloud droplet number concentration (CDNC) derived from observed and COSP simulated values of cloud optical thickness and effective radius. Also known as the first aerosol indirect effect (AIE) or sensitivity, the ACI is as an indicator ratio defined as the change in an observable cloud property (e.g., cloud optical depth, cloud effective radius, cloud droplet number

https://doi.org/10.5194/acp-2019-631
Preprint. Discussion started: 13 September 2019


Atmospheric Chemistry and Physics Discussions

concentration) to a change in a cloud condensation nuclei proxy (e.g. aerosol optical depth, aerosol index, or aerosol particle number concentration). Originally introduced by Twomey (1977), the topic of ACI is still a major uncertainty in understanding climate change (e.g. Lohmann et al., 2007; Quaas et al., 2009; Storelvmo, 2012; Flato et al., 2013; Lee et al., 2016)). The analysis of aerosol-cloud interaction has been reported in literature by a variety of methods: studies presenting results from global scales (Feingold et al., 2001; Quaas et al., 2010) to regional scales (e.g. Saponaro et al., 2017; Ban-Weiss et al., 2014; Liu et al., 2017, 2018) and in-situ observations (e.g. Sporre et al., 2014), using different approaches, i.e. observations from satellites, airborne and ground based instrumentation, or modelling.

The choice of observations and spatial scale of a study presents intrinsic uncertainties when quantifying aerosol-cloud interactions, and some of them relate to spatial or temporal limitations or artifacts (McComiskey and Feingold, 2012). When considering satellite observations, cloud and aerosols properties are provided at a quite comprehensive spatial and temporal coverage; however several aspects bring challenges in the analysis of these observations. The primary artifacts known to affect satellite estimation of aerosol-cloud interactions are related to (1) the inability of untangling aerosol and cloud retrievals from meteorology (e.g. aerosol humidification, entrainment, cloud regimes dependency), (2) inaccuracies in the retrieval algorithms (e.g. twilight zone, contamination, statistical aggregation) and (3) assumptions in the retrieval algorithms (Koren et al., 2007; Oreopoulos et al., 2017; Christensen et al., 2017; Wen et al., 2007).

In this work, the Cloud Feedback Model Intercomparison Project (CFMIP) Observation Simulator Package (COSP) (Bodas-Salcedo et al., 2011) is implemented in three climate models to obtain satellite-like diagnostics that enable a direct comparison with satellite retrieval fields. In particular, we focus on liquid cloud properties, which are used to derived CDNC. Cloud droplet number concentration is computed for both satellite observations and satellite-simulated values in a consistent way using an algorithm presented in Bennartz (2007). Aerosol-cloud interactions (ACI) are quantified by dln(CDNC)/dln(AI). By considering the changes in CDNC, it is possible to isolate the microphysical component of the ACI without the need for constraining the liquid water path.

In Section 2 we provide details of the MODIS data, the models, and the COSP simulator. Section 3 presents the methods used in the analysis of the data. The evaluation of the simulator cloud diagnostics with MODIS satellite data on a global scale is pre-

https://doi.org/10.5194/acp-2019-631
Preprint. Discussion started: 13 September 2019


Atmospheric Chemistry and Physics Discussions

sented in subsections 4.1 and 4.2, while the ACI results are shown in subsection 4.3. Conclusions are summarised in Section 5.

2 Data

2.1 MODIS

The Moderate Resolution Imaging Spectrometer (MODIS) is a 36-channel radiometer flying aboard the Terra and Aqua platforms since 2000 and 2002, respectively, which views the entire Earth's surface every 1 to 2 days, thus representing an extensive data set of global Earth observations. MODIS delivers a wide range of atmospheric products including aerosol properties, water vapour, cloud properties, and atmospheric stability variables.

We consider data for the year 2008 from MODIS-Aqua since its equatorial crossing time (13:30 local time) ensures a more complete development of the cloud during its daily cycle. MODIS Level-1 (L1) products are geo-located brightness and temperature values, which are elaborated into geophysical data products at Level-2 (L2), and aggregated onto a uniform space-time grid at Level-3 (L3). We used the latest Collection 6.1 daily MODIS/Aqua MYD08L3, which is a regular gridded Level-3 daily global product (Hubanks et al., 2016). It contains daily 1° x 1° gridded average values of atmospheric aerosols properties and cloud optical and physical properties, along with a suite of statistical quantities, which are derived from the corresponding L2 atmosphere data product. The dataset is limited to observations made during daytime, as these contain a richer set of retrievals and better accuracy in cloud detection.

The Level-2 MODIS aerosol products provide information regarding the aerosol loading and aerosol properties over cloud-, snow-, and ice-free land and ocean surfaces at a spatial resolution of 10 km x 10 km. The primary aerosol product is the aerosol optical depth (AOD), derived globally at the wavelength of 550 nm, while the other parameters accounting for the aerosol size distribution, such as the Ångström exponent (AE) or fine-mode aerosol optical depth, are only derived over ocean (Levy et al., 2013). Additionally, the aerosol index (AI) can be derived by multiplying AOD by AE. The MODIS aerosol products have been extensively validated using highly-accurate observations made by the Aerosol Robotic Network (AERONET) (Sayer et al., 2014) showing good agreement with in-situ measurements. The uncertainty in MODIS retrievals of AOD from validation studies (Levy et al., 2007) was quantified at $0.03 + 0.05 \times \tau_A$ over ocean and $0.05 + 0.15 \times \tau_A$ over land, where τ_A is the refer-

https://doi.org/10.5194/acp-2019-631
Preprint. Discussion started: 13 September 2019


Atmospheric Chemistry and Physics Discussions

ence AOD value from AERONET. In this study we primarily focus on the analysis of liquid cloud properties. However, MODIS aerosol data (Levy et al., 2013) is needed to assess aerosol-cloud interactions.

The Level-2 MODIS physical and optical cloud properties are derived trough a combination of infrared emission and shortwave reflectance techniques at a spatial resolution varying from 1 km to 5 km, depending on the parameter (Platnick et al., 2017). Collection 6.1, which is used in this work, provides cloud optical parameters divided into different products accordingly to the cloud phase and retrieved at wavelengths of 2.1 μm, at 1.6 μm and 3.7 μm (Hubanks et al., 2016; Platnick et al., 2017). As the COSP simulator simulates cloud properties at 2.1 μm, the same wavelength is selected in the MODIS observations for both ice and liquid clouds. MODIS offers two scientific L3 cloud fractions datasets, namely the cloud mask cloud fraction and the cloud optical properties cloud fraction (datasets with prefix 'Cloud Fraction' and 'Cloud Retrieval Fraction', respectively). From now on we refer to the cloud mask cloud fraction as CF, and to the cloud optical properties cloud fraction as COP CF. While the CF counts the proportion of the pixels classified by the cloud mask as cloudy or partly cloudy, the COP CF counts the proportion of the pixels for which cloud optical properties have been successfully derived. The main difference between these two definitions roots in the approach of handling partly cloudy pixels. As the task of the cloud mask is to identify fully clear pixels, partly cloudy pixels are counted as cloudy in CF, while in the COP CF they are counted as clear because the retrieval algorithm aims to include only fully cloudy pixels. The different treatment of partly cloudy pixels directly impacts the number of cloud pixels, and consequently many other retrieved cloud properties. Therefore differences are expected in our results and as already reported by Pincus et al. (2012). MODIS observations are here used as a reference dataset. However, MODIS data contains its own errors and limitations. Many studies compared MODIS liquid cloud microphysical properties with in-situ and airborne campaign measurements finding strong correlations for COT but a systematic significant overestimation of MODIS cloud-top droplet effective radius (CER) for marine stratus and stratus cumulus clouds due to possible instrument limitation and algorithm retrieval assumptions (e.g. Noble and Hudson, 2015; Painemal and Zuidema, 2011; Min et al., 2012). A good CER correlation between MODIS and in-situ data was however observed by e.g. Preißler et al. (2016) for marine warm stratiform clouds at higher latitudes. A bias in MODIS CER is propagated into the derivation of MODIS LWP, which also shows a positive bias with respect to the observations (e.g. King

https://doi.org/10.5194/acp-2019-631
Preprint. Discussion started: 13 September 2019

et al., 2013; Noble and Hudson, 2015; Painemal and Zuidema, 2011; Min et al., 2012). Overestimated MODIS LWP were also found over a high-latitude measurement land site (e.g. Sporre et al., 2016) for clouds from all altitudes in the atmosphere. Marchant et al. (2016) showed that the C6 cloud phase discrimination algorithm is significantly improved over C5 but some situations continue to be problematic over regions located at higher latitudes (i.e., polar areas, Greenland, and large desert areas).

In this study, we derive CDNC following the method presented in Bennartz (2007) and this additional cloud parameter is used in the computation of ACI. More information is provided in Sect. 3.2.

2.2 COSP - The CFMIP Observation Software Package

The simulator COSP (Bodas-Salcedo et al., 2011) is a publicly available software package (https://www.earthsystemcog.org/projects/cfmip/) developed by the CMIP community (Webb et al., 2017). It consists of a module coded in FORTRAN90 which simulates cloud properties and can be implement in any model.

The simulator's working principle is based on using climate model fields to mimic radiances to which a retrieval algorithm is applied to obtain satellite-like fields for the comparison with satellite observations.

This process is summed up in three main phases. As model grids are very coarse ($\sim$100 km), the model fields are first down-scaled: each model gridbox mean profile is broken into subcolumns, whose size is more representative of a satellite retrieval area ($\sim$10 km). Next, each sub-column profile is processed by a forward radiative transfer model to create synthetic radiances at the satellite retrieval area-level. The last step aggregates the simulator outputs to produce diagnostics (for example temporal averages and histograms) statistically comparable to the real satellite observations. A comprehensive explanation about the methodology and results of the COSP MODIS simulator is presented in Pincus et al. (2012).

2.3 Models

2.3.1 ECHAM-HAM

ECHAM-HAMMOZ (echam6.3-ham2.3-moz1.0) is a global aerosol-chemistry climate model (Schultz et al., 2018; Kokkola et al., 2018; Tegen et al., 2019; Neubauer et al., 2019) where ECHAM refers to the atmospheric model of the model configuration, HAM to the aerosol model, and MOZ to the chemistry model. In this study only

https://doi.org/10.5194/acp-2019-631
Preprint. Discussion started: 13 September 2019

the global aerosol-climate model part of ECHAM-HAMMOZ is used. Instead of the comprehensive MOZ chemistry model, sulphate chemistry is calculated in HAM for which the details have been given by Zhang et al. (2012) and references therein.

ECHAM-HAMMOZ, referred to as ECHAM-HAM, consists of the general circulation model ECHAM (Stevens et al., 2013) coupled to the latest version of the aerosol module HAM (Tegen et al., 2019) and uses a two-moment cloud microphysics scheme that includes prognostic equations for the cloud droplet and ice crystal number concentrations as well as cloud water and cloud ice (Lohmann and Diehl, 2006; Lohmann et al., 2007, 2008; Lohmann and Hoose, 2009).

Next to the two-moment cloud microphysics scheme the stratiform cloud scheme includes an empirical cloud cover scheme (Sundqvist et al., 1989).

The cirrus scheme is based on Kärcher and Lohmann (2002) and described in Lohmann et al. (2008), cloud droplet activation uses the Abdul-Razzak and Ghan (2000) parameterization, the autoconversion of cloud droplets to rain follows the method from Khairoutdinov and Kogan (2000), immersion and contact freezing in mixed-phase clouds follows the scheme from Lohmann and Diehl (2006), and cumulus convection is represented by the parameterization of Tiedtke (1989) with modifications developed by Nordeng for deep convection.

Simulations were performed at T63 ($1.9° \times 1.9°$) spatial resolution using 31 vertical levels (L31) and COSP v1.4. Horizontal winds and surface pressure were nudged towards the ERA-Interim (Dee et al., 2011) reanalysis for 2008, and observed sea surface temperatures and sea ice cover for 2008 were used (Taylor et al., 2000). Three-hourly instantaneous output was used. The COSP output is almost instantaneous as it is the three hour average over two hour time steps i.e. 50% of the values are instantaneous and the other 50% are an average over two time steps.

2.3.2 ECHAM-HAM-SALSA

ECHAM-HAM-SALSA is identical to the ECHAM-HAM setup (echam6.3-ham2.3-moz1.0), with the difference that the sectional aerosol module SALSA (Kokkola et al., 2008, 2018) is used instead of the modal model M7 used in the ECHAM-HAM setup. SALSA calculates the aerosol microphysical processes: nucleation, coagulation, condensation, and hydration. In this setup, the aerosol model HAM applies also the sectional scheme for the rest of the aerosol processes, i.e. emissions, removal, aerosol radiative properties, and aerosol-cloud interactions. In addition to differences in the aerosol size distribution scheme, also the wet deposition schemes differ between

https://doi.org/10.5194/acp-2019-631
Preprint. Discussion started: 13 September 2019

the ECHAM-HAM and ECHAM-HAM-SALSA setups. In addition, while ECHAM-HAM uses the cloud activation parameterization for modal models (Abdul-Razzak and Ghan, 2000), SALSA uses the activation parameterization for the sectional representation (Abdul-Razzak and Ghan, 2002). Along with the details of these differences, the implementation and the evaluation of SALSA with the ECHAM-HAMMOZ model version which is used in this study has been presented by Kokkola et al. (2018).

Similarly to ECHAM-HAM, simulations were performed at T63 ($1.9° \times 1.9°$) spatial resolution using 47 vertical levels (L47) and COSP v1.4. Horizontal winds and surface pressure were nudged towards the ERA-Interim (Dee et al., 2011) reanalysis for 2008, and observed sea surface temperatures and sea ice cover for 2008 were used (http://www-pcmdi.llnl.gov/projects/amip/). Three-hourly instantaneous output was used.

2.3.3 NorESM

The Norwegian Earth System Model (NorESM) (Kirkevåg et al., 2013; Bentsen et al., 2013; Iversen et al., 2013) is largely based on the Community Earth System Model (CESM) model (http://www.cesm.ucar.edu) but uses a different ocean model and a different aerosol scheme in the Community Atmospheric Model (CAM) (Neale et al., 2010).

The aerosol scheme in the NorESM version of CAM, called CAM-Oslo, can be described as an aerosol life cycle scheme which calculates production tagged mass concentrations of different aerosol species (Kirkevåg et al., 2018).

In the current simulations, the NorESM model was run with the CAM-Oslo version 5.3 (Kirkevåg et al., 2018) which is configured with the microphysical two moment scheme MG1.5 (Morrison and Gettelman, 2008; Gettelman et al., 2015) for stratiform clouds. The scheme includes prognostic equations for liquid (mass and number) and ice (mass and number) and a version of the Khairoutdinov and Kogan (2000) autoconversion scheme where subgrid variability of cloud water (Morrison and Gettelman, 2008) has been included. The aerosol activation into cloud droplets is based on Abdul-Razzak and Ghan (2000) and the heterogeneous freezing in CAM5.3-Oslo is based on Wang et al. (2014) with a correction applied to the contact angle model (Kirkevåg et al., 2018). Moreover, CAM5.3-Oslo has a shallow convection scheme (Park and Bretherton, 2009) and a deep convection scheme (Zhang and McFarlane, 1995). The simulation was run with the Community Land Model (CLM) version 4.5 (Oleson et al.) with satellite phenology. Included in CLM is the Model of Emissions

https://doi.org/10.5194/acp-2019-631
Preprint. Discussion started: 13 September 2019


Atmospheric Chemistry and Physics Discussions

of Gases and Aerosols from Nature (MEGAN) version 2.1 (Guenther et al., 2012) which interactively calculates the emissions of biogenic volatile organic vapors. Both isoprene and monoterpenes take part in the formation of secondary organic aerosol in CAM5.3-Oslo. The sea surface temperatures and sea ice in the simulation were prescribed monthly averages for the years 1982-2001.

The resolution for the simulation was $0.9^\circ \times 1.25^\circ$ and the surface pressures as well as horizontal winds were nudged against ERA-Interim reanalysis data (Berrisford et al., 2011) from 2008. CAM-Oslo was run with COSP version 1.4 producing three-hourly instantaneous outputs.

3 Methods

3.1 Post-processing of the datasets

The comparison of satellite retrievals and model variables is not always straightforward. Satellite-retrieved physical quantities may be derived slightly differently than the corresponding parameters in the model, and differences can be attributed to discrepancies in the retrieved quantities viewed from space versus model fields (i.e. retrieval assumptions, sensor limitations, spatial resolution) (Bodas-Salcedo et al., 2011). In this study we aim at highlighting the differences between observations and models which stem from different aerosol and cloud physical parametrization by using the COSP satellite simulator. Satellite simulators, such as COSP, represent a compromise between model fields and retrieved fields. Simulators use model fields to reproduce what the satellite sensor would see if the atmosphere had the clouds of a climate model. By taking the characteristics of the MODIS instrument into account, COSP generates simulated fields of cloud parameters which can be quantitatively compared to MODIS observations. The COSP diagnostics are then successively aggregated to the simulator outputs and are provided at the original model resolution. Prior to their intercomparison, post-processing of the COSP diagnostics and satellite data is necessary for obtaining a robust evaluation. COSP-derived parameters are in the original model resolution and represent grid-averaged values. As MODIS observations are grid values representative only of in-cloud pixels, the COSP grid-averaged values are divided by the corresponding cloud fractions. The three-hour outputs from the models were aggregated to daily averages and successively re-gridded and co-located by linear interpolation onto the finer satellite regular grid of $1^\circ \times 1^\circ$. Each grid cell point of cloud variables from MODIS observations and MODIS diagnostics was screened

https://doi.org/10.5194/acp-2019-631
Preprint. Discussion started: 13 September 2019


Atmospheric Chemistry and Physics Discussions

using a minimum threshold of 30% of cloud fraction to minimize the source of errors introduced by the retrieval algorithm and to ensure the existence of large-scale clouds. The screening does not introduce a significant loss in the data pool and provide grounds for a robust intercomparison as also shown in Bennartz (2007) and Ban-Weiss et al. (2014). For each time step, only grid points having a valid observation simultaneously in each one of the four datasets were included in the final dataset for the statistical analysis.

The MODIS algorithm retrieves cloud properties in the proximity of the top of a cloud while the direct model outputs provide values through the entire vertical structure of a simulated atmospheric column. To overcome this issue, when comparing the direct model output CDNC and satellite-derived CDNC, for each grid box we selected the CDNC value at the top of the modeled cloud. Additionally, we selected only grid-points with temperature T > 273° K to exclude mixed-phase and ice clouds.

Note that all discussed cloud parameter are diagnosed using satellite simulators and are compared to the corresponding MODIS satellite observations. However, we use two direct model diagnostics in the study:

- AOD, which is used to derive the AI, a proxy for cloud condensation nuclei for the computation of ACI
- $\mathrm{CDNC}_{\mathrm{direct}}$, which is compared with COSP-simulated and MODIS-derived estimates

3.2 Cloud droplet number concentration (CDNC)

The CDNC were derived from CER and COT from MODIS observations and COSP simulations by combining Eqs. (6) and (9) from Bennartz and Rausch (2017) in the following equation:

$$\mathrm{CDNC} = \gamma \cdot \mathrm{COT}^{0.5} \cdot \mathrm{CER}^{-2.5},$$

where COT is cloud optical thickness, CER is the cloud droplet effective radius and γ = 1.37 · 10^{-5} $\mathrm{m}^{0.5}$ (Quaas et al., 2006). The assumption of not accounting for temperature effect and setting γ as a bulk costant applies rather well to the stratiform clouds in the marine boundary layer but less so for convective clouds (Bennartz, 2007; Rausch et al., 2010).

https://doi.org/10.5194/acp-2019-631
Preprint. Discussion started: 13 September 2019


Atmospheric Chemistry and Physics Discussions

3.3 Aerosol-cloud-interaction (ACI) computation

The aerosol-cloud-interaction (ACI) is defined here as the change in the selected cloud property, CDNC, to a change in AI, which is used here as a proxy for cloud condensation nuclei (CCN):

$$\mathrm{ACI} = \frac{\mathrm{dln(CDNC)}}{\mathrm{dln(AI)}}$$

The CDNC was computed from the CER and COT from the COSP-MODIS simulations and MODIS retrievals. Additionally, AI was derived from ECHAM-HAM, ECHAM-HAM-SALSA, and NorESM MODIS-COSP diagnostics, and MODIS satellite observations following Feingold et al. (2001). The mean values and standard deviations of the parameters involved in the computation of ACI are presented in Table 1. We discarded pixels retrieved when liquid cloud fraction is $\leq$0.3 to reduce noise-contamination and to focus on large-scale clouds. The screened parameters were used to derive CDNC.

The ACI was calculated globally for each season. When computing ACI for large areas, the ACI of each gridbox needs to be weighted by the corresponding number of data points (Grandey and Stier, 2010). This step was included in the post-processing of the datasets.

4 Results

4.1 Global bias distributions

In this section we compare on a global scale aerosol and cloud properties from the three models by subtracting MODIS retrievals from the modeled COSP diagnostics. From now on we will refer to the difference between the simulated parameters and MODIS retrieved values using the term bias.

Overall, the spatial distributions of the biases always show large discrepancies around the polar and ice-covered areas, such as Greenland and Antarctica. Over these areas large discrepancies are expected due to the inaccuracy of the MODIS retrieval algorithm due to viewing geometry (i.e. large zenith or viewing angles) and to correctly classify opaque clouds, snow/ice surfaces and optically thin clouds over really bright or warm surfaces (Marchant et al., 2016).

https://doi.org/10.5194/acp-2019-631
Preprint. Discussion started: 13 September 2019


Atmospheric Chemistry and Physics Discussions

Figure 1 presents the differences between the MODIS-COSP cloud fraction diagnostics and COP CF for ice clouds CF_{ice} (Fig. 1b-d), and liquid clouds CF_{liq} (Fig. 1f-h), as well as the differences between MODIS total COP CF (Fig. 1j-l), and CF (Fig. 1n-p). Additionally, for each comparison the MODIS spatial distribution is presented as reference (Fig. 1a,e,i,m). It was already highlighted in section 2.1 that the cloud fraction retrieved from the optical properties (CF_{ice}, CF_{liq} and COP CF) excludes partly cloudy pixels, representing a limitation in the comparison of the data. Thus, lower values of MODIS COP cloud fractions are expected. A widespread positive bias is observed for CF_{ice} and CF_{liq}, indicating higher values of the COSP-simulated cloud fractions than the MODIS observations. Prevalent cloud regimes can be recognized in the bias distributions. ECHAM-HAM and ECHAM-HAM-SALSA well represent the amount of ice clouds which are generally found in the intertropical convergence zone (ITCZ) and the marine subtropical stratocumulus and stratus regions, whereas liquid clouds are better represented over land areas and in the subtropical stratocumulus region. NorESM shows positive biases for ice cloud amount over stratus clouds regions and around the ITCZ, but shows smaller biases for liquid stratus cloud regimes than ECHAM-HAM and ECHAM-HAM-SALSA

The total cloud fraction bias shows a positive bias between the MODIS-COSP CF simulated by the three models and MODIS COP CF (Fig. 1j-l) and a negative bias when MODIS CF is considered (Fig. 1n-p). Consequently, MODIS CF is higher than the MODIS COP CF product. This outcome is to be expected, and possibly originates from the different treatment in the MODIS algorithm of partly cloudy pixels in the computation of CF and COP CF, as discussed in section 2.1. Additionally, all models underestimate CF in marine subtropical stratocumulus regions.

The spatial distribution of the cloud physical and optical properties is remarkably similar among the datasets with the exception of CER_{ice}, IWP (Fig. 2 d and l) and COT (Fig. 3g,k) for NorESM. These strong biases are explained by the fact that in the NorESM COSP 1.4 implementation code includes radiative active snow in the computation of the effective radius and optical thickness of ice clouds. However, this does not affect the properties of liquid clouds.

CER_{ice} and IWP are underestimated in ECHAM-HAM and ECHAM-HAM-SALSA. This is likely caused by the cirrus scheme which does not account for heterogenous nucleation or pre-existing ice crystals during formation of cirrus clouds (Neubauer et al., 2019; Lohmann and Neubauer, 2018). Interestingly, dissimilarities can also be observed between ECHAM-HAM and ECHAM-HAM-SALSA, despite the fact that

https://doi.org/10.5194/acp-2019-631
Preprint. Discussion started: 13 September 2019

the models share the same cloud module. ECHAM-HAM CER_{liq} is on average 5μm smaller than in ECHAM-HAM-SALSA in the mid-latitude belt, and ECHAM-HAM-SALSA CER_{liq} is larger around the polar areas (Fig. 2g) and shows a large positive bias for LWP over ocean (Fig. 2o) in comparison to ECHAM-HAM. LWP is also overestimated by NorESM but over land areas (Fig. 2p), while ECHAM-HAM shows a good agreement with MODIS (Fig. 2n).

The evaluation of COT shows homogeneous results and comparable values of root mean square errors (Fig. 3) with the exception of NorESM COT biases for ice and liquid clouds which are particularly high over land. It appears that some tuning parameters, for example the autoconversion parameter, are particularly low and affect the convection scheme by suppressing precipitation, thus creating thick clouds. The comparison of the differences between the biases of ECHAM-HAM and of ECHAM-HAM-SALSA shows localized differences over India, China and Russia for IWP (Fig. 2j,k) and over China for water cloud COT (Fig. 3e,f). These are also regions where aerosol microphysics has a fundamental role as shown in Kokkola et al. (2018). ECHAM-HAM and ECHAM-HAM-SALSA generally overestimate COT. The atmospheric model ECHAM shows a similar estimation when running without an aerosol model. This overestimation has been previouslt reported by Stevens et al. (2013).

Figure 4 shows global biases for CDNC derived from the MODIS retrievals and the COSP diagnostics following the method presented in Sect.3.2 (Fig. 4b-d), and the daily averages of the direct output of the models (Fig. 4e-g). The differences between MODIS-COSP diagnostics and MODIS observations are very clear. Overall the MODIS derived CDNC is lower than that derived from COSP simulated values, but higher than the direct output values. Consequently, the CDNC from direct model output is lower than MODIS-COSP diagnostics, as also found by Ban-Weiss et al. (2014). Possible explanations could be either related to the COSP method for deriving CER_{liq} and COT_{liq} or the approach used for deriving CDNC from CER_{liq} and COT_{liq}. The biases between CDNC COSP-derived and modeled direct values are very different, but within each product the biases are similar, although local differences are observed. For example, the CDNC values from ECHAM-HAM-SALSA are lower in the polar regions and higher in the mid-latitude belt in comparison with the ECHAM-HAM and NorESM diagnostics. Local differences can also be observed in the direct output where ECHAM-HAM-SALSA shows higher values of CDNC over the oceans in the southern Hemisphere (Fig. 4f). A direct comparison of CDNC derived from MODIS-COSP simulated variable and the model CDNC direct outputs is

https://doi.org/10.5194/acp-2019-631
Preprint. Discussion started: 13 September 2019


Atmospheric Chemistry and Physics Discussions

shown in the supplementary material. ECHAM-HAM and ECHAM-HAM-SALSA were run with identical tuning parameter settings which were optimized for ECHAM-HAM. This choice was made to distinguish the differences in aerosol-cloud interactions coming from different aerosol microphysics modules. The differences in CDNC between these two model setups originates from the cloud activation schemes, i.e. for HAM the modal cloud activation scheme of Abdul-Razzak and Ghan (2000) and for HAM-SALSA the sectional cloud activation scheme (Abdul-Razzak and Ghan, 2002). The cloud activation scheme of ECHAM-HAM-SALSA produces a higher number of CDNC than ECHAM-HAM (Fig. 4c) because SALSA microphysics module simulates generally higher number of particles larger than 100 nm in diameter which act as cloud condensation nuclei. Despite the higher CDNC, $CER_{liq.}$ seems to be larger in ECHAM-HAM-SALSA than in ECHAM-HAM which is unexpected when assuming that both model version have similar LWC. This discrepant result may be explained by the fact that in ECHAM-HAM LWC is lower than in ECHAM-HAM-SALSA as a results of a systematically higher IWC. Thus, the CER_{liq} diagnosed by ECHAM-HAM is also smaller despite of less CDNC. Differences in convective detrainment are likely linked with the result. In fact, a higher cloud droplet freezing rates are simulated in ECHAM-HAM-SALSA (except near the Equator) which could suggest reduced sedimentation of ice crystals less condensate being detrained as ice (and more as liquid) in ECHAM-HAM-SALSA than ECHAM-HAM.

Figure 5 presents AOD and AI biases. The values of AI from direct model output and MODIS observations are quite close with an average bias of +0.2. The main divergence is observed in the ECHAM-HAM bias where higher AI values are simulated around the mid-latitude belt. Tegen et al. (2019) found indications that the particle size of mineral dust and sea salt aerosol particles may be too small in ECHAM-HAM. More discrepancies can be observed in the AOD bias: ECHAM-HAM-SALSA AOD values are higher over ocean, and NorESM AOD are much higher over deserts and other bright surfaces (such as Africa and Australia). Other localized distinctions in aerosol loading distribution can be observed over regions which are typically strongly affected by primary emissions (such as the Sahara, India, Southeast Asia, Russia, Canada, central Africa, and South America). The different representation of size distribution, microphysical processing of aerosols and sink processes has a significant effect on the modelled AOD as shown for the aerosol module SALSA2.0 by Kokkola et al. (2018). The overestimation of AOD in the tropical oceans and underestimation

https://doi.org/10.5194/acp-2019-631
Preprint. Discussion started: 13 September 2019

of AOD at higher latitudes and over land in ECHAM-HAM has also been found by Tegen et al. (2019).

4.2 Joint histogram

The analysis of the CTP-COT joint histogram enables to determine how well the data sources represent the vertical cloud structures and regimes. Figure 6 shows the comparison of the simulated and observed global mean cloud fraction as a function of cloud top pressure and cloud optical thickness. ECHAM-HAM and ECHAM-HAM-SALSA (Fig. 6a,b) show a nearly identical result by concentrating a large fraction of clouds at low level (CTP $\leq$ 680 hPa) and in the interval 3.6 $\leq$ COT $\leq$ 23. NorESM (Fig. 6c) also concentrates its largest amount of clouds at low levels in the same COT interval as in Fig. 6a and Fig. 6b, but detects also a higher fraction (about 2-2.5%) of optically thick clouds 9.4 $\leq$ COT $\leq$ 60 throughout the atmosphere. A second cloud fraction peak is observed for optically thin clouds (COT $\leq$ 1.3) at very high levels (180 $\leq$ CTP $\leq$ 310) for NorESM. This bimodal distribution resembles the vertical distribution of the MODIS cloud fraction shown in Fig.6d. The MODIS observations are mostly in the category of high-level clouds (CTP $\leq$ 440 hPa) and low-level clouds (680 hPa $\leq$ CTP). MODIS shows on average more mid-level clouds than NorESM and a higher fraction at low-level for 3.6 $\leq$ COT $\leq$ 23 similarly to ECHAM-HAM and ECHAM-HAM-SALSA. Figure 6e shows the differences in cloud vertical distribution where MODIS is generally having the highest cloud fraction except for mid-level. MODIS also presents the highest percentage of clouds for COT $\geq$ 3.6. NorESM and MODIS detects nearly the same amount of clouds for 1.3 $\leq$ COT $\leq$ 3.6, while for optically very thin clouds (COT $\leq$ 1.3) a good agreement is obtained between all datasets and NorESM shows the highest percentage of cloud fractions.

4.3 Aerosol-cloud interactions

The global daily mean values of CDNC and AI were used to assess how clouds are affected by the changes of the CCN proxy. Uncertainties were computed as the 95% confidence intervals using daily averages. Positive estimates of ACI indicate an increase of CDNC as a function of AI, which could be an indication of the aerosol indirect effects. The potential limitations to this approach are further discussed in Sect. 5.

Figure 7 shows estimates of ACI on a global scale, including both land and ocean, for each season and, separately, for the entire period under study as 'All'. The same

https://doi.org/10.5194/acp-2019-631
Preprint. Discussion started: 13 September 2019

analysis is iterated on a regional scale and presented in the supplementary material (Fig.S4) Error bars are representative of the boundaries of the 95% confidence interval. ACI from the model results is generally positive suggesting that changes in AI are connected with an increase of CDNC and the trend seems to be independent of the time of the year. The modeling ACI estimates are similar in the models; however, the results are statistically indistinguishable owing to fully overlapping confidence bars (Cumming et al., 2007). MODIS ACI estimates show negative values for the winter months (DJF), especially over the Northern Hemisphere (Fig.S4). As the global estimates include land areas, these negative values could be indicative of retrieval biases over bright surfaces (i.e. snow or ice). Furthermore, negative ACI values may be associated with the presence of different types of aerosol (i.e. hydrophobic aerosol such as dust, black carbon) and their proximity to clouds, which may affect or inhibits the growth of cloud droplets (Chen et al.; Jiang et al., 2018; Costantino and Bréon, 2013). Over ocean negative ACI values from MODIS observations have been systematically found over subtropical marine stratuscumulus regions (i.e. N. Atlantic Ocean, N.America, S.Atlantic Ocean). In these regions Chen et al. (2014) found a decrease in LWP with increasing AI for non-precipitating scenes. Additionally, negative ACI values were suggested owing to wet scavenging or mixing of environmental air by entrainment (Ackerman et al., 2004). While both processes affect LWP, CDNC is not necessarily changing. This indicates limits in the derivation of CDNC from retrieved quantities for MODIS. Also water uptake by aerosol particles and effects of meteorology can have a significant impact on the estimation of ACI derived from the relationship between CDNC and AI (Neubauer et al., 2017).

Cloud properties (Fig. 2 and Fig. 3) are more similar for ECHAM-HAM and ECHAM-HAM-SALSA, which share the same atmospheric model, rather than between the two and NorESM. Nevertheless, the ACI estimates show good agreement between the three models and, even more important, with ACI derived from MODIS observations.

5 Summary and Conclusions

The differences between observed and modeled aerosol and cloud properties can be related to many factors, among which are the different parametrizations of aerosol and cloud physical processes in the models, or differences in observation characteristics by satellite, as well as meteorological influences on aerosol-cloud interactions. In this study we focus on the differences due to the physical parametrization of aerosol

https://doi.org/10.5194/acp-2019-631
Preprint. Discussion started: 13 September 2019


Atmospheric Chemistry and Physics Discussions

and cloud properties, and minimize the impact of the other factors. This objective was achieved by using a satellite simulator, which resolves the issue related to the incongruities between model and satellite views, and by nudging modeled winds to meteorological observation, solving the discrepancies between observed and modeled meteorology.

The results show that the aerosol module in a climate model, in our case ECHAM-HAM and ECHAM-HAM-SALSA, has a smaller effect on the simulation of cloud properties than switching to another atmospheric model, NorESM. However, the three models differ from each other in the spatial and vertical representation of clouds. The COSP cloud fraction diagnostics are comparable to MODIS products but the difference between the two MODIS products of total cloud fractions is significant. Despite having identical cloud modules, ECHAM-HAM and ECHAM-HAM-SALSA diverge when comparing liquid water cloud properties yet both fail to represent high level clouds. The discrepancies between ECHAM-HAM and ECHAM-HAM-SALSA may originate from different amounts of activated droplets and different ice nucleation rates. While the NorESM cloud vertical distribution is closer to MODIS, large biases are found globally for cloud droplet size and water content in ice clouds due to the contribution of radiatively active snow (Kay et al., 2012). The inclusion of radiatively active snow in the physical model and the COSP module mitigates the underestimation of model mid-level and high clouds but heavily impacts the magnitude of the global values of the cloud properties in ice clouds.

The differences observed in the simulation of cloud properties are reflected in the estimations of ACI. ACI is generally larger for ECHAM-HAM and NorESM, while being lower for ECHAM-HAM-SALSA and MODIS where the latter is the only dataset leading to negative ACI values possibly owing to the linkages between aerosol and cloud type and their location in the atmosphere.

Although satellite simulators allow robust comparisons, their reliability is flawed when the observational data is not well explained or the simulator itself fails to address specific characteristics. Therefore, their strengths and weaknesses need to be accounted for as to successfully use simulation diagnostics in model-observation comparisons as illustrated in details by Pincus et al. (2012), and Kay et al. (2012) to successfully use simulator diagnostics in model-observation comparisons. For example, simulators have limitations in depicting horizontally heterogeneous cloud regimes as they do not account for sub-pixel clouds which may explain the differences in the detection of small cloud fractions between observations and models. However, simulator

https://doi.org/10.5194/acp-2019-631
Preprint. Discussion started: 13 September 2019


Atmospheric Chemistry and Physics Discussions

and observational errors are here neglected because we considered them to be less important in the explanation of the model biases. The observed biases in the modeled clouds could originate from errors in the model calculation as well from the cloud parametrization; the identification of the specific reasons for these discrepancies is beyond the scope of this study.

The results presented here indicate that the cloud droplet number concentration appears to be more sensitive to changes in aerosols in models than observations and these results are in agreement with many previous studies found in the literature (e.g. Ban-Weiss et al., 2014; Quaas et al., 2004; McComiskey and Feingold, 2012; Penner et al., 2011). Some of the differences in the ACI estimates from satellites and models could be associated with limitations in satellite measurements. For example, the estimates of ACI might suffer from an averaging effect due to the large spatial averages of satellite aerosol and cloud properties. L3 data can introduce spurious relationships between aerosols and cloud properties (e.g. McComiskey and Feingold, 2012; Christensen et al., 2017), and provide a rather limited pool of data samples enabling the analysis only over large regions. This was not explored in this study because we used the same spatial resolution for both the true model estimate and for the satellite-based model estimate for the ACI. Neubauer et al. (2017) performed a detailed study on the impact of meteorology, cloud regimes, aerosol swelling, and wet scavenging on microphysical cloud properties using ECHAM-HAM. The results highlight that a minimum distance between cloud and aerosol gridded data should be taken into account, and that dry aerosols should be selected to reduce the influence of aerosol growth due to humidity. Similarly to our results, Neubauer et al. (2017) find a systematical overestimation of the sensitivity of modeled LWP and CDNC compared to MODIS observations, and often a disagreement in sign in the comparison of cloud parameters. The results suggest that the derivation of CDNC from satellite observations may be limited by entrainment mixing of environmental air or precipitation. Furthermore, the models can not resolve the entrainment mixing at the top of stratocumulus clouds, which puts the LWP sensitivity to aerosol change in the models into question. In conclusion, this study identified limitations and deficiencies in the models, and their acknowledgment is important for the model development process and the correct interpretation of modelling diagnostics. We highlighted many discrepancies in cloud spatial and vertical representations and the results showed that the three models overall similarly represent the stratocumulus cloud regime being underestimate when compared to MODIS. We discovered that IWC is systematically

https://doi.org/10.5194/acp-2019-631
Preprint. Discussion started: 13 September 2019

lower in ECHAM-HAM-SALSA than in ECHAM-HAM due to a higher cloud droplet freezing rate which consecutively triggers a reduced sedimentation of ice clouds. This outcome explains the contradictory result in ECHAM-HAM-SALSA that shows the largest global averages for CER among the models despite having the highest number of CDNC. Further investigation is needed to explain the differences in ice cloud properties between ECHAM-HAM and ECHAM-HAM-SALSA. The clouds simulated by NorESM are too thick over land and this issue is not only seen in COSP-variables but also in the default model output due to a very low autoconversion parameter which caused the suppression of precipitation over land, thus thicker clouds. Additionally, in support to Ban-Weiss et al. (2014), the study revealed that the direct model CDNC is systematically larger than the values derived from COSP-diagnostics and MODIS observation.

Finally, we point out that the model deficiencies identified here may lead to an improvement of model parametrization and to more robust results. As future work, a regional-based analysis would enable a better understanding of the physical processes responsible for the model biases. Additional research should be conducted to evaluate the aerosol-cloud-interaction following the approach suggested by Neubauer et al. (2017). These further steps would potentially benefit the modeling community interested in climate applications.

Data availability. The MODIS satellite data used in this study are publicly available at https://ladsweb.nascom.nasa.gov. ECHAM-HAM data are available from David Neubauer (david.neubauer@env.ethz.ch), ECHAM-HAM-SALSA data are available from Harri Kokkola (harri.kokkola@fmi.fi) and NorESM data from Moa K. Sporre (moa.sporre@nuclear.lu.se).

Author contributions. ECHAM-HAM-SALSA, ECHAM-HAM, and NorESM data (and corresponding descriptive text in Sect. 2.3 Data) were provided by DN, HK, and MS, respectively. IH assisted in setting up the NorESM simulations. GS conducted the data analysis, and wrote the majority of manuscript, except for the sections describing the models. PK, HK, AA participated in reading the results. GL, UL, PS helped to set up the concept idea of the paper. MS, DV, HK, PK, UL and GL contributed to review the manuscript.

Competing interests. No competing interests to declare.

https://doi.org/10.5194/acp-2019-631
Preprint. Discussion started: 13 September 2019

Atmospheric Chemistry and Physics Discussions

Acknowledgements. The research leading to these results has received funding from the European Union's Seventh Framework Programme (FP7/2007-2013) Project BACCHUS under Grant Agreement 603445. We would like to thank Jennifer E. Kay for support in the implementation of COSP1.4 in NorESM. The ECHAM-HAMMOZ model is developed by a consortium composed of ETH Zurich, Max Planck Institut für Meteorologie, Forschungszentrum Jülich, University of Oxford, the Finnish Meteorological Institute and the Leibniz Institute for Tropospheric Research, and managed by the Center for Climate Systems Modeling (C2SM) at ETH Zurich.

https://doi.org/10.5194/acp-2019-631
Preprint. Discussion started: 13 September 2019

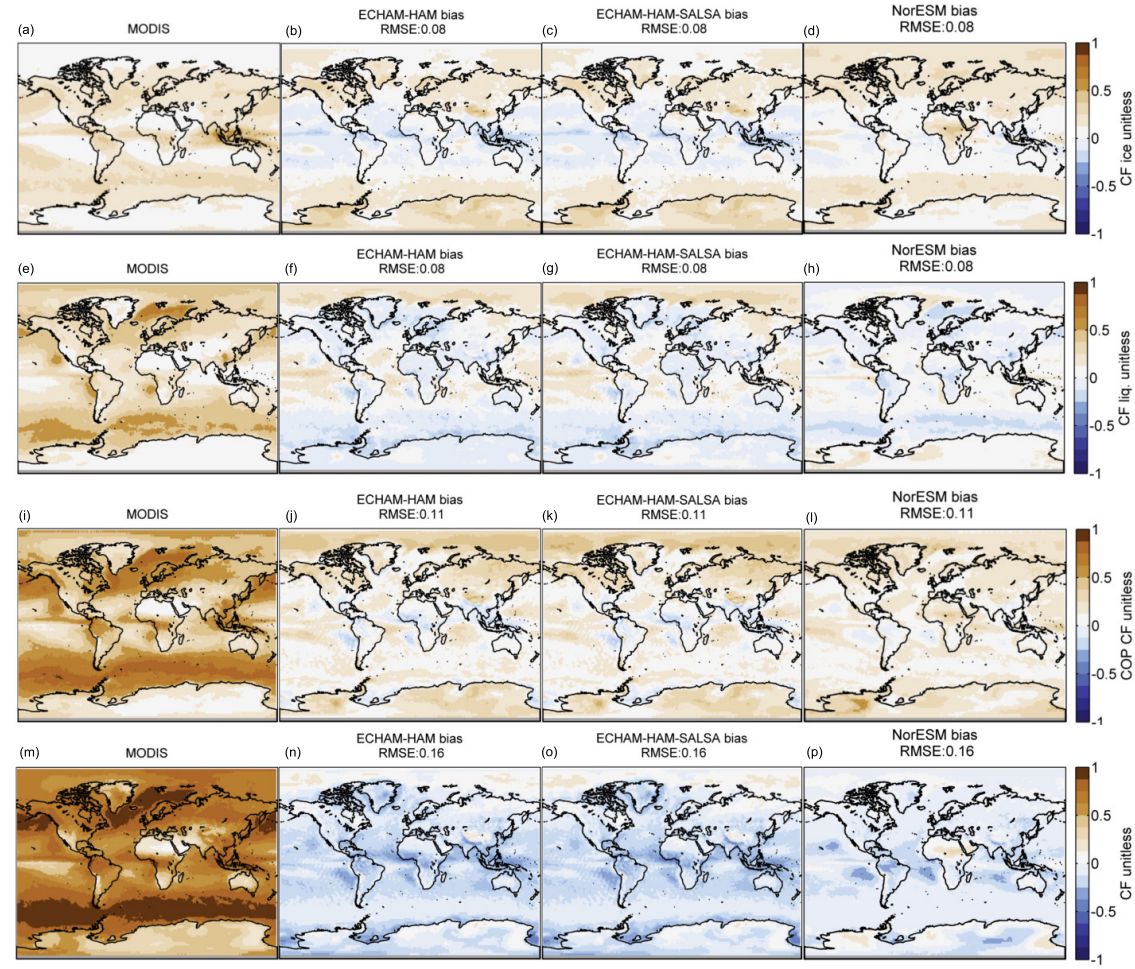

Figure 1. Annual global mean bias in cloud fraction. The bias represents the difference between MODIS-COSP diagnostics from ECHAM-HAM, ECHAM-HAM-SALSA, NorESM and MODIS observations. COSP-simulated total ice and liquid cloud fractions are compared with MODIS retrieval ice fraction (b-d), and with MODIS retrieval liquid cloud fraction (f-h), respectively. COSP-simulated total cloud fraction is compared with MODIS retrieval total cloud fraction (COP CF) (j-l), and cloud mask cloud fraction (CF) (n-p). Pixels with liquid cloud fraction $\leq$ 30% are screened.The averages represent in-cloud values. High latitudes (Lat $>$ 60° N or Lat $>$ 60° S) are excluded in the computation of the root mean square error (RMSE). MODIS spatial distribution is presented as reference (a,e,i,m).

https://doi.org/10.5194/acp-2019-631
Preprint. Discussion started: 13 September 2019

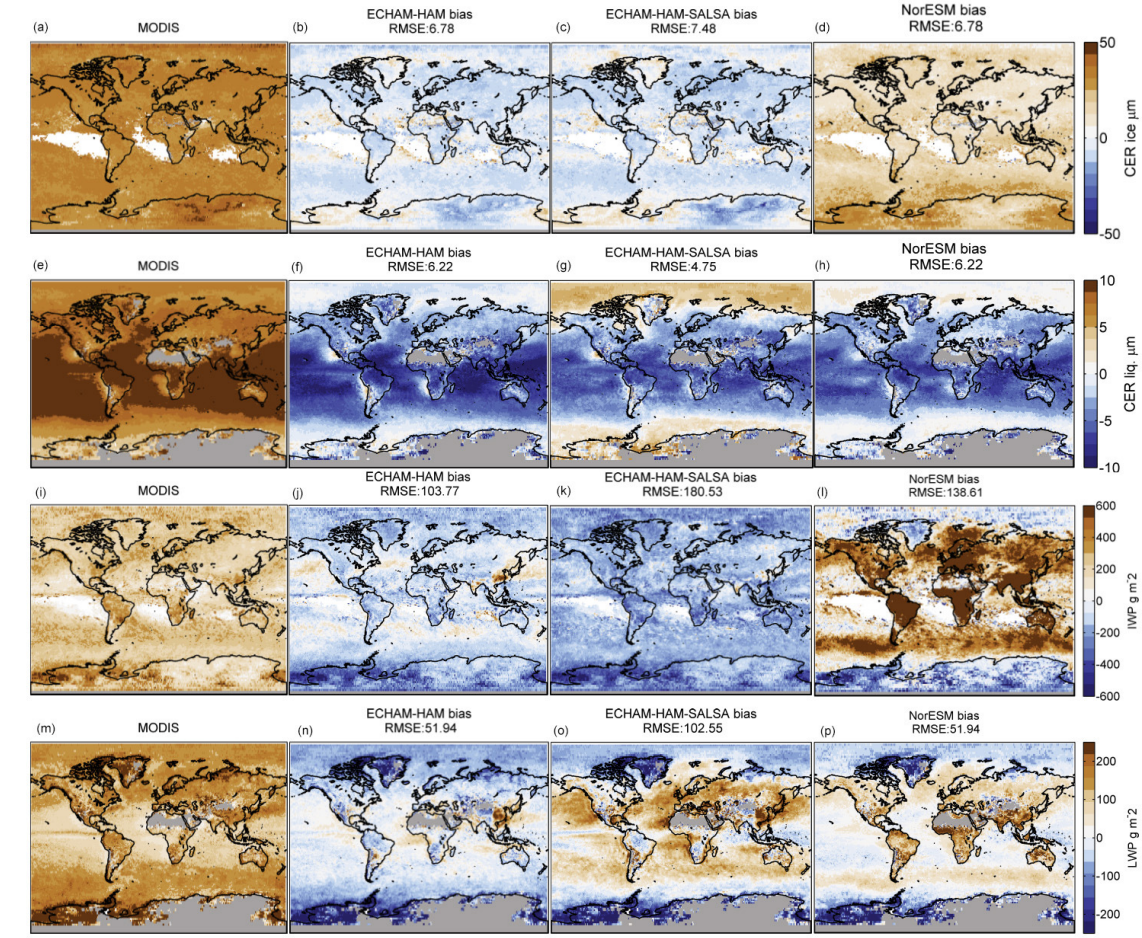

Figure 2. Annual global mean bias in cloud effective radius and water path. The bias represents the difference calculated subtracting MODIS observation to MODIS-COSP diagnostics from ECHAM-HAM, ECHAM-HAM-SALSA, and NorESM. Ice cloud effective radius (CER_{ice}) from MODIS-COSP is compared with MODIS observations in (b)-(d) and liquid cloud effective radius (CER_{liq}) in (f)-(h). The biases related to the comparison of COSP-simulated ice water path (IWP) are showed in (j)-(l) and for liquid water path (LWP) in (n)-(p). Pixels with liquid cloud fraction $\leq$ 30% are screened. The averages represent in-cloud values. Pixels with liquid cloud fraction $\leq$ 30% are screened. Values are in-cloud concentrations. High latitudes (Lat $>$ 60° N or Lat $>$ 60° S) are excluded in the computation of the root mean square error (RMSE). MODIS spatial distribution is presented as reference (a,e,i,m).

https://doi.org/10.5194/acp-2019-631
Preprint. Discussion started: 13 September 2019

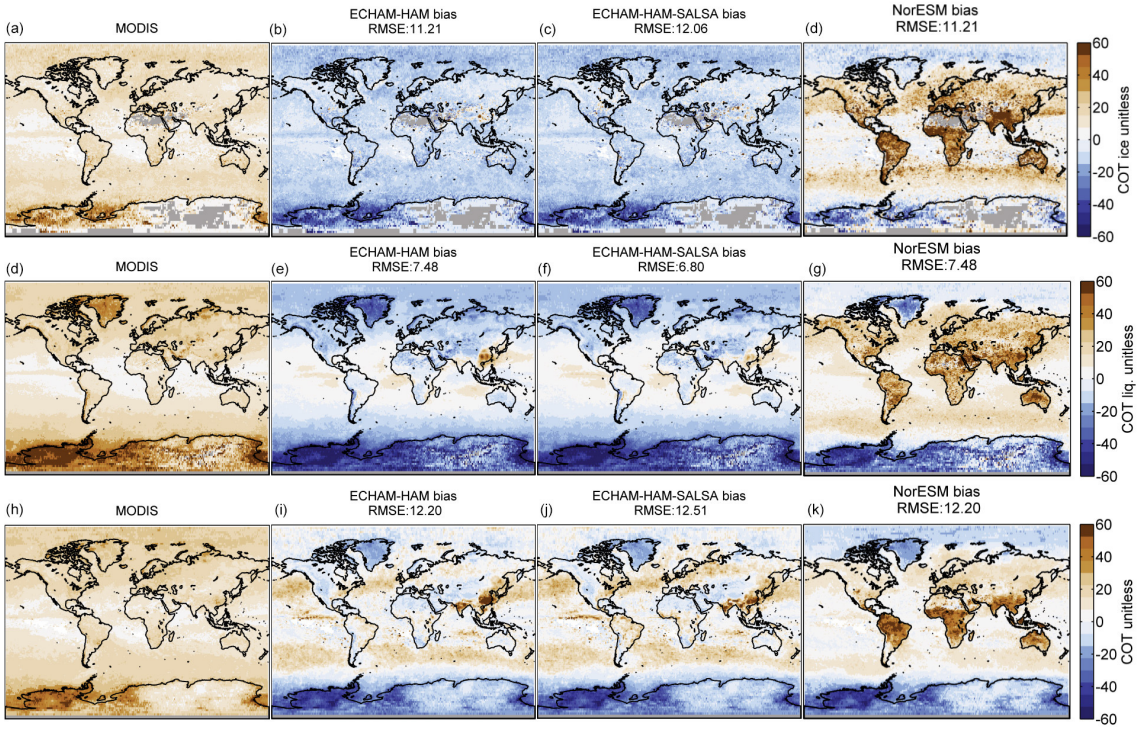

Figure 3. Annual global mean bias in cloud optical thickness for ice clouds (b-d), liquid water clouds (e-g) and total (combined ice and water clouds) COT (i-k) between MODIS and ECHAM-HAM, ECHAM-HAM-SALSA, and NorESM. The bias represents the difference between MODIS-COSP diagnostics and MODIS observations. Pixels with liquid cloud fraction $\leq 30\%$ are screened. The averages represent in-cloud values. High latitudes (Lat $> 60^{\circ}$ N or Lat $> 60^{\circ}$ S) are excluded in the computation of the root mean square error (RMSE). MODIS spatial distribution is presented as reference (a,d,h).

,

https://doi.org/10.5194/acp-2019-631
Preprint. Discussion started: 13 September 2019

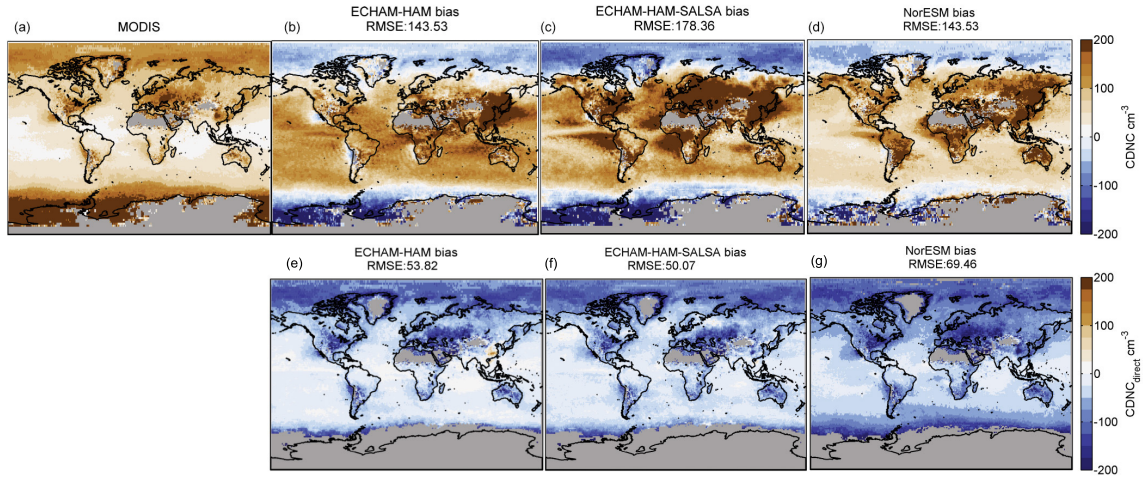

Figure 4. Cloud droplet number concentration (CDNC) annual mean bias.The bias represents the difference between CDNC derived from MODIS-COSP diagnostics and MODIS observations(b-d), and the model direct outputs and MODIS observations (f-h). Pixels with liquid cloud fraction $\leq 30\%$ are screened. The averages represent in-cloud values. High latitudes (Lat $> 60^{\circ}$ N or Lat $> 60^{\circ}$ S) are excluded in the computation of the root mean square error (RMSE). MODIS spatial distribution is presented as reference (a,e).

https://doi.org/10.5194/acp-2019-631
Preprint. Discussion started: 13 September 2019

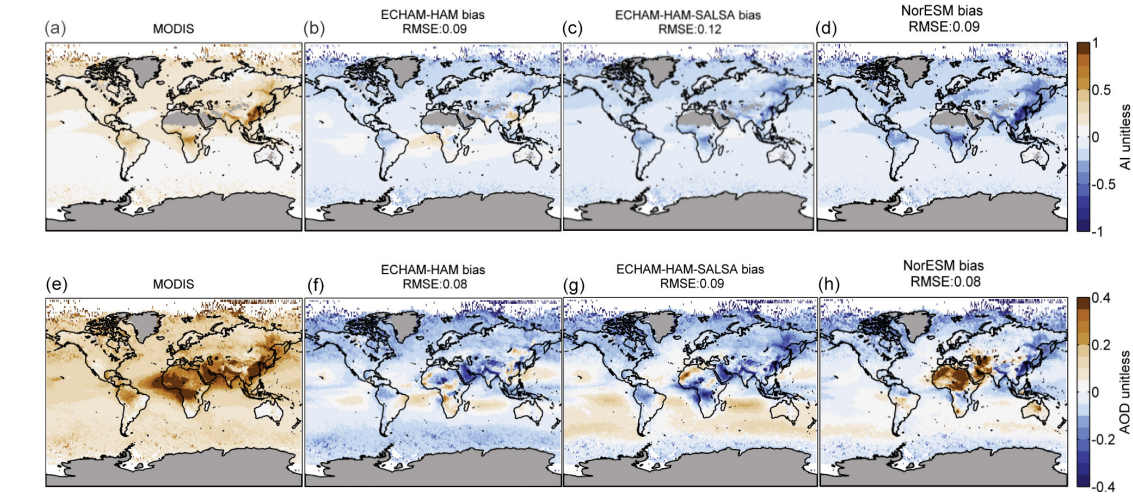

Figure 5. Aerosol Index (AI) (b-d) and Aerosol Optical Depth (f-h) annual mean bias. The bias represents the difference between the model direct outputs and MODIS observations. High latitudes (Lat $>$ 60° N or Lat $>$ 60° S) are excluded in the computation of the root mean square error (RMSE). MODIS spatial distribution is presented as reference (a,e).

https://doi.org/10.5194/acp-2019-631
Preprint. Discussion started: 13 September 2019

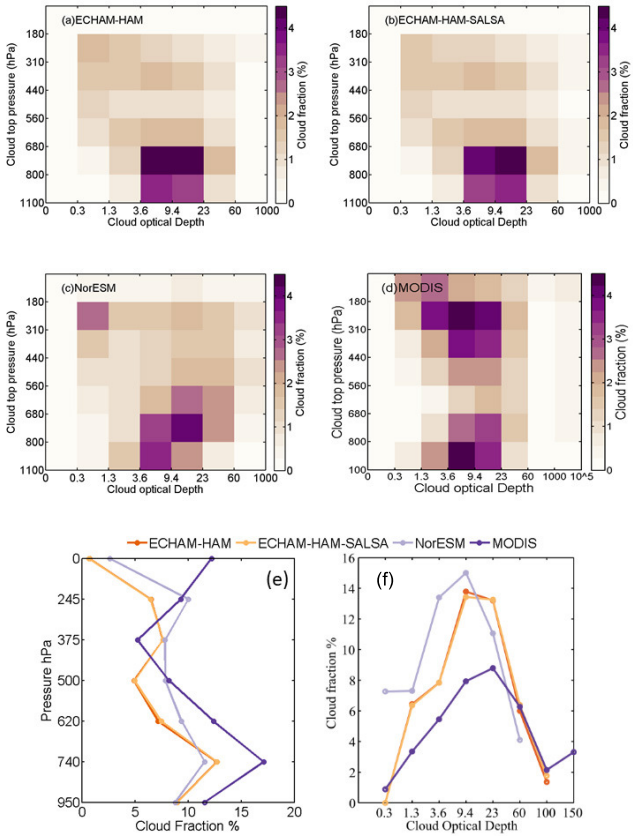

Figure 6. Vertical distribution analysis. Cloud fraction as a function of cloud top pressure and optical thickness for (a) ECHAM-HAM, (b) ECHAM-HAM-SALSA, (c) NorESM and (d) MODIS. The color scale represents the cloud fraction percentage. (e) Cloud fraction as a function of CTP (sum of all optical depth $\geq$0.3, and (f) cloud fraction as a function of COT (sum of all CTP layers for each COD-bin).

https://doi.org/10.5194/acp-2019-631
Preprint. Discussion started: 13 September 2019

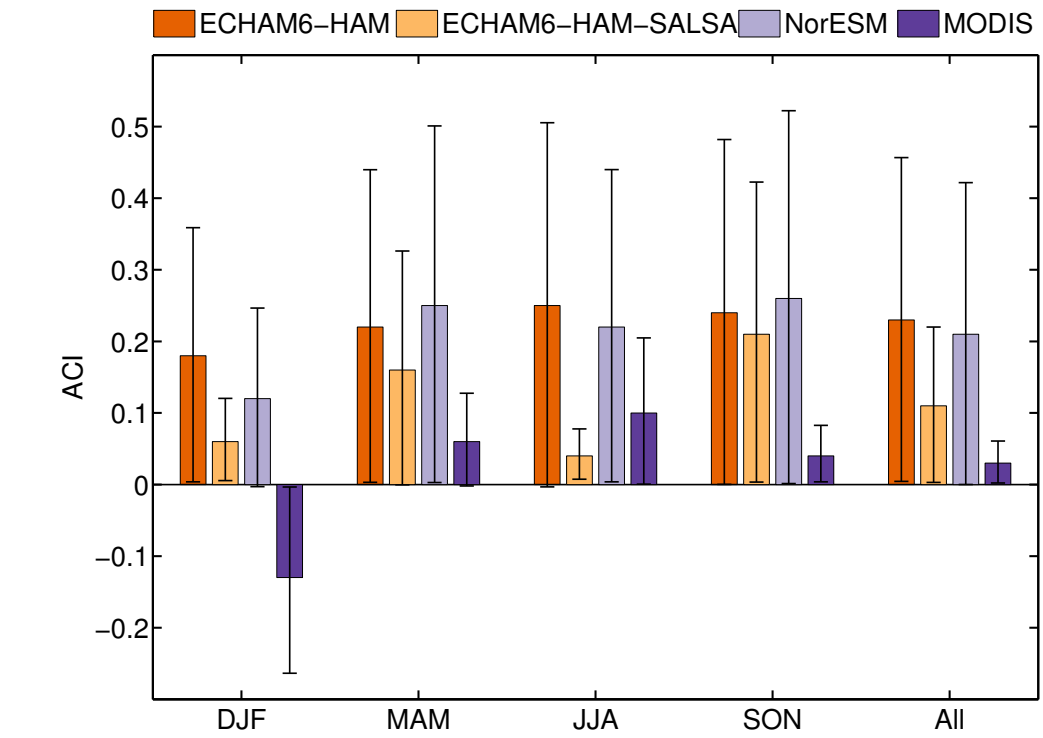

Figure 7. Global estimates of the aerosol-cloud interaction (ACI) computed as the changes of ln(CDNC) to ln(AI). CDNC are derived from corresponding daily grid points of LWP and COT from MODIS observations and COSP-MODIS outputs following Bennartz (2007). Global ACI values are calculated by season and for the entire period (1 January 2008 – 31 December 2008). Uncertainties estimates are calculated as 95% confidence interval from the daily values.

https://doi.org/10.5194/acp-2019-631
Preprint. Discussion started: 13 September 2019

Atmospheric Chemistry and Physics Discussions

Table 1. Annual global in-cloud mean value ± standard deviation for the parameters used in the study. If a grid point has CF $\leq$ 30%, the point is set to fill values in all the datasets. The process leads to a reduction of 35% of datapoints in each dataset. 'CF all' is not screened for CF $\leq$ 30%.

Source	CF all	CF	LWP gm^{-2}	CER μm	COT	CDNC cm^{-3}	AI
MODIS	0.68± 0.35	0.83 ± 0.21	140 ± 142	15.3 ± 4.7	18.5±18.7	82 ± 82.12	0.15±0.20
ECHAM-HAM	0.56 ± 0.36	0.70 ± 0.21	106 ± 83	11 ± 1.9	9.6 ± 11.9	168 ± 122	0.14±0.20
ECHAM-HAM-SALSA	0.56 ± 0.36	0.70 ± 0.20	168 ± 159	12.5 ± 3.5	9.9± 11.9	177 ± 183	0.11±0.18
NorESM	0.63 ± 0.34	0.42 ± 0.28	161 ± 133	11.9 ± 2.7	28.3 ± 53.6	167 ± 124	0.17 ± 0.26

https://doi.org/10.5194/acp-2019-631
Preprint. Discussion started: 13 September 2019

Atmospheric Chemistry and Physics Discussions

Table 2. Summary of the the models used in the study.

Model	Reference	Resolution	Aerosol scheme	Cloud microphysics
ECHAM-HAM	Tegen et al. (2019)	1.9° lat ×1.9° lon, 31 levels	HAM 2.3-M7	2-moment scheme
ECHAM-HAM-SALSA	Kokkola et al. (2018)	1.9° lat ×1.9° lon, 31 levels	HAM2.3-SALSA	2-moment scheme
NorESM	Kirkevåg et al. (2018)	0.9 ° lat × 1.25 ° lon, 30 levels	OsloAero	2-moment scheme MG1.5

https://doi.org/10.5194/acp-2019-631
Preprint. Discussion started: 13 September 2019

References

Abdul-Razzak, H. and Ghan, S. J.: A parameterization of aerosol activation: 2. Multiple aerosol types, Journal of Geophysical Research: Atmospheres, 105, 6837–6844, https://doi.org/10.1029/1999JD901161, https://agupubs.onlinelibrary.wiley.com/doi/abs/10.1029/1999JD901161, 2000.

Abdul-Razzak, H. and Ghan, S. J.: A parameterization of aerosol activation 3. Sectional representation, J. Geophys. Res., 107(D3), https://doi.org/10.1029/2001JD000483, 2002.

Ackerman, A. S., Kirkpatrick, M. P., Stevens, D. E., and Toon, O. B.: The impact of humidity above stratiform clouds on indirect aerosol climate forcing, Nature, 432, 1014–1017, https://doi.org/10.1038/nature03174, 2004.

Ban-Weiss, G. A., Jin, L., Bauer, S. E., Bennartz, R., Liu, X., Zhang, K., Ming, Y., Guo, H., and Jiang, J. H.: Evaluating clouds, aerosols, and their interactions in three global climate models using satellite simulators and observations, Journal of Geophysical Research: Atmospheres, 119, 10,876–10,901, https://doi.org/10.1002/2014JD021722, https://agupubs.onlinelibrary.wiley.com/doi/abs/10.1002/2014JD021722, 2014.

Bennartz, R.: Global assessment of marine boundary layer cloud droplet number concentration from satellite, Journal of Geophysical Research: Atmospheres, 112, https://doi.org/10.1029/2006JD007547, https://agupubs.onlinelibrary.wiley.com/doi/abs/10.1029/2006JD007547, 2007.

Bennartz, R. and Rausch, J.: Global and regional estimates of warm cloud droplet number concentration based on 13 years of AQUA-MODIS observations, Atmospheric Chemistry and Physics, 17, 9815–9836, https://doi.org/10.5194/acp-17-9815-2017, https://www.atmos-chem-phys.net/17/9815/2017/, 2017.

Bentsen, M., Bethke, I., Debernard, J. B., Iversen, T., Kirkevåg, A., Seland, Ø., Drange, H., Roelandt, C., Seierstad, I. A., Hoose, C., and Kristjánsson, J. E.: The Norwegian Earth System Model, NorESM1-M â€“ Part 1: Description and basic evaluation of the physical climate, Geoscientific Model Development, 6, 687–720, https://doi.org/10.5194/gmd-6-687-2013, https://www.geosci-model-dev.net/6/687/2013/, 2013.

Berrisford, P., Kållberg, P., Kobayashi, S., Dee, D., Uppala, S., Simmons, A. J., Poli, P., and Sato, H.: Atmospheric conservation properties in ERA-Interim, Quarterly Journal of the Royal Meteorological Society, 137, 1381–1399, https://doi.org/10.1002/qj.864, https://rmets.onlinelibrary.wiley.com/doi/abs/10.1002/qj.864, 2011.

Bodas-Salcedo, A., Webb, M. J., Bony, S., Chepfer, H., Dufresne, J.-L., Klein, S. A., Zhang, Y., Marchand, R., Haynes, J. M., Pincus, R., and John, V. O.: COSP: Satellite simulation software for model assessment, Bulletin of the American Meteorological Society, 92, 1023–1043, https://doi.org/10.1175/2011BAMS2856.1, https://doi.org/10.1175/2011BAMS2856.1, 2011.

https://doi.org/10.5194/acp-2019-631
Preprint. Discussion started: 13 September 2019

Boucher, O., Randall, D., Artaxo, P., Bretherton, C., Feingold, G., Forster, P., Kerminen, V.-M., Kondo, Y., Liao, H., Lohmann, U., Rasch, P., Satheesh, S. K., Sherwood, S., Stevens, B., and Zhang, X. Y.: Clouds and aerosols, pp. 571–657, Cambridge University Press, Cambridge, UK, https://doi.org/10.1017/CBO9781107415324.016, 2013.

Chen, J., Liu, Y., Zhang, M., and Peng, Y.: Height Dependency of Aerosol-Cloud Interaction Regimes, Journal of Geophysical Research: Atmospheres, 123, 491–506, https://doi.org/10.1002/2017JD027431, https://agupubs.onlinelibrary.wiley.com/doi/abs/10.1002/2017JD027431.

Chen, Y.-C., Christensen, M. W., Stephens, G. L., and Seinfeld, J. H.: Satellite-based estimate of global aerosol–cloud radiative forcing by marine warm clouds, Nature Geoscience, 7, https://doi.org/10.1038/ngeo2214, https://doi.org/10.1038/ngeo2214, 2014.

Christensen, M. W., Neubauer, D., Poulsen, C. A., Thomas, G. E., McGarragh, G. R., Povey, A. C., Proud, S. R., and Grainger, R. G.: Unveiling aerosol–cloud interactions – Part 1: Cloud contamination in satellite products enhances the aerosol indirect forcing estimate, Atmospheric Chemistry and Physics, 17, 13 151–13 164, https://doi.org/10.5194/acp-17-13151-2017, https://www.atmos-chem-phys.net/17/13151/2017/, 2017.

Costantino, L. and Bréon, F.-M.: Aerosol indirect effect on warm clouds over South-East Atlantic, from co-located MODIS and CALIPSO observations, Atmospheric Chemistry and Physics, 13, 69–88, https://doi.org/10.5194/acp-13-69-2013, https://www.atmos-chem-phys.net/13/69/2013/, 2013.

Cumming, G., Fidler, F., and Vaux, D. L.: Error bars in experimental biology, The Journal of Cell Biology, 177, 7–11, https://doi.org/10.1083/jcb.200611141, http://jcb.rupress.org/content/177/1/7, 2007.

Dee, D. P., Uppala, S. M., Simmons, A. J., Berrisford, P., Poli, P., Kobayashi, S., Andrae, U., Balmaseda, M. A., Balsamo, G., Bauer, P., Bechtold, P., Beljaars, A. C. M., van de Berg, L., Bidlot, J., Bormann, N., Delsol, C., Dragani, R., Fuentes, M., Geer, A. J., Haimberger, L., Healy, S. B., Hersbach, H., Hólm, E. V., Isaksen, L., Kållberg, P., Köhler, M., Matricardi, M., McNally, A. P., Monge-Sanz, B. M., Morcrette, J.-J., Park, B.-K., Peubey, C., de Rosnay, P., Tavolato, C., Thépaut, J.-N., and Vitart, F.: The ERA-Interim reanalysis: configuration and performance of the data assimilation system, Quarterly Journal of the Royal Meteorological Society, 137, 553–597, https://doi.org/10.1002/qj.828, https://rmets.onlinelibrary.wiley.com/doi/abs/10.1002/qj.828, 2011.

Eyring, V., Bony, S., Meehl, G. A., Senior, C. A., Stevens, B., Stouffer, R. J., and Taylor, K. E.: Overview of the Coupled Model Intercomparison Project Phase 6 (CMIP6) experimental design and organization, Geoscientific Model Development, 9, 1937–1958, https://doi.org/10.5194/gmd-9-1937-2016, https://www.geosci-model-dev.net/9/1937/2016/, 2016a.

https://doi.org/10.5194/acp-2019-631
Preprint. Discussion started: 13 September 2019

Eyring, V., Gleckler, P. J., Heinze, C., Stouffer, R. J., Taylor, K. E., Balaji, V., Guilyardi, E., Joussaume, S., Kindermann, S., Lawrence, B. N., Meehl, G. A., Righi, M., and Williams, D. N.: Towards improved and more routine Earth system model evaluation in CMIP, Earth System Dynamics, 7, 813–830, https://doi.org/10.5194/esd-7-813-2016, https://www.earth-syst-dynam.net/7/813/2016/, 2016b.

Eyring, V., Righi, M., Lauer, A., Evaldsson, M., Wenzel, S., Jones, C., Anav, A., Andrews, O., Cionni, I., Davin, E. L., Deser, C., Ehbrecht, C., Friedlingstein, P., Gleckler, P., Gottschaldt, K.-D., Hagemann, S., Juckes, M., Kindermann, S., Krasting, J., Kunert, D., Levine, R., Loew, A., Mäkelä, J., Martin, G., Mason, E., Phillips, A. S., Read, S., Rio, C., Roehrig, R., Senftleben, D., Sterl, A., van Ulft, L. H., Walton, J., Wang, S., and Williams, K. D.: ESMValTool (v1.0) – a community diagnostic and performance metrics tool for routine evaluation of Earth system models in CMIP, Geoscientific Model Development, 9, 1747–1802, https://doi.org/10.5194/gmd-9-1747-2016, https://www.geosci-model-dev.net/9/1747/2016/, 2016c.

Feingold, G., Remer, L. A., Ramaprasad, J., and Kaufman, Y. J.: Analysis of smoke impact on clouds in Brazilian biomass burning regions: An extension of Twomey's approach, Journal of Geophysical Research: Atmospheres, 106, 22 907–22 922, https://doi.org/10.1029/2001JD000732, https://agupubs.onlinelibrary.wiley.com/doi/abs/10.1029/2001JD000732, 2001.

Flato, G., Marotzke, J., Abiodun, B., Braconnot, P., Chou, S., Collins, W., Cox, P., Driouech, F., Emori, S., Eyring, V., Forest, C., Gleckler, P., Guilyardi, E., Jakob, C., Kattsov, V., Reason, C., and Rummukainen, M.: Evaluation of Climate Models, book section 9, p. 741–866, Cambridge University Press, Cambridge, United Kingdom and New York, NY, USA, https://doi.org/10.1017/CBO9781107415324.020, www.climatechange2013.org, 2013.

Flato, G. M.: Earth system models: an overview, Wiley Interdisciplinary Reviews: Climate Change, 2, 783–800, https://doi.org/10.1002/wcc.148, https://onlinelibrary.wiley.com/doi/abs/10.1002/wcc.148, 2011.

Gettelman, A., Morrison, H., Santos, S., Bogenschutz, P., and Caldwell, P. M.: Advanced Two-Moment Bulk Microphysics for Global Models. Part II: Global Model Solutions and Aerosol–Cloud Interactions, Journal of Climate, 28, 1288–1307, https://doi.org/10.1175/JCLI-D-14-00103.1, https://doi.org/10.1175/JCLI-D-14-00103.1, 2015.

Grandey, B. S. and Stier, P.: A critical look at spatial scale choices in satellite-based aerosol indirect effect studies, Atmospheric Chemistry and Physics, 10, 11 459–11 470, https://doi.org/10.5194/acp-10-11459-2010, https://www.atmos-chem-phys.net/10/11459/2010/, 2010.

https://doi.org/10.5194/acp-2019-631
Preprint. Discussion started: 13 September 2019

Guenther, A. B., Jiang, X., Heald, C. L., Sakulyanontvittaya, T., Duhl, T., Emmons, L. K., and Wang, X.: The Model of Emissions of Gases and Aerosols from Nature version 2.1 (MEGAN2.1): an extended and updated framework for modeling biogenic emissions, Geoscientific Model Development, 5, 1471–1492, https://doi.org/10.5194/gmd-5-1471-2012, https://www.geosci-model-dev.net/5/1471/2012/, 2012.

Hubanks, P., Platnick, S., King, M., and Ridgway, B.: MODIS Algorithm Theoretical Basis Document No.ATBD−MOD−30 for Level−3 Global Gridded Atmosphere Products (08 D3, 08 E3, 08 M3) and User Guide (Collection 6.0 6.1), 2016.

Iversen, T., Bentsen, M., Bethke, I., Debernard, J. B., Kirkevåg, A., Seland, Ø., Drange, H., Kristjansson, J. E., Medhaug, I., Sand, M., and Seierstad, I. A.: The Norwegian Earth System Model, NorESM1-M â€“ Part 2: Climate response and scenario projections, Geoscientific Model Development, 6, 389–415, https://doi.org/10.5194/gmd-6-389-2013, https://www.geosci-model-dev.net/6/389/2013/, 2013.

Jiang, J. H., Su, H., Huang, L., Wang, Y., Massie, S., Zhao, B., Omar, A., and Wang, Z.: Contrasting effects on deep convective clouds by different types of aerosols, 9, https://doi.org/10.1038/s41467-018-06280-4, https://doi.org/10.1038/s41467-018-06280-4, 2018.

Kay, J. E., Hillman, B. R., Klein, S. A., Zhang, Y., Medeiros, B., Pincus, R., Gettelman, A., Eaton, B., Boyle, J., Marchand, R., and Ackerman, T. P.: Exposing Global Cloud Biases in the Community Atmosphere Model (CAM) Using Satellite Observations and Their Corresponding Instrument Simulators, Journal of Climate, 25, 5190–5207, https://doi.org/10.1175/JCLI-D-11-00469.1, https://doi.org/10.1175/JCLI-D-11-00469.1, 2012.

Khairoutdinov, M. and Kogan, Y.: A New Cloud Physics Parameterization in a Large-Eddy Simulation Model of Marine Stratocumulus, Monthly Weather Review, 128, 229–243, https://doi.org/10.1175/1520-0493(2000)128<0229:ANCPPI>2.0.CO;2, https://doi.org/10.1175/1520-0493(2000)128<0229:ANCPPI>2.0.CO;2, 2000.

King, N. J., Bower, K. N., Crosier, J., and Crawford, I.: Evaluating MODIS cloud retrievals with in situ observations from VOCALS-REx, Atmospheric Chemistry and Physics, 13, 191–209, https://doi.org/10.5194/acp-13-191-2013, https://www.atmos-chem-phys.net/13/191/2013/, 2013.

Kirkevåg, A., Iversen, T., Seland, Ø., Hoose, C., Kristjánsson, J. E., Struthers, H., Ekman, A. M. L., Ghan, S., Griesfeller, J., Nilsson, E. D., and Schulz, M.: Aerosolâ€“climate interactions in the Norwegian Earth System Model â€“ NorESM1-M, Geoscientific Model Development, 6, 207–244, https://doi.org/10.5194/gmd-6-207-2013, https://www.geosci-model-dev.net/6/207/2013/, 2013.

Kirkevåg, A., Grini, A., Olivié, D., Seland, Ø., Alterskjær, K., Hummel, M., Karset, I. H. H., Lewinschal, A., Liu, X., Makkonen, R., Bethke, I., Griesfeller, J., Schulz, M., and Iversen, T.: A production-tagged aerosol module for Earth system models, OsloAero5.3

https://doi.org/10.5194/acp-2019-631
Preprint. Discussion started: 13 September 2019

– extensions and updates for CAM5.3-Oslo, Geoscientific Model Development, 11, 3945–3982, https://doi.org/10.5194/gmd-11-3945-2018, https://www.geosci-model-dev.net/11/3945/2018/, 2018.

Klein, S. and Webb, M.: ISCCP simulator implementation instructions: Readme, http://cfmip.metoffice.com/README, 2009.

Kokkola, H., Korhonen, H., Lehtinen, K. E. J., Makkonen, R., Asmi, A., Järvenoja, S., Anttila, T., Partanen, A.-I., Kulmala, M., Järvinen, H., Laaksonen, A., and Kerminen, V.-M.: SALSA: a Sectional Aerosol module for Large Scale Applications, 8, 2469–2483, http://www.atmos-chem-phys.net/8/2469/2008/, 2008.

Kokkola, H., Kühn, T., Laakso, A., Bergman, T., Lehtinen, K. E. J., Mielonen, T., Arola, A., Stadtler, S., Korhonen, H., Ferrachat, S., Lohmann, U., Neubauer, D., Tegen, I., Siegenthaler-Le Drian, C., Schultz, M. G., Bey, I., Stier, P., Daskalakis, N., Heald, C. L., and Romakkaniemi, S.: SALSA2.0: The sectional aerosol module of the aerosol-chemistry-climate model ECHAM6.3.0-HAM2.3-MOZ1.0, Geoscientific Model Development Discussions, 2018, 1–43, https://doi.org/10.5194/gmd-2018-47, https://www.geosci-model-dev-discuss.net/gmd-2018-47/, 2018.

Koren, I., Remer, L. A., Kaufman, Y. J., Rudich, Y., and Martins, J. V.: On the twilight zone between clouds and aerosols, Geophysical Research Letters, 34, https://doi.org/10.1029/2007GL029253, https://agupubs.onlinelibrary.wiley.com/doi/abs/10.1029/2007GL029253, 2007.

Kärcher, B. and Lohmann, U.: A Parameterization of cirrus cloud formation: Homogeneous freezing including effects of aerosol size, Journal of Geophysical Research: Atmospheres, 107, AAC 9–1–AAC 9–10, https://doi.org/10.1029/2001JD001429, https://agupubs.onlinelibrary.wiley.com/doi/abs/10.1029/2001JD001429, 2002.

Lee, L. A., Reddington, C. L., and Carslaw, K. S.: On the relationship between aerosol model uncertainty and radiative forcing uncertainty, Proceedings of the National Academy of Sciences, 113, 5820–5827, https://doi.org/10.1073/pnas.1507050113, https://www.pnas.org/content/113/21/5820, 2016.

Levy, R. C., Remer, L. A., Mattoo, S., Vermote, E. F., and Kaufman, Y. J.: Second-generation operational algorithm: Retrieval of aerosol properties over land from inversion of Moderate Resolution Imaging Spectroradiometer spectral reflectance, Journal of Geophysical Research: Atmospheres, 112, https://doi.org/10.1029/2006JD007811, https://agupubs.onlinelibrary.wiley.com/doi/abs/10.1029/2006JD007811, 2007.

Levy, R. C., Mattoo, S., Munchak, L. A., Remer, L. A., Sayer, A. M., Patadia, F., and Hsu, N. C.: The Collection 6 MODIS aerosol products over land and ocean, Atmospheric Measurement Techniques, 6, 2989–3034, https://doi.org/10.5194/amt-6-2989-2013, https://www.atmos-meas-tech.net/6/2989/2013/, 2013.

https://doi.org/10.5194/acp-2019-631
Preprint. Discussion started: 13 September 2019

Liu, Y., de Leeuw, G., Kerminen, V.-M., Zhang, J., Zhou, P., Nie, W., Qi, X., Hong, J., Wang, Y., Ding, A., Guo, H., Krüger, O., Kulmala, M., and Petäjä, T.: Analysis of aerosol effects on warm clouds over the Yangtze River Delta from multi-sensor satellite observations, Atmospheric Chemistry and Physics, 17, 5623–5641, https://doi.org/10.5194/acp-17-5623-2017, https://www.atmos-chem-phys.net/17/5623/2017/, 2017.

Liu, Y., Zhang, J., Zhou, P., Lin, T., Hong, J., Shi, L., Yao, F., Wu, J., Guo, H., and de Leeuw, G.: Satellite-based estimate of the variability of warm cloud properties associated with aerosol and meteorological conditions, Atmospheric Chemistry and Physics, 18, 18 187–18 202, https://doi.org/10.5194/acp-18-18187-2018, https://www.atmos-chem-phys.net/18/18187/2018/, 2018.

Lohmann, U. and Diehl, K.: Sensitivity Studies of the Importance of Dust Ice Nuclei for the Indirect Aerosol Effect on Stratiform Mixed-Phase Clouds, Journal of the Atmospheric Sciences, 63, 968–982, https://doi.org/10.1175/JAS3662.1, https://doi.org/10.1175/JAS3662.1, 2006.

Lohmann, U. and Hoose, C.: Sensitivity studies of different aerosol indirect effects in mixed-phase clouds, Atmospheric Chemistry and Physics, 9, 8917–8934, https://doi.org/10.5194/acp-9-8917-2009, https://www.atmos-chem-phys.net/9/8917/2009/, 2009.

Lohmann, U. and Neubauer, D.: The importance of mixed-phase and ice clouds for climate sensitivity in the global aerosol–climate model ECHAM6-HAM2, Atmospheric Chemistry and Physics, 18, 8807–8828, https://doi.org/10.5194/acp-18-8807-2018, https://www.atmos-chem-phys.net/18/8807/2018/, 2018.

Lohmann, U., Stier, P., Hoose, C., Ferrachat, S., Kloster, S., Roeckner, E., and Zhang, J.: Cloud microphysics and aerosol indirect effects in the global climate model ECHAM5-HAM, Atmospheric Chemistry and Physics, 7, 3425–3446, https://doi.org/10.5194/acp-7-3425-2007, https://www.atmos-chem-phys.net/7/3425/2007/, 2007.

Lohmann, U., Spichtinger, P., Jess, S., Peter, T., and Smit, H.: Cirrus cloud formation and ice supersaturated regions in a global climate model, Environmental Research Letters, 3, 045 022, https://doi.org/10.1088/1748-9326/3/4/045022, 2008.

Luo, Z. J., Anderson, R. C., Rossow, W. B., and Takahashi, H.: Tropical cloud and precipitation regimes as seen from near-simultaneous TRMM, CloudSat, and CALIPSO observations and comparison with ISCCP, Journal of Geophysical Research: Atmospheres, 122, 5988–6003, https://doi.org/10.1002/2017JD026569, https://agupubs.onlinelibrary.wiley.com/doi/abs/10.1002/2017JD026569, 2017.

Marchant, B., Platnick, S., Meyer, K., Arnold, G. T., and Riedi, J.: MODIS Collection 6 shortwave-derived cloud phase classification algorithm and comparisons with CALIOP, Atmospheric Measurement Techniques, 9, 1587–1599, https://doi.org/10.5194/amt-9-1587-2016, https://www.atmos-meas-tech.net/9/1587/2016/, 2016.

https://doi.org/10.5194/acp-2019-631
Preprint. Discussion started: 13 September 2019

McComiskey, A. and Feingold, G.: The scale problem in quantifying aerosol indirect effects, Atmospheric Chemistry and Physics, 12, 1031–1049, https://doi.org/10.5194/acp-12-1031-2012, https://www.atmos-chem-phys.net/12/1031/2012/, 2012.

Min, Q., Joseph, E., Lin, Y., Min, L., Yin, B., Daum, P. H., Kleinman, L. I., Wang, J., and Lee, Y.-N.: Comparison of MODIS cloud microphysical properties with in-situ measurements over the Southeast Pacific, Atmospheric Chemistry and Physics, 12, 11 261–11 273, https://doi.org/10.5194/acp-12-11261-2012, https://www.atmos-chem-phys.net/12/11261/2012/, 2012.

Morrison, H. and Gettelman, A.: A New Two-Moment Bulk Stratiform Cloud Microphysics Scheme in the Community Atmosphere Model, Version 3 (CAM3). Part I: Description and Numerical Tests, Journal of Climate, 21, 3642–3659, https://doi.org/10.1175/2008JCLI2105.1, https://doi.org/10.1175/2008JCLI2105.1, 2008.

Neale, R. B., Gettelman, A., Park, S., Conley, A. J., Kinnison, D., Marsh, D., Smith, A. K., Vitt, F., Morrison, H., Cameron-smith, P., Collins, W. D., Iacono, M. J., Easter, R. C., Liu, X., Taylor, M. A., chieh Chen, C., Lauritzen, P. H., Williamson, D. L., Garcia, R., francois Lamarque, J., Mills, M., Tilmes, S., Ghan, S. J., Rasch, P. J., and Meteorology, M.: Description of the NCAR Community Atmosphere Model (CAM 5.0), Tech. Note NCAR/TN-486+STR, Natl. Cent. for Atmos, in: 6of7 ZHAO ET AL.: AEROSOL FIELD SIMULATED BY CAMS L08806, pp. 2009–038 451, 2010.

Neubauer, D., Christensen, M. W., Poulsen, C. A., and Lohmann, U.: Unveiling aerosol–cloud interactions – Part 2: Minimising the effects of aerosol swelling and wet scavenging in ECHAM6-HAM2 for comparison to satellite data, Atmospheric Chemistry and Physics, 17, 13 165–13 185, https://doi.org/10.5194/acp-17-13165-2017, https://www.atmos-chem-phys.net/17/13165/2017/, 2017.

Neubauer, D., Ferrachat, S., Siegenthaler-Le Drian, C., Stier, P., Partridge, D. G., Tegen, I., Bey, I., Stanelle, T., Kokkola, H., and Lohmann, U.: The global aerosol-climate model ECHAM6.3-HAM2.3 - Part 2: Cloud evaluation, aerosol radiative forcing and climate sensitivity, Geoscientific Model Development Discussions, 2019, 1–52, https://doi.org/10.5194/gmd-2018-307, https://www.geosci-model-dev-discuss.net/gmd-2018-307/, 2019.

Noble, S. and Hudson, J.: MODIS comparisons with northeastern Pacific in situ stratocumulus microphysics, Journal of geophysical research. Atmospheres : JGR, 120, 8332–344, https://doi.org/10.1002/2014JD022785, https://www.ncbi.nlm.nih.gov/pubmed/27708990, 2015.

Nordeng, T. E.: Extended versions of the convective parameterization scheme at ECMWF and their impact on the mean and transient activity of the model in the tropics, 206 edn.

https://doi.org/10.5194/acp-2019-631
Preprint. Discussion started: 13 September 2019

Oleson, K. W.and Lawrence, D. M., Gordon, B., Flanner, M. G., Kluzek, E., Peter, J., Levis, S., Swenson, S. C., Thornton, E., and Feddema, J.: Technical description of version 4.0 of the Community Land Model (CLM), organization.

Oreopoulos, L., Cho, N., and Lee, D.: Using MODIS cloud regimes to sort diagnostic signals of aerosol-cloud-precipitation interactions, Journal of Geophysical Research: Atmospheres, 122, 5416–5440, https://doi.org/10.1002/2016JD026120, https://agupubs.onlinelibrary.wiley.com/doi/abs/10.1002/2016JD026120, 2017.

Painemal, D. and Zuidema, P.: Assessment of MODIS cloud effective radius and optical thickness retrievals over the Southeast Pacific with VOCALS-REx in situ measurements, Journal of Geophysical Research: Atmospheres, 116, https://doi.org/10.1029/2011JD016155, https://agupubs.onlinelibrary.wiley.com/doi/abs/10.1029/2011JD016155, 2011.

Park, S. and Bretherton, C. S.: The University of Washington Shallow Convection and Moist Turbulence Schemes and Their Impact on Climate Simulations with the Community Atmosphere Model, Journal of Climate, 22, 3449–3469, https://doi.org/10.1175/2008JCLI2557.1, https://doi.org/10.1175/2008JCLI2557.1, 2009.

Penner, J. E., Xu, L., and Wang, M.: Satellite methods underestimate indirect climate forcing by aerosols, 108, 13 404–13 408, https://doi.org/10.1073/pnas.1018526108, 2011.

Pincus, R., Platnick, S., Ackerman, S. A., Hemler, R. S., and Hofmann, P. R. J.: Reconciling Simulated and Observed Views of Clouds: MODIS, ISCCP, and the Limits of Instrument Simulators, Journal of Climate, 25, 4699–4720, https://doi.org/10.1175/JCLI-D-11-00267.1, https://doi.org/10.1175/JCLI-D-11-00267.1, 2012.

Platnick, S., Meyer, K. G., King, M. D., Wind, G., Amarasinghe, N., Marchant, B., Arnold, G. T., Zhang, Z., Hubanks, P. A., Holz, R. E., Yang, P., Ridgway, W. L., and Riedi, J.: The MODIS Cloud Optical and Microphysical Products: Collection 6 Updates and Examples From Terra and Aqua, IEEE Transactions on Geoscience and Remote Sensing, 55, 502–525, https://doi.org/10.1109/TGRS.2016.2610522, 2017.

Preißler, J., Martucci, G., Saponaro, G., Ovadnevaite, J., Vaishya, A., Kolmonen, P., Ceburnis, D., Sogacheva, L., de Leeuw, G., and O'Dowd, C.: Six years of surface remote sensing of stratiform warm clouds in marine and continental air over Mace Head, Ireland, Journal of Geophysical Research: Atmospheres, 121, 14,538–14,557, https://doi.org/10.1002/2016JD025360, https://agupubs.onlinelibrary.wiley.com/doi/abs/10.1002/2016JD025360, 2016.

Quaas, J., Boucher, O., and Bréon, F.-M.: Aerosol indirect effects in POLDER satellite data and the Laboratoire de Météorologie Dynamique–Zoom (LMDZ) general circulation model, Journal of Geophysical Research: Atmospheres, 109, n/a–n/a, https://doi.org/10.1029/2003JD004317, http://dx.doi.org/10.1029/2003JD004317, d08205, 2004.

https://doi.org/10.5194/acp-2019-631
Preprint. Discussion started: 13 September 2019

Quaas, J., Boucher, O., and Lohmann, U.: Constraining the total aerosol indirect effect in the LMDZ and ECHAM4 GCMs using MODIS satellite data, Atmospheric Chemistry and Physics, 6, 947–955, https://doi.org/10.5194/acp-6-947-2006, https://www.atmos-chem-phys.net/6/947/2006/, 2006.

Quaas, J., Ming, Y., Menon, S., Takemura, T., Wang, M., Penner, J. E., Gettelman, A., Lohmann, U., Bellouin, N., Boucher, O., Sayer, A. M., Thomas, G. E., McComiskey, A., Feingold, G., Hoose, C., Kristjánsson, J. E., Liu, X., Balkanski, Y., Donner, L. J., Ginoux, P. A., Stier, P., Grandey, B., Feichter, J., Sednev, I., Bauer, S. E., Koch, D., Grainger, R. G., Kirkevaring;g, A., Iversen, T., Seland, Ø., Easter, R., Ghan, S. J., Rasch, P. J., Morrison, H., Lamarque, J.-F., Iacono, M. J., Kinne, S., and Schulz, M.: Aerosol indirect effects - general circulation model intercomparison and evaluation with satellite data, Atmospheric Chemistry and Physics, 9, 8697–8717, https://doi.org/10.5194/acp-9-8697-2009, https://www.atmos-chem-phys.net/9/8697/2009/, 2009.

Quaas, J., Stevens, B., Stier, P., and Lohmann, U.: Interpreting the cloud cover - aerosol optical depth relationship found in satellite data using a general circulation model, Atmospheric Chemistry and Physics, 10, 6129–6135, https://doi.org/10.5194/acp-10-6129-2010, https://www.atmos-chem-phys.net/10/6129/2010/, 2010.

Rausch, J., Heidinger, A., and Bennartz, R.: Regional assessment of microphysical properties of marine boundary layer cloud using the PATMOS-x dataset, Journal of Geophysical Research: Atmospheres, 115, https://doi.org/10.1029/2010JD014468, https://agupubs.onlinelibrary.wiley.com/doi/abs/10.1029/2010JD014468, 2010.

Saponaro, G., Kolmonen, P., Sogacheva, L., Rodriguez, E., Virtanen, T., and de Leeuw, G.: Estimates of the aerosol indirect effect over the Baltic Sea region derived from 12 years of MODIS observations, Atmospheric Chemistry and Physics, 17, 3133–3143, https://doi.org/10.5194/acp-17-3133-2017, https://www.atmos-chem-phys.net/17/3133/2017/, 2017.

Sayer, A. M., Munchak, L. A., Hsu, N. C., Levy, R. C., Bettenhausen, C., and Jeong, M.-J.: MODIS Collection 6 aerosol products: Comparison between Aqua's e-Deep Blue, Dark Target, and "merged" data sets, and usage recommendations, Journal of Geophysical Research: Atmospheres, 119, 13,965–13,989, https://doi.org/10.1002/2014JD022453, https://agupubs.onlinelibrary.wiley.com/doi/abs/10.1002/2014JD022453, 2014.

Schultz, M. G., Stadtler, S., Schröder, S., Taraborrelli, D., Franco, B., Krefting, J., Henrot, A., Ferrachat, S., Lohmann, U., Neubauer, D., Siegenthaler-Le Drian, C., Wahl, S., Kokkola, H., Kühn, T., Rast, S., Schmidt, H., Stier, P., Kinnison, D., Tyndall, G. S., Orlando, J. J., and Wespes, C.: The chemistry–climate model ECHAM6.3-HAM2.3-MOZ1.0, Geoscientific Model Development, 11, 1695–1723, https://doi.org/10.5194/gmd-11-1695-2018, https://www.geosci-model-dev.net/11/1695/2018/, 2018.

https://doi.org/10.5194/acp-2019-631
Preprint. Discussion started: 13 September 2019

Sporre, M. K., Swietlicki, E., Glantz, P., and Kulmala, M.: Aerosol indirect effects on continental low-level clouds over Sweden and Finland, Atmospheric Chemistry and Physics, 14, 12 167–12 179, https://doi.org/10.5194/acp-14-12167-2014, https://www.atmos-chem-phys.net/14/12167/2014/, 2014.

Sporre, M. K., O'Connor, E. J., Håkansson, N., Thoss, A., Swietlicki, E., and Petäjä, T.: Comparison of MODIS and VIIRS cloud properties with ARM ground-based observations over Finland, Atmospheric Measurement Techniques, 9, 3193–3203, https://doi.org/10.5194/amt-9-3193-2016, https://www.atmos-meas-tech.net/9/3193/2016/, 2016.

Stevens, B., Giorgetta, M., Esch, M., Mauritsen, T., Crueger, T., Rast, S., Salzmann, M., Schmidt, H., Bader, J., Block, K., Brokopf, R., Fast, I., Kinne, S., Kornblueh, L., Lohmann, U., Pincus, R., Reichler, T., and Roeckner, E.: Atmospheric component of the MPI-M Earth System Model: ECHAM6, Journal of Advances in Modeling Earth Systems, 5, 146–172, https://doi.org/10.1002/jame.20015, https://agupubs.onlinelibrary.wiley.com/doi/abs/10.1002/jame.20015, 2013.

Storelvmo, T.: Uncertainties in aerosol direct and indirect effects attributed to uncertainties in convective transport parameterizations, Atmospheric Research, 118, 357 – 369, https://doi.org/https://doi.org/10.1016/j.atmosres.2012.06.022, http://www.sciencedirect.com/science/article/pii/S0169809512002190, 2012.

Sundqvist, H., Berge, E., and Kristjánsson, J. E.: Condensation and Cloud Parameterization Studies with a Mesoscale Numerical Weather Prediction Model, Monthly Weather Review, 117, 1641–1657, https://doi.org/10.1175/1520-0493(1989)117<1641:CACPSW>2.0.CO;2, https://doi.org/10.1175/1520-0493(1989)117<1641:CACPSW>2.0.CO;2, 1989.

Taylor, K., Williamson, D., and Zwiers, F.: The sea surface temperature and sea ice concentration boundary conditions for AMIP II simulations. PCMDI Report 60, Program for Climate Model Diagnosis and Intercomparison, Lawrence Livermore National Laboratory, 25 pp., https://pcmdi.llnl.gov/report/pdf/60.pdf?id=86, 2000.

Tegen, I., Neubauer, D., Ferrachat, S., Siegenthaler-Le Drian, C., Bey, I., Schutgens, N., Stier, P., Watson-Parris, D., Stanelle, T., Schmidt, H., Rast, S., Kokkola, H., Schultz, M., Schroeder, S., Daskalakis, N., Barthel, S., Heinold, B., and Lohmann, U.: The global aerosol–climate model ECHAM6.3–HAM2.3 – Part 1: Aerosol evaluation, Geoscientific Model Development, 12, 1643–1677, https://doi.org/10.5194/gmd-12-1643-2019, https://www.geosci-model-dev.net/12/1643/2019/, 2019.

Tiedtke, M.: A Comprehensive Mass Flux Scheme for Cumulus Parameterization in Large-Scale Models, Monthly Weather Review, 117, 1779–1800, https://doi.org/10.1175/1520-0493(1989)117<1779:ACMFSF>2.0.CO;2, https://doi.org/10.1175/1520-0493(1989)117<1779:ACMFSF>2.0.CO;2, 1989.

Twomey, S.: The Influence of Pollution on the Shortwave Albedo of Clouds, Journal of the Atmospheric Sciences, 34, 1149–1152, https://doi.org/10.1175/1520-

https://doi.org/10.5194/acp-2019-631
Preprint. Discussion started: 13 September 2019

0469(1977)034<1149:TIOPOT>2.0.CO;2, https://doi.org/10.1175/1520-0469(1977)034<1149:TIOPOT>2.0.CO;2, 1977.

Wang, Y., Liu, X., Hoose, C., and Wang, B.: Different contact angle distributions for heterogeneous ice nucleation in the Community Atmospheric Model version 5, Atmospheric Chemistry and Physics, 14, 10 411–10 430, https://doi.org/10.5194/acp-14-10411-2014, https://www.atmos-chem-phys.net/14/10411/2014/, 2014.

Webb, M. J., Andrews, T., Bodas-Salcedo, A., Bony, S., Bretherton, C. S., Chadwick, R., Chepfer, H., Douville, H., Good, P., Kay, J. E., Klein, S. A., Marchand, R., Medeiros, B., Siebesma, A. P., Skinner, C. B., Stevens, B., Tselioudis, G., Tsushima, Y., and Watanabe, M.: The Cloud Feedback Model Intercomparison Project (CFMIP) contribution to CMIP6, Geoscientific Model Development, 10, 359–384, https://doi.org/10.5194/gmd-10-359-2017, https://www.geosci-model-dev.net/10/359/2017/, 2017.

Wen, G., Marshak, A., Cahalan, R. F., Remer, L. A., and Kleidman, R. G.: 3-D aerosol-cloud radiative interaction observed in collocated MODIS and ASTER images of cumulus cloud fields, Journal of Geophysical Research: Atmospheres, 112, https://doi.org/10.1029/2006JD008267, https://agupubs.onlinelibrary.wiley.com/doi/abs/10.1029/2006JD008267, 2007.

Williams, K. D. and Bodas-Salcedo, A.: A multi-diagnostic approach to cloud evaluation, Geoscientific Model Development, 10, 2547–2566, https://doi.org/10.5194/gmd-10-2547-2017, https://www.geosci-model-dev.net/10/2547/2017/, 2017.

Yu, W., Doutriaux, M., Sèze, G., Le Treut, H., and Desbois, M.: A methodology study of the validation of clouds in GCMs using ISCCP satellite observations, Climate Dynamics, 12, 389–401, https://doi.org/10.1007/BF00211685, https://doi.org/10.1007/BF00211685, 1996.

Zhang, G. and McFarlane, N.: Sensitivity of climate simulations to the parameterization of cumulus convection in the Canadian climate centre general circulation model, Atmosphere-Ocean, 33, 407–446, https://doi.org/10.1080/07055900.1995.9649539, https://doi.org/10.1080/07055900.1995.9649539, 1995.

Zhang, Y., Klein, S. A., Boyle, J., and Mace, G. G.: Evaluation of tropical cloud and precipitation statistics of Community Atmosphere Model version 3 using CloudSat and CALIPSO data, Journal of Geophysical Research: Atmospheres, 115, n/a–n/a, https://doi.org/10.1029/2009JD012006, http://dx.doi.org/10.1029/2009JD012006, d12205, 2010.

Zhang, Z., Ackerman, A. S., Feingold, G., Platnick, S., Pincus, R., and Xue, H.: Effects of cloud horizontal inhomogeneity and drizzle on remote sensing of cloud droplet effective radius: Case studies based on large-eddy simulations, Journal of Geophysical Research: Atmospheres, 117, n/a–n/a, https://doi.org/10.1029/2012JD017655, http://dx.doi.org/10.1029/2012JD017655, d19208, 2012.

ILMATIETEEN LAITOS
METEOROLOGISKA INSTITUTET
FINNISH METEOROLOGICAL INSTITUTE

FINNISH METEOROLOGICAL INSTITUTE
Erik Palménin aukio 1
P.O. Box 503
FI-00560 HELSINKI
tel. +358 29 539 1000
WWW.FMI.FI

FINNISH METEOROLOGICAL INSTITUTE
CONTRIBUTIONS No. 156
ISSN 0782-6117
ISBN 978-952-336-086-0 (paperback)
ISBN 978-952-336-087-7 (pdf)
https://doi.org/10.35614/isbn.9789523360877
Helsinki, 2020

Edita Prima Oy